Aggregate Evolution in Shear Flow: Numerical Investigation of the Role of Cohesive and Hydrodynamic Forces

by

Akash Saxena

A thesis submitted in partial fulfillment of the requirements for the degree of

Doctor of Philosophy

in

Chemical Engineering

Department of Chemical and Materials Engineering

University of Alberta

Abstract

Multiphase flows with a dispersed phase of micron-sized solid particles are common to many industrial applications, ranging from wastewater treatment to metal purification. These particles are in a size range where surface forces are significant, and thus are likely to form aggregates. When these aggregates are exposed to hydrodynamic forces, their size and structure evolve which consequently impacts the process efficiency. This research investigates the size and structure of aggregates as they evolve, under the action of hydrodynamic shear stresses. The goal of this project is to establish the effect of short-range particle-particle interactions and hydrodynamic forces on aggregate size, structure and breakage kinetics. The effect of flow inertia on aggregate behaviour is also investigated.

An Eulerian-Lagrangian approach is used to model aggregates in a dilute system. The initial aggregates are generated using an algorithm, and consist of 50 or 70 discrete spherical primary particles. Aggregate morphology is characterized by their size, their number of primary particles, and their density. The particle-particle interactions are represented using widely accepted models, and are implemented in a Discrete Element Method (DEM) that tracks the motion of every primary particle. The flow dynamics are solved by a Lattice Boltzmann Method (LBM), and the two phases are coupled through an Immersed Boundary Method (IBM). Therefore, the particles are fully resolved in the flow. For each simulation, the free-to-move aggregates are placed at the center of the domain, and their size and structure evolution is studied over time.

Initially, the role of particle-particle interaction forces relative to the viscous drag was established. Aggregates were assigned different normal and tangential components of the inter-particle cohesive forces, and submitted to a shear flow by imposing a shear stress in the liquid phase. Hydrodynamic forces are also estimated using the free draining approximation, where hydrodynamic interactions between particles are not included, and the results are compared with those obtained from a fully resolved flow. It is found that while the normal forces contribute significantly to the overall bond strength of the aggregates, they have no impact on aggregate restructuring. On the other hand, tangential forces are found to play a two-fold role. While tangential forces contribute to the overall bond strength, they also make the aggregates brittle. This leads to enhanced aggregate breakage when the tangential forces are large compared to normal forces and viscous drag. Furthermore, it is discovered that the resistance to deformation at the aggregate scale induces a flow

disturbance that reduces drag forces compared to the free-draining approximation, and significantly impacts aggregate breakage and restructuring.

With the role of interaction forces established, the impact of flow inertia on aggregate evolution was then explored. The aggregates were exposed to shear flow with non-negligible flow inertia. Initially, the breakage rate depends on the strength of particle-particle interactions relative to viscous forces. However as the drag force increases, the breakage rate is governed by momentum diffusion, which induces a delay for the imposed stresses to reach the aggregate. Simulations with scaled particle-particle forces demonstrated that flow inertia has no impact on the aggregates' stable morphology, but significantly favors breakage; a power-law relationship was found between breakage time and aggregate-scale Reynolds number.

Since flow inertia at finite Reynolds number (that also controls momentum diffusion) was found to play a significant role in aggregate breakage, an attempt to simulate aggregate evolution in accelerating flows mimicking turbulent flows at sub-Kolmogorov length scales is explored. In these simulations, the imposed shear stress is increased linearly with time. It is found that although aggregates restructure due to shear flow, their structure at breakage does not depend on the shear stress in the flow. Furthermore, their breakage is found to be delayed on increasing the flow acceleration. A possible explanation for this phenomenon is inertial effects in the flow at aggregate scale. The delay results in aggregates undergoing more rotations before breaking for higher flow accelerations. These findings suggest that models of breakage rate, as used in population balances for example, should probably consider the effect of flow inertia under accelerated flows, although no such models are readily available in the literature.

Preface

This thesis is an original work by the author, Akash Saxena, with support from supervisors Professor R.S. Sanders and Dr. Jean-Sébastien Kroll-Rabotin.

Chapter 4 of this thesis has been accepted for publication in the Journal of Colloid and Interface Science as:

> *A. Saxena, J.-S. Kroll-Rabotin, and R.S. Sanders. Numerical investigation of the respective roles of cohesive and hydrodynamic forces in aggregate restructuring under shear flow.* doi:10.1016/j.jcis.2021.08.208.

Some of the material was also presented at SINTEF CFD2017, and published as:

> *A. Saxena, J.-S. Kroll-Rabotin, and R.S. Sanders. A numerical approach to model aggregate restructuring in shear flow using DEM in Lattice-Botlzmann Simulations. Progress in Applied CFD – CFD2017, Proceedings of the 12th International Conference on Computational Fluid Dynamics in the Oil & Gas, Metallurgical and Process Industries, 2017, 791-772.*

Some of the results of this chapter have also been published as:

> *Jean-Pierre Bellot, Jean-Sébastien Kroll-Rabotin, Matthieu Gisselbrecht, Manoj Joishi, Akash Saxena, R. Sean Sanders, and Alain Jardy. Toward better control of inclusion cleanliness in a gas stirred ladle using multiscale numerical modeling. Materials 11, no. 7 (2018), 1179.*

Chapter 5 of this thesis is submitted for publication in Langmuir as

> *A. Saxena, J.-S. Kroll-Rabotin, and R.S. Sanders. Role of flow inertia in aggregate restructuring and breakage at finite Reynolds numbers.*

Also, parts of this chapter were presented at the 10th International Conference on Multiphase Flow, Rio de Janeiro, May 19-24, 2019, and parts of it have been accepted for presentation at the 21st Int. Conference on Hydrotransport (May 2022).

Chapter 6 of this thesis is ready for submission to the Journal of Fluid Mechanics as

A. Saxena, J.-S. Kroll-Rabotin, and R.S. Sanders. Exposure of fractal aggregates to accelerating flows at finite Reynolds numbers

Dedicated to my mother, who prioritized education for her kids above everything else.

Acknowledgements

First, I would like to express my deepest gratitude to my supervisors Prof. Sean Sanders and Dr. Jean-Sébastien Kroll-Rabotin. I was fortunate enough to have two great supervisors, who always supported and trusted me with the project. Without them this thesis would not have been possible.

To Dr. Kroll-Rabotin, thank you for guiding me with this project. Your technical prowess inspires me to be a better researcher, and has helped me establish the foundation of my career. You kindness and support kept me strong when times seemed hard. A conversation with you always uplifted my spirit, and motivated me to keep the pursuit for excellence going. Despite the distance, you were always available to guide me, even late into evenings. I am deeply grateful for your support.

To Prof. Sanders, thank you for considering me worthy of this project. I am grateful to you for providing me with numerous learning opportunities. From you, I have learned skills which helped me in professional as well in personal life. Your feedback always helped me see the root cause clearly, and enabled me to approach a problem more fundamentally. Thank you for the opportunities to work as your teaching assistant on multiple occasions, I learnt what it takes to be a great educator. The experience helped me greatly to learn how to express and communicate ideas.

I am thankful to David Breakey, Marcio Machado, Manoj Joishi, Matthieu Gisselbrecht, Gustavo Cifuentes Diaz and Ricardo Rossi, with whom I have had the opportunity to share and discuss ideas. Special thanks to Terry Runyon for the administrative support. I also want to thank my friends and colleagues at the Pipeline Transport Process (PTP) Research Laboratory as well as at Intitut Jean Lamour, who added a lot of fun to the years of my degree.

I am thankful to my wife Lina, whose passion and dedication for her research greatly inspires me everyday. She has always pushed me to my full potential. Lastly, I am deeply thankful to my brother Mayur, who inspired me to pursue a Phd degree in the first place.

Contents

List of Figures

List of Tables

List of symbols

Greek

α	Acceleration force coefficient, [kg]
α^+	Post-collision solution vector in LBM
α^-	Pre-collision solution vector in LBM
$\alpha^\pm$	Solution vector in LBM
β	Velocity force coefficient, [kg s]
Δ	Discrete step, []
μ	Dynamic viscosity, [Pa s]
γ	Force coefficient independent of particle velocity, [N]
$\mathcal{V}$	Volume, [m^3]
$\ddot{\gamma}$	Flow acceleration, [s^{-2}]
ρ	Fluid density, [kg m^{-3}]
ρ_p	Particle density, [kg m^{-3}]
ν	Kinematic viscosity, [m^2 s^{-1}]
$\dot{\gamma}$	Shear rate, [s^{-1}]
τ	Shear stress imposed at boundary for target shear rate, [Pa]
$\ddot{\gamma}^*$	Dimensionless flow acceleration normalized by the squared rate of diffusion across a particle, []

$\ddot{\gamma}_K$	Flow acceleration at sub-Kolmogorov length scale, [s^{-2}]
$\dot{\gamma}^*$	Dimensionless shear rate normalized by rate of diffusion across a particle, []
$\dot{\gamma}_K$	Shear rate at sub-Kolmogorov length scale, [s^{-1}]
γ_c^*	Dimensionless shear rate at the center of the domain, []
θ	Rotation in the imposed flow, [rad]
θ_c	Rotation at the center of the domain, [rad]
$\boldsymbol{\omega}$	Rotation, [rad s^{-1}]
$\underline{\boldsymbol{\sigma}}$	Stress tensor, [Pa]
$\underline{\boldsymbol{\tau}}$	Viscous stress tensor, [Pa]
τ^{BGK}	Relaxation in Bhatnagar-Gross-Krook collision operator, []
τ_K	Smallest time scale in turbulent flows, [s]
ω	Rate of rotation, [rad s^{-1}]
Ω_i^{BGK}	Collision Operator for lattice direction i given by Bhatnagar-Gross-Krook, []
$\Omega_i^{E\&S}$	Collision Operator for lattice direction i given by Eggels and Somers, []
$\underline{\boldsymbol{\omega}}$	Rotation rate tensor, [s^{-1}]
$\boldsymbol{\xi}_{ij}$	Spring elongation between particle i and j, [m]

Roman

A_H	Hamaker constant, [J]
$\boldsymbol{c_i}$	Lattice velocity in direction i, [lattice units for length]
C_i	Shielding Coefficient, []
C_n	Coordination number, []
c_s	Lattice speed of sound, [m s^{-1}] or [lattice unit for length]·[lattice unit for time]$^{-1}$
$\underline{\boldsymbol{D}}$	Strain rate tensor, [s^{-1}]
D_f	Mass fractal dimension, []

$\boldsymbol{d}_{\max}$	Critical spring elongation in tangential force model, [m]
$\mathrm{d}S$	Surface element for integration, [m^2]
$\boldsymbol{e}$	Unit vector, []
E	Young's modulus, [Pa]
$\boldsymbol{F}$	Force, [N]
f	Mass density distribution function, [kg m^{-6} s^3]
$\boldsymbol{F_{bend}}$	Bending force on a rod of particles, [N]
$\boldsymbol{F}_b$	Body force, [N]
F_{drag}	Drag force given by Stokes law for primary particles, [N]
f^{eq}	Equilibrium mass density distribution function, [kg m^{-6} s^3]
$\boldsymbol{F}_{f/p}$	Force on particle by fluid, [N]
$\boldsymbol{F}_{\text{lub}}$	Lubrication force, [N]
$\boldsymbol{f_m}$	Force of marker m, [N]
F_n	Maximum normal cohesive forces between two particles, [N]
F_n^*	Normalized maximum normal cohesive forces between two particles, [N]
$(F_n^*)_{\text{stable}}$	Stable maximum normal force for the flow conditions, [N]
$\boldsymbol{f}_{p/f}$	Force of particle on fluid, [N]
F_t	Maximum tangential cohesive forces between two particles, [N]
F_t^*	Normalized maximum tangential cohesive forces between two particles, [N]
h	domain height, [m]
$\underline{\boldsymbol{I}}$	Identity tensor, []
I	Moment of area, [kg]
$\mathcal{J}$	Tensor of inertia, [kg m]
k_b	Boltzmann constant, [J K^{-1}]

k_t	Spring constant for tangential force model, [N m^{-1}]
m	Mass, [kg]
m_i	Mass of particle i, [kg]
m_p	Mass of particle, [kg]
$\boldsymbol{n_{ij}}$	Unit vector between two particles, []
$\boldsymbol{n}$	Unit vector normal to a surface, []
N	Number of particles in an aggregate, []
N_{Born}	Born constant, []
$\tilde{N}_i$	Post-collision lattice Boltzmann distribution in direction i
N_i	Lattice Boltzmann density in direction i
N_i^{eq}	Equilibrium density distribution in direction i
$[P]$	Projection Matrix, []
p_{BGK}	Pressure in BGK operator, [Pa]
$p_{\text{E\&S}}$	Pressure in E&S operator, [Pa]
Re	Reynolds number, []
Re_{agg}	Reynolds number at aggregate scale, []
$\text{Re}_{\text{agg}}^{\text{init}}$	Reynolds number for parent aggregate, []
Re_{p}	Reynolds number at particle scale, []
R_g	Radius of gyration, [m]
r_i	Distance of particle i from the center of gravity of the aggregate, [m]
R_{ig}	Initial radius of gyration, [m]
R_p	Radius of primary particles, [m]
S	Fractal dimension structure factor, []
s	Dimensionless surface-to-surface distance between particles, []

$\mathrm{St_p}$	Particle Stokes number, []
$\boldsymbol{T}$	Torque, [N m]
t	Time, [s]
t^*	Time normalized by diffusion time across a particle, [m^4]
t_b	Aggregate breakage time in accelerated flows, [s]
t_{break}	Aggregate breakage time, [s]
t_c	Time for flow to diffuse across a particle under accelerated shear rates, [s]
t_d	Diffusion time for the imposed shear to reach the domain's center, [s]
t_d^*	Non-dimensional diffusion time for the imposed shear to reach the domain's center, []
$\boldsymbol{T}_{f/p}$	Torque on particle by fluid, [N]
T_k	Absolute temperature, [K]
F_{viscous}	Viscous force acting on a body, [N]
T_{viscous}	Force per unit area on a surface due to flow, [Pa]
u_x	Velocity of fluid in x-direction, [m s^{-1}]
$\boldsymbol{u_f}$	Fluid velocity, [m s^{-1}]
$\boldsymbol{u}_\infty$	Undisturbed velocity field, [m s^{-1}]
$\boldsymbol{u_m}$	Velocity of marker m, [N]
$\boldsymbol{u_p}$	Particle velocity, [m s^{-1}]
$\boldsymbol{v}$	Velocity, [m s^{-1}]
V_{Born}	Born repulsion potential, [J]
V_{VDW}	van der Waals potential, [J]
w_i	Weight associated with lattice velocity in direction i, []
w_m	Weight associated with Lagrangian markers in the Immersed Boundary Method, []

Operators and notations

$\langle \cdot \rangle$	Mean value
∇	Del operator
∇^2	Laplacian operator
∇_c	Del operator over velocity space
∇_x	Del operator over physical space
$\underline{\cdot}$	Tensor

Acronyms

CFD	Computational Fluid Dynamics
DEM	Discrete Element method
DLCA	Diffusion limited cluster aggregation
DLVO	Derjaguin-Landau-Verwey-Overbeek
FDA	Free Draining Approximation
FEM	Finite Element Method
FVM	Finite Volume Method
IBM	Immersed Boundary Method
LBE	Lattice Boltzmann equation
LBM	Lattice Boltzmann method
PBM	Population Balance Method
PMMA	Polymethyl methacrylate
RLCA	Reaction limited cluster aggregation
SD	Stokesian Dynamics

Chapter 1

Introduction

Multiphase flows with solids forming a dispersed phase are common to many industrial processes. Prediction of multiphase flow behavior is crucial to design, control and troubleshoot such processes. However, prediction of multiphase flow behavior is complex and is greatly affected by the dispersed phase. For example, properties such as size, density and concentration of the solid particles in the dispersed phase are known to significantly alter the rheology of multiphase systems [1]. The complexity of the problem increases when these properties change dynamically (or evolve) with the flow conditions. Therefore, over the last few decades, controlling and predicting properties of the dispersed solid particles as they evolve has been an area of active research. This project focuses on identifying the mechanisms involved in evolution of the dispersed solid phase through a mesoscale investigation, where the structure and dynamics of the solid phase are spatially and temporally resolved under flow conditions representative of macro scale systems.

1.1 Background and motivation

In many industrial processes, the solid particles that comprise the dispersed phase are often in the micron or smaller size range and thus can be described as colloidal particles [2]. Colloidal particles are known to exhibit surface charge, which results in short-range electrostatic forces between particles, commonly known as the DLVO forces (named after Derjaguin, Landau, Verwey and Overbeek). The DLVO forces describe the inter-particle colloidal interactions as a combination of a typically attractive van der Waals force and a typically repulsive electric double layer force. In the absence of the latter,

the attractive van der Waals forces can form 'bonds' between particles in close proximity, holding them together and making a singular structure. These singular structures are called aggregates.

An aggregate can be defined as a cluster of smaller discrete, mechanically stable 'primary' particles. While colloidal particles often form aggregates, the phenomenon of aggregation is not exclusive to particles in the colloidal size range. As long as surface forces are strong enough to allow a given particle to interact with other particles in the system, aggregates can be formed. For example, aggregation of primary particles with sizes beyond colloidal range can be seen in liquid metal processing and even biological systems [3]. Nonetheless, the basic mechanism of aggregation, that is, formation of bonds due to attractive forces is consistent between colloidal and the aforementioned non-colloidal systems. This allows for modeling of non-colloidal aggregates following a similar approach as for colloids.

Humans have used aggregation since 1500 BC in applications such as water purification [4]. However, it was only a century ago that the mechanism of aggregation was correctly identified [5]. Later, the electrostatic and van der Waals interactions between particles in a colloidal system were explained and quantified through the DLVO theory [6, 7]. Since the forces are short-ranged, the particles must collide (that is, brought in proximity) to form aggregates. The collision between particles can be powered by thermal energy (Brownian motion), or through the motion of the suspending fluid medium.

When the hydrodynamic forces on an aggregate increase, they can overcome bonds between primary particles and disturb the structural equilibrium of the aggregate. Particles thus rearrange such that the internal forces holding the aggregate together balance the external hydrodynamic forces. This rearrangement of particles within the aggregate is known as restructuring. If the hydrodynamic stresses are too large, such a balance is not achieved by restructuring and the aggregate will break.

This process of aggregation, breakage and restructuring is commonly seen in many industrial processes. Control and prediction of these phenomena are crucial to the processes. Some examples include:

- *Oil Sands Tailings:* In the aqueous extraction process, to extract one barrel of bitumen, 2.5 m^3 of hot water is used [8]. During the extraction process, this hot water becomes contaminated with solids consisting mainly of sand and clay particles. These solids leave the process-affected

water unfit for reuse unless it is separated from the solid fraction. This contaminated mixture of solids and water is called tailings. The solids in the tailings mainly consist of coarse sand particles (particle size > 44 μm) and fine clay particles (particle size < 44 μm) [9]. As per Stokes' law, the settling velocity of a particle depends on its density and diameter. Thus, coarse particles separate out quickly from the tailings due to their larger diameter, whereas the fine clay particles can remain suspended for decades [8]. This slow separation poses two problems. First, these tailings have to be stored in huge tailings ponds. These tailings ponds pose an environmental threat of contaminating fresh water sources [10], and poses a hazard to the wildlife [11]. Secondly, this water cools over time, and has to be heated again as the commercial extraction processes require the recycled process water to be hot [12].

One of the methods to enhance the separation process involves the use of polymers to flocculate the fine particles into larger diameter aggregates. The entire process of tailings treatment can be described as: fresh tailings are treated in a centrifuge, where the coarser particles separate as *cyclone underflow*, and tailings containing finer particles form the *cyclone overflow*. In many applications, this stream is then treated with polymers, where polymer produces larger aggregates (see Figure 1.1). This accelerates the separation process from several years to less than an hour, as the larger aggregates settle rapidly. The supernatant water, which is still hot, is recycled to the extraction process. The remaining tailings, called *thickened tailings*, can have solids concentrations of up to 50% by weight. The thickened tailings are then transported to dedicated disposal areas for further settling and water release. A major challenge with these tailings thickening processes is that after the significant effort of generating large aggregates with polymers, the tailings are sheared during transportation. Unfortunately, this can result in restructuring and breakage of aggregates, significantly reducing the effectiveness of the thickening process [13–16].

- *Liquid Metal Treatment:* For higher quality steel, secondary steelmaking processes are often used to meet the desired specifications [18]. In these processes, molten metal is stirred through a gas injected at the bottom of the ladle to achieve chemical homogeneity as illustrated in Figure 1.2a. During this process, a huge number of impurities in the metal, commonly known as 'inclusions' (see Figure 1.2b) are also removed. The inclusions in secondary steelmaking

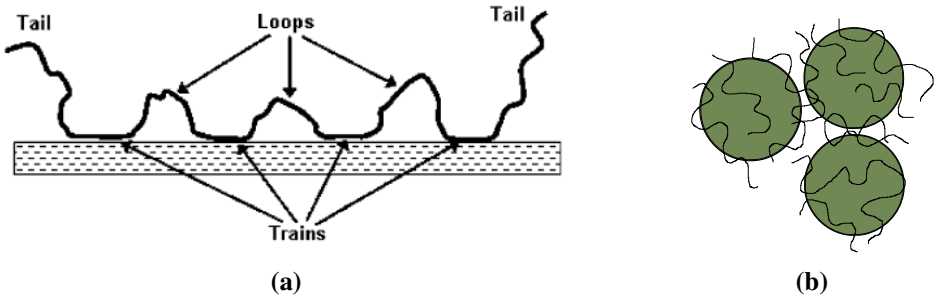

Figure 1.1: Polymer attachment to particle surfaces: (a) Model of an adsorbed polymer chain as described by Lichti et al. [17]; (b) polymer chains *bridging* different particles

processes are typically sulfides or oxides that precipitate and form aggregates. While most of the inclusions are removed during the process, the concentration and size distribution of the remaining inclusions are known to severely impact the formability and fatigue life of the metal [19]. Even a single large inclusion can lead to catastrophic failure of the steel [20]. Therefore, efficient removal of these inclusions from liquid metal is an active area of research. One way to remove these inclusions is through aggregation of small particles to form larger aggregates, which are easier to remove through flotation. The aggregates are generated due to collisions induced by turbulence in the liquid metal. Consequently, the size distribution and concentration of these inclusions is greatly impacted by the the hydrodynamics at both local and global scales [18]. Controlling and predicting the size distribution and concentrations of inclusions by simulating flow conditions representative of gas-stirred ladles has been a focus of many studies [21–24].

- *Solvent deasphalting:* Bitumen is a complex hydrocarbon mixture characterized by its high density and viscosity (greater than 10^3 kg.m^{-3} and 10^5 Pa.s at 15° C respectively [26]), presence of heteroatoms (such as nitrogen, sulfur and oxygen) and concentration of n-paraffin insoluble material called asphaltenes [27]. Asphaltenes, by definition, are a solubility class that encompasses a wide variety of molecules which can differentiate greatly from each other in terms of size or polarity [28].

  Asphaltenes represent a problem for the production, processing and transportation of bitumen [26]. They are susceptible to any changes in pressure, temperature and/or composition [29]. Any alteration to any of the mentioned parameters could favour asphaltene's tendency to

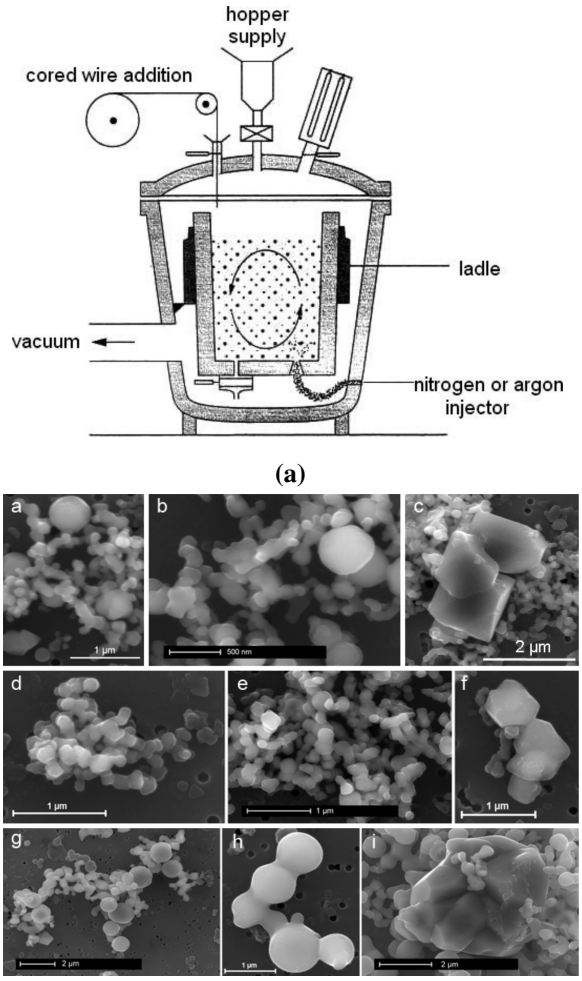

Figure 1.2: Aggregates in Metal refining: (a) Schematics of liquid metal refining through degassing taken from De Felice et al. [24], (b) Inclusions of Al_2O_3 as observed by Van Ende [25] under different oxygen concentrations and mixing duration.

associate or precipitate. In order to avoid the potential damage that asphaltenes can cause (e.g. fouling precursor), solvent deasphalting has been developed to help remove the heaviest material in the bitumen (i.e. asphaltenes) by using paraffinic solvents. This is achieved through the addition of n-paraffins which remove the suggested resin coating on the asphaltenes [30]. With no resin coating to limit solid-solid interactions, the asphaltene particles (macromolecules) aggregate into larger structures, resulting in phase separation through settling of the asphaltene aggregates. Figure 1.3 shows an aggregate extracted from solvent deasphalting. Since settling depends on the shape and size of the aggregates, these parameters also determine the design of the equipment. The two parameters can be manipulated through mixing. Therefore, mixing of

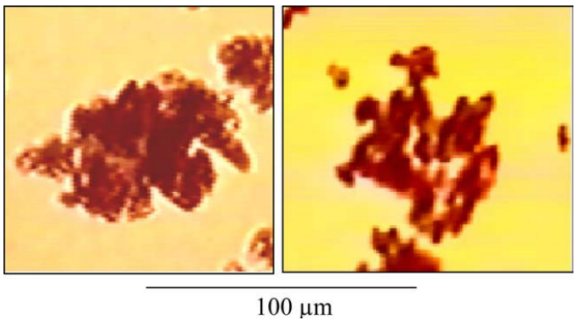

Figure 1.3: Image of aggregate obtained through asphaltene precipitation, taken from Long et al. [31]. The aggregates are porous, therefore, susceptible to restructuring under hydrodynamic forces.

aggregates has been known to contribute to phase separation of the solid-liquid phase, that is, asphaltene and oil [31]. However, mixing intensity must be optimized to obtain the ideal rate of phase separation as high shear rates are known to break aggregates [16].

- *Mineral Processing:* Recovery of fine mineral particles (size less than 100 µm) from waste or gangue minerals is mostly accomplished by froth flotation. In this process, the difference in surface wettability between valuable mineral and waste, often induced by adding chemical reagents, is exploited. A pulp of solids in water is purged with air, leading to collision of air bubbles with particles. The mineral particles attach to the bubble and float to the surface [32]. One of the parameters that determines the efficiency of collisions between particles and bubbles is the size of the mineral particles; larger sized mineral particles result in higher mineral recovery [33]. Increasing the apparent size of mineral particles by aggregation, known as shear-flocculation, is an active area of research [34].

Another important industrial system involving aggregate formation is civic waste water treatment, where the majority of organic and inorganic impurities are removed through polymer induced aggregation. Similar to treatment of oil sands tailings with polymers, aggregation removes inorganic particles such as clay and silica [35]. On the other hand, organic material, which is usually in the form of naturally anionic polyelectrolytes (also called humic substances), is removed through surface charge neutralization with cationic polymers. With the neutralization of negative charges, the humic particles form aggregates and precipitate. Aggregation through polymer bridges or through charge neutralization greatly depends on factors such as polymer properties (molecular weight and charge density), its dosage, and mixing conditions [36–38]. In other words, the effectiveness of a civic

wastewater treatment process greatly depends on its ability to form aggregates.

Aggregate control is critical to many other processes as well such as polymer manufacturing [39], food processing [40], pharmaceutical [41], silicon wafer chemical polishing [42] and paper manufacturing [43, 44].

It is evident that regardless of the engineering application, controlling aggregate properties, such as their size and shape, is critical to the process. Therefore, understanding the fundamentals of aggregate evolution based on flow conditions, primary particle characteristics, solids concentration and system chemistry is of prime importance.

Overall understanding of colloidal systems with aggregating particles is a multiscale problem. Investigations with large scale systems are often oriented towards modeling the overall processes at the scale of the treatment unit [45, 46]. Such models are used to improve the efficiency of the processes [47]. However, due to the computational costs of resolving smaller scales present in the system, the details of the two phases may be limited. Instead, CFD models at large scales often incorporate information and models developed through investigations performed at macroscopic scale. For instance, Vajihinejad and Soares [48] developed a population balance model (PBM) to predict aggregate kinetics for tailings treatment, which can be combined with large scale CFD simulations. The PBM is essentially a balance of the number of particles present in the system, while accounting for the birth and death of the particles in a given size range [49]. This birth or death of particles is often accompanied by removal or production of particles in a different size range. The model requires information such as size of the solid particles, the size of the aggregates and breakage kinetics. Often, information required for PBMs is obtained by the studies performed on the mesoscale. These mesoscale studies focus at the aggregate scale, and provide empirical or semi-empirical models for the properties as they evolve. For example, Harshe and Lattuada [50] gave correlations between breakage kinetics and the hydrodynamic stresses in simple shear flow using numerical simulations. More often, these studies are oriented towards understanding the physics involved in the process of aggregation, restructuring and breakage [51–61]. Although some experimental studies have also attempted to capture the phenomena at mesoscale [59, 62–66], it has been a challenge due to the demanding requirements for optical imaging. Therefore, many studies instead focus on numerical investigations of aggregate evolution, which typically investigate aggregate size and structure under different flow conditions [56, 67, 68]. Some studies have also

focused on the forces involved [51, 54, 55, 69], while exploring how hydrodynamic stresses are transferred to and balanced by the inter-particle forces [58, 60, 61].

Despite the numerous studies performed at the mesoscale, the fundamental physics of restructuring and breakage, such as the impact of flow inertia [66], are still under investigation. The complexities in studying these systems has several sources:

- *Interplay of physics:* Aggregate size and shape evolve due to an imbalance of inter-particle and hydrodynamic forces. Investigations to evaluate their discrete impact through experiments are limited in the amount of information they can provide. For example, while hydrodynamics can be controlled at the scale of the experimental setup [16, 53, 70, 71], the hydrodynamics around the aggregate are particularly difficult to control [63], and thus have often been approximated [53, 59]. Furthermore, the inter-particle interactions depend greatly on the material and the interface [72, 73], and varying the characteristics of the forces such as their sensitivity to separation distance, without changing other parameters is rather difficult. In contrast, simulations have been an excellent tool for studying such parameters without the limitations of a physical system, and allow for investigation of systems where individual features and their impact on aggregate evolution can be studied in a controlled manner.

- *Scale of the system:* By definition, colloidal suspensions consist of particles smaller than a micron [2, 16, 59, 70]. Due to their size, capturing the aggregate dynamics at the scale of these primary particles requires complex optical setups capable of capturing aggregate evolution as it moves along with the flow [63]. Even numerical simulations to resolve the particles and their hydrodynamic interactions require significant computational resources. Consequently, simulations must be limited to small aggregates (a few hundreds of primary particles at most) [50, 59, 74], or involve simplified, less accurate mathematical models [56, 67, 68]. Nonetheless, the results obtained from numerical simulations have compared well with the available experimental data [56, 59, 60, 66], while also evaluating the effect of particle size, particle-particle interactions, aggregate density and hydrodynamics [55, 59, 60, 69].

- *Dynamic nature of the system:* As the aggregates evolve, so does the hydrodynamic interactions among the particles of the aggregates. This has been known to play a significant role in aggregate evolution [69]. Furthermore, the restructuring and breakage occur over fractions of

a second [50, 59]. Capturing these events at such time scales has been attempted [62, 64–66], but not in a statistically meaningful way or not at primary particle scales to clearly define the breakage event. On the other hand, simulations have provided information regarding aggregate breakage rates [50], which can be used to inform macro-scale models.

From the above discussion, it can be inferred that modeling and simulations are useful tools to investigate the fundamentals of aggregate evolution by isolating and targeting specific mechanisms. This project is focused on the use of modeling and simulations to develop further understanding of aggregate evolution.

1.2 Research objectives

This project is centered around the investigation of the forces involved and their contributions towards aggregate restructuring and breakage. The investigated forces are inter-particle and hydrodynamic interactions. The hydrodynamic forces considered here are either purely viscous or include inertial contributions at the aggregate scale. The objectives of this study are

- To conduct a numerical investigation to determine respective roles of inter-particle forces in aggregate restructuring under shear flow (Chapter 4).
- To establish the role of hydrodynamic forces and flow inertia on restructuring and breakage (Chapter 5).
- To investigate the dynamic response of aggregates in transient shear flow where inertial effects are non-negligible (Chapter 6).

Through the above objectives, this project provides novel perspectives to correlate the cohesive strength of the aggregate to its inter-particle forces. Furthermore, this is a first-of-its-kind project that includes and goes as far as to establish the role of flow inertia in aggregate breakage and restructuring. Most importantly, the findings of this project question some of the long believed assumptions regarding aggregate breakage and flow inertia, and will greatly impact future numerical investigations as well as population balance models.

1.3 Thesis outline

Chapter 1 lays out the background and motivation for the project while providing an overview of the current approaches in practice to investigate aggregate evolution at both local and global level.

Chapter 2 discusses the literature involving aggregate evolution and the development of the associated theory. Further, it describes the theory involved, the current understanding and the knowledge gaps that need to be addressed for a comprehensive understanding of aggregate evolution.

Chapter 3 lays out the details of the numerical methods employed in this project and presents their validation and performance.

Chapter 4 expands the understanding of the forces involved in aggregate restructuring and breakage. Additionally, the effects of hydrodynamics are explored. A manuscript based on this chapter has been accepted for publication by the Journal of Colloid and Interface Science.

Chapter 5 picks up from the findings of Chapter 4, and incorporates flow inertia as another parameter which has not been thoroughly investigated in the literature. First, the flow inertia is studied as a combination of drag force and inertial forces. Some of the findings are compared to some available experimental data. The effect of flow inertia is then distinguished from the drag forces. The contents of this chapter has been submitted for publication in Langmuir.

Chapter 6 furthers the investigation of flow inertia into accelerated flows. The investigation is conducted to establish the effect of flow acceleration and flow inertia on aggregate evolution. The results are discussed in the context of aggregate breakage in turbulent flows. The contents of this chapter are ready for submission to the Journal of Fluid Mechanics.

Chapter 7 discusses the summary of the project and key findings. Uncertainties and challenges are addressed with ways to mitigate them for future studies. It also lists author's recommendations for future work.

1.4 Statement of author's contribution

In this thesis, the author compiled the literature review, implemented and validated the numerical models for inter-particle interactions, framed the experimental plans, conducted simulations, and processed data. The models were implemented in FORTRAN. Most of the simulations were conducted on clusters provided by Compute Canada and EXPLOR centre at the University de

Lorraine. Data was processed using MATLAB and Python. The author also validated the flow solver for the investigated flow conditions against available literature. All analysis of simulations data, results interpretation and presentation of novel findings were completed by the author, with invaluable inputs from the supervisors Prof. Sanders and Dr. Kroll-Rabotin.

References

[1] J. Mewis and N. J. Wagner. *Colloidal Suspension Rheology*. Cambridge Series in Chemical Engineering. Cambridge University Press, 2011. doi:10.1017/CBO9780511977978.

[2] International Union of Pure and Applied Chemistry. *Compendium of Polymer Terminology and Nomenclature, IUPAC Recommendations 2008*. Cambridge - Royal Society of Chemistry, 2008.

[3] F. Vernerey, E. Benet, L. Blue, A. Fajrial, S. L. Sridhar, J. Lum, G. Shakya, K. Song, A. Thomas, and M. Borden. Biological active matter aggregates: Inspiration for smart colloidal materials. *Advances in Colloid and Interface Science*, 263:38–51, 2019. ISSN 0001-8686. doi:10.1016/j.cis.2018.11.006.

[4] Office of Water (4606). 25 years of the safe drinking water act: History and trends, 1999.

[5] W. B. Hardy. A preliminary investigation of the conditions which determine the stability of irreversible hydrosols. *The Journal of Physical Chemistry*, 4(4):235–253, 1900. doi:10.1021/j150022a001.

[6] B. V. Derjaguin, N. V. Churaev, and V. M. Muller. The Derjaguin-Landau-Verwey-Overbeek (DLVO) theory of stability of lyophobic colloids. In *Surface Forces*, pages 293–310. Springer US, Boston, MA, 1987. ISBN 978-1-4757-6639-4.

[7] H. C. Hamaker. The London-van der Waals attraction between spherical particles. *Physica*, 4 (10):1058–1072, 1937. ISSN 00318914. doi:10.1016/S0031-8914(37)80203-7.

[8] J. H. Masliyah, J. Czarnecki, and Z. Xu. *Handbook on theory and practice of bitumen recovery from Athabasca oil sands*. Kingsley, 2011.

[9] J. Masliyah, Z. J. Zhou, Z. Xu, J. Czarnecki, and H. Hamza. Understanding water-based bitumen extraction from Athabasca oil sands. *The Canadian Journal of Chemical Engineering*, 82(4):628–654, 2004.

[10] R. A. Frank, J. W. Roy, G. Bickerton, S. J. Rowland, J. V. Headley, A. G. Scarlett, C. E. West, K. M. Peru, J. L. Parrott, F. M. Conly, and L. M. Hewitt. Profiling oil sands mixtures from industrial developments and natural groundwaters for source identification. *Environmental Science & Technology*, 48(5):2660–2670, 2014. doi:10.1021/es500131k.

[11] P. Gosselin, S. E. Hrudey, M. A. Naeth, A. Plourde, R. Therrien, G. Van Der Kraak, and Z. Xu. Environmental and health impacts of canada's oil sands industry, 2010.

[12] V. Wallwork, Z. Xu, and J. Masliyah. Processibility of athabasca oil sand using a laboratory hyd ro t ransport extraction system (lhes). *The Canadian Journal of Chemical Engineering*, 82 (4):687–695, 2004.

[13] P. Watson, T. Fenderson, A. Mahmoudkhani, M. Nair, A. Patel, and G. Roberts. Breakage and reformation of flocs in oil sands tailings slurries. In *Tailings and Mine Waste*, pages 293–302, 2011.

[14] A. J. McFarlane, J. Addai-Mensah, K. Bremmell, et al. Rheology of flocculated kaolinite dispersions. *Korea-Australia Rheology Journal*, 17(4):181–190, 2005.

[15] A. Demoz, V. Munoz, and R. Mikula. Optimizing mft dewatering by controlling polymer mixing. In *Second International Oil Sands Tailings Conference*, pages 107–121, 2010.

[16] F. Vaezi, R. S. Sanders, and J. H. Masliyah. Flocculation kinetics and aggregate structure of kaolinite mixtures in laminar tube flow. *Journal of Colloid and Interface Science*, 355(1): 96–105, 2011.

[17] G. Lichti, R. G. Gilbert, and D. H. Napper. The mechanisms of latex particle formation and growth in the emulsion polymerization of styrene using the surfactant sodium dodecyl sulfate. *Journal of Polymer Science Part A: Polymer Chemistry*, 21(1):269–291, 1983.

[18] J.-P. Bellot, J.-S. Kroll-Rabotin, M. Gisselbrecht, M. Joishi, A. Saxena, S. Sanders, and A. Jardy.

Toward better control of inclusion cleanliness in a gas stirred ladle using multiscale numerical modeling. *Materials*, 11:1179, July 2018. doi:10.3390/ma11071179.

[19] M. Kinoshi and A. Koyanagi. Effect of nonmetallic inclusions on rolling-contact fatigue life in bearing steels. *Bearing Steels: The Rating Nonmetallic Inclusion*, 575:138, 1975.

[20] L. Zhang and B. G. Thomas. State of the art in evaluation and control of steel cleanliness. *ISIJ International*, 43(3):271–291, 2003. doi:10.2355/isijinternational.43.271.

[21] C. G. Méndez, N. Nigro, and A. Cardona. Drag and non-drag force influences in numerical simulations of metallurgical ladles. *Journal of Materials Processing Technology*, 160(3): 296–305, 2005.

[22] M. Madan, D. Satish, and D. Mazumdar. Modeling of mixing in ladles fitted with dual plugs. *ISIJ International*, 45(5):677–685, 2005.

[23] H. Liu, Z. Qi, and M. Xu. Numerical simulation of fluid flow and interfacial behavior in three-phase argon-stirred ladles with one plug and dual plugs. *Steel Research International*, 82 (4):440–458, 2011.

[24] V. De Felice, I. L. A. Daoud, B. Dussoubs, A. Jardy, and J.-P. Bellot. Numerical modelling of inclusion behaviour in a gas-stirred ladle. *ISIJ International*, 52(7):1273–1280, 2012.

[25] M.-A. Van Ende. *Formation and morphology of non-metallic inclusions in aluminium killed steels*. PhD thesis, Université Catholique de Louvain, Leuven, Belgium, 2010.

[26] G. Murray R. *Upgrading Oilsands Bitumen and Heavy Oil*. Pica Pica Press, 2015.

[27] O. P. Strausz and E. M. Lown. *The chemistry of Alberta oil sands, bitumens and heavy oils*. Alberta Energy Research Institute Calgary, AB, 2003.

[28] I. A. Wiehe. *Process Chemistry of Petroleum Macromolecules*. CRC Press, 2008.

[29] J. Ancheyta, F. Trejo, and M. S. Rana. *Asphaltenes: Chemical Transformation during Hydroprocessing of Heavy Oils*. CRC Press, 2009.

[30] R. P. Crowley. Solvent deasphalting, 1978. US Patent No. 4,101,415.

[31] Y. Long, T. Dabros, and H. Hamza. Structure of water/solids/asphaltenes aggregates and effect of mixing temperature on settling rate in solvent-diluted bitumen. *Fuel*, 83(7-8):823–832, 2004.

[32] B. Wang and Y. Peng. The effect of saline water on mineral flotation – a critical review. *Minerals Engineering*, 66-68:13–24, 2014. ISSN 0892-6875. doi:10.1016/j.mineng.2014.04.017. Froth Flotation.

[33] R. Sivamohan. The problem of recovering very fine particles in mineral processing—a review. *International Journal of Mineral Processing*, 28(3-4):247–288, 1990.

[34] W. Chen, Q. Feng, G. Zhang, L. Li, and S. Jin. Effect of energy input on flocculation process and flotation performance of fine scheelite using sodium oleate. *Minerals Engineering*, 112: 27–35, 2017. ISSN 0892-6875. doi:10.1016/j.mineng.2017.07.002.

[35] B. Bolto and J. Gregory. Organic polyelectrolytes in water treatment. *Water Research*, 41(11): 2301–2324, 2007.

[36] M. M. Ghosh, C. D. Cox, and T. M. Prakash. Polyelectrolyte selection for water treatment. *Journal AWWA*, 77(3):67–73, 1985. doi:10.1002/j.1551-8833.1985.tb05510.x.

[37] M. Lurie and M. Rebhun. Effect of properties of polyelectrolytes on their interaction with particulates and soluble organics. *Water Science and Technology*, 36(4):93–101, 1997. ISSN 0273-1223. doi:10.1016/S0273-1223(97)00425-3. The Role of Particle Characteristics in Separation Processes.

[38] J. Gregory and L. Guibai. Effects of dosing and mixing conditions on polymer flocculation of concentrated suspensions. *Chemical Engineering Communications*, 108(1):3–21, 1991. doi:10.1080/00986449108910948.

[39] B. Pukánszky and J. Móczó. Morphology and properties of particulate filled polymers. In *Macromolecular Symposia*, volume 214, pages 115–134. Wiley Online Library, 2004. doi: 10.1002/masy.200451009.

[40] R. Mezzenga, P. Schurtenberger, A. Burbidge, and M. Michel. Understanding foods as soft materials. *Nature Materials*, 4(10):729–740, 2005.

[41] L. Nicoud, M. Owczarz, P. Arosio, and M. Morbidelli. A multiscale view of therapeutic protein aggregation: a colloid science perspective. *Biotechnology Journal*, 10(3):367–378, 2015.

[42] E. Matijević and S. Babu. Colloid aspects of chemical–mechanical planarization. *Journal of Colloid and Interface Science*, 320(1):219–237, 2008.

[43] M. Rundlöf. *Interaction of dissolved and colloidal substances with fines of mechanical pulp-Influence on sheet properties and basic aspects of adhesion*. PhD thesis, Institutionen för pappers-och massateknologi, 2002.

[44] Q. Miao, L. Huang, and L. Chen. Advances in the control of dissolved and colloidal substances present in papermaking processes: A brief review. *BioResources*, 8(1):1431–1455, 2013.

[45] A. G. Griborio. *Secondary Clarifier Modeling: A multi-process approach*. PhD thesis, University of New Orleans, 2004.

[46] M. Hallberg, P. G. Jönsson, T. L. I. Jonsson, and R. Eriksson. Process model of inclusion separation in a stirred steel ladle. *Scandinavian Journal of Metallurgy*, 34(1):41–56, 2005. doi:10.1111/j.1600-0692.2005.00716.x.

[47] S. Zhou, J. McCorquodale, J. Richardson, and T. Wilson. State of the art clarifier modeling technology-part ii. In *Proceedings of the WEFTEC 78th Annual Technical Exhibition and Conference*, 2005.

[48] V. Vajihinejad and J. B. Soares. Monitoring polymer flocculation in oil sands tailings: A population balance model approach. *Chemical Engineering Journal*, 346:447–457, 2018.

[49] M. v. Smoluchowski. Grundriß der Koagulationskinetik kolloider Lösungen. *Kolloid-Zeitschrift*, 21(3):98–104, September 1917. ISSN 0303-402X. doi:10.1007/BF01427232.

[50] Y. M. Harshe and M. Lattuada. Breakage rate of colloidal aggregates in shear flow through Stokesian dynamics. *Langmuir*, 28(1):283–292, January 2012. ISSN 0743-7463. doi:10.1021/la2038476.

[51] M. Zeidan, B. H. Xu, X. Jia, and R. A. Williams. Simulation of aggregate deformation and breakup in simple shear flows using a combined continuum and discrete model. *Chemical*

Engineering Research and Design, 85(12):1645–1654, January 2007. ISSN 0263-8762. doi:10.1016/S0263-8762(07)73208-2.

[52] L. Ehrl, M. Soos, and M. Morbidelli. Dependence of aggregate strength, structure, and light scattering properties on primary particle size under turbulent conditions in stirred tank. *Langmuir*, 24(7):3070–3081, April 2008. ISSN 0743-7463. doi:10.1021/la7032302.

[53] M. Soos, A. S. Moussa, L. Ehrl, J. Sefcik, H. Wu, and M. Morbidelli. Effect of shear rate on aggregate size and morphology investigated under turbulent conditions in stirred tank. *Journal of Colloid and Interface Science*, 319(2):577–589, 2008. doi:10.1016/j.jcis.2007.12.005.

[54] V. Becker and H. Briesen. Tangential-force model for interactions between bonded colloidal particles. *Physical Review E*, 78(6):061404, December 2008. doi:10.1103/PhysRevE.78.061404.

[55] V. Becker and H. Briesen. A master curve for the onset of shear induced restructuring of fractal colloidal aggregates. *Journal of Colloid and Interface Science*, 346(1):32–36, June 2010. ISSN 0021-9797. doi:10.1016/j.jcis.2010.02.015.

[56] M. L. Eggersdorfer, D. Kadau, H. J. Herrmann, and S. E. Pratsinis. Fragmentation and restructuring of soft-agglomerates under shear. *Journal of Colloid and Interface Science*, 342 (2):261–268, 2010. ISSN 00219797. doi:10.1016/j.jcis.2009.10.062.

[57] M. Soos, L. Ehrl, M. U. Bäbler, and M. Morbidelli. Aggregate breakup in a contracting nozzle. *Langmuir*, 26(1):10–18, 2010. doi:10.1021/la903982n.

[58] M. Vanni and A. Gastaldi. Hydrodynamic forces and critical stresses in low-density aggregates under shear flow. *Langmuir*, 27(21):12822–12833, November 2011. ISSN 0743-7463. doi:10.1021/la2024549.

[59] Y. M. Harshe, M. Lattuada, and M. Soos. Experimental and modeling study of breakage and restructuring of open and dense colloidal aggregates. *Langmuir*, 27(10):5739–5752, May 2011. doi:10.1021/la1046589.

[60] K. Horii, R. Yamada, and S. Harada. Strength deterioration of nonfractal particle aggregates in simple shear flow. *Langmuir*, 31(29):7909–7918, 2015.

[61] M. Vanni. Accurate modelling of flow induced stresses in rigid colloidal aggregates. *Computer Physics Communications*, 192:70–90, July 2015. ISSN 0010-4655. doi:10.1016/j.cpc.2015.02.022.

[62] S. X. Liu and L. A. Glasgow. Aggregate disintegration in turbulent jets. *Water, Air, and Soil Pollution*, 95(1-4):257–275, 1997.

[63] S. Blaser. Flocs in shear and strain flows. *Journal of Colloid and Interface Science*, 225(2): 273–284, 2000.

[64] M. Vlieghe, C. Coufort-Saudejaud, C. Frances, and A. Liné. In situ characterization of floc morphology by image analysis in a turbulent taylor–couette reactor. *AIChE Journal*, 60(7): 2389–2403, 2014.

[65] D. Saha, M. Soos, B. Lüthi, M. Holzner, A. Liberzon, M. U. Babler, and W. Kinzelbach. Experimental characterization of breakage rate of colloidal aggregates in axisymmetric extensional flow. *Langmuir*, 30(48):14385–14395, 2014.

[66] D. Saha, M. U. Bäbler, M. Holzner, M. Soos, B. Lüthi, A. Liberzon, and W. Kinzelbach. Breakup of finite-size colloidal aggregates in turbulent flow investigated by three-dimensional (3d) particle tracking velocimetry. *Langmuir*, 32(1):55–65, 2016. doi:10.1021/acs.langmuir.5b03804.

[67] M. Kroupa, M. Vonka, M. Soos, and J. Kosek. Size and structure of clusters formed by shear induced coagulation: Modeling by discrete element method. *Langmuir*, 31(28):7727–7737, July 2015. ISSN 0743-7463. doi:10.1021/acs.langmuir.5b01046.

[68] D. Liu, Z. Wang, X. Chen, and M. Liu. Simulation of agglomerate breakage and restructuring in shear flows: Coupled effects of shear gradient, surface energy and initial structure. *Powder Technology*, 336:102–111, 2018. doi:10.1016/j.powtec.2018.05.051.

[69] V. Becker, E. Schlauch, M. Behr, and H. Briesen. Restructuring of colloidal aggregates in shear flows and limitations of the free-draining approximation. *Journal of Colloid and Interface Science*, 339(2):362–372, 2009. doi:10.1016/j.jcis.2009.07.022.

[70] R. C. Sonntag and W. B. Russel. Structure and breakup of flocs subjected to fluid stresses: I. Shear experiments. *Journal of Colloid and Interface Science*, 113(2):399–413, 1986.

[71] A. Zaccone, M. Soos, M. Lattuada, H. Wu, M. U. Bäbler, and M. Morbidelli. Breakup of dense colloidal aggregates under hydrodynamic stresses. *Phys. Rev. E*, 79:061401, Jun 2009. doi:10.1103/PhysRevE.79.061401.

[72] J. P. Pantina and E. M. Furst. Colloidal aggregate micromechanics in the presence of divalent ions. *Langmuir*, 22(12):5282–5288, 2006. doi:10.1021/LA0534120.

[73] G. Frungieri. *A novel Monte Carlo - Discrete Element Method approach for the micro-mechanics of colloidal suspensions*. PhD thesis, Politecnico di Torino, Turin, Italy, 2018.

[74] S. Harada, R. Tanaka, H. Nogami, M. Sawada, and K. Asakura. Structural change in non-fractal particle clusters under fluid stress. *Colloids and Surfaces A: Physicochemical and Engineering Aspects*, 302(1):396–402, 2007.

Chapter 2

Colloidal aggregates in shear flow

This chapter lays out the approaches used in the literature to investigate aggregate behavior in shear flow. Later, the mathematical background and the involved physics as reported in literature is presented, followed by knowledge gaps and how this project attempts to address them.

Due to the importance of aggregates in industrial processes, attempts to understand and predict aggregate behavior date back to more than a century ago. In 1917, v. Smoluchowski [1] first established the population balance equation (PBE) to predict the aggregate kinetics deterministically. The PBE is a balance of the number of particles or aggregates present in a system, while considering the aggregation and breakage rates. The PBE has proven to be invaluable in predicting aggregate kinetics in applications ranging from liquid metal treatment [2] to mineral wastewater treatment [3]. Despite its wide applicability, the equation is unable to identify the mechanisms responsible for the observed aggregate behavior. Instead, it utilizes information obtained through other studies which investigate aggregate behavior and involved mechanisms over its 'lifespan'.

The lifespan of an aggregate starts with its birth, that is when its constituent particles form bonds resulting in a set of particles behaving as a single deformable body. This is known as *aggregation*. Under the action of hydrodynamic stresses, some bonds between primary particles can be overcome and new bonds can form, so that the structure of the aggregate changes, or constituent particles separate from the others. Theses phenomena are known as *restructuring* and *breakage*. In general, aggregates can also interact with other aggregates, leading to more complex aggregation and breakage mechanisms. For the scope of this project, only dilute systems were investigated where aggregate–aggregate interactions are minimal. Therefore, the term "aggregate evolution" with reference to this

project is limited to its restructuring and breakage in isolation.

The process of aggregation has been investigated widely, through both experiments [4–8] and simulations [9–13]. The overall understanding of aggregation can be described as follows. Aggregation occurs when spatial proximity between two primary particles is enough for the attractive forces to form 'bonds' between particles. While the attractive forces are often found to be DLVO [14], the spatial proximity of primary particles can be caused either due to Brownian motion (perikinetic aggregation), or due to the motion of the fluid media (orthokinetic aggregation). The dominating mechanism is determined by the dimensionless Péclet number (Pe), which is the ratio of convective transport rate and the diffusive transport rate (thermal diffusion for quantifying Brownian motion). For a sphere in a flow where motion is induced by shear stress, the Péclet number is defined as [15]

$$\mathrm{Pe} = \frac{6\pi\tau R_p^3}{k_b T_k} \tag{2.1}$$

where τ is the shear stress, R_p is the radius of the particle, k_b is the Boltzmann constant and T_k is the absolute temperature. At $\mathrm{Pe} < 1$, perikinetic aggregation dominates the process. When $\mathrm{Pe} \gg 1$, orthokinetic aggregation becomes the dominant mechanism.

Another classification of aggregation often used in the literature is based on collision efficiency, which is the probability of two particles forming bonds when spacial proximity is reached. The collision efficiency can depend on particle-particle interactions and flow conditions [16]. When the collision efficiency is high (for instance, colloidal particles under stagnant conditions), perikinetic aggregation occurs resulting in aggregates that are low in density. This is known as diffusion-limited cluster aggregation (DLCA). Due to the low density, the average number of bonds in the aggregate, also known as the coordination number, is also lower. This makes DLCA aggregates weak, and prone to breakage under flow. When collision efficiency is not high (for example, under shear flow conditions), only the strongest of the bonds survive, resulting in aggregates that are denser and have a higher coordination number. This type of aggregation is known as reaction-limited cluster aggregation (RLCA). Since stagnant conditions are rarely observed in industrial processes, RLCA is the most common aggregation mechanism observed.

Once an aggregate is formed, the primary particles are held together by cohesive inter-particle forces. When the aggregates are transported, they are exposed to hydrodynamic forces, which

compete with the cohesive forces. As a result, under such conditions, the primary particles in the aggregate are rearranged such that the hydrodynamic stresses may be balanced through redistribution of inter-particle stresses inside the aggregate [17, 18]. This rearrangement leads to a change in the size of the aggregates [19, 20]. If the balance is not achieved, the aggregate breaks.

This project is focused around investigation of restructuring and breakage of aggregates in shear flows.

2.1 Aggregate characterization

As aggregates evolve, they undergo changes in size and density. Therefore, aggregates are commonly characterized by their size and density [20, 21]. One way to define size is through the radius of gyration R_g. Mathematically, R_g^2 is the ratio of the second moment of mass around the center of the aggregate to the total mass.

$$R_g^2 = \frac{1}{m}\int r^2 \mathrm{d}m \tag{2.2}$$

For an aggregate consisting of N primary particles, as long as their size is small enough compared to the aggregate size ($R_p \ll R_g$), the radius of gyration of the aggregate can be approximated as

$$R_g = \sqrt{\frac{\sum_{i=1}^{N} m_i r_i^2}{\sum_{i=1}^{N} m_i}} = \sqrt{\frac{\sum_{i=1}^{N} r_i^2}{N}} \tag{2.3}$$

where r_i is the distance between particle i and the center of gravity of the aggregate, and m_i is its mass.

For aggregate density estimation, fractal dimensions are widely used. An object made up of self-repeating units is called a fractal. Aggregates made of identical particles (same size and mass), can be seen as fractal objects when they contain enough primary particles ($N \gg 1$). Their fractal dimension appears in the relation between their number of particles and their size as

$$N = S\left(\frac{R_g}{R_p}\right)^{D_f} \tag{2.4}$$

where D_f, the fractal dimension, is the exponent by which the mass scales with respect to the size

of the aggregate. The coefficient S is called *structure factor* and for aggregates made of spherical particles, Gmachowski [22] indicated an empirical relation between D_f and S

$$S = \left(\sqrt{1.56-\left(1.728-\frac{D_f}{2}\right)^2}-0.228\right)^{D_f}\left(\frac{2+D_f}{D_f}\right)^{\frac{D_f}{2}} \tag{2.5}$$

The fact that S varies with D_f illustrates that aggregates are not truly fractal objects and the finite size of their primary particles can rarely be ignored. Nonetheless, their treatment as fractal objects helps in quantifying density as fractal dimension, which is easy to measure in experiments through methods such as light scattering [4, 19, 23, 24], image analysis [19, 20, 25, 26] and even through settling velocities of aggregates [20]. Moreover, for D_f from 1 to 3, Equation (2.5) shows that S remains of the order of 1 with relatively little variation (between 0.5 and 2), which confirms that the fractal model applies relatively well to aggregates.

Equations (2.4) and (2.5) show that if the number of particles within an aggregate remain the same, its fractal dimension depends only on its radius of gyration, inferring that radius of gyration can also be used to quantify aggregate density when the number of particles is known. Other density estimation parameters include *coordination number* C_n, which is the average bonds per particle in the aggregate, and radial distribution of particles. However, there is no direct method to extract them from experiments. Therefore, their use has been limited to simulation studies, although their evolution over time can provide useful insights into the structural changes of aggregates [27–29].

2.2 Restructuring and breakage

Since restructuring and breakage of aggregates depend on the interplay of the involved forces, investigation into the evolution of aggregates in flow can give insights into the mechanics at play. For example, several studies have estimated the cohesive forces between particles by correlating hydrodynamic forces and breakage [30–34]. Studies such as Blaser [35] observed the restructuring of individual aggregates, which later helped understand how the hydrodynamic stresses acting on the aggregate evolve along with the aggregate [18].

2.2.1 Experimental works

A common experimental approach for investigating aggregate evolution has been to create flow conditions and evaluate the size of aggregates as they evolve. One of the earliest experimental study of aggregate evolution was performed by Hannah et al. [36] in a Couette cell device. The study was the first to use a sheared flow in a Couette cell instead of the traditionally used 'jar tests', where turbidity was the criteria for aggregation. Sonntag and Russel [4] performed further analysis in Couette cell. They investigated the evolution of aggregates under shear flow conditions at different shear rates, and measured the stable size at the end of shearing. Since higher shear rates lead to higher hydrodynamic forces competing against the fixed cohesive forces, the aggregates break into smaller fragments till a stable size is achieved. While this was known at the time, Sonntag and Russel [4] were the first to report a power-law relationship between the maximum stable aggregate size and shear stresses. The power-law relationship served as a proxy for aggregate strength [26]. Later, Sonntag and Russel [37] presented a theoretical background to explain the observed phenomenon based on internal structure of the aggregate, such as the hydrodynamic shielding due to the neighbouring particles within an aggregate. Several other experimental studies also measured the final stable size of aggregates [23, 26, 30, 38, 39]. These studies explored the questions such as the mechanisms of breakage and restructuring, and the role of the hydrodynamic and cohesive forces.

To investigate the mechanisms of aggregate evolution, image analysis of aggregates provided insights at the level of individual aggregates. Since aggregates are fragile, they can break while extracting sample for microscopic observations [20]. Therefore, imaging must be done in situ. One of the early studies with imaging was performed by Glasgow and Hsu [40], where they observed aggregate breakage in turbulent jets. They reported that the strength per unit mass decreases with increasing aggregate size. This was one of the first studies to estimate aggregate strength. Later, Smith and Van De Ven [41] used imaging to observe breakage of solid-liquid clusters, and found the volume fraction within the aggregates to greatly determine the cluster strength. Using imaging, Rwei et al. [42] identified the mechanisms of breakage, namely rupture and erosion. Erosion was characterized as detachment of small fragments from the outer surface of the aggregate. The ratio of cohesive forces to applied stress was identified as the parameter for determining the mechanism. Similar breakage by erosion was observed by others [41, 43, 44].

Due to the inherent value in optically observing the aggregates as demonstrated by Rwei et al. [42], attempts were made to optically track their evolution in situ. Liu and Glasgow [44] used high-speed imaging to observe aggregate breakage in a turbulent jet, and observed breakage events within one second of aggregates encountering the flow. Further, they observed the importance of hydrodynamics. In particular, they found that the size distribution of the broken fragments was influenced by smaller eddies acting on the rotating and elongated branches of the aggregate. Later, Blaser [35] used a four-roll mill to study aggregates evolution discretely in shear flow, and observed restructuring as the aggregates rotated with the vorticity of the flow. However, both of these studies could not capture images of a statistically significant number of aggregates; Liu and Glasgow [44] studied five aggregates, while Blaser [35] captured 19 aggregates. The captured aggregates may not have been representative of the entire population of aggregates in their respective systems. Nonetheless, attempts at capturing the details of aggregate evolution through imaging are still conducted in more recent works [26, 45].

2.2.2 Modeling and simulations

Due to the limits of information obtainable from experiments, attempts to understand the fundamentals of aggregate evolution through modeling and simulations have been conducted in parallel to experimental work. Specifically, the fundamentals of focus have been the hydrodynamic stresses and cohesive forces.

Due to the complexity of the physics, the aggregates were first assumed to be of simple shapes such as spheres, and stresses across the sphere were calculated in shear flow to predict aggregate breakage [46]. The cohesive forces were estimated through the Bingham yield stress. The assumption of uniform structure (and thus, uniform strength) within the aggregate failed to explain the decrease in aggregate strength with size. Later, Adler and Mills [47] refined the model by considering porosity. Although the model qualitatively explained phenomenon such as yield stress, explanation for results presented by Sonntag and Russel [4] required consideration of complex shape and flow within the aggregate [37]. Thus, aggregates were required to be represented as a set of discrete particles, held together by cohesive forces.

Cundall and Strack [48] created the framework for numerically tracking large numbers of interacting particles by solving their force and torque balance. The framework came to be known as

the Discrete Element Method (DEM), and it opened pathways for investigating aggregates consisting of 'discrete' individual particles. Through DEM, it was possible to model inter-particle forces between any two primary particles. Therefore, rather than oversimplifying aggregate's shape to spheres, the aggregates were built from discrete particles interacting with each other, described with Lagrangian approach. Hydrodynamic forces were modeled or calculated by fully resolving the flow around the primary particles.

2.2.3 Particle-particle interactions

Since aggregates are commonly found in colloidal systems, particle-particle interactions have commonly been represented through the DLVO theory [14]. Particles of the same material are known to exhibit attraction through van der Waals (VDW) forces [49]. The VDW potential between two spheres of radii R_p is

$$V_{VDW}(s) = -\frac{A_h}{12(s-2)} \tag{2.6}$$

where s is the distance between particle centers normalized by particle radius R_p, and A_h is the Hamaker constant for the two spheres separated by a 2$^{\text{nd}}$ (continuous) phase.

Since VDW forces are generally attractive in nature, a 'non-overlapping' force is often described in conjunction with VDW. One such commonly used non-overlapping force is known as Born repulsion [52] and its potential V_{Born} is expressed as

$$V_{\text{Born}}(s) = \frac{A_H N_{\text{Born}}}{s}\left[\frac{s^2-14s+54}{(s-2)^7} + \frac{60-2s^2}{s^7} + \frac{s^2+14s+54}{(s+2)^7}\right] \tag{2.7}$$

This expression, given by Feke et al. [52], originates from the theory of overlapping electron clouds: when two particles are too close, the electron clouds start to overlap. This results in an infinitely high repulsive force at very short distances between the two particles, which prevents any possibility of particle-particle overlapping. Together, VDW and Born repulsion provide a force profile as shown in Figure 2.1. When two particles approach each other, they experience a net force given by the combination of the two. Initially, when the separation distance is large, the attractive forces dominate, till a peak (maximum) attractive force is reached. When the separation distance is too small, the repulsive forces dominate and prevent any particle overlap. This also implies that when two particles are bonded through a combination of VDW and Born repulsion, the external force to break the bond

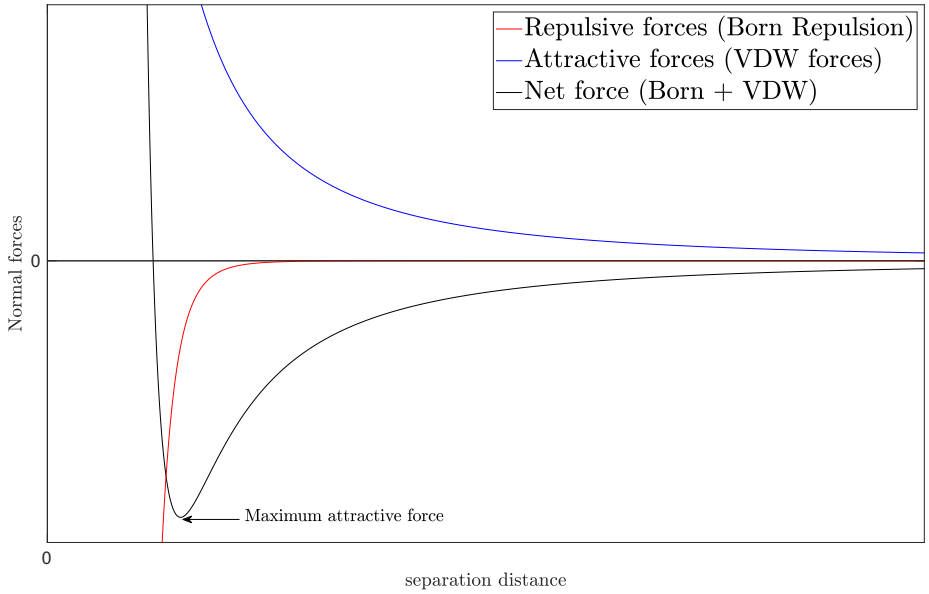

Figure 2.1: Normal force profile with separation distance.

must be larger than the maximum attractive force. Such a combination of VDW and Born repulsion to represent cohesive forces is often used in aggregate evolution studies [19, 53].

More general models such as spring-dashpot model [54, 55] and magnetic model [56] have also been used. While VDW+Born forces are conservative (or elastic) in nature, spring-dashpot model involves energy dissipation. However, since aggregates are surrounded by fluid, any movement of particle is accompanied by opposing drag forces which dissipate kinetic energy as heat. This results in VDW+Born forces to effectively behave as non-conservative forces in nature.

Since VDW+Born forces act normal to the surfaces, they are also referred as the normal forces. Other than normal interactions, forces tangential to the surfaces have also been observed in colloidal systems. Pantina and Furst [57] observed aggregates of polymethyl methacrylate (PMMA) in the shape of linear chain. Application of torque at the ends of the aggregate resulted in bending of the aggregate (Figure 2.2a). The bending observed was analogous to that of a thin rod under similar torque. Later, Becker and Briesen [58] developed a tangential force model which imparted a bending moment to the aggregate. The model described a tangential force through elastic springs between two adjacent particles (Figure 2.2b). This tangential force model has been used widely in aggregate studies [19, 59–61]. Similar to the tangential forces, a torsional force can also be defined as described by Becker et al. [59]. Although a torsional force is reasoned to exist, so far there is no evidence of its existence in colloidal aggregates, and is often ignored to reduce tuning parameters [18].

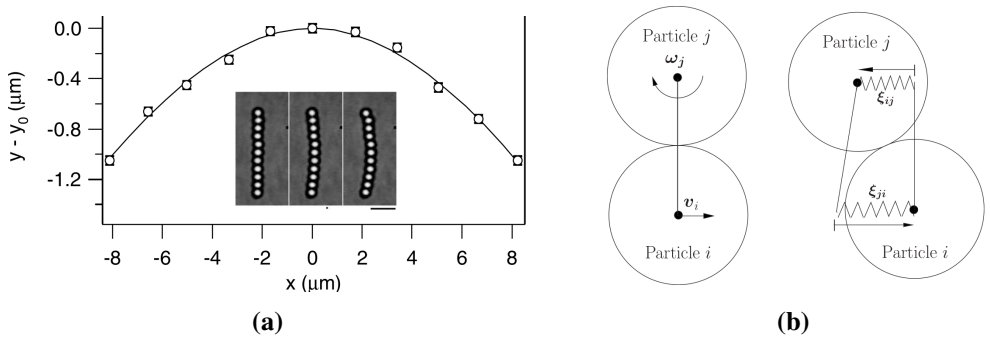

(a) **(b)**

Figure 2.2: Tangential forces in aggregates. (a) Bending of 11 particle aggregate as reported by Pantina and Furst [57]. (b) Bending moment modelled through tangential forces represented through linear elastic springs in tangential directions, taken from Becker and Briesen [58]

Any force between two particles can be decomposed into a normal force and a tangential force. Although the force models are often derived from DLVO theory, by tuning the maximum values of the normal and tangential components, they can be used to model interactions of any nature as long as they can be represented as contact forces. For instance, such a combination can be used to model particle-particle interaction forces in aggregates bonded through polymers in bridging flocculation.

The structural evolution of aggregates is driven by the response of contact interactions between particles to hydrodynamic forces. Therefore, modeling of the hydrodynamics is as important as inter-particle forces to capture aggregate restructuring and breakage dynamics.

2.2.4 Hydrodynamics

In early studies of aggregate behavior, hydrodynamics were approximated at the aggregate scale, ignoring the intricate details of the flow inside the aggregate. For example, Bagster and Tomi [46] calculated the hydrodynamic stresses across the entire aggregate, and attempted to establish the critical stresses for breakage. Adler and Mills [47] attempted to include the stresses inside porous aggregates, and later also plotted the streamlines around them [62]. Due to the porosity of the aggregates, the fluid experiences a body force as it flows through the porous structures of the aggregate. This was theorized to impact the long-range hydrodynamic interactions, that is the overall Stokesian drag force on the aggregate. Later, Sonntag and Russel [4] evaluated the 'shielding effect' of neighboring particles; since a particle in an aggregate is surrounded by other particles, its hydrodynamic interactions result in a reduction of the drag forces. These interactions are also termed as short-range hydrodynamic interactions as they are greatly influenced by immediate surroundings

of the particle.

The concept of shielding effect is based on the works of O'Neill [63], where an exact solution was developed for slow viscous flow due to two contacting (bonded) spheres translating perpendicular to the line of contact. The drag forces for each particle of this 'dimer' (⬭) were found to be reduced by a factor of roughly 0.724. This lead to the definition of shielding effect which is the coefficient C_i by which Stokesian drag is reduced on a particle of the aggregate in the presence of the neighbouring particles [64]. For any particle in the aggregate it can be expressed as

$$\boldsymbol{F_{f/p}} = \boldsymbol{F_{drag}} = \underbrace{6\,\pi\mu R_p(\boldsymbol{u_f} - \boldsymbol{u_p})}_{\text{Stokesian drag}}\, C_i \tag{2.8}$$

The coefficient C_i is a function of the number of immediate neighbours of the particle in consideration. These neighboring particles prevent the particles from "feeling the full force of the flow" [64]. Although exact solutions were not available for anything other than a dimer, shielding coefficients were estimated through models and experimental data of polymers using intrinsic viscosity [64, 65].

When aggregates were modeled to consist of discrete interacting particles, and the motion was solved through the DEM, it was possible to include the hydrodynamic interactions in the form of Stokesian drag on each particle as

$$m\,\frac{d\boldsymbol{v}}{dt} = \boldsymbol{F_{p/p}} + \boldsymbol{F_{drag}} \tag{2.9}$$

For simplicity, the shielding coefficient C_i was not included. This approach to include hydrodynamic forces is called the Free-Draining Approximation (FDA). By ignoring the shielding effects as described in Equation (2.8), FDA is only a one-way coupling between the two phases, that is, solid and fluid. Thus, it ignores the impact on hydrodynamics due to the presence of particles. Further, since it is based on the Stokes drag which itself originates from creeping flow around a sphere, it is inherently limited to low Reynolds number conditions. Therefore, FDA cannot account for any inertial effect in the flow. Despite its shortcomings, its simplicity in numerical implementation and low computational costs made the method popular in studying aggregate behaviour of large low density aggregates in low Reynolds number conditions [9, 66, 67].

To improve upon the shortcoming of FDA, the flow around the aggregate must be solved. In

1988, Brady and Bossis [68] developed Stokesian Dynamics (SD) to accurately solve the flow around multiple rigid spheres in motion by expanding disturbance in the flow induced by spherical particles as multipole series. The method is based on Faxen's laws that give analytical solutions of the force caused by the fluid on particles. In essence, these laws are corrections to the Stokesian drag expression and the first law is expressed as

$$\boldsymbol{F_{f/p}} = \underbrace{6\,\pi\mu R_p[\boldsymbol{u}_\infty - \boldsymbol{u}_p]}_{\text{Stokesian drag}} + \underbrace{\pi\mu R_p^3 \nabla^2 \boldsymbol{u}_\infty}_{\text{Correction for disturbance}} \tag{2.10}$$

where $\boldsymbol{u}_\infty$ is the undisturbed velocity field at the center of the spherical particle, and $\boldsymbol{u}_p$ is the velocity of the spherical particle. The so-called undisturbed flow is the flow that would be in the absence of the considered particle. In SD, the disturbance flow field induced by a particle is derived from the force it exerts on the fluid. The second Faxen's law describes the torque that couples the fluid and the particle motions. Force and torque acting on particles are also ruled by Newton's momentum equation. This closes the equation system and yields a two-way coupled equation set which relates the solid and fluid phases. In low Reynolds number conditions, the disturbances in the fluid velocity field induced by each individual particles can be superimposed and result in the total disturbance on the flow caused by all the particles.

Although SD was developed in 1988, the computation costs at that time were too high for studying aggregate evolutions. Twenty years later, as computational power have been catching up, SD has been widely adopted to investigate aggregate evolution [17–19, 53, 59, 60, 69]. However, since SD fundamentally depends on superimposition of the multipole expansion of the viscous creeping flow between spheres, superimposition of solutions only applies to linear systems. Such a linear system is derived from the Navier-Stokes equations by assuming the convective terms (inertial terms) to be negligible compared to the viscous terms. Therefore, application of SD is limited to low Reynolds number conditions. Other similar methods based on Stokes equations such as Finite Element Method (FEM) [70, 71] have the same limitations.

To account for any inertial effects, full Navier-Stokes equation must be solved. Due to the non-linear partial differential nature of the Navier-Stokes equations, no general solution has been found yet. As an alternate, numerous numerical methods have been widely adopted to fully solve Navier-Stokes equations with reasonable accuracy. For example, Finite Volume Method (FVM) is

one of the most common solvers, where the entire volume is discretized into smaller finite sized volumes, and integral form of the Navier-Stokes equations is discretized at each volume. Although FVM is widely used for industrial applications, it is ill suited for aggregate evolution studies as it is computationally expensive for complex moving boundaries.

Another promising Navier-Stokes solver is the Lattice Boltzmann Method (LBM). This method originates from lattice gas automata, which are molecular dynamics models. It is an indirect Navier-Stokes solver, that is, it actually solves a discretized form of Boltzmann equation, which leads to second order accurate solution of the Navier-Stokes equations that can be recovered by calculating the moments of the Boltzmann distributions. Since LBM is known to be good at solving flow through complex boundaries [72], it is suitable to solve flow around aggregates where complex dynamic geometries exist between particles. Further, due to its explicit nature, it is easy to parallelize [72] and take advantage of modern CPU architectures. One of the earliest implementations of LBM to study aggregate evolution was published by Inamuro and Ii [73] where they evaluated the role of hydrodynamic and cohesive forces in determining the breakage of aggregates. However, due to the computation costs at the time, they assumed that the solid-liquid interface to be of non-zero thickness. Therefore, inaccuracy in the results was expected, although they could not verify their results due to lack of experimental data. Later, Schlauch et al. [70] compared FEM and LBM to SD for flow through aggregates, and found both FEM and LBM to evaluate torque and drag forces in good agreement with values obtained through SD. This proved the viability for using LBM with well resolved particles in the flow. Therefore the advantages for using LBM in aggregate evolution studies are that it

1. Can solve full Navier-Stokes equation which accounts for inertial effects in the flow;
2. Is good at resolving complex boundaries;
3. Is easy to implement and parallelize;
4. Provides reasonably accurate results.

To couple the two phases, an Immersed Boundary Method (IBM) is often used [74] to impose a no-slip boundary condition at the interface between liquid and solids, that is, the relative velocity of the fluid and the particle at the particle surface is zero. With particles represented and tracked through

DEM, fluid-solid coupled through IBM, and flow solved through LBM, the combined approach becomes a powerful tool to solve fully coupled solid-fluid multiphase flows where flow and particle dynamics are fully resolved.

2.3 Current understanding of aggregate evolution and its governing physics

2.3.1 Hydrodynamic forces acting on aggregates

Aggregate evolution is a hydrodynamics driven process. In the absence of body force, Navier-Stokes equations read

$$\rho\left(\frac{\partial \boldsymbol{u}}{\partial t} + \nabla \boldsymbol{u} \cdot \boldsymbol{u}\right) = \nabla \cdot \underline{\boldsymbol{\sigma}} \tag{2.11}$$

where, $\underline{\boldsymbol{\sigma}}$ is the stress tensor. For an incompressible flow of an isotropic Newtonian fluid with viscosity μ, the stress tensor is related to the pressure p and the strain rate tensor $\underline{\boldsymbol{D}}$ as

$$\begin{aligned} \underline{\boldsymbol{\sigma}} &= -p\underline{\boldsymbol{I}} + 2\mu\underline{\boldsymbol{D}} \\ \text{with } \underline{\boldsymbol{D}} &= \frac{1}{2}(\nabla \boldsymbol{u} + \nabla \boldsymbol{u}^T) \end{aligned} \tag{2.12}$$

If rigid bodies, such as particles of an aggregate, are present in the flow, they will also experience the hydrodynamic stresses as given by Equation (2.12). For example, under the assumption of viscous flow, integration of the stresses over the surface of a stationary spherical particle leads to the Stokesian drag as

$$\boldsymbol{F_{drag}} = \int_{\text{Sphere}} (\underline{\boldsymbol{\sigma}} \cdot \boldsymbol{n}) \mathrm{d}S = 6\pi\mu R_p \boldsymbol{u}^{\infty} \tag{2.13}$$

In case of aggregates where multiple spherical particles are present, the Equation (2.12) is solved numerically as it requires the resolved flow field $\boldsymbol{u}$. The flow field is disturbed due to the presence and motion of particles, or/and due to the flow inertia. Numerical studies where the particles are resolved in the flow have shown the resolved hydrodynamics impact aggregate behavior significantly. For example, Becker et al. [59] solved the flow using Finite Element Method (FEM) and compared the drag forces on particles of an aggregate with those from the Free Draining Approximation FDA. As

an improvement to FDA, they suggested using an effective shear rate determined from fully resolved simulations. Later, Seto et al. [75] investigated aggregates evolving under accelerating flow and observed the size of the aggregates as the flow accelerated. They compared the aggregate evolution with hydrodynamics using Stokesian Dynamics (SD) with FDA. The aggregates had significantly different size evolution for SD when compared to FDA. As has been long been suggested by Sonntag and Russel [37], this difference in evolution for FDA vs SD originates from the short-range hydrodynamic interactions.

When we consider a velocity field which can be described through a smooth function such that

$$\boldsymbol{u} = \boldsymbol{u}(\boldsymbol{x}, t) \tag{2.14}$$

its gradient can be expressed as a combination of a symmetric part $\underline{\boldsymbol{D}}$ and an antisymmetric part $\underline{\boldsymbol{\omega}}$ as

$$\underline{\boldsymbol{D}} = \frac{1}{2}(\nabla \boldsymbol{u} + \nabla \boldsymbol{u}^T) \tag{2.15}$$

$$\underline{\boldsymbol{\omega}} = \frac{1}{2}(\nabla \boldsymbol{u} - \nabla \boldsymbol{u}^T) \tag{2.16}$$

$$\implies \nabla \boldsymbol{u} = \underline{\boldsymbol{D}} + \underline{\boldsymbol{\omega}} \tag{2.17}$$

The physical meaning of this decomposition of the velocity gradient can be extracted from the Taylor series relating the velocities of two points separated by a small distance $\delta \boldsymbol{x}$

$$\boldsymbol{u}(\boldsymbol{x} + \delta \boldsymbol{x}, t) = \boldsymbol{u}(\boldsymbol{x}, t) + \nabla \boldsymbol{u}(\boldsymbol{x}, t) \cdot \delta \boldsymbol{x} + O(\delta \boldsymbol{x}) \tag{2.18}$$

so that any velocity field can locally be approximated by a translation velocity, a strain rate and rotation rate. As the flow rotates, any free-to-move particle in the system also follows the rotation along with the fluid. Therefore, a freely suspended particle in a flow will have an angular velocity $\boldsymbol{\omega}$ defined so that

$$\boldsymbol{\omega} \times \delta \boldsymbol{x} = \underline{\boldsymbol{\omega}} \cdot \delta \boldsymbol{x} \tag{2.19}$$

In the absence of particles, a flow driven by a constant shear stress flows in layers that have all

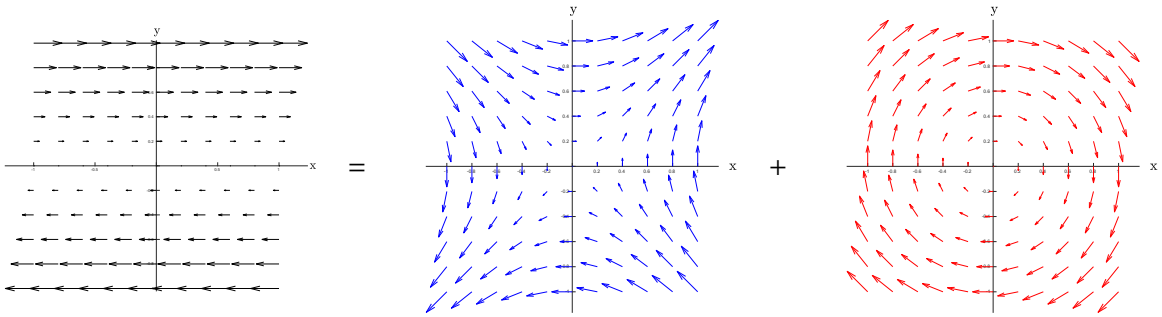

Figure 2.3: Example of simple shear flow described as a combination of pure straining and pure rotational flow. Plots are made through expressions of Equation (2.17) for simple shear flow.

the same velocity direction. Such a flow is called simple shear flow, and can be expressed as

$$u_x = \dot{\gamma} y \tag{2.20}$$

$$u_y = u_z = 0 \tag{2.21}$$

where x is the direction of the flow and y is the direction across which opposite shear stresses are imposed. Figure 2.3 plots the symmetric and antisymmetric parts of the velocity gradient in such a flow and illustrates the respective elongation and rigid-like rotation of the flow. For such a case, the undisturbed flow field is given as

$$\boldsymbol{u} = \underline{\boldsymbol{D}} \cdot \boldsymbol{x} + \underline{\boldsymbol{\omega}} \cdot \boldsymbol{x} \tag{2.22}$$

$$\underline{\boldsymbol{D}} = \frac{\dot{\gamma}}{2}\begin{pmatrix} 0 & 1 & 0 \\ 1 & 0 & 0 \\ 0 & 0 & 0 \end{pmatrix}, \quad \underline{\boldsymbol{\omega}} = -\frac{\dot{\gamma}}{2}\begin{pmatrix} 0 & 1 & 0 \\ -1 & 0 & 0 \\ 0 & 0 & 0 \end{pmatrix} \tag{2.23}$$

Therefore, an aggregate in simple shear flow will rotate with a rotation rate of $\dot{\gamma}/2$, and will experience viscous stresses as

$$\underline{\boldsymbol{\tau}} = 2\mu \underline{\boldsymbol{D}} \tag{2.24}$$

Considering a sphere centered at $\boldsymbol{x} = \mathbf{0}$, the force per unit area $\boldsymbol{T}_{\text{viscous}}$ on its surface due to the viscous stress can be expressed as a function of the viscous stress tensor $\underline{\boldsymbol{\tau}}$ and of the unit vector $\boldsymbol{n}$

normal to the sphere surface

$$\boldsymbol{T}_{\text{viscous}} = \underline{\boldsymbol{\tau}} \cdot \boldsymbol{n} \tag{2.25}$$

In a 2D plan, the sphere reduces to a circle and the relation for $\boldsymbol{T}$ can be written using the polar angle θ as

$$\boldsymbol{T}_{\text{viscous}} = 2\mu \underline{\boldsymbol{D}} \cdot (\cos\theta \boldsymbol{i} + \sin\theta \boldsymbol{j}) \tag{2.26}$$

$$= \mu\dot{\gamma}(\sin\theta \boldsymbol{i} + \cos\theta \boldsymbol{j}) \tag{2.27}$$

Such stresses are as shown in Figure 2.4 for spheres of various radii. The arrow fields show that the domain divides into 4 quadrants, where stresses in the first and third quadrant exert traction on the sphere surfaces, while in second and fourth quadrant they exert compression. Further, the traction and compression stresses are maximum at θ where the viscous stresses are normal to the surface, that is

$$\frac{\partial(\underline{\boldsymbol{\tau}} \cdot \boldsymbol{n})}{\partial\theta} = 0 \tag{2.28}$$

$$\implies \frac{\partial}{\partial\theta}\Big[(\sin\theta \boldsymbol{i} + \cos\theta \boldsymbol{j}) \cdot (\cos\theta \boldsymbol{i} + \sin\theta \boldsymbol{j})\Big] = 0 \tag{2.29}$$

$$\implies \sin^2\theta - \cos^2\theta = 0 \implies \tan^2\theta = 1$$

$$\implies \theta = n\pi \pm \frac{\pi}{4} \tag{2.30}$$

The axes at angle $n\pi \pm \frac{\pi}{4}$ are also called the *principal axes of stress*.

When an aggregate is present in a shear flow, it rotates due to the anti-symmetric part of the velocity gradient. While rotating, its parts pass through the zones of traction and compression as depicted in Figure 2.4, and the corresponding stresses increase as aggregate parts become closer to the principal axes. This results in a cyclic change in structure of the aggregate. This was first theorized for soft-matter by Zia et al. [76]. Schroeder et al. [77] observed the periodic change in size of DNA molecules. Blaser [35] also observed periodic change in colloidal aggregate size in simple shear flow but noted that the deformation was not along the principal axes as previously believed. Instead, the deformation was found to reach its maximum value along the streamlines, that is close to $\theta = 0°$ instead of $\theta = 45°$. Blaser [35] attributed this discrepancy to delay in compression

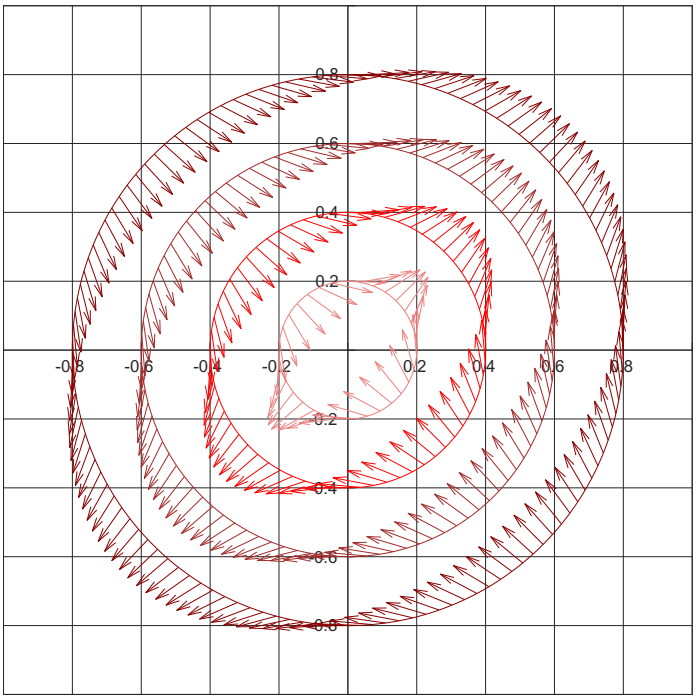

Figure 2.4: Representation of viscous stresses on spheres of different radii, as calculated from Equation (2.25).

and elongation experienced by the aggregate due to restructuring during rotation. Horii et al. [18] confirmed this behaviour by performing numerical simulations for similar shaped aggregates as the experimental data from Blaser [35]. They also tried to visualize how the hydrodynamic stresses were acting on aggregates to evaluate the forces acting on them assuming their shape to be an ellipsoid. Their study did not address the transfer of hydrodynamic stresses at individual particle scales through the complex structure of the aggregate.

2.3.2 Hydrodynamic stresses against aggregate bonds

With the understanding of how hydrodynamic stresses are exerted on the aggregate as a whole, it is the distribution of these stresses through the aggregate structure which determines the strength of the aggregate. Gastaldi and Vanni [78] studied the stress distribution on rigid aggregates in uniform flow field, and later in simple shear flow [17]. They concluded that hydrodynamic stress redistribution within an aggregate depends on its density. An aggregate with high density (D_f> 2.3) without any prominent filamentous structures redistributes the stresses uniformly as it has a higher coordination number C_n. They showed that for less dense aggregates (1.3<D_f<2.3) where filamentous structures

are present, the stresses are accumulated at the root of the filamentous structures, which happens to be close to the aggregate core. Later, Vanni [69] used structural mechanics to evaluate stress distribution in dynamic aggregates. This allowed capturing stresses between bonds of an aggregate as it evolved. The author found that breakup for low density aggregate was due to breakage of single bond usually located close to the aggregate core, whereas breakage in dense aggregates initiates due to breakage of bonds in the outer regions of the aggregate. Either, a small fragment of particles breaks away, or the broken bonds lead to generation of cracks (as proposed by Horii et al. [18]) through the aggregate resulting in aggregate breakage into fragments of comparable sizes.

Since hydrodynamic stresses are balanced through the inter-particle bonds, breakage depends on the strength of the bonds compared to the hydrodynamic stresses. As discussed earlier, the normal bonds break when an external force greater than the maximum attractive force is applied. This makes the maximum attractive/cohesive force the parameter of interest in determining the strength of aggregates [71]. In most systems, the maximum attractive force occurs at inter-particle separation distances that are much smaller than the size of the primary particles. For example, in a colloidal suspension of micrometric latex beads in water ($\sim 10^{-6}$ m), the maximum attractive force is over a few nanometers for DLVO bonds ($\sim 10^{-9}$ m). Even longer range polymer bridging reaches a maximum over 40 to 50 nm that is still small compared to the bead size. As a result, the distance over which attractive forces vary are negligible compared to the smallest dimension that characterizes aggregates, that is, the size of their primary particles. Therefore, the variation of the attractive force with separation distance is not a scaling parameter to study aggregate evolution.

The role of cohesive forces has been investigated extensively in the literature. For example, Zeidan et al. [79] performed simulations to investigate the effect of cohesive forces in the breakage mechanism. They found that relatively higher cohesive forces lead to breakage through erosion of particles, while lower cohesive forces lead to breakage through rupturing. A study performed by Becker et al. [59] investigated the effect of cohesive forces on restructuring, and observed no significant correlation. They also investigated the role of maximum tangential forces, and found them to severely impact restructuring, high tangential forces leading to less restructuring. Since Becker et al. [59] studied tangential forces for aggregates with very high cohesive forces, these were too strong to break in the flow conditions and the effect of tangential forces on breakage could not be explored.

2.3.3 Combined effect on aggregate strength and breakage rates

The interplay of characteristics such as cohesive forces, aggregate structure and hydrodynamic forces determine if an aggregate will break. It can be seen from Equation (2.6) that VDW cohesive forces scale with the size of the primary particles. On the other hand, forces induced by viscous stresses scale with aggregate size. Indeed, the order of magnitude of the hydrodynamic forces can be estimated by approximating the aggregate to a sphere of radius equivalent to its radius of gyration R_g, hence

$$\boldsymbol{F}_{\text{viscous}} = \int \underline{\boldsymbol{\tau}} \cdot \boldsymbol{n} \mathrm{d}S \propto \mu \dot{\gamma} R_g^2 \tag{2.31}$$

Therefore, for a given fractal dimension, there is a critical aggregate size for which the hydrodynamic forces acting on the aggregate are just balanced by the inter-particle forces. When large aggregates break into smaller fragments, this critical size is attained by the largest fragments that are stable, that is, they do not themselves break into smaller fragments. Therefore, the largest stable size is also used as an indicator for the aggregate strength. Many studies have found a power-law relationship between the largest stable size of aggregate R_g^{max} and viscous stresses given as

$$R_g^{max} \propto \mu \dot{\gamma}^{-n} \tag{2.32}$$

The value of the scaling exponent n has been reported to range from 0.35 to 0.6 throughout the literature [4, 19, 23, 24, 26, 38, 66, 71]. The exponent is seen to depend on the fractal dimension of the parent aggregates [19] while the size of the primary particles, and therefore the number of particles in the aggregate, has no impact on its value [19, 23].

Although mechanisms of breakage are largely explored, studies with focus on breakage rate are limited. Among the few studies, Harshe and Lattuada [53] investigated the breakage rates for aggregates with varying hydrodynamic stresses. They conducted Stokesian Dynamics simulations to measure the time taken for aggregates to break since its exposure to shear flow. The breakage rate was reported to depends on the fractal dimension, size of the aggregates and on the hydrodynamic stresses. However, the simulations assumed abrupt flow, which lead to almost instantaneous breakage. Such a condition mimics aggregates that have just been created by the collision of smaller aggregates

carried in the flow. Since it means that their bonds are not strong enough to resist the flow that created them, they hardly qualify as aggregates, as discussed in the introduction of this chapter. To address this issue, Seto et al. [75] investigated aggregates in accelerating flows, by tracking their evolution when submitted to step increase in hydrodynamic stresses (through step increases in shear rates). This allowed for aggregates to restructure into denser aggregates, forming new bonds between primary particles. Although it can be inferred from such a study that slowly accelerating flows lead to stronger aggregates that survive higher shear rates, breakage rates were not evaluated because only infinitely strong aggregates were considered in their simulations.

2.3.4 Effect of flow inertia

While aggregate evolution in viscosity dominated flows has been a topic of interest in both experimental and simulation studies, the effect of flow inertia has been mostly investigated only through experiments. The ratio of inertial to viscous effects in the flow can be quantified by the Reynolds number, defined for shear flow as

$$\mathrm{Re} = \frac{\dot{\gamma} L^2}{\nu} \tag{2.33}$$

where L is the characteristic length of the object submitted to shear in the flow. It is well known that finite Reynolds number conditions result in a lower rate of rotation [80]. Although Harshe et al. [19] and Soos et al. [38] had few experimental data points in turbulent regime, they still assumed negligible flow inertia at aggregate scale. Nonetheless, Zaccone et al. [24] and Soos et al. [33] investigated the evolution of aggregates in turbulent regime in stirred tanks, and observed a stable size scaling coefficient n (as in Equation (2.32)) of 0.5, which falls within the reported range obtained through purely viscous studies. Therefore, it indicates that flow inertia does not contribute significantly to hydrodynamic stresses, leading to no distinct effect on of the aggregate strength. More recently, Saha et al. [26] recorded size and breakage rates of individual aggregates evolving under turbulent conditions through imaging. The flow conditions were well defined for aggregates to be about 9 times larger than the Kolmogorov length scale. They observed a scaling coefficient of 0.6. Further, they tried to capture the breakage rate as well, and compared it to the power law scaling with hydrodynamic stress as given by Harshe and Lattuada [53]. They stated a good agreement. However,

the breakage rate relations given by Harshe and Lattuada [53] were estimated at low Reynolds number conditions, where inertial effects of the flow are not present. Also, due to the lack of inertial effects, the shear flow was immediately present throughout the domain. This lead to instantaneous breakage of aggregates, resulting in very high breakage rates. Any agreement with such results is not a conclusive proof of lack of inertial effects on aggregate breakage. While the assumption of instantaneous breakage may apply at aggregates larger than the Kolmogorov length scales in the flow, the breakage at sub-Kolmogorov length scales may be affected by flow inertia.

On the other hand, flow inertia has been found to play a significant role in determining trajectories of approaching particles. For example, collision efficiency of two approaching particles has been found to be impacted at Reynolds numbers as low as 0.3 [81]. Similarly, recirculations around spheres have been found to grow with flow inertia, and the effect has been observed for Reynolds numbers as low as 0.3 [12]. Therefore, it is expected that flow inertia may have an effect on aggregate evolution.

2.4 Summary of knowledge gaps

From the above discussion, the following knowledge gaps can been identified

1. *Role of inter-particle forces:*

   The impact of tangential forces on breakage has not been investigated. While cohesive forces are not expected to play a prevalent role in restructuring, their impact on restructuring has not been quantified, contrary to their role in breakage, highlighted by several numerical studies.

2. *Aggregate evolution with flow inertia:*

   Since most results in the literature were obtained at infinitely low Reynolds number, their applicability to finite Reynolds number conditions must be explored. Additionally, the contribution of flow inertia to the overall hydrodynamic stresses experienced by the aggregates and its impact on the resulting evolution of the aggregates is not well understood. Therefore, an investigation into the role of flow inertia on aggregate evolution and on breakage rates can address these knowledge gaps.

3. *Aggregate evolution in transient flows with non-negligible flow inertia:*

Although breakage rate is critical to understanding the aggregate kinetics, it has not been explored for transient flow conditions. As a first approach, aggregate evolution could be investigated in accelerating flows. Further, the approach can be extended to include finite Reynolds number effects to provide a more comprehensive understanding. An investigation into accelerated flows can also be related to aggregate evolution at sub-Kolmogorov length scales in turbulent flows.

The fundamentals to be explored in the above identified knowledge gaps will have multilayered implications in understanding and predicting aggregate evolution. For instance, a direct application of a well established role of inter-particle forces could help relate the size and structure observed in experimental studies to the inter-particle forces of the aggregate. A better understanding of hydrodynamics around an aggregate and hydrodynamic interactions can help refine the current models, such as FDA. Determining the effect of flow inertia and including the effect of flow acceleration will provide information about breakage and restructuring of aggregates in systems like mixing tanks, where size of smallest eddies (and thus, hydrodynamic forces) vary over large ranges. The findings will serve as a stepping stone to investigating more complex systems where turbulence plays an important role.

References

[1] M. v. Smoluchowski. Grundriß der Koagulationskinetik kolloider Lösungen. *Kolloid-Zeitschrift*, 21(3):98–104, September 1917. ISSN 0303-402X. doi:10.1007/BF01427232.

[2] J.-P. Bellot, J.-S. Kroll-Rabotin, M. Gisselbrecht, M. Joishi, A. Saxena, S. Sanders, and A. Jardy. Toward Better Control of Inclusion Cleanliness in a Gas Stirred Ladle Using Multiscale Numerical Modeling. *Materials*, 11:1179, July 2018. doi:10.3390/ma11071179.

[3] V. Vajihinejad and J. B. Soares. Monitoring polymer flocculation in oil sands tailings: A population balance model approach. *Chemical Engineering Journal*, 346:447–457, 2018.

[4] R. C. Sonntag and W. B. Russel. Structure and breakup of flocs subjected to fluid stresses: I. Shear experiments. *Journal of Colloid and Interface Science*, 113(2):399–413, 1986.

[5] K. A. Kusters. *The influence of turbulence on aggregation of small particles in agitated vessels*. PhD thesis, Technische Univ., Eindhoven (Netherlands), 1991.

[6] P. T. Spicer and S. E. Pratsinis. Shear-induced flocculation: the evolution of floc structure and the shape of the size distribution at steady state. *Water Research*, 30(5):1049–1056, 1996.

[7] T. Serra and X. Casamitjana. Structure of the aggregates during the process of aggregation and breakup under a shear flow. *Journal of Colloid and Interface Science*, 206(2):505–511, 1998.

[8] C. Selomulya, G. Bushell, R. Amal, and T. Waite. Aggregation mechanisms of latex of different particle sizes in a controlled shear environment. *Langmuir*, 18(6):1974–1984, 2002.

[9] D. Chen and M. Doi. Simulation of aggregating colloids in shear flow. II. *The Journal of Chemical Physics*, 91(4):2656–2663, August 1989. doi:10.1063/1.456975.

[10] G. Lian, C. Thornton, and M. J. Adams. Discrete particle simulation of agglomerate impact coalescence. *Chemical Engineering Science*, 53(19):3381–3391, 1998.

[11] M. Ernst and M. Sommerfeld. Resolved numerical simulation of particle agglomeration. In *Colloid Process Engineering*, pages 45–71. Springer, 2015.

[12] H. Haddadi and J. F. Morris. Topology of pair-sphere trajectories in finite inertia suspension shear flow and its effects on microstructure and rheology. *Physics of Fluids*, 27(4):043302, 2015. doi:10.1063/1.4917030.

[13] G. Frungieri and M. Vanni. Shear-induced aggregation of colloidal particles: A comparison between two different approaches to the modelling of colloidal interactions. *The Canadian Journal of Chemical Engineering*, 95(9):1768–1780, 2017.

[14] J. N. Israelachvili. *Intermolecular and Surface Forces*. Academic press, 2015.

[15] T. N. Phung, J. F. Brady, and G. Bossis. Stokesian Dynamics simulation of brownian suspensions. *Journal of Fluid Mechanics*, 313:181–207, 1996. doi:10.1017/S0022112096002170.

[16] S. Lazzari, L. Nicoud, B. Jaquet, M. Lattuada, and M. Morbidelli. Fractal-like structures in colloid science. *Advances in Colloid and Interface Science*, 235:1–13, 2016.

[17] M. Vanni and A. Gastaldi. Hydrodynamic forces and critical stresses in low-density aggregates under shear flow. *Langmuir*, 27(21):12822–12833, November 2011. ISSN 0743-7463. doi: 10.1021/la2024549.

[18] K. Horii, R. Yamada, and S. Harada. Strength deterioration of nonfractal particle aggregates in simple shear flow. *Langmuir*, 31(29):7909–7918, 2015.

[19] Y. M. Harshe, M. Lattuada, and M. Soos. Experimental and modeling study of breakage and restructuring of open and dense colloidal aggregates. *Langmuir*, 27(10):5739–5752, May 2011. doi:10.1021/la1046589.

[20] F. Vaezi, R. S. Sanders, and J. H. Masliyah. Flocculation kinetics and aggregate structure of kaolinite mixtures in laminar tube flow. *Journal of Colloid and Interface Science*, 355(1): 96–105, 2011.

[21] J. Gregory. The density of particle aggregates. *Water Science and Technology*, 36(4):1–13, 1997. ISSN 0273-1223. doi:10.1016/S0273-1223(97)00452-6. The Role of Particle Characteristics in Separation Processes.

[22] L. Gmachowski. Calculation of the fractal dimension of aggregates. *Colloids and Surfaces A: Physicochemical and Engineering Aspects*, 211(2):197–203, 2002. ISSN 09277757. doi: 10.1016/S0927-7757(02)00278-9.

[23] L. Ehrl, M. Soos, and M. Morbidelli. Dependence of aggregate strength, structure, and light scattering properties on primary particle size under turbulent conditions in stirred tank. *Langmuir*, 24(7):3070–3081, April 2008. ISSN 0743-7463. doi:10.1021/la7032302.

[24] A. Zaccone, M. Soos, M. Lattuada, H. Wu, M. U. Bäbler, and M. Morbidelli. Breakup of dense colloidal aggregates under hydrodynamic stresses. *Phys. Rev. E*, 79:061401, Jun 2009. doi:10.1103/PhysRevE.79.061401.

[25] D. Saha, M. Soos, B. Lüthi, M. Holzner, A. Liberzon, M. U. Babler, and W. Kinzelbach. Experimental characterization of breakage rate of colloidal aggregates in axisymmetric extensional flow. *Langmuir*, 30(48):14385–14395, 2014.

[26] D. Saha, M. U. Bäbler, M. Holzner, M. Soos, B. Lüthi, A. Liberzon, and W. Kinzelbach. Breakup of finite-size colloidal aggregates in turbulent flow investigated by three-dimensional (3d) particle tracking velocimetry. *Langmuir*, 32(1):55–65, 2016. doi:10.1021/acs.langmuir.5b03804.

[27] S. Harada, R. Tanaka, H. Nogami, and M. Sawada. Dependence of fragmentation behavior of colloidal aggregates on their fractal structure. *Journal of Colloid and Interface Science*, 301(1): 123–129, 2006.

[28] S. Harada, R. Tanaka, H. Nogami, M. Sawada, and K. Asakura. Structural change in non-fractal particle clusters under fluid stress. *Colloids and Surfaces A: Physicochemical and Engineering Aspects*, 302(1):396–402, 2007.

[29] U. T. Lieu and S. Harada. Stability of restructured non-fractal aggregates in simple shear flow. *Advanced Powder Technology*, 26(3):705–710, 2015.

[30] M. Kobayashi, Y. Adachi, and S. Ooi. Breakup of fractal flocs in a turbulent flow. *Langmuir*, 15(13):4351–4356, 1999.

[31] S. Blaser. Break-up of flocs in contraction and swirling flows. *Colloids and Surfaces A: Physicochemical and Engineering Aspects*, 166(1):215–223, 2000. ISSN 0927-7757. doi:10.1016/S0927-7757(99)00450-1.

[32] M. Kobayashi. Breakup and strength of polystyrene latex flocs subjected to a converging flow. *Colloids and Surfaces A: Physicochemical and Engineering Aspects*, 235(1):73–78, 2004. ISSN 0927-7757. doi:10.1016/j.colsurfa.2004.01.008.

[33] M. Soos, A. S. Moussa, L. Ehrl, J. Sefcik, H. Wu, and M. Morbidelli. Effect of shear rate on aggregate size and morphology investigated under turbulent conditions in stirred tank. *Journal of Colloid and Interface Science*, 319(2):577–589, 2008. doi:10.1016/j.jcis.2007.12.005.

[34] G. Frappier, B. S. Lartiges, and S. Skali-Lami. Floc cohesive force in reversible aggregation: A couette laminar flow investigation. *Langmuir*, 26(13):10475–10488, 2010. doi:10.1021/la9046947.

[35] S. Blaser. Flocs in shear and strain flows. *Journal of Colloid and Interface Science*, 225(2): 273–284, 2000.

[36] S. Hannah, J. Cohen, and G. Robeck. Measurement of floc strength by particle counting. *American Water Works Association*, 59(7):843–858, 1967.

[37] R. C. Sonntag and W. B. Russel. Structure and breakup of flocs subjected to fluid stresses: Ii. theory. *Journal of Colloid and Interface Science*, 115(2):378–389, 1987.

[38] M. Soos, L. Ehrl, M. U. Bäbler, and M. Morbidelli. Aggregate breakup in a contracting nozzle. *Langmuir*, 26(1):10–18, 2010. doi:10.1021/la903982n.

[39] M. U. Babler, L. Biferale, and A. S. Lanotte. Breakup of small aggregates driven by turbulent hydrodynamical stress. *Physical Review E*, 85(2):025301, 2012.

[40] L. A. Glasgow and J. P. Hsu. An experimental study of floc strength. *AIChE Journal*, 28(5): 779–785, 1982. doi:10.1002/aic.690280512.

[41] P. Smith and T. Van De Ven. Shear-induced deformation and rupture of suspended solid/liquid clusters. *Colloids and Surfaces*, 15:191–210, 1985.

[42] S.-P. Rwei, I. Manas-Zloczower, and D. Feke. Observation of carbon black agglomerate dispersion in simple shear flows. *Polymer Engineering & Science*, 30(12):701–706, 1990.

[43] L. A. Glasgow and X. Liu. Response of aggregate structures to hydrodynamic stress. *AIChE journal*, 37(9):1411–1414, 1991.

[44] S. X. Liu and L. A. Glasgow. Aggregate disintegration in turbulent jets. *Water, Air, and Soil Pollution*, 95(1-4):257–275, 1997.

[45] M. Vlieghe, C. Coufort-Saudejaud, C. Frances, and A. Liné. In situ characterization of floc morphology by image analysis in a turbulent taylor–couette reactor. *AIChE Journal*, 60(7): 2389–2403, 2014.

[46] D. F. Bagster and D. Tomi. The stresses within a sphere in simple flow fields. *Chemical Engineering Science*, 29(8):1773–1783, August 1974. doi:10.1016/0009-2509(74)87036-3.

[47] P. M. Adler and P. M. Mills. Motion and rupture of a porous sphere in a linear flow field. *Journal of Rheology*, 23(1):25–37, February 1979. doi:10.1122/1.549514.

[48] P. A. Cundall and O. D. Strack. A discrete numerical model for granular assemblies. *Geotechnique*, 29(1):47–65, 1979.

[49] H. C. Hamaker. The London-van der Waals attraction between spherical particles. *Physica*, 4 (10):1058–1072, 1937. ISSN 00318914. doi:10.1016/S0031-8914(37)80203-7.

[50] G. Wiese and T. W. Healy. Effect of particle size on colloid stability. *Transactions of the Faraday Society*, 66:490–499, 1970.

[51] M. U. Bäbler, J. Sefcik, M. Morbidelli, and J. Bałdyga. Hydrodynamic interactions and orthokinetic collisions of porous aggregates in the stokes regime. *Physics of fluids*, 18(1): 013302, 2006.

[52] D. L. Feke, N. D. Prabhu, J. A. J. Mann, and J. A. L. Mann. A formulation of the short-range repulsion between spherical colloidal particles. *The Journal of Physical Chemistry*, 88(23): 5735–5739, November 1984. ISSN 0022-3654. doi:10.1021/j150667a055.

[53] Y. M. Harshe and M. Lattuada. Breakage rate of colloidal aggregates in shear flow through Stokesian dynamics. *Langmuir*, 28(1):283–292, January 2012. ISSN 0743-7463. doi:10.1021/la2038476.

[54] K. Iwashita and M. Oda. Rolling resistance at contacts in simulation of shear band development by DEM. *Journal of Engineering Mechanics*, 124(3):285–292, mar 1998. doi:10.1061/(ASCE)0733-9399(1998)124:3(285).

[55] D. Kadau, G. Bartels, L. Brendel, and D. E. Wolf. Contact dynamics simulations of compacting cohesive granular systems. *Computer Physics Communications*, 147(1-2):190–193, aug 2002. doi:10.1016/S0010-4655(02)00242-4.

[56] C. Dominik and H. Nübold. Magnetic aggregation: dynamics and numerical modeling. *Icarus*, 157(1):173–186, may 2002. doi:10.1006/icar.2002.6813.

[57] J. P. Pantina and E. M. Furst. Colloidal aggregate micromechanics in the presence of divalent ions. *Langmuir*, 22(12):5282–5288, 2006. doi:10.1021/LA0534120.

[58] V. Becker and H. Briesen. Tangential-force model for interactions between bonded colloidal particles. *Physical Review E*, 78(6):061404, December 2008. doi:10.1103/PhysRevE.78.061404.

[59] V. Becker, E. Schlauch, M. Behr, and H. Briesen. Restructuring of colloidal aggregates in shear flows and limitations of the free-draining approximation. *Journal of Colloid and Interface Science*, 339(2):362–372, 2009. doi:10.1016/j.jcis.2009.07.022.

[60] V. Becker and H. Briesen. A master curve for the onset of shear induced restructuring of fractal colloidal aggregates. *Journal of Colloid and Interface Science*, 346(1):32–36, June 2010. ISSN 0021-9797. doi:10.1016/j.jcis.2010.02.015.

[61] G. Frungieri. *A novel Monte Carlo - Discrete Element Method approach for the micro-mechanics of colloidal suspensions*. PhD thesis, Politecnico di Torino, 2018.

[62] P. Adler. Streamlines in and around porous particles. *Journal of Colloid and Interface Science*, 81(2):531–535, 1981. doi:10.1016/0021-9797(81)90434-3.

[63] M. O'Neill. On asymmetrical slow viscous flows caused by the motion of two equal spheres almost in contact. In *Mathematical Proceedings of the Cambridge Philosophical Society*, volume 65, pages 543–556. Cambridge University Press, 1969.

[64] R. B. Bird, C. F. Curtiss, R. C. Armstrong, and O. Hassager. *Dynamics of Polymeric Liquids, Volume 2: Kinetic Theory*. Wiley, 1987.

[65] S. Abdel-Khalik and R. B. Bird. Estimation of the zero shear rate viscosity for dilute solutions of rigid macromolecules with complex configurations. *Biopolymers: Original Research on Biomolecules*, 14(9):1915–1932, 1975.

[66] M. L. Eggersdorfer, D. Kadau, H. J. Herrmann, and S. E. Pratsinis. Fragmentation and restructuring of soft-agglomerates under shear. *Journal of Colloid and Interface Science*, 342 (2):261–268, 2010. ISSN 00219797. doi:10.1016/j.jcis.2009.10.062.

[67] D. Liu, Z. Wang, X. Chen, and M. Liu. Simulation of agglomerate breakage and restructuring in shear flows: Coupled effects of shear gradient, surface energy and initial structure. *Powder Technology*, 336:102–111, 2018. doi:10.1016/j.powtec.2018.05.051.

[68] J. F. Brady and G. Bossis. Stokesian dynamics. *Annual Review of Fluid Mechanics*, 20(1): 111–157, 1988. doi:10.1146/annurev.fluid.20.1.111.

[69] M. Vanni. Accurate modelling of flow induced stresses in rigid colloidal aggregates. *Computer Physics Communications*, 192:70–90, July 2015. ISSN 0010-4655. doi:10.1016/j.cpc.2015.02.022.

[70] E. Schlauch, M. Ernst, R. Seto, H. Briesen, M. Sommerfeld, and M. Behr. Comparison of three simulation methods for colloidal aggregates in Stokes flow: Finite elements, lattice Boltzmann and Stokesian dynamics. *Computers & Fluids*, 86:199–209, 2013. doi:10.1016/j.compfluid.2013.07.005.

[71] M. Kroupa, M. Vonka, M. Soos, and J. Kosek. Size and Structure of Clusters Formed by Shear Induced Coagulation: Modeling by Discrete Element Method. *Langmuir*, 31(28):7727–7737, July 2015. ISSN 0743-7463. doi:10.1021/acs.langmuir.5b01046.

[72] T. Krüger, H. Kusumaatmaja, A. Kuzmin, O. Shardt, G. Silva, and E. M. Viggen. *The Lattice Boltzmann Method: Principles and Practice*. Springer, 2016.

[73] T. Inamuro and T. Ii. Lattice Boltzmann simulation of the dispersion of aggregated particles under shear flows. *Mathematics and Computers in Simulation*, 72(2):141–146, September 2006. ISSN 0378-4754. doi:10.1016/j.matcom.2006.05.022.

[74] C. S. Peskin. Flow patterns around heart valves: A numerical method. *Journal of Computational Physics*, 10(2):252–271, October 1972. ISSN 00219991. doi:10.1016/0021-9991(72)90065-4.

[75] R. Seto, R. Botet, G. K. Auernhammer, and H. Briesen. Restructuring of colloidal aggregates in shear flow. *The European Physical Journal E*, 35(12):128, December 2012. ISSN 1292-8941. doi:10.1140/epje/i2012-12128-4.

[76] I. Zia, R. Cox, and S. Mason. Ordered aggregates of particles in shear flow. *Proceedings of the Royal Society of London. Series A. Mathematical and Physical Sciences*, 300(1463):421–441, 1967.

[77] C. M. Schroeder, R. E. Teixeira, E. S. Shaqfeh, and S. Chu. Characteristic periodic motion of polymers in shear flow. *Physical Review Letters*, 95(1):018301, 2005.

[78] A. Gastaldi and M. Vanni. The distribution of stresses in rigid fractal-like aggregates in a uniform flow field. *Journal of Colloid and Interface Science*, 357(1):18–30, 2011.

[79] M. Zeidan, B. H. Xu, X. Jia, and R. A. Williams. Simulation of Aggregate Deformation and Breakup in Simple Shear Flows Using a Combined Continuum and Discrete Model. *Chemical Engineering Research and Design*, 85(12):1645–1654, January 2007. ISSN 0263-8762. doi: 10.1016/S0263-8762(07)73208-2.

[80] D. R. Mikulencak and J. F. Morris. Stationary shear flow around fixed and free bodies at finite reynolds number. *Journal of Fluid Mechanics*, 520:215, 2004. doi:10.1017/S0022112004001648.

[81] J.-S. Kroll-Rabotin, M. Gisselbrecht, B. Ott, R. May, J. Fröhlich, and J.-P. Bellot. Multiscale simulation of non-metallic inclusion aggregation in a fully resolved bubble swarm in liquid steel. *Metals*, 10:517, 2020. doi:10.3390/met10040517.

Chapter 3

Numerical tools and methods

This project focuses on addressing each of the knowledge gaps identified in Chapter 2 through a numerical study. Particle tracking is done through a Discrete Element Method. Due to the advantages of the Lattice Boltzmann Method for solving flows around aggregates, a LBM scheme is employed for the liquid phase [1]. The coupling between the LBM and DEM is achieved through an Immersed Boundary Method that leverages the specificities of LBM to represent complex geometries [2].

Numerical simulations are conducted using a parallel code written in Fortran and named "Flua", developed in team "Process Metallurgy" at Institut Jean Lamour by Dr. Jean-Sébastien Kroll-Rabotin. In this study, only OpenMP was utilized. Most simulations were run on computing resources provided by Compute Canada and Westgrid. Visualizations were done in Paraview, and data processing was done with MATLAB, GNU Octave and Python.

This chapter lays out the numerical methods used in "Flua" to solve the system of differential equations ruling aggregate evolution in shear flow.

3.1 Flow solver: Lattice Boltzmann Method

In the 1980s, lattice gas automata were developed to simulate gas behaviour at molecular scale [3, Section 2.2.2]. These methods were based on discrete gas particles moving in a discrete space represented by nodes of lattice imposing two constraints on particle dynamics. The first constraint restricted the magnitude of velocities of all the particles so that, in one time step, each particle could only move from one node to one of its neighbours along the lattice connections. The second constraint

defined the outcome in case of collision between particles moving to the same node. Together, this set of rules ensured conservation of mass and momentum at microscopic levels. However, due to discrete nature of gas particles, the macroscopic properties of the gas as a continuum did not hold at microscopic level, that is, at the nodes. Therefore, the results were noisy and it introduced spurious terms in the Navier-Stokes equations. Therefore, lattice gas automata could not serve as general fluid simulation tools.

In the late 1980s, discrete particles were replaced with density distribution functions through the Boltzmann equation [4]. Therefore, the discrete representation of particles moving in the lattice was replaced by a statistical representation. Later, with the inclusion of a "collision operator" acting on the statistical distributions, the Lattice Boltzmann method (LBM) was born [5, 6]. The LBM solves the Navier-Stokes equations indirectly by resolving them through a Boltzmann like problem and using a collision operator which results in a Navier-Stokes solution with second order accuracy. The mathematical proof of Navier-Stokes solution through LBM was published by Chapman [7] and Enskog [8] independently.

3.1.1 The Boltzmann equation

Boltzmann equation describes the mass density distribution function (f) as a function of position ($\boldsymbol{x}$), microscopic particle velocity ($\boldsymbol{c}$) and time (t) as

$$f = f(\boldsymbol{x}, \boldsymbol{c}, t) \tag{3.1}$$

such that

$$\rho(\boldsymbol{x}, t) = \int_{\mathbb{R}^3} f(\boldsymbol{x}, \boldsymbol{c}, t)\, \mathrm{d}^3\boldsymbol{c} \tag{3.2}$$

A total derivative of the density distribution function gives

$$\frac{\mathrm{d}f}{\mathrm{d}t} = \frac{\partial f}{\partial t}\frac{\mathrm{d}t}{\mathrm{d}t} + \nabla_{\boldsymbol{x}} f \cdot \frac{\mathrm{d}\boldsymbol{x}}{\mathrm{d}t} + \nabla_{\boldsymbol{c}} f \cdot \frac{\mathrm{d}\boldsymbol{c}}{\mathrm{d}t} \tag{3.3}$$

Since the dynamics of microscopic particles is ruled by collisions, the variation of their distribution over time is represented by a so-called collision operator Ω. Some of the terms of Equation (3.3) can be simplified further. The variation of position of each particle over time, that is $\mathrm{d}\boldsymbol{x}/\mathrm{d}t$ is

its velocity $\boldsymbol{c}$. Furthermore, the change in distribution due to non-collision induced acceleration of individual particles results from external forces $\boldsymbol{F}_b$, following Newton's equation of motion $m\mathrm{d}\boldsymbol{c}/\mathrm{d}t = \boldsymbol{F}_b$. Replacing the respective terms with velocity and external force, the Boltzmann equation finally reads

$$\Omega(f) = \frac{\partial f}{\partial t} + \boldsymbol{c} \cdot \nabla_{\boldsymbol{x}} f + \frac{\boldsymbol{F}_b}{m} \cdot \nabla_{\boldsymbol{c}} f \tag{3.4}$$

where $\boldsymbol{F}_b/m$ is a body force per unit of mass.

3.1.2 Discretization of Boltzmann equation

Since the Boltzmann equation is a non-linear partial differential equation, numerical methods are the only general approach to obtain a solution. Looking at Equation (3.4), other than usual discretization in space $\boldsymbol{x}$ and time t (as in Finite Volume Method for example), it additionally requires discretization in the velocity space $\boldsymbol{c}$. To understand velocity discretization, consider a gas made of mono-sized gas particles as shown in Figure 3.1, with a macroscopic velocity $\boldsymbol{u}$. Such a velocity results from of the local contributions of many particles in a given volume $\mathcal{V}$, each particle within this volume having its own momentum. Together, all the particles in the considered volume have a net momentum given by volume averaging their contributions

$$\frac{1}{\mathcal{V}} \sum m_i \boldsymbol{c}_i = \rho \boldsymbol{u} \tag{3.5}$$

which for a dense medium where density of particles per volume can be represented by a statistical distribution turns out as

$$\int_{\mathbb{R}^3} f \boldsymbol{c} \, \mathrm{d}^3 c = \rho \boldsymbol{u} \tag{3.6}$$

Particle velocities can be along any directions with an infinite number of possible magnitudes. To discretize the velocity space, instead of infinite directions and magnitudes, velocities are limited to a finite subset of possible directions such that

$$\rho \boldsymbol{u} = \sum N_i \boldsymbol{c}_i \tag{3.7}$$

where N_i and $\boldsymbol{c}_i$ are the density and the velocity corresponding to direction i. As an illustration, a discretized velocity space in two dimensions (2D) is shown in Figure 3.1 with 8 velocity directions.

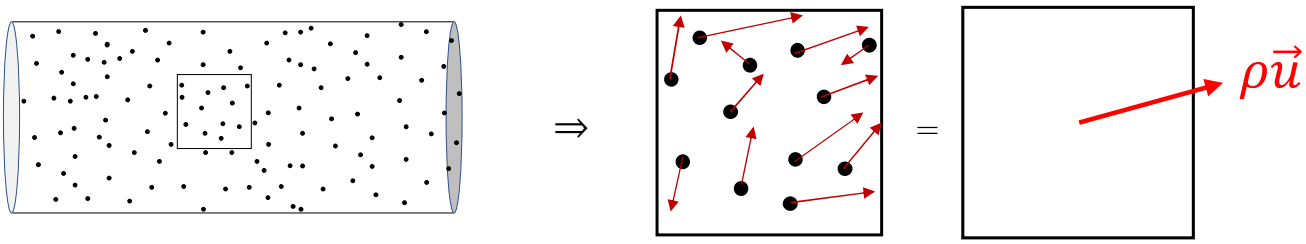

(a) Continuum model

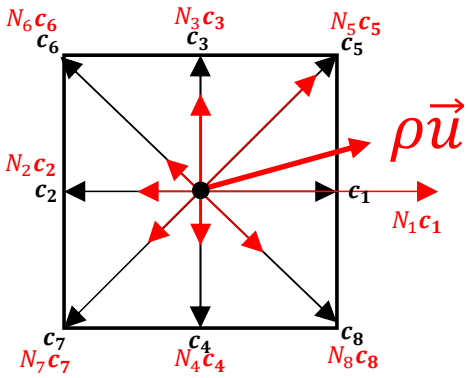

(b) Velocity Discretization

Figure 3.1: Continuum model and its discretization in velocity space. (a) Gas flow in a pipe, where molecules in a small volume have randomly distributed velocities, with an average momentum of $\rho\boldsymbol{u}$. (b) Discretization of the velocity space into a finite number of directions $\boldsymbol{c}_i$, with i ranging from 1 to 8 in this 2-D demonstration. The density in each direction i is N_i such that the sum of momentum $\sum_i N_i\boldsymbol{c}_i$ over the velocity space gives them momentum $\rho\boldsymbol{u}$.

This discretization of velocity space forms the basis for all LBM implementations from which macroscopic mass, momentum and energy can be calculated as zeroth, first and second moments of the Boltzmann distribution as

$$\rho = \int_c f \mathrm{d}^3\boldsymbol{c} = \sum_i N_i \tag{3.8}$$

$$\rho\boldsymbol{u} = \int_c \boldsymbol{c}\, f \mathrm{d}^3\boldsymbol{c} = \sum_i N_i \boldsymbol{c}_i \tag{3.9}$$

$$\rho e = \int_c \frac{1}{2}\boldsymbol{c}^2 f \,\mathrm{d}^3\boldsymbol{c} = \frac{1}{2}\sum_i N_i \boldsymbol{c}_i^2 \tag{3.10}$$

For LBM to conserve mass and momentum, the moments of its collision operator must satisfy

$$\sum_i \Omega(N_i) = 0 \tag{3.11}$$

$$\sum_i \boldsymbol{c}_i\, \Omega(N_i) = \mathbf{o} \tag{3.12}$$

It must be noted that the body force term can be treated as a source term such that the Boltzmann equation discretized in velocity space can be written for direction i as

$$\frac{\partial N_i}{\partial t} + \boldsymbol{c}_i \cdot \nabla_{\boldsymbol{x}} N_i + \frac{\boldsymbol{F}_b}{m} \cdot \nabla_{\boldsymbol{c}} N_i = \Omega_i(N_1, \ldots, N_i, \ldots) \tag{3.13}$$

Approximating the integration of this equation over time using the trapezoidal rule yields the Lattice Boltzmann Equation (LBE)

$$N_i(\boldsymbol{x} + \boldsymbol{c_i}\Delta t, t + \Delta t) = N_i(\boldsymbol{x}, t) + \Delta t\left(\Omega_i(N(\boldsymbol{x}, t)) - \frac{\boldsymbol{F}_b}{m} \cdot w_i \boldsymbol{c}_i\right) \tag{3.14}$$

The calculation of the source term is not detailed here because it will not be used in this form in this work, but details about source terms in LBM can be found in Guo et al. [9].

Such lattice Boltzmann equation is fully explicit. The equation describes that density N_i at the next node in direction i is a sum of density associated to direction i in the local node plus the component along i of the local collision operator Ω. The collision operator calculates redistribution among densities using only information local to its node. Therefore, Equation (3.14) breaks down into two steps: *collision* and *streaming*. In the collision step, the collision operator Ω is applied, and

a new "post-collision" distribution $\tilde{N}_i$ at the node x is determined as

$$\tilde{N}_i(\boldsymbol{x},t) \;=\; N_i(\boldsymbol{x},t) + \Delta t\Big(\Omega_i(N(\boldsymbol{x},t)) - \frac{\boldsymbol{F}_b}{m}\cdot w_i\boldsymbol{c}_i\Big) \tag{3.15}$$

In a dense medium, the kinetic theory of gases states that collisions statistically result in a redistribution of momentum among constituent particles so that it evolves towards an equilibrium distribution given by the Maxwell-Boltzmann distribution

$$f^{eq} = \rho\left(\frac{m}{2\pi k_b T_k}\right)^{3/2}\exp\left(-\frac{m\,(\boldsymbol{c}-\boldsymbol{u})^2}{kT}\right) \tag{3.16}$$

where k_b is the Boltzmann constant, T_k is the temperature. Based on this, Bhatnagar et al. [10] were the first to propose a collision operator Ω_i^{BGK} for the LBE in the form of simple relaxation towards this equilibrium distribution discretized on the lattice velocities, that is relaxing the densities toward their equilibrium distribution N^{eq} as

$$\Omega_i^{\mathrm{BGK}} = \frac{1}{\tau^{\mathrm{BGK}}}\left(N_i^{eq} - N_i\right) \tag{3.17}$$

where τ^{BGK} is the relaxation time, and is related to the kinematic viscosity ν as

$$\nu = c_s^2\left(\tau^{\mathrm{BGK}} - \frac{\Delta t}{2}\right) \tag{3.18}$$

Once the new distribution $\tilde{N}_i$ is determined through Equation (3.15), the distribution is propagated to the next corresponding node in the i direction. The propagation to neighboring node in i direction is ensured by having velocity c_i and time step Δt such that N_i moves by one lattice node in a time step. This propagation of information is called streaming, and can be written as

$$N_i(\boldsymbol{x}+\boldsymbol{c}_i\Delta t, t+\Delta t) = \tilde{N}_i(\boldsymbol{x},t) \tag{3.19}$$

Figure 3.2 and Figure 3.3 illustrate these two steps. Together, collision and streaming make one time step.

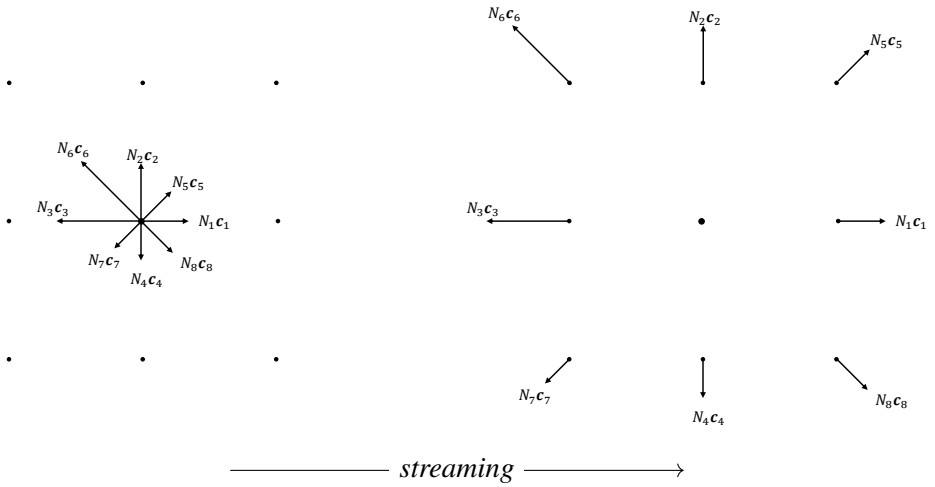

Figure 3.2: Illustration of streaming from Equation (3.19)

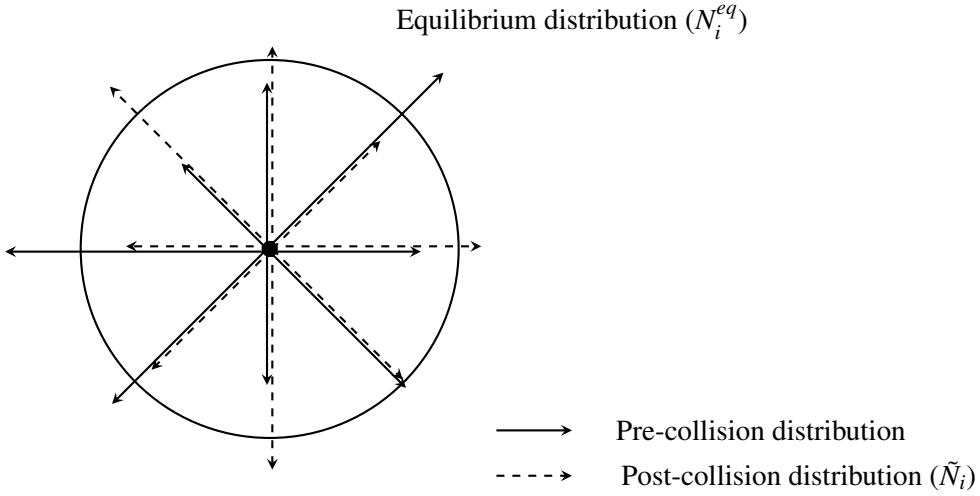

Figure 3.3: Illustration of collision from Equation (3.15)

3.1.3 Collision operator

The LBM used in this project was developed by Eggels and Somers [1]. It describes for a three dimensional (3D) problem by discretizing velocities in 18 directions velocity directions, hence its lattice is commonly referred to as D3Q18. Figure 3.4 shows all the velocity directions in D3Q18 lattice. The velocity vectors in lattice units for each direction can be written as

$$\boldsymbol{c_i} = \frac{\Delta x}{\Delta t}\begin{cases}(\pm 1,0,0)\,,\ (0,\pm 1,0)\,,\ (0,0,\pm 1)\,, & \text{for } i = 1,\ldots,6 \quad \text{(Group I)}\\ (\pm 1,\pm 1,0)\,,\ (0,\pm 1,\pm 1)\,,\ (\pm 1,0,\pm 1)\,, & \text{for } i = 7,\ldots,18 \quad \text{(Group II)}\end{cases} \tag{3.20}$$

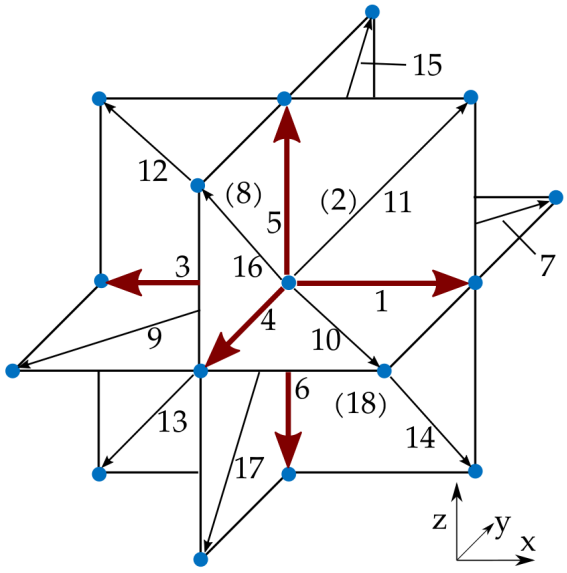

Figure 3.4: D3Q18 velocity space discretization [11]

By convention, when dealing with lattice Boltzmann variables, they are usually expressed in lattice units, that is so that lattice units $\Delta x = 1$ and $\Delta t = 1$. Then the physical problem to be simulated is converted in lattice units using similitude, and preserving dimensionless numbers such as the Reynolds number between physical and lattice units. Therefore, Δx and Δt will be assumed to be 1 in the following equations.

It must be noted that in D3Q18, the velocity space is not discretized uniformly. Each velocity in Group I has a magnitude of 1, while in Group II, the magnitude is $\sqrt{2}$. To address this and ensure other constraints on LBM schemes that are detailed in Krüger et al. [3], each velocity $\boldsymbol{c}_i$ is associated to a weight w_i

$$w_i = \begin{cases} \dfrac{1}{12} & \text{for } i \in (1 \dots 6) \\ \dfrac{1}{24} & \text{for } i \in (7 \dots 18) \end{cases} \tag{3.21}$$

Eggels and Somers [1] proposed collision operator that combines the application of the source and the relaxation towards the equilibrium distribution, such that Equation (3.13) becomes

$$\frac{\partial N_i}{\partial t} + \boldsymbol{c}_i \cdot \nabla_{\boldsymbol{x}} N_i = \Omega_i^{E\&S}\left(N, \frac{F_b}{m}\right) \tag{3.22}$$

Based on the work by Frisch et al. [12], the expression of equilibrium distribution in the dis-

cretized lattice velocities used in Eggels and Somers [1] is

$$N_i^{eq} = \rho\, w_i \Bigg[1 + 2\boldsymbol{c_i}\cdot\boldsymbol{u} + 3\left((\boldsymbol{c_i}\cdot\boldsymbol{u})^2 - \frac{1}{2}\boldsymbol{u}^2\right) - 6\nu\left(\boldsymbol{c_i}\cdot\nabla_x\left(\boldsymbol{c_i}\cdot\boldsymbol{u}\right) - \frac{1}{2}\nabla_x\boldsymbol{u}\right) + O\left(\boldsymbol{u}^3, \boldsymbol{u}\nabla\boldsymbol{u}\right)\Bigg] \quad (3.23)$$

where, $O\left(\boldsymbol{u}^3, \boldsymbol{u}\nabla\boldsymbol{u}\right)$ are higher order terms that do not exist in the Navier-Stokes equation, and must be kept small. This is ensured by keeping the velocity in lattice units small enough, or more precisely by satisfying $\|\boldsymbol{u}\| \ll c_s$, where c_s is the "speed of sound" in the system. This speed of sound is inherent to the LBM that is an explicit method and that, as such, cannot ensure incompressibility of the flow globally. The speed of sound directly results from the speed limit at which information can travel during one time step. Due to the way streaming is implemented, this is of the order of $\Delta x/\Delta t \sim 1$. More precisely, it can be calculated from the lattices properties $\boldsymbol{c}_i$ and w_i as

$$c_s = \sqrt{\sum_{i=1}^{18} w_i (\boldsymbol{c}_i \cdot \boldsymbol{e})^2} \quad (3.24)$$

where $\boldsymbol{e}$ is a unit vector. For D3Q18 velocity set, the speed of sound c_s from Equation (3.24) is found to be $c_s = \frac{1}{\sqrt{2}}$.

The BGK collision operator Ω_i^{BGK} from Equation (3.17) relaxes all moments of the LBE with the same relaxation time τ^{BGK}. Another way to obtain the post collision distribution is by relaxing different moments of the distribution by different relaxation times. This approach is known as Multiple-Relaxation-Time (MRT), and it allows for better stability and accuracy [3, 13] of the LBM. The idea of MRT is to relax moments instead of the densities. This is achieved by projecting the density distribution into different moment spaces, followed by relaxing each moment by a different relaxation time. Finally, the relaxed moments are projected back into the velocity space. Although the method by Eggels and Somers [1] does not derive from the MRT as invented by d'Humieres [13], their collision operation uses a similar approach. The physical moments of the density distribution (that is the mass, momentum and energy) and higher order moments that do not appear in Navier-Stokes are relaxed separately. Making the projections explicitly appear with projection matrix $[P]$,

the LBE becomes

$$N_i(\boldsymbol{x}+\boldsymbol{c_i},t+1) = [P]_i^{-1}\underbrace{\left(1+\left[\Omega^{E\&S}\right]\right)\overbrace{[P]_i\,N_i(\boldsymbol{x},t)}^{\alpha^-}}_{\alpha^+} \tag{3.25}$$

Recalling Equation (3.15) and Equation (3.19), α^- and α^+ are defined as the pre- and post-collision solution vectors (that is, moments of the density distribution) respectively. They can be expressed as

$$\alpha^- = [P]\ N_i(\boldsymbol{x},t) \qquad \text{pre-collision solution vector} \tag{3.26}$$

$$\alpha^+ = [P]\ \tilde{N}_i(\boldsymbol{x},t) \qquad \text{post-collision solution vector} \tag{3.27}$$

The collision operator $\Omega^{E\&S}$ it then directly expressed as a relation between the solution vectors $\alpha^{\pm}$ in the form

$$\alpha^{\pm} = \begin{bmatrix} \rho \\ \rho\boldsymbol{u} \pm \frac{1}{2}\boldsymbol{f} \\ \rho\boldsymbol{u}\boldsymbol{u} + \rho\frac{\pm 1 - 6\nu}{6\nu}\left(\nabla\boldsymbol{u} + \nabla\boldsymbol{u}^T\right) \\ O\left(\boldsymbol{u}^3,\ \boldsymbol{u}\nabla\boldsymbol{u}\right) \\ O\left(\boldsymbol{u}^4,\ \boldsymbol{u}^2\nabla\boldsymbol{u}\right) \end{bmatrix} \tag{3.28}$$

The solution vectors $\alpha^{\pm}$ have 18 components: 1 for density, 3 for momentum, 6 for energy terms and 8 for higher order terms. The higher order terms are damped down with a damping factor (-0.8 in this case) as suggested by the inventors of the method [1].

3.2 Fluid-solid coupling: Immersed Boundary Method

The Immersed Boundary Method was first developed by Peskin [14], where the surface of the solid phase is described in Lagrangian space. The fundamental objective of the method is to impose a no-slip condition at the liquid-solid interface.

The IBM scheme used in this project is based on Niu et al. [2] that is designed to ensure liquid-solid coupling for non-deformable surfaces in a flow solved with any LBM.

3.2.1 Surface discretization

To capture the geometry of the solids, first their surface is discretized by marker points, distributed as regularly as possible, each given a weight corresponding to the area of the surface element they are associated to. For a sphere, it is illustrated in Figure 3.5.

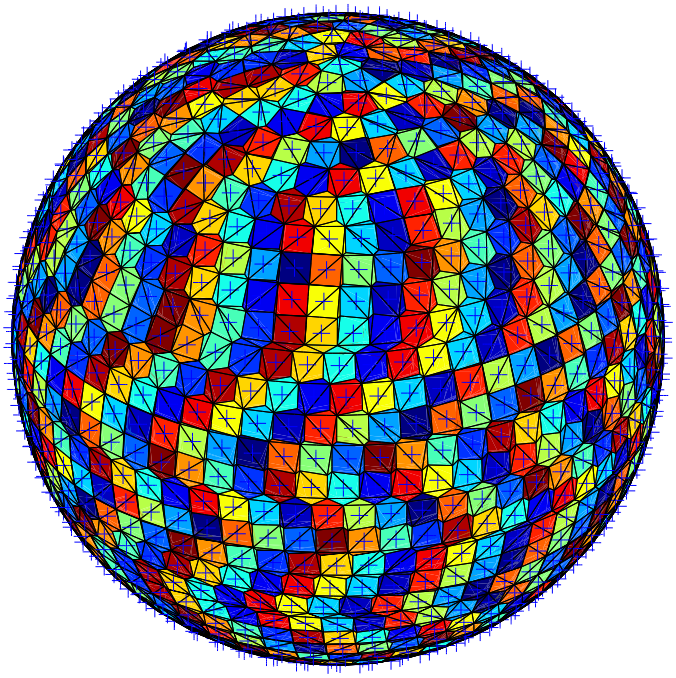

Figure 3.5: Representation of a sphere using a surface distribution of marker points (+) and their corresponding surface elements (each represented with a different color)

The weight w_m of each marker point m, is calculated as the area of its corresponding surface element δS_m, determined by Voronoï tessellation, such that

$$w_m = \delta S_m \tag{3.29}$$

$$\sum_m w_m = \frac{4\pi}{3} R_p^3 \tag{3.30}$$

Although is it mathematically impossible to homogeneously distribute points over the surface of a sphere, marker points are distributed as homogeneously on the surface as possible, which gives

$$w_m \approx \frac{4\pi R_p^3}{3M} \tag{3.31}$$

where M is the total number of marker points on the surface. In the marker point distribution used in

the simulations and illustrated in Figure 3.5, the maximum relative deviation from this average in less than 10% and more than 90% of weights deviate by less than 1%.

3.2.2 Momentum exchange

To ensure no-slip condition at the liquid-solid interface, in the momentum exchange based IBM described by Niu et al. [2], LBM densities are interpolated at each marker position and the local momentum exchange required to set the fluid velocity equal to that of the marker point is calculated for each surface element. Then, the calculated momentum exchange, which is a force, is distributed back to the surrounding LBM nodes and is accounted for in the flow solver as a source term. This scheme is fully explicit.

In the IBM provided by Niu et al. [2], the density distribution from nearby nodes in Eulerian phase is interpolated at marker m at position $\boldsymbol{x_m}$ to give density distribution N_m as

$$N_m = \sum_{\boldsymbol{x}} N(\boldsymbol{x})\, \delta(\boldsymbol{x}_m - \boldsymbol{x}) \tag{3.32}$$

where δ is a weighing function for interpolation. The calculation of the momentum exchange contains two parts: one that would stop the flow, achieved through the LBM bounce-back boundary condition, and one that corresponds to the force that would accelerate the flow from 0 to the velocity of the solid body in one time step. The bounce-back condition gives a density distribution from which a "stopping force" can be deducted through the first moment of the variation between the interpolated distribution and the bounced distribution. This is the same as the variation of the first moment of density distribution, that is also the variation of momentum. The resulting force $\boldsymbol{f_M}$ at each marker can be written as

$$\boldsymbol{f_m} = \overbrace{w_m}^{\text{marker weight}} \sum_i \left(\overbrace{N_m(-\boldsymbol{c}_i) - N_m(\boldsymbol{c}_i)}^{\text{full way bounce back}} + \overbrace{\left[\mathrm{P}\right]^{-1}_{(\boldsymbol{c_i})} \rho \boldsymbol{u}_m}^{\text{solid velocity}} \right) \boldsymbol{c}_i \tag{3.33}$$

Finally, the force on the fluid $\boldsymbol{f}_{p/f}$ is distributed back to the LBM nodes and summed over all marker points so that the source term at position $\boldsymbol{x}$ is

$$\boldsymbol{f}_{p/f}(\boldsymbol{x}) = \sum_M \boldsymbol{f_m}\, \delta(\boldsymbol{x_m} - \boldsymbol{x}) \tag{3.34}$$

The weighting function to distribute the force into the LBM nodes is the regularized Dirac function

as described in Roma et al. [15]. In this work, the same weights for IBM markers were also used for interpolation in Equation (3.32).

Due to the way the coupling force $\boldsymbol{f}_{p/f}$ is computed, it ensures that the fluid velocity, after the collision operator is applied, is the velocity of the solid. On the other hand, the force and the torque acting on the solid phase are calculated by summing the reciprocal actions.

$$\boldsymbol{F}_{f/p}^{\mathrm{IBM}} = -\sum_{m=1}^{M} \boldsymbol{f}_{\boldsymbol{m}} \tag{3.35}$$

$$\boldsymbol{T}_{f/p}^{\mathrm{IBM}} = -\sum_{m=1}^{M} (\boldsymbol{x}_m - \boldsymbol{x}_O) \times \boldsymbol{f}_{\boldsymbol{m}} \tag{3.36}$$

where $\boldsymbol{x_O}$ is the center of mass of the considered solid particle.

It must be pointed out that the volume within the solid body is seen as fluid in the Eulerian representation of the flow. The fluid enclosed in the sphere exchanges momentum with the immersed boundary in the same way as the fluid in the outside does. However, only the contribution of the fluid outside has physical sense, which must be accounted for in particle motion equations. One way to address this is by forcing the enclosed fluid within each particle to behave as a solid body. This is achieved by adding layers of marker points inside of the sphere. In this study, the external layer has 1302 marker points, and the sphere also have extra layers consisting of 326 and 82 marker points at radii 0.7 and 0.3 times the sphere radius respectively. These points ensure that the virtual mass of fluid inside the solid particles moves as a solid body, which makes it straightforward to calculate the force it exerts on the solids with an analytical expression for its inertia

$$\boldsymbol{F}_{f/p}^{\mathrm{in}} = -\rho \frac{4\pi}{3} R_p^3 \frac{\mathrm{d}\boldsymbol{v}_p}{\mathrm{d}t} \tag{3.37}$$

$$\boldsymbol{T}_{f/p}^{\mathrm{in}} = -\rho \frac{8\pi}{15} R_p^5 \frac{\mathrm{d}\boldsymbol{\omega}_p}{\mathrm{d}t} \tag{3.38}$$

This virtual actions exerted by the liquid on particles are numerical artifacts that must be cancelled in the physical equations of motion of particles. This is achieved by subtracting them from the total

IBM force and torque, which makes the physical force applied by the liquid flow on the sphere

$$\boldsymbol{F}_{f/p} = \boldsymbol{F}^{\text{IBM}}_{f/p} - \boldsymbol{F}^{\text{in}}_{f/p} \tag{3.39}$$

$$\boldsymbol{T}_{f/p} = \boldsymbol{T}^{\text{IBM}}_{f/p} - \boldsymbol{T}^{\text{in}}_{f/p} \tag{3.40}$$

Such inertia corrections are included in the numerical resolution of the particle as a force and a torque that depend on particle acceleration.

3.3 Particle dynamics: Discrete Element Method

Discrete Element Method (DEM) is a numerical framework for Lagrangian tracking of a large number of particles with resolved particle-particle interactions. The method allows for tracking displacement, rotations and contacts between the particles. These features make DEM ideal for tracking aggregates with discrete primary particles.

In an aggregate, each particle experiences at least two types of forces, namely the hydrodynamic forces and particle-particle forces. In this project, the latter were further categorized into a cohesive force represented through a combination of van der Waals forces and Born repulsion, and a tangential force represented through the model described by Becker and Briesen [16].

3.3.1 Particle dynamics

In DEM, particle velocities are calculated by solving Newton's equations of motion for every particle. The equations can be written as

$$m\frac{\mathrm{d}\boldsymbol{v}_i}{\mathrm{d}t} = \sum \boldsymbol{F}_i \tag{3.41}$$

$$\mathcal{J}\frac{\mathrm{d}\boldsymbol{\omega}_i}{\mathrm{d}t} = \sum \boldsymbol{T}_i \tag{3.42}$$

where $\boldsymbol{v}_i$ and $\boldsymbol{\omega}_i$ are velocity and angular velocity of particle i, and $\boldsymbol{F}_i$ and $\boldsymbol{T}_i$ are the forces and torques acting on the particle.

In this project, these equations are solved through a linear system of equations where all forces and torques that depend on particle acceleration and velocity are accounted for as linear functions.

Forces are represented by coefficients α and β in Equation (3.43).

$$m_p \frac{\mathrm{d}\boldsymbol{v}}{\mathrm{d}t} = \alpha \frac{\mathrm{d}\boldsymbol{v}}{\mathrm{d}t} + \beta \boldsymbol{v} + \boldsymbol{\gamma} \tag{3.43}$$

The velocity calculation at each time step comes directly from Equation (3.43) which yields a simple linear equation.

$$m_p \frac{\boldsymbol{v}(t) - \boldsymbol{v}(t-\Delta t)}{\Delta t} = \alpha \frac{\boldsymbol{v}(t) - \boldsymbol{v}(t-\Delta t)}{\Delta t} + \beta \boldsymbol{v}(t) + \boldsymbol{\gamma} \tag{3.44}$$

Equation (3.44) is solved for $\boldsymbol{v}(t)$.

$$\boldsymbol{v}(t) = \frac{\left(\frac{m_p - \alpha}{\Delta t}\right)\boldsymbol{v}(t-\Delta t) + \boldsymbol{\gamma}}{\frac{m_p - \alpha}{\Delta t} - \beta} \tag{3.45}$$

The term $\boldsymbol{\gamma}$ contains the forces that do not depend on particle motion. Representation of forces as linear functions enables velocity calculation for any Stokes number conditions. If the particle inertia is high, the acceleration term dominates, whereas for low Stokes number conditions, the other two terms can prevail.

Since particle acceleration is usually not the right parameter to calculate first in most liquid-solid systems, the aforementioned scheme does not resolve it but merely estimates it as

$$\frac{\mathrm{d}\boldsymbol{v}}{\mathrm{d}t}(t) \approx \frac{\boldsymbol{v}(t) - \boldsymbol{v}(t-\Delta t)}{\Delta t} \tag{3.46}$$

3.3.2 Trajectory integration

To track the position of the particles, an integration scheme is required. In this study, Adams-Bashforth scheme was utilized.

$$\boldsymbol{x}(t+\Delta t) = \boldsymbol{x}(t) + \frac{\Delta t}{2}[3\boldsymbol{v}(t) - (\boldsymbol{v}(t-\Delta t))] \tag{3.47}$$

It allows for second-order accuracy without having to approximate the acceleration term.

Also note that when $\alpha = 0, \beta = 0$ and $\boldsymbol{\gamma} = \boldsymbol{\gamma}(t) \neq \mathbf{o}$, Equation (3.45) can be written as

$$\boldsymbol{v}(t) = \boldsymbol{v}(t-\Delta t) + \Delta t \frac{\boldsymbol{\gamma}(t)}{m_p} \tag{3.48}$$

Equation (3.47) then becomes

$$\boldsymbol{x}(t+\Delta t) = \boldsymbol{x}(t) + \Delta t\, \boldsymbol{v}(t) + \frac{\Delta t^2}{2m_p}\boldsymbol{\gamma}(t) \tag{3.49}$$

By shifting back in time Equation (3.49) by one time step, the old velocity can be expressed as a function of the positions over time

$$\boldsymbol{v}(t-\Delta t) = \frac{1}{\Delta t}\left[\boldsymbol{x}(t) - \boldsymbol{x}(t-\Delta t) - \frac{\Delta t^2}{2}\frac{\boldsymbol{\gamma}(t-\Delta t)}{m_p}\right] \tag{3.50}$$

Substituting Equation (3.50) into Equation (3.49) gives

$$\boldsymbol{x}(t+\Delta t) = 2\boldsymbol{x}(t) - \boldsymbol{x}(t-\Delta t) + \frac{\Delta t^2}{2m_p}\Big(3\boldsymbol{\gamma}(t) - \boldsymbol{\gamma}(t-\Delta t)\Big) \tag{3.51}$$

It is worth noting that Equation (3.51) resembles a Verlet scheme where $\frac{\mathrm{d}^2\boldsymbol{x}}{\mathrm{d}x^2}(t)$ is estimated as $\frac{3}{2m_p}\boldsymbol{\gamma}(t) - \frac{1}{2m_p}\boldsymbol{\gamma}(t-\Delta t)$ instead of $\frac{1}{m_p}\boldsymbol{\gamma}(t)$.

In general collision driven physics, particle acceleration is not a smooth function (discontinuities happen for example, when contacts between particles instantaneously appear and disappear). Therefore, predicting particle acceleration based on the time variation of its acceleration, as in Equation (3.51), is not accurate. This is why most explicit DEM use a Verlet scheme [17]. However, when particle-particle interacting forces derive from a potential which is a function of the separation distance between particles, acceleration becomes a smooth function. In such a case, the prediction of instantaneous acceleration using more than one past time step may improve the accuracy in solving interaction dynamics between particles.

3.3.3 Considered forces

In this project, only short range particle-particle interactions are considered. These forces are finite only at separation distances $h \ll R_p$. In this study, these short-ranged particle-particle interactions have been modeled as a combination of a normal and a tangential force.

Normal forces are represented as a combination of van der Waals forces ($\boldsymbol{F}_{\mathrm{VDW}}$) and Born Repulsion ($\boldsymbol{F}_{\mathrm{Born}}$) derived from Equations (2.6). and (2.7).

Tangential forces are modeled with the expression of Becker and Briesen [16]. In this model, the

tangential force $\boldsymbol{F}_t$ acting on particle i due to its close proximity with particle j and its corresponding bending moment $\boldsymbol{T}_t$ are represented as

$$\boldsymbol{F}_t = k_t \left(\boldsymbol{\xi}_{ji} - \boldsymbol{\xi}_{ij}\right) \tag{3.52}$$

$$\boldsymbol{T}_t = 2\, R_p\, k_t\, \boldsymbol{n}_{ij} \times \boldsymbol{\xi}_{ij} \tag{3.53}$$

where k_t is spring stiffness and $\boldsymbol{\xi_{ij}}$ is a spring elongation corresponding to the tangential displacement vector since the bond was created (particle "contact"), calculated as:

$$\frac{\mathrm{d}\boldsymbol{\xi}_{ij}}{\mathrm{d}t} = (1 - \boldsymbol{n}_{ij} \otimes \boldsymbol{n}_{ij})(\boldsymbol{v}_j - \boldsymbol{v}_i) - 2\, R_p\, (\boldsymbol{\omega}_j \times \boldsymbol{n}_{ij}) \tag{3.54}$$

where $\boldsymbol{v}$ is their velocity, $\boldsymbol{\omega}$ is their angular velocity and n_{ij} is the unit vector pointing from the center of particle i to the center of particle j. The maximum bending moment that particles can exert on each other is fixed through a critical elongation ($\boldsymbol{d}_{\max}$) after which springs can no longer elongate. Thus, the maximum tangential force between a pair of particles is given as:

$$\boldsymbol{F_t} = k_t\, \boldsymbol{d}_{\max} \tag{3.55}$$

Tangential forces implemented for this project are fully explicit, that is, the velocities used for calculation of elongation are taken from the previous time step. Therefore, Tangential forces acting on each particle are effectively added to the term $\boldsymbol{\gamma}$ of Equation (3.45).

Hydrodynamic forces are estimated either using Free Draining approximation (FDA), or with a combination of LBM+IBM.

Therefore, the parameters to calculate velocity in Equation (3.45) are:

- FDA: $\alpha = 0, \beta = -6\pi\mu R_p, \boldsymbol{\gamma} = 6\pi\mu R_p \dot{\gamma} y + \boldsymbol{F}_{\mathrm{VDW}} + \boldsymbol{F}_{\mathrm{Born}} + \boldsymbol{F}_t$. Similar expressions are implemented for torque calculation.

- LBM+IBM: $\alpha = \rho_f V$ (cancellation of inertia of the fluid inside the sphere), $\beta = 0$, $\boldsymbol{\gamma} = \boldsymbol{F}_{\mathrm{IBM}} + \boldsymbol{F}_{\mathrm{VDW}} + \boldsymbol{F}_{\mathrm{Born}} + \boldsymbol{F}_t$.

It must be pointed out that the inter-particle forces used in this study make the problem stiff, that is, DEM requires very small time steps. While the usual practice is to use separate time steps for the

two phases, in this study, both LBM and DEM had the same time step, that is

$$\delta t_{\mathrm{LBM}} = \delta t_{\mathrm{DEM}} \tag{3.56}$$

This is because, at low Reynolds number conditions, LBM also requires time steps to be small. An exception was made in Chapter 5 Section 5.3.2, when particle-particle forces are scaled with the drag forces. This scaling also resulted in inter-particle forces to become even more stiff (that is, more sensitive to separation distance), requiring even smaller time steps. Therefore, the time steps in Section 5.3.2 were refined, and are related as

$$\Delta t_{\mathrm{LBM}} = F \Delta t_{\mathrm{DEM}} \tag{3.57}$$

where $F \in \{1, 10, 100, 1000\}$ for a corresponding normal force ratio of $\{0.4, 4.0, 10.0, 40.0\}$.

3.4 Validation of the employed numerical methods

In this section, first, implementation of the particle-particle interactions is validated, followed by validation of the implemented LBM+IBM+DEM at low Reynolds numbers. Finally, performance of the code at finite Reynolds number is presented. When possible, results are compared with those available in literature.

3.4.1 Normal forces: Born Repulsion and van der Waals forces

To validate the implementation of the normal forces, two particles are brought close but at a finite distance from each other, and the calculated normal forces are plotted and compared to those obtained through a plot of their analytical expression in Figure 3.6. Unsurprisingly, the plots superimpose perfectly for all the Hamaker constant values (A_H) used in this study, showing that the implementation of normal forces is correct.

3.4.2 Tangential Forces: Bending a rod

For validation of implemented tangential forces, a rod-like arrangement of particles is simulated with forces acting on the particles at the ends as shown in Figure 3.7. The rod of particle consists in

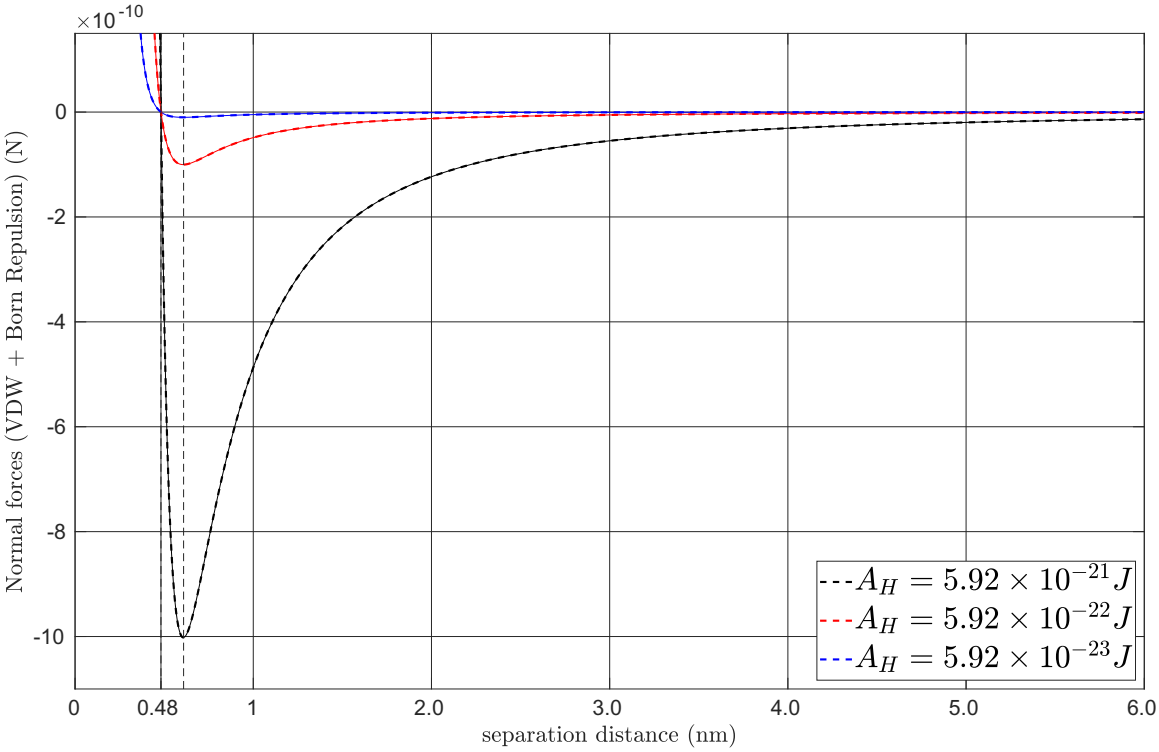

Figure 3.6: Force profile with separation distance for VDW+Born Repulsion as obtained through the implemented code and compared with a plot of their analytical expression. The dashed line ("- -") represents the analytical expression, while the solid line represents the output from the implemented scheme.

11 particles, with the particle at the middle of the rod having its position fixed. Due to the forces acting at the ends of the rod, a bending moment acts on the rod resulting in a bent shape. For a rod of length L, with Young modulus E and second moment of area I, its final shape can be expressed as

$$y(x) = -\frac{2F_{bend}}{EI}\left(\frac{L}{4}x^2 - \frac{|x|^3}{6}\right) \tag{3.58}$$

For a rod made of identical spherical particles, Becker and Briesen [16] showed that EI can be expressed as

$$EI = 8R_p^3 k_t \tag{3.59}$$

Combining Equations (3.58) and (3.59), the solution for the rod of particles is

$$y(x) = -\frac{F_{bend}}{4R_p^3 k_t}\left(\frac{L}{4}x^2 - \frac{|x|^3}{6}\right) \tag{3.60}$$

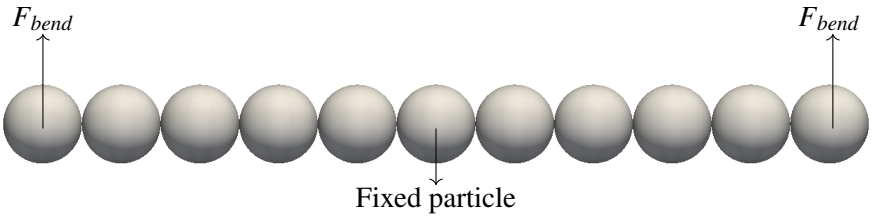

Figure 3.7: A rod of aggregates with bending forces at the ends at t=0.

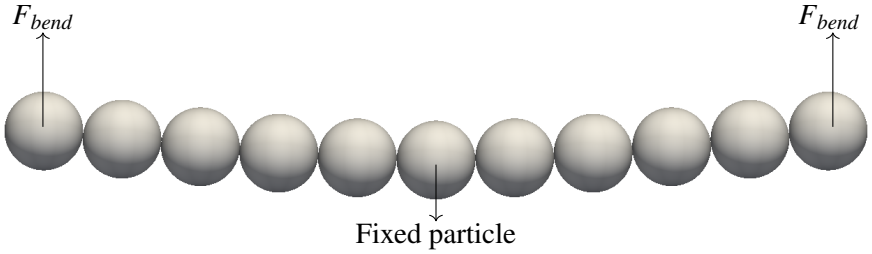

Figure 3.8: Bent rod of aggregates at steady state.

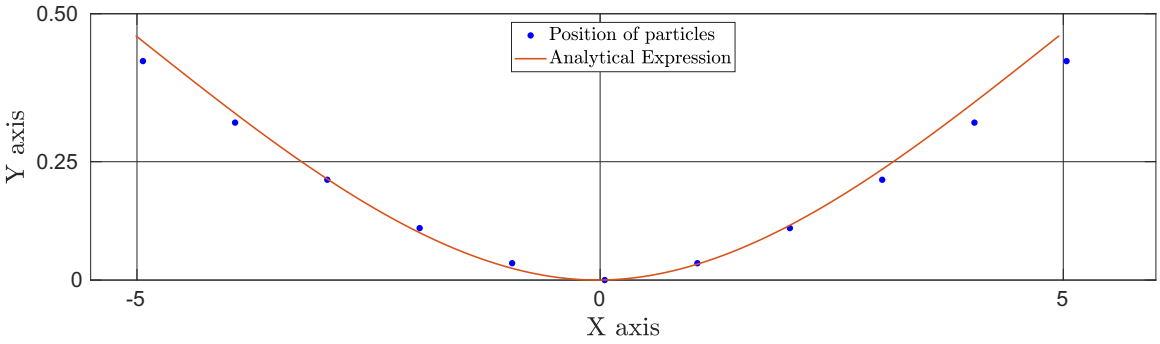

Figure 3.9: Shape of the simulated aggregate compared to analytical solution as obtained through Equation (3.58). Units in X and Y axis are expressed in terms of particle diameters.

The shape of the aggregate before the forces at the ends are applied and at steady state are respectively presented in Figures 3.7 and 3.8. Figure 3.9 shows the comparison against the analytical solution from Equation (3.58). The R^2 value was found to be 0.98 indicating a good agreement between the two, validating the implemented tangential force model. It must be pointed out that the error decreases for longer rods that contain more particles as their behaviour becomes closer to a continuous medium.

3.4.3 Flow resolution in low Reynolds number conditions: dimer in simple shear flow

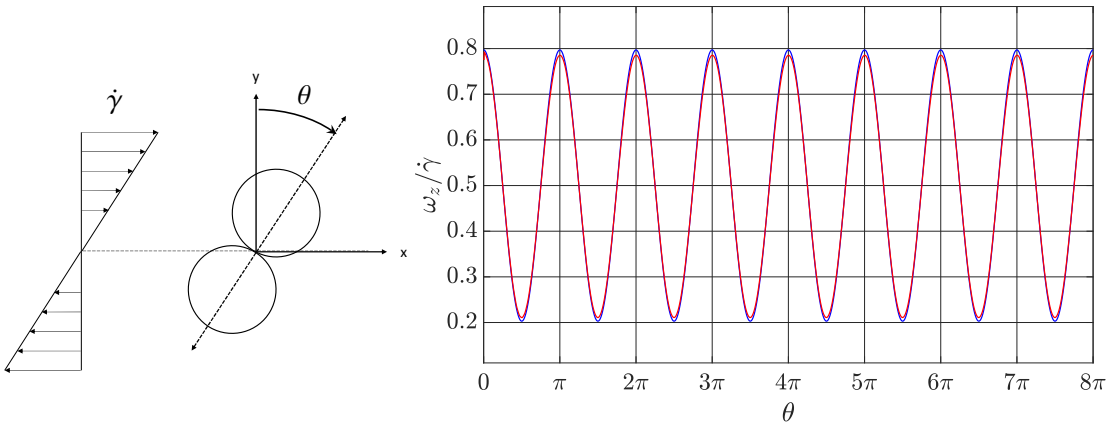

(a) **(b)**

Figure 3.10: Validation for angular speed for a dimer at low Reynolds number conditions: (a) simulation setup, (b) evolution of angular speed over time compared (—)to the analytical solution by Nir and Acrivos [18] shown as (—).

To validate the implemented DEM+LBM+IBM under viscosity dominated flow conditions, the simulated motion of two free-to-rotate particles in contact, so-called "dimer", at particulate Reynolds number 0.09 was simulated is presented in Figure 3.10a. Nir and Acrivos [18] presented an analytical solution, for infinitely small Reynolds number, of the angular velocity ω_z of a doublet of particles under simple shear flow with a shear rate $\dot{\gamma}$

$$\frac{\omega_z}{\dot{\gamma}} = -\frac{1}{2}\left[\,1 + 0.594\,\cos(2\theta)\,\right] \tag{3.61}$$

where θ is the angle between the dimer axis and the cross flow direction. Figure 3.10b shows a good agreement between the simulation results and Equation (3.61). The relative error for the produced amplitude of ω_z is 3.3%.

3.4.4 Finite Reynolds number conditions: approaching spheres

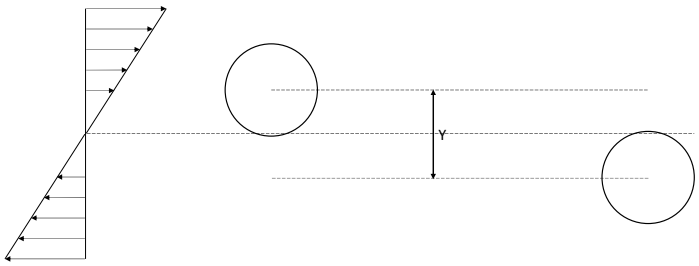

Figure 3.11: Setup to simulation conditions from Haddadi and Morris [19]: two equal sized spherical particles separated by distance Y, approaching each other due to the shear flow

For validation in finite Reynolds number conditions, a case of two particles approaching each other in simple shear flow at particle Reynolds number $\mathrm{Re_p}$ of 2.4 was considered. Figure 3.11 shows the simulation setup. As the particles approach each other, their relative trajectory is plotted and compared with the results produced by Haddadi and Morris [19] for $\mathrm{Re_p}$ of 2.4 calculated as

$$\mathrm{Re_p} = \frac{4\dot{\gamma}R_p^2}{\nu} \tag{3.62}$$

Results at different levels of mesh refinement are presented in Figure 3.12.

In Figure 3.12a, lattice spacing is set to one-tenth of particle radius, that is

$$\Delta x = R_p/10 \tag{3.63}$$

A lubrication correction as described by Haddadi and Morris [19] is included to account for the lubrication forces at scales smaller than the lattice spacing. Figure 3.12a shows the comparison for different initial Y distances trajectories. There is a very good agreement between the trajectories, validating the implementation of LBM+IBM+DEM at finite Reynolds number conditions.

For coarser discretization of particles, as shown in Figure 3.12b for $\Delta x = R_p/5$, the trajectories deviate from the reference curves when the separation distance between the two particles is small. Because the IBM distributes momentum as a source term at nodes surrounding the interface, the forcing induced by the two particles interact with each other and create a numerical repelling force between the particles for separation distances shorter than the lattice spacing. This force is not very big and the particles are still able to get very close to each other, but it is enough to prevent particles

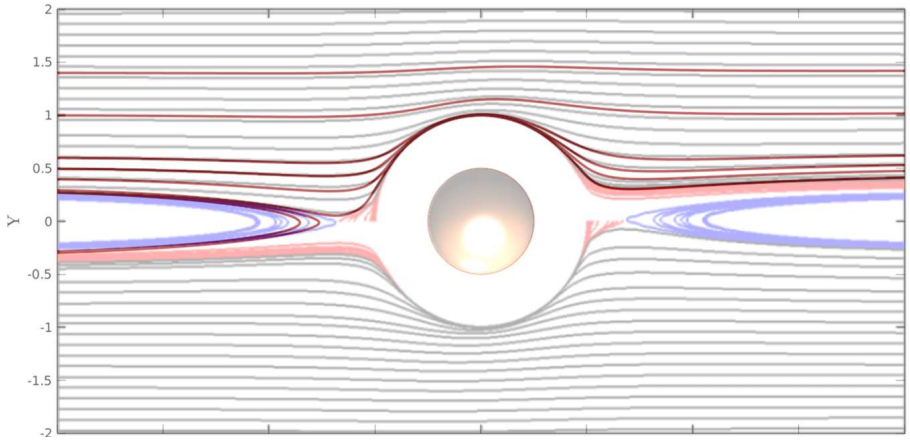

(a) $\Delta x_{LBM} = R_p/10$, with lubrication correction.

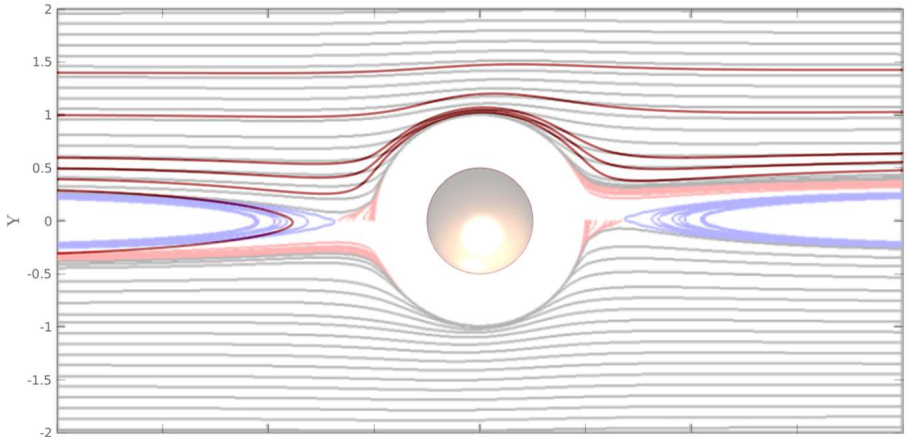

(b) $\Delta x_{LBM} = R_p/5$, with lubrication correction.

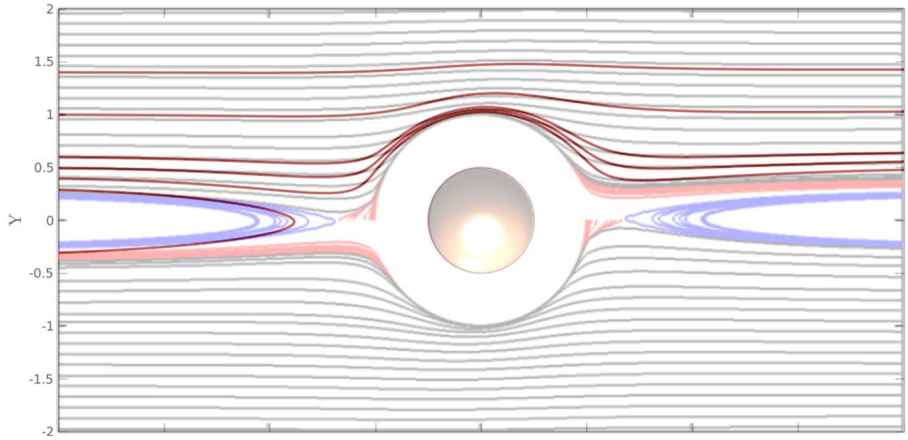

(c) $\Delta x_{LBM} = R_p/5$, without lubrication correction.

Figure 3.12: Relative trajectory of the two particles plotted and superimposed for comparison to those produced by Haddadi and Morris [19] at $\mathrm{Re_p}$ of 2.4, for different conditions. Brown colors represents the trajectories obtained through the implemented LBM+IBM+DEM scheme. Both axes have units of particle diameter.

from colliding in simple shear flow. As illustrated in Figure 3.12c for $\Delta x = R_p/5$, lubrication correction does not contribute significantly to alter particle trajectories and is thus not included in the simulation of aggregates. Results for $\Delta x = R_p/5$ are obviously not as good as for $\Delta x = R_p/10$, but their accuracy seems reasonable, especially considering that in colloidal aggregates, particle interactions at short distances will be dominated by contact forces and that the particulate Reynolds number of primary particles will remain lower than 2.4. Therefore, a spatial discretization with their diameter spreading over 10 LBM nodes is chosen as it gives reasonable accuracy for a much lower computational cost.

References

[1] J. G. M. Eggels and J. A. Somers. Numerical simulation of free convective flow using the lattice-Boltzmann scheme. *International Journal of Heat and Fluid Flow*, 16(5):357–364, 1995. ISSN 0142-727X. doi:10.1016/0142-727X(95)00052-R.

[2] X. D. Niu, C. Shu, Y. T. Chew, and Y. Peng. A momentum exchange-based immersed boundary-lattice Boltzmann method for simulating incompressible viscous flows. *Physics Letters A*, 354 (3):173–182, 2006. doi:10.1016/j.physleta.2006.01.060.

[3] T. Krüger, H. Kusumaatmaja, A. Kuzmin, O. Shardt, G. Silva, and E. M. Viggen. *The Lattice Boltzmann Method: Principles and Practice*. Springer, 2016.

[4] G. R. McNamara and G. Zanetti. Use of the boltzmann equation to simulate lattice-gas automata. *Phys. Rev. Lett.*, 61:2332–2335, Nov 1988. doi:10.1103/PhysRevLett.61.2332.

[5] F. J. Higuera, S. Succi, and R. Benzi. Lattice gas dynamics with enhanced collisions. *Europhysics Letters (EPL)*, 9(4):345–349, jun 1989. doi:10.1209/0295-5075/9/4/008.

[6] F. J. Higuera and J. Jiménez. Boltzmann approach to lattice gas simulations. *Europhysics Letters (EPL)*, 9(7):663–668, aug 1989. doi:10.1209/0295-5075/9/7/009.

[7] S. Chapman. Vi. on the law of distribution of molecular velocities, and on the theory of viscosity and thermal conduction, in a non-uniform simple monatomic gas. *Philosophical Transactions*

of the Royal Society of London. Series A, Containing Papers of a Mathematical or Physical Character, 216(538-548):279–348, 1916.

[8] D. Enskog. *Kinetische theorie der vorgänge in mässig verdünnten gasen: I. Allgemeiner teil*, volume 1. Almqvist & Wiksells boktryckeri-a.-b., 1917.

[9] Z. Guo, C. Zheng, and B. Shi. Discrete lattice effects on the forcing term in the lattice boltzmann method. *Physical Review E*, 65:046308, 2002. doi:10.1103/PhysRevE.65.046308.

[10] P. L. Bhatnagar, E. P. Gross, and M. Krook. A model for collision processes in gases. i. small amplitude processes in charged and neutral one-component systems. *Phys. Rev.*, 94:511–525, May 1954. doi:10.1103/PhysRev.94.511.

[11] M. Gisselbrecht. *Simulation des interactions hydrodynamiques entre inclusions dans un métal liquide : établissement de noyaux d'agrégation dans les conditions représentatives du procédé de flottation*. PhD thesis, Université de Lorraine, 2019.

[12] U. Frisch, D. d'Humieres, B. Hasslacher, P. Lallemand, Y. Pomeau, J.-P. Rivet, et al. Lattice gas hydrodynamics in two and three dimensions. *Complex Systems*, 1:649–707, 1987.

[13] D. d'Humieres. Multiple–relaxation–time lattice boltzmann models in three dimensions. *Philosophical Transactions of the Royal Society of London. Series A: Mathematical, Physical and Engineering Sciences*, 360(1792):437–451, 2002.

[14] C. S. Peskin. Flow patterns around heart valves: A numerical method. *Journal of Computational Physics*, 10(2):252–271, October 1972. ISSN 00219991. doi:10.1016/0021-9991(72)90065-4.

[15] A. M. Roma, C. S. Peskin, and M. J. Berger. An adaptive version of the immersed boundary method. *Journal of Computational Physics*, 153:509–534, 1999.

[16] V. Becker and H. Briesen. Tangential-force model for interactions between bonded colloidal particles. *Physical Review E*, 78(6):061404, December 2008. doi:10.1103/PhysRevE.78.061404.

[17] J. H. Walther and I. F. Sbalzarini. Large-scale parallel discrete element simulations of granular flow. *Engineering Computations*, 26(6), 2009. doi:10.1108/02644400910975478.

[18] A. Nir and A. Acrivos. On the creeping motion of two arbitrary-sized touching spheres in a linear shear field. *Journal of Fluid Mechanics*, 59(2):209–223, 1973.

[19] H. Haddadi and J. F. Morris. Topology of pair-sphere trajectories in finite inertia suspension shear flow and its effects on microstructure and rheology. *Physics of Fluids*, 27(4):043302, 2015. doi:10.1063/1.4917030.

Chapter 4

Numerical investigation of the respective roles of cohesive and hydrodynamic forces in aggregate restructuring under shear flow

Abstract

Hypothesis

Aggregate structure is a key parameter to many processes in a large variety of domains, from inclusion cleanliness in steel making to settling of fine clay tailings from the oil sands industries. Despite the very different nature of the cohesive forces acting in such processes (i.e. partial wetting and colloidal surface interactions) and the different flow conditions such aggregates undergo, their structure is conditioned by a balance between cohesive forces between primary particles in the aggregates and hydrodynamic forces induced by the flow that transports them. Numerical simulations for different ratios between radial and tangential components of cohesive forces to hydrodynamic forces have been conducted from which evolution of aggregate structure over time has been evaluated.

Experiments

Aggregates sharing similar morphological characteristics were algorithmically created. The forces

between primary particles were accounted for using models taken from the literature. Aggregates with different cohesive forces were then submitted to shear by imposing a shear stress in the liquid phase. Hydrodynamic forces were calculated following two approaches: first, with a free draining approximation to extract general trends, then with immersed boundaries in a lattice Boltzmann flow solver to fully resolve the flow and particle dynamics.

Findings

Aggregate structural changes were tracked over time and their stable final size, or eventual breakage, was recorded. Their final structure was found to depend little on normal cohesive forces but is strongly impacted by tangential forces. Normal forces, however, strongly affect breakage probability. Furthermore, resistance to deformation at the aggregate scale induces a flow disturbance that reduces drag forces compared to the free-draining approximation, significantly impacting aggregate restructuring.

4.1 Introduction

Formation of aggregates is common in many solid-liquid processes. For example, waste water treatment often involves aggregation of particles of size range 1 to 44 μm [1] into larger units, which are easier to separate. Another example includes recovery of metallurgical inclusions (size as small as 1 μm) from liquid alloys [2]. Similarly, during pipeline transport of heavy oil, fouling due to the precipitation and aggregation of micron-sized asphaltene particles has been observed [3].

Regardless of the system, aggregate size, shape and structure are key parameters in such solid-liquid processes. Aggregate morphology determines properties such as porosity and dimensions of the solids. These properties in turn affect the solid-liquid and solid-solid interactions in the mixture, leading to changes in system rheology which directly affects the transport of the solids. While morphology of the solids affects the system properties, the flow itself can induce morphological changes to the aggregates. Particularly, shear flow can change the size and density of the particles. Therefore, the coupled response of aggregates and system properties in terms of mixture rheology and aggregate shear history has thus been studied in many fields using experimental approaches [4].

An aggregate's lifetime, from birth by collision of smaller particles (or aggregates) to its death by breakage, may last only fractions of a second [5]. Capturing phenomena with such time scales requires

complex experimental setups [6–8], and even then, microscopic details such as real-time structural changes are nearly impossible to track. On the other hand, modeling and simulation of aggregates in shear flow have enabled scientists to investigate the aggregate behavior at a more fundamental level, where the physics at play can be selectively implemented to see their relative impact on aggregate behavior. Recent aggregate studies through simulations have complemented experimental results [7, 9, 10], proving the viability of numerical studies. Such numerical investigations of aggregation dynamics and aggregate restructuring have been conducted at infinitely low Reynolds conditions using Stokesian Dynamics [11], or even using the Free Draining Approximation (FDA) in which the fluid-particle interactions are simplified to consider only Stokesian drag [12].

In this study, a fully coupled Eulerian-Lagrangian approach has been developed to evaluate the restructuring of aggregates in shear flows for low but finite Reynolds numbers. In particular, a Discrete Element Method (DEM) is used for primary particle interactions and tracking as it is one of the few methods which can accommodate resolved particle-particle interactions. A lattice Boltzmann method (LBM) is used for solving the liquid flow. Both are coupled using an Immersed Boundary Method (IBM) so that any flow disturbance induced by primary particles and consequent hydrodynamic interactions are fully resolved [13]. Selected particle-particle interaction models have been implemented in the DEM to represent the mechanical behaviour of aggregates. General attractive and repulsive force models, and the bending moment as described by Pantina and Furst [14], have been included.

Artificial aggregates were created and characterized using fractal dimension and radius of gyration. The evolution of these shape indicators over time has been studied while aggregates are subjected to a shear flow. Preliminary results obtained with fully coupled liquid-solid simulations were also compared with results based on FDA. Not only does FDA provide computationally economical insights into the effect of particle-particle interactions, the results obtained through FDA also act as a point of reference to highlight the effect of hydrodynamic interactions. In fully coupled simulations, significant perturbations in the flow field were observed due to the presence of particles, which leads to significantly different aggregate structures. This provides a novel perspective into the hydrodynamics, showing that damping of the strain rate around an aggregate results in a shielding effect on particles in the periphery of the aggregate. The cohesive force between a pair of particles is described as the combination of a tangential force and a normal force. The tangential force is

applied in the direction perpendicular to the line-of-centers between primary particles. It imparts a bending moment to the aggregate. Normal cohesive forces are applied in the direction of the line-of-centers. Together, combinations of normal and tangential components can be used to model short-range particle-particle interactions, making the results applicable to non-DLVO interactions. The contributions of these interactions and their underlying impact on aggregate restructuring have been compared, at a given shear rate. This is a pioneering study in establishing the respective roles of tangential and normal forces in aggregate restructuring and breakage. While increased shear produced denser aggregates, the effect of tangential forces on aggregate morphology appears to be more complex. Also, larger tangential forces were found to make aggregates brittle, that is, they were resilient to restructuring but prone to breakage.

4.2 Governing physics in aggregate restructuring under shear flow

Aggregate structure refers to the spatial organization, and connectivity, of the constituent primary particles. Aggregate restructuring can be defined as change in structure without breakage or fragmentation. The extent of restructuring can be quantified using morphological parameters such as fractal dimension and radius of gyration. Particles within an aggregate are held together by the cohesive forces, such that the aggregate is in a structural equilibrium. When aggregates are transported in a liquid phase, they experience hydrodynamic forces that compete with the cohesive forces holding them together. Consequently, aggregate morphology evolves according to the balance of the cohesive forces holding the aggregate together and the external hydrodynamic forces. This happens through re-distribution of the hydrodynamic stresses and the cohesive forces within the aggregate [15]. When the hydrodynamic forces are not balanced by the combined cohesive forces within an aggregate, it will restructure and/or eventually break [10].

Normal cohesive forces, such as van der Waals interactions, hold particles within an aggregate, at separation distances much smaller than the particle size. Therefore, the particles are practically bonded to each other through the cohesive forces. The relation between normal cohesive forces and aggregate restructuring and breakage has been discussed extensively in the literature. For example, Zeidan et al. [16] found that aggregates ruptured at low cohesive forces, while relatively higher cohesive forces lead to breakage through erosion of particles. Kroupa et al. [17] observed that higher

normal cohesive forces produced larger stable aggregates in similar hydrodynamic conditions. These studies clearly showed that strong cohesive forces are necessary for strong aggregates. Furthermore, Kroupa et al. [17] also showed that it is only the maximum attractive force that determines structural evolution of an aggregate. However when it comes to restructuring, normal forces have been shown to have little impact while tangential forces reduce restructuring [18].

Some studies have covered the relative effect of forces on aggregate evolution [18, 19] by approximating the hydrodynamic forces through FDA, where primary particles comprising an aggregate do not see any disturbance in the flow due to the presence of other particles. To account for the role of hydrodynamic interactions, numerical investigations of aggregate behaviour at very low Reynolds number have been conducted using Stokesian Dynamics (SD). Some of these studies focused on cohesive force distribution in rigid aggregates [20–22], and have related the hydrodynamic stresses to a stable critical size of aggregates. Other studies identified a power law relation between the hydrodynamic stresses and the critical mass of the aggregates [5, 23, 24].

Finally, studies resolving the hydrodynamics using SD and their impact on aggregation [11, 25], restructuring [10, 26, 27] and breakage kinetics [5] have shown how aggregates evolve under different hydrodynamic stresses, but are still not numerous enough to cover the full set of parameters at play. For example, Horii et al. [10] did not include the tangential forces which have been seen to be rather crucial in restructuring. Furthermore, since SD uses multipole expansion of the velocity field to solve the linear Stokes equations, it is restricted to low Reynolds number conditions. Consequently SD simulations are likely to produce inaccurate predictions of hydrodynamic interactions whenever the shear rates are high or the aggregates are too rigid to restructure, in which case inertial effects at aggregate scale appear. Overall, even with these recent studies, there is a knowledge gap in the understanding of aggregate evolution in shear flow. Firstly, the role of constituent primary particle interactions in aggregate evolution, especially on breakage, is not well documented. Secondly, while the importance of resolved hydrodynamics has been demonstrated, their effects on restructuring and breakage have not been thoroughly investigated.

4.3 Simulation setup and numerical methods

This paper aims to relate aggregate restructuring to the normal and tangential components of cohesive forces between its constituent particles. To do so, the usual interaction potentials for colloidal particles (such as van der Waals and Born repulsion) have been used. However, the results have been interpreted by considering only the maximum values of the force components. Therefore, the observations do not depend on the underlying interaction potential. Breakage events are recorded in order to distinguish conditions under which aggregate evolution kinetics are driven by breakage (and eventual re-aggregation) or restructuring. First, a model with simplified hydrodynamics using FDA is used. Through FDA, the role of cohesive forces between constituent particles is established. Then, a lattice Boltzmann method, where particles are represented using an Immersed Boundary Method, is used to fully couple aggregate and flow dynamics.

4.3.1 Modelling of the physical problem

The objective of the numerical investigations is to capture and quantify the morphological evolution of aggregates in shear conditions that are representative of transport and mixing processes. In such processes, shear is induced by wall shear stress, and by turbulent agitation. Small aggregates are typically smaller than the Kolmogorov length scale of the turbulent flows that carry them. Therefore, the flow field that drives their restructuring is approximated by a plane shear flow, which combines a strain [7, 8, 10] with a rotation. Fig. 4.1 shows the velocity field in a plane shear flow in the vicinity of an aggregate. The aggregate is placed at the center of the domain and is free to move and rotate according to the forces it experiences.

While aggregates undergo shear flows, process quantities such as energy dissipation are often used to estimate shear stresses in the flow. In the idealized case of a plane, the shear stress tensor is reduced to one off-diagonal component and can thus be characterized by a single value τ. In a Newtonian fluid, such as water, there is a direct relation between the shear stress and the resulting shear rate $\dot{\gamma}$:

$$\dot{\gamma} = \tau/\mu \tag{4.1}$$

where μ is the dynamic viscosity of the fluid. Using this relation, all following simulation data are processed with shear rate as a parameter, even when shear stresses were the actual control parameters

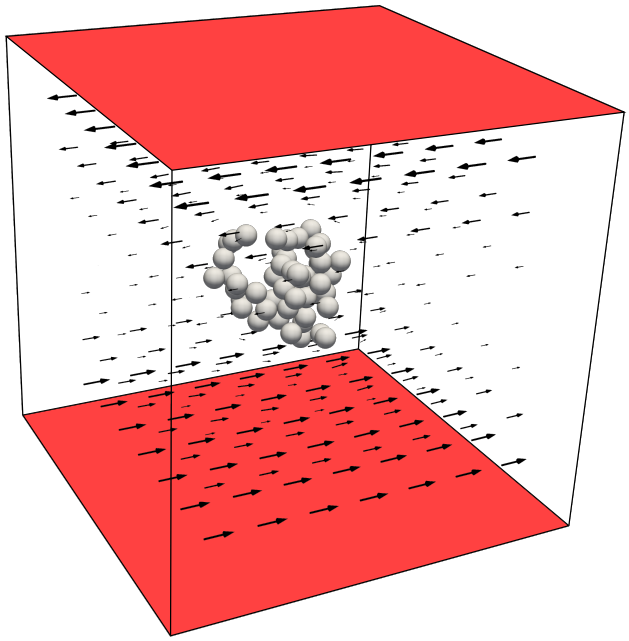

Figure 4.1: Domain setup for simulations with hydrodynamics. The arrows show the flow induced through top and bottom walls.

in simulations.

To study aggregate restructuring, aggregates were placed in simulated, simple plane shear flows. The hydrodynamic forces from the liquid phase that are endured by the aggregates were either modelled through analytical approximations or calculated by resolving the flow. For the latter part, a lattice Boltzmann method coupled with the solid phase through an Immersed Boundary Method was used. As stated earlier, aggregate restructuring depends on the balance between hydrodynamic forces and the cohesive forces between constituent primary particles.

Cohesive forces between primary particles were thus implemented and characterized by their maximum values; that is, the one that needs to be overcome by the drag force from the flow in order to break the bonds between them. Then, the morphological evolution of aggregates was recorded by tracking the variations of their radii of gyration over time. To extract average trends, all simulations were repeated for a set of 10 different aggregates comprised of the same number of particles, and the same initial radius of gyration.

With the flow characterized by its shear rate $\dot{\gamma}$ and an aggregate by its radius of gyration R_g, the

aggregate Reynolds number is defined as

$$\mathrm{Re} = \frac{4\dot{\gamma}R_g^2}{\nu} \tag{4.2}$$

which varies over the duration of a simulation since R_g varies. In some simulations presented later, R_g can be 1.8 times greater than its initial value corresponding to a multiplication of this Reynolds number by more than 3. However, the primary particle Reynolds number Re_p is constant since R_p, the primary particle radius, is fixed, so that

$$\mathrm{Re}_p = \frac{4\dot{\gamma}R_p^2}{\nu} \tag{4.3}$$

4.3.2 Coupling aggregate dynamics and hydrodynamics

Although FDA is an approximation of the hydrodynamic action on the particles, its simplicity in implementation and low computation times makes it a valuable tool to study aggregate evolution in simple shear flows. Thus, it has been widely utilized [12, 18, 28–30]. Because FDA cannot fully capture the hydrodynamic effects on aggregate restructuring, and such interactions are known to play a significant role in the restructuring of aggregates [18, 27], they have been resolved in this study using a lattice Boltzmann method (LBM).

Free Draining Approximation (FDA)

Aggregates are introduced to a shear profile characterized by its shear rate $\dot{\gamma}$. In FDA, the effect of the flow on each particle in an aggregate is modelled through the shear force and torque that are responsible for driving the aggregate evolution. One way to calculate this shear force ($F_{f/p}$) and torque ($T_{f/p}$) is by using Stokes' drag law as

$$\boldsymbol{F}_{f/p} = 6\pi\mu R_p(\boldsymbol{v}_p - \dot{\gamma}\, z\, \boldsymbol{e}_x) \tag{4.4}$$

$$\boldsymbol{T}_{f/p} = 8\pi\mu R_p^3(\boldsymbol{\omega}_p - \frac{1}{2}\,\dot{\gamma}\, \boldsymbol{e}_y) \tag{4.5}$$

This method assumes that the flow is not affected by the particles, so that hydrodynamic interactions between particles within an aggregate are not considered. Thus, it tends to overestimate

the hydrodynamic forces as it does not compensate for the surface of a particle shielded from the flow by other surrounding particles [9, 31–34]. This phenomenon is commonly referred to as the "shielding effect". Some studies have made attempts to correct for the shielding effect either by calculating the area of the aggregate exposed to the shear flow [9], or by correcting the shear forces by comparing with hydrodynamic forces for resolved particles [18], but in the end local hydrodynamics always strongly rely on models and are only loosely approximated in FDA. Despite these drawbacks, FDA has been widely used to study aggregate evolution due to its simplicity and computational efficiency [12, 18, 19]. Since FDA overestimates the hydrodynamic forces, it can be expected that a relative study of forces will yield qualitatively the same results as a study done with fully resolved hydrodynamics. Therefore, FDA was used for an initial study of the forces involved in aggregate restructuring.

Fully resolved hydrodynamics

To accurately account for the hydrodynamics, a lattice Boltzmann method is coupled with a Discrete Element Method through an Immersed Boundary Method. The LBM used in this research was first published by Eggels and Somers [35] and extensively described in the more recent work of Sungkorn and Derksen [36]. It is coupled with the solid phase using the IBM presented by Niu et al. [13]. Particle diameter is discretized over 10 lattice nodes, and the domain size is set to $198 \times 198 \times 198$ lattice nodes. The details of this LBM approach and its coupling with the solid phase through IBM have been described in Chapter 3. As discussed in Chapter 3, the particles are tracked individually and the surface of each particle is discretized by Lagrangian marker points. It must be pointed out that the volume within the solid body is seen as fluid in the Eulerian representation of the flow. The momentum of this fluid enclosed in the sphere must also be accounted for in the momentum balance equations. One way to treat this is by making the enclosed fluid within each particle behave as a solid body. This is achieved with layers of Lagrangian marker points also on the inside of the sphere. The diameters of the primary spheres in aggregates span over 10 LBM meshes and their surfaces are covered by 1302 regularly distributed marker points for the IBM. The inner layers consist of 326 and 82 Lagrangian marker points at distances of 0.7 and 0.3 times the sphere radius, respectively. These points ensure that the flow inside the solid particles follows the motion of the solid body. The action on the marker points by the fluid inside the spheres is subtracted from the

total IBM force to obtain the force of the surrounding fluid acting on the solid particle. Since the fluid inside the sphere behaves as a solid body, the force and torque produced by the enclosed fluid can be calculated as

$$\boldsymbol{F}_{f/p}^{\text{in}} = \rho \frac{4\pi}{3} R_p^3 \frac{\mathrm{d}\boldsymbol{v}_p}{\mathrm{d}t} \tag{4.6}$$

$$\boldsymbol{T}_{f/p}^{\text{in}} = \rho \frac{8\pi}{15} R_p^5 \frac{\mathrm{d}\boldsymbol{\omega}_p}{\mathrm{d}t} \tag{4.7}$$

which makes the physical force applied by the liquid flow on the sphere

$$\boldsymbol{F}_{f/p} = \boldsymbol{F}_{f/p}^{\text{IBM}} - \boldsymbol{F}_{f/p}^{\text{in}} \tag{4.8}$$

$$\boldsymbol{T}_{f/p} = \boldsymbol{T}_{f/p}^{\text{IBM}} - \boldsymbol{T}_{f/p}^{\text{in}} \tag{4.9}$$

where $\boldsymbol{F}_{f/p}^{\text{IBM}}$ and $\boldsymbol{T}_{f/p}^{\text{IBM}}$ are the total momentum exchange between the liquid phase and the marker distribution [13]. Such inertia corrections are included in the numerical resolution of the particle as a force and a torque that depend on particle acceleration.

To induce flow, shear stresses are imposed at the top and bottom planes of the simulation domain, illustrated as red planes in Fig. 4.1. To impose a controlled shear stress, the boundaries are treated as free-slip at the LBM level and an extra source term is added to the liquid layer adjacent to the free-slip boundary condition. The other boundary conditions, in streamwise and spanwise directions, are periodic. The liquid is initially at rest and the aggregate inside is not moving. When the simulation begins the fluid starts to be sheared under the combined action of stresses on the top and bottom planes.

4.3.3 Aggregate creation and characterization

Aggregate size and density are the most obvious quantities to characterize its structure [37]. Radius of gyration (R_g) is widely used to quantify aggregate size. In the context of aggregates, R_g^2 is defined as the ratio of the second moment of mass around the center of the aggregate to the total mass:

$$R_g^2 = \frac{1}{m} \int r^2 \mathrm{d}m \tag{4.10}$$

For an aggregate consisting of N primary particles, as long as their size is small compared to the aggregate size ($R_p \ll R_g$), the radius of gyration of the aggregate can be approximated as

$$R_g = \sqrt{\frac{\sum_{i=1}^{N} m_i r_i^2}{\sum_{i=1}^{N} m_i}} \tag{4.11}$$

where r_i is the distance between particle i and the center of gravity of the aggregate, and m_i is its mass. If primary particles have the same mass, it simplifies as

$$R_g = \sqrt{\frac{\sum_{i=1}^{N} r_i^2}{N}} \tag{4.12}$$

On the other hand, density is widely reported as aggregate fractal dimension D_f obtained through techniques such as light scattering [7], imaging and settling [6]. However, Gmachowski [38] showed that D_f depends only on two parameters: R_g and the number of particles N in an aggregate. Therefore, if the number of constituent particles within an aggregate remains the same (that is, the aggregate does not break), R_g can be used to represent density. Essentially, R_g reflects the distribution of mass in an aggregate relative to its center of mass: the lower its value, the more densely packed the aggregate. Another parameter sometimes used for density measurement is the ratio of hydrodynamic radius R_h to radius of gyration. However, Harshe et al. [39] showed that R_g/R_h varies roughly between 1.0 and 1.3 as the density changes, and therefore R_g can be reasonably used to estimate R_h. When R_g is normalized by the radius of the constituent primary particle (R_p), it gives the relative size R_g^* of the aggregate as

$$R_g^* = R_g/R_p \tag{4.13}$$

Since all aggregates in this work have the same number of primary particles, the dimensionless radius of gyration R_g^* is a useful aggregate morphological parameter that reflects both aggregate size and density: bigger aggregates with the same number of particles are less dense.

The initial aggregates were produced algorithmically, which are shown in Fig. 4.2. The aggregate creation algorithm takes two parameters: the number of primary spherical particles in the aggregate, and a target radius of gyration. After the first pair of particles, all other spheres are added iteratively to the aggregate. Each new sphere position is chosen among sixteen (16) random positions on a randomly selected sphere from the already added spheres. The positions that lead to particle overlap

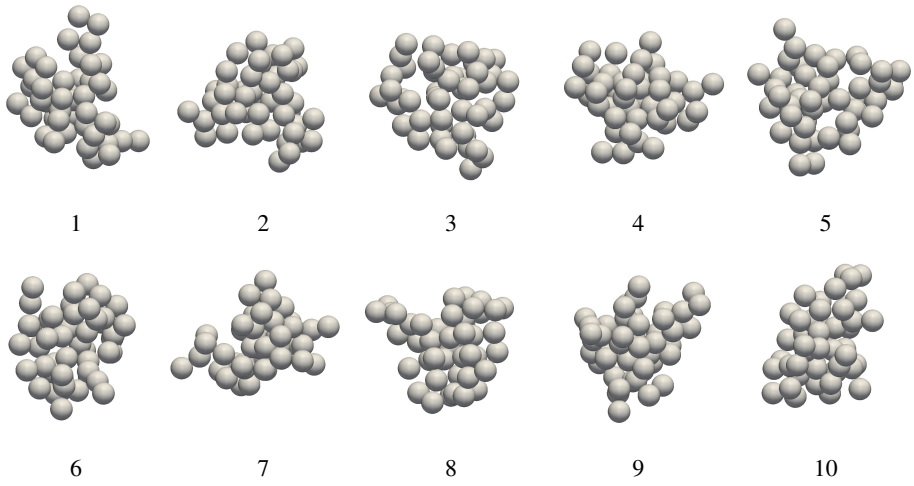

Figure 4.2: The 10 algorithmically created aggregates that have been used as initial conditions in the simulations ($N = 50$, $R_p = 1\,\mu\text{m}$, $R_g = 4.55\,\mu\text{m}$).

are discarded and the new sphere is created at the remaining position that yields the radius of gyration closest to the target value. This process is repeated until the aggregate contains the desired number of primary particles.

It must be pointed out that the method of aggregate generation is expected to have little impact since the aggregates experience significant restructuring in the first rotation, and the final structure is obtained after several more rotations. Therefore, the final structure is expected to reflect the effect of the shear flow more than the method of aggregate generation.

The aggregates used in these simulations are composed of 50 primary particles. Each primary particle has a radius R_p of 1 μm, and each aggregate has a radius of gyration ratio $R_g^* = 4.55 \pm 0.02$. This latter value corresponds to a fractal dimension of 2.3, according to the empirical expression given by Gmachowski [38]. The number of primary particles is chosen so that the aggregates show a fractal structure while remaining small enough to keep the simulation time within practical limits. The fractal dimension is set to 2.3 because it is a value widely observed for colloidal aggregates [31, 40–43].

The simulations were run for ten (10) different aggregates produced using the algorithm described above to extract general trends from their average behavior. Recall that the 10 algorithmically generated aggregates are presented in Fig. 4.2.

4.3.4 Particle interactions

The non-hydrodynamic interactions between primary particles, also referred to as cohesive forces, have been modeled according to the DLVO theory [44] which is commonly used to capture particle interactions in colloidal aggregates. In this theory, forces are derived from potentials that depend on the distance between the centers of two particles. A simplified form for the van der Waals potential between two spherical particles has been used [45]:

$$V_{\mathrm{VdW}}(s) = -\frac{A_H}{12(s-2)} \tag{4.14}$$

where s is the distance between particle centers divided by particle radius, so that $s = 2$ corresponds to exact particle contact. This potential yields attractive forces that must be balanced by a very short-range force to prevent particle overlapping. Born repulsion [46] fulfils this role. For two spherical particles, the Born repulsion potential is given by

$$V_{\mathrm{Born}}(s) = \frac{A_H N_{\mathrm{Born}}}{s}\left[\frac{s^2-14s+54}{(s-2)^7} + \frac{60-2s^2}{s^7} + \frac{s^2+14s+54}{(s+2)^7}\right] \tag{4.15}$$

Although Born repulsion originates from the theory of overlapping electron clouds, its application in the study of colloidal aggregates represents a repulsive force steeper than the VDW forces, and acts as a non-overlapping force. Together, the linear dependence of VDW forces and Born repulsion on the Hamaker constant allows manipulation of the maximum attractive force by a single parameter. Since these forces act on spherical particles along the line joining the two centers, they are normal to the surfaces. Hereinafter, the resulting force derived from van der Waals and Born repulsion potentials is thus called the normal force:

$$\boldsymbol{F}_n = -\frac{1}{R_p}\frac{\mathrm{d}}{\mathrm{d}s}(V_{\mathrm{VdW}} + V_{\mathrm{Born}})\boldsymbol{n} \tag{4.16}$$

Normal forces form a barrier, which must be overcome by external forces in order to break the "bond" between two particles. This barrier corresponds to the maximum attractive force F_n between two particles. Consequently, aggregate restructuring is governed by the maximum attractive force [17], regardless of the force dependence on particle distance s.

Fig. 3.6 from Chapter 3 shows the force profiles obtained for the values of Hamaker constant

used in the manuscript. It can be seen that peak attraction is achieved at separation distance of less than 1 nm for the particles considered here, and this separation distance for maximum attractive force does not change with the Hamaker constant. Similarly, the equilibrium separation distance, that is the position of net zero force, is at 0.48 nm for all Hamaker constants. Although this equilibrium distance was used as the initial separation distance while generating aggregates, any other separation value also results in the particles to settle at this equilibrium condition by energy dissipation through viscous losses.

Tangential forces have also been considered and modeled with the expression of Becker and Briesen [29] that applies to colloidal particles. Tangential forces induce a resistance to bending in the aggregate. In this model, the tangential force $\boldsymbol{F}_t$ acting on particle i due to its close proximity with particle j and its corresponding bending moment $\boldsymbol{T}_t$ are represented as

$$\boldsymbol{F}_t = k_t \left(\boldsymbol{\xi}_{ji} - \boldsymbol{\xi}_{ij} \right) \tag{4.17}$$

$$\boldsymbol{T}_t = 2\, R_p\, k_t\, \boldsymbol{n}_{ij} \times \boldsymbol{\xi}_{ij} \tag{4.18}$$

where k_t is a spring stiffness and ξ_{ij} is a spring elongation corresponding to the tangential displacement vector since the bond was created (particle "contact"). The spring stops elongating after this critical elongation $d_{\max}$. Thus, the maximum tangential force F_t is

$$F_t = k_t\, d_{\max} \tag{4.19}$$

The value of $d_{\max}$ was chosen considering two factors. First, it must be small compared to the particle size, preventing it from becoming another parameter which may influence the results. Secondly, too small value $d_{\max}$ can make the F_t over-sensitive to distance, resulting in force calculation to be numerically unstable. Therefore, a value of $d_{\max}$=0.02 R_p was chosen, and the maximum tangential force F_t was varied through k_t.

A tangential bond is formed between two particles when the surface-to-surface distance is shorter than $d_{\max}$. The tangential force increases with the elongation of the spring in the tangential direction until the maximum elongation $d_{\max}$ is reached. The spring then stops elongating any further and tangential forces remain capped to the corresponding maximum force. When the surface-to-surface

distance exceeds $d_{\max}$, the tangential bond is broken, and no tangential force is applied anymore. If a new bond is made later between the same two particles, it starts with a spring elongation reset to 0.

This combination of VDW, Born repulsion and tangential forces to model particle-particle interactions has produced results that compare well with experimental results [7, 29] and is therefore often found in investigations of colloidal aggregates [18, 19, 47]. Since the range of these cohesive forces is very short compared to the size of primary particles, they behave as apparent contact forces at particle scale, which is the relevant length scale for hydrodynamics and aggregate restructuring. These apparent contact forces are bounded by the maximum value of the normal and tangential force profiles, and these maxima characterize bond strength between particles in aggregate restructuring.

4.3.5 Particle motion

Although only the maxima of force components matter in the end, the resolution of particle motion uses smooth potentials so that the balance between hydrodynamic actions on particles and cohesive forces is achieved by letting particles adjust their distances from each other. Particle motion is thus tracked and updated by solving Newton's equation of motion for every particle following the Discrete Element Method (DEM). The equations are detailed for linear moment only, because angular momentum is solved in the exact same way, i.e.

$$m\frac{\mathrm{d}\boldsymbol{v}}{\mathrm{d}t} = \boldsymbol{F}_{f/p} + \boldsymbol{F}_n + \boldsymbol{F}_t \tag{4.20}$$

Equation (4.20) is solved for particle velocity $\boldsymbol{v}$. Due to high sensitivity of the particle-particle interactions to separation distance, a time step of 4×10^{-9}s is used. Trajectory is integrated using a first-order scheme. Details are presented in the Chapter3, Section 3.3.

Particle interactions are very short ranged, they impose very short time steps in the simulation to be captured accurately. Very short time steps are also required by low-Reynolds simulations with a LBM flow solver. In the end, because of the strong constraints limiting the time step, particle trajectory integration is achieved using a very simple Euler integration scheme as

$$\boldsymbol{x}(t+\Delta t) = \boldsymbol{x}(t) + \boldsymbol{v}(t)\,\Delta t \tag{4.21}$$

In LBM+IBM simulations, the inertia of the liquid inside the particles is approximated as in Equation (4.6) and moved to the left hand side of Equation (4.20). Particle acceleration is thus calculated from Equation (4.20) and velocity and position are obtained through the same first-order integration scheme as used in FDA. The inertia correction from Equation (4.6) is only numerically stable if particle density is sufficiently greater than liquid density. Thus, particle density is taken to be twice the liquid density in the simulations. Although this value was somewhat arbitrarily chosen, the actual particle density is not important, since the Reynolds numbers remain very low and gravity force is neglected, and thus particle inertia has no impact on their dynamics. Quantitatively, the inertial effects of a primary particle can be estimated by the Stokes number, which is given in such conditions as

$$\mathrm{St}_p = \frac{1}{18}\mathrm{Re}_p \ll 1 \tag{4.22}$$

The results obtained with $\rho_p = 2\rho$ will thus be applicable to aggregates made of any materials, such as clay or latex, as long as they undergo low Reynolds number flow dynamics.

4.3.6 Tracking of aggregate evolution

Under the effect of the hydrodynamic forces from the shear flow, aggregates rotate. With rotation, the positions of particles change and so do the hydrodynamic forces acting on them. Consequently, aggregates change their structure to redistribute normal and tangential forces F_n and F_t and balance the shear they undergo. The amount of restructuring required to balance the external drag force depends on F_n and F_t. If shear forces cannot be balanced by restructuring, aggregates eventually break. In other words, the force configuration within aggregates can lead to drastically different aggregate evolutions.

To capture the impact of different force configurations on aggregate evolution, various ratios of the normal and tangential cohesive forces to hydrodynamic forces were considered over several orders of magnitudes, and their impact on restructuring and breakage was analyzed. For any two given particles, Eq. (4.14) and (4.15) show that the maximum normal force F_n depends on the Hamaker constant A_H, which is generally of the order 10^{-20} J. Pantina and Furst [14] suggested that the resulting maximum tangential force is of the order 10^{-11} N for colloidal particles. Also, it is common to see shear rates of order 10^2 s^{-1} in experiments involving colloidal aggregates. The

Table 4.1: Simulation parameters: values of the physical constants and corresponding maximum forces.

Normal force		**Tangential force**		**Drag force**	
A_H (J)	F_n (N)	k_t (N/m)	F_t (N)	$\dot{\gamma}$ (s^{-1})	$F_{f/p}$ (N)
5.92×10^{-21}	10^{-9}	2.5×10^{-2}	10^{-9}	2.653×10^{3}	10^{-10}
5.92×10^{-22}	10^{-10}	2.5×10^{-3}	10^{-10}	2.653×10^{2}	10^{-11}
5.92×10^{-23}	10^{-11}	2.5×10^{-4}	10^{-11}	2.653×10^{1}	10^{-12}
		2.5×10^{-5}	10^{-12}		

maximum hydrodynamic force can be estimated by the Stokesian drag relation

$$F_{f/p} \sim 12\,\pi\,\mu\,\dot{\gamma}\,R_p^2 \tag{4.23}$$

These simulation parameters give a base case for the maximum forces. Table 4.1 lists all the parameters used for controlling the forces, along with the resulting maximum force values. Each simulation case was defined by a combination of these forces, covering several orders of magnitudes for the forces considered. This allows for comparison of conditions where the components of the short-range forces are widely different. Due to the range of shear rates considered, the Stokes and Reynolds numbers at particle scale range from 10^{-4} to 10^{-2} and thus remain much smaller than 1. Consequently the inertial effects in particle motion and in the flow are negligible, so that only the ratio between the cohesive and hydrodynamic forces plays a role, not their absolute values. The normal force F_n and tangential force F_t are thus normalized by the drag force to quantify their relative effects on aggregate evolution. As a result, the dimensionless force ratios F_t^* and F_n^* vary over several order of magnitudes

$$\begin{aligned} F_n^* &= \frac{F_n}{F_{f/p}} \in \{10^1, 10^2, 10^3\} \\ F_t^* &= \frac{F_t}{F_{f/p}} \in \{10^{-2}, \ldots, 10^3\} \end{aligned} \tag{4.24}$$

To capture the evolution of aggregates, their dimensionless radii of gyration R_g^* were recorded over the simulation run. Fig. 4.3 shows the evolution tracking of Aggregate #3 presented in Fig. 4.2 for different values of F_n^*. Due to shear flow, the aggregate rotates and restructures. The rotation is

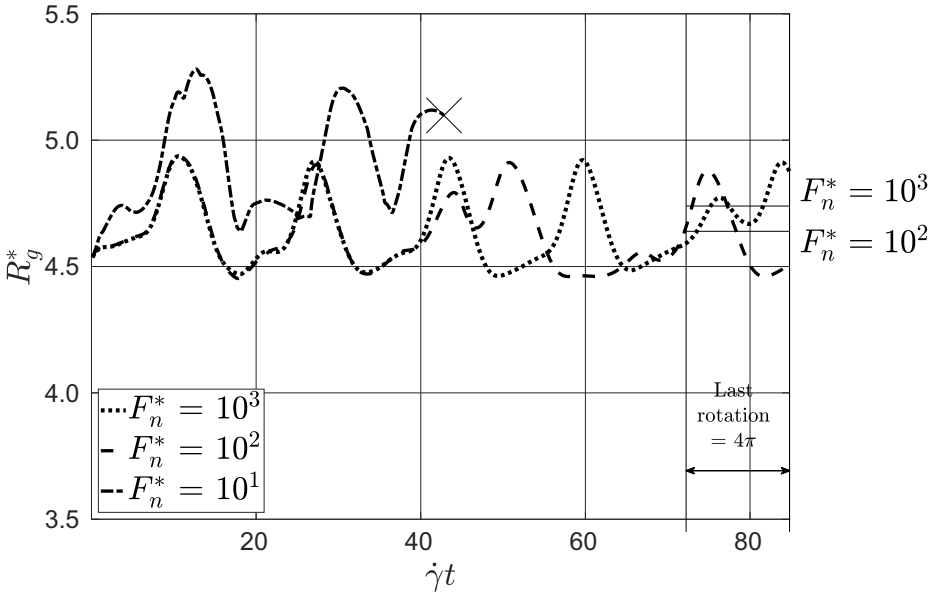

Figure 4.3: Illustration of aggregate evolution tracking. Breakage is marked by '×'. If an aggregate survives, its final size is taken as the average value over its last rotation period.

observed only around the vorticity axis. As it restructures, its radius of gyration R_g^* fluctuates over time, and it evolves towards a denser structure. Some force ratios lead to breakage, as illustrated by the interrupted R_g^* trajectories and the cross marker in Fig. 4.3 for $F_n^* = 10$. Otherwise, the final size of non-breaking aggregates is quantified by their average radius of gyration over the last rotation period given by $4\pi\ \dot{\gamma}t$. Final sizes and breakage events (if any) are recorded for each of the ten (10) aggregates of Fig. 4.2 and for each different force configuration. The final values of R_g^* are then averaged over the surviving aggregates to give $\langle R_g^* \rangle$ which represents the average final size of the aggregate for each force ratio. This $\langle R_g^* \rangle$ is then analyzed to quantify the impact of the different forces on restructuring. The evolution of all ten aggregates for various force ratios is provided in Fig. 4.4 and Fig. 4.7.

All simulations were run for a period of $84.8\ \dot{\gamma}t$. Since the fluid has a rotation rate of $4\pi\ \dot{\gamma}t$ in simple shear flow conditions, and fractal aggregates rotate at a rate close to that of a sphere, $84.8\ \dot{\gamma}t$ provides sufficient time for approximately 7 rotations for an aggregate. In each rotation, the aggregate goes through 2 cycles of compression and elongation.

4.4 Results and discussion

The evolution of each aggregate under all considered force ratios is shown in Fig. 4.4. All graphs in the same column have the identical normal force ratio, while the tangential forces increase from top to bottom. It can be seen that aggregate to aggregate behavior for same force ratios can vary significantly (cases in point include $F_n^* = 10$ and $F_t^* \in \{.01, 0.1, 100\}$). Also, under the same conditions and force ratios, fate of the aggregates in terms of breakage or survival can be very different. Nonetheless, even in such a chaotic system, general trends can be observed: radii of gyration at the end of most simulation cases are distributed around an average value that clearly changes with force ratios. Meaningful data for restructuring can be extracted from aggregates that survive, while broken aggregates can provide information about breakage mechanism. Although some aggregates do not reach structural equilibrium in 6–7 rotations, all aggregates undergo enough restructuring to highlight the effects of the involved forces.

The radius of gyration towards the end of the evolution is averaged over all aggregates that are not broken after $84.8\,\dot{\gamma}t$. This results in one scalar value $\langle R_g^* \rangle$ that characterizes aggregate morphologies for each set of force ratios. For the aggregates that broke, the impact of forces on breakage is quantified through a "breakage probability". In this study, it is defined as the total number of aggregates broken after $84.8\,\dot{\gamma}t$ divided by the total number of aggregates, that is 10, as simulations were repeated for the 10 different aggregates presented in Fig. 4.2.

Eventually, the effects of the ratios of the normal and tangential forces to hydrodynamic force are quantified by comparing these two scalar characteristic values, that is the average dimensionless radius of gyration $\langle R_g^* \rangle$ and breakage probability, for various force conditions.

4.4.1 Effect of normal force

Fig. 4.5 shows aggregate evolution for various values of the normal cohesive force. Fig. 4.5a shows the effect of normal forces on the final structure of the aggregates that did not break. The horizontal axis is the dimensionless normal force F_n^*. The vertical axis shows the final average value $\langle R_g^* \rangle$ attained by the aggregate after evolving for $84.8\,\dot{\gamma}t$. In Fig. 4.5a, cases with the same tangential force to drag ratio are joined by lines. The $\langle R_g^* \rangle$ varies at most by 2.6 % even though the normal forces vary by two orders of magnitude. The small variation shows that the lines are essentially flat,

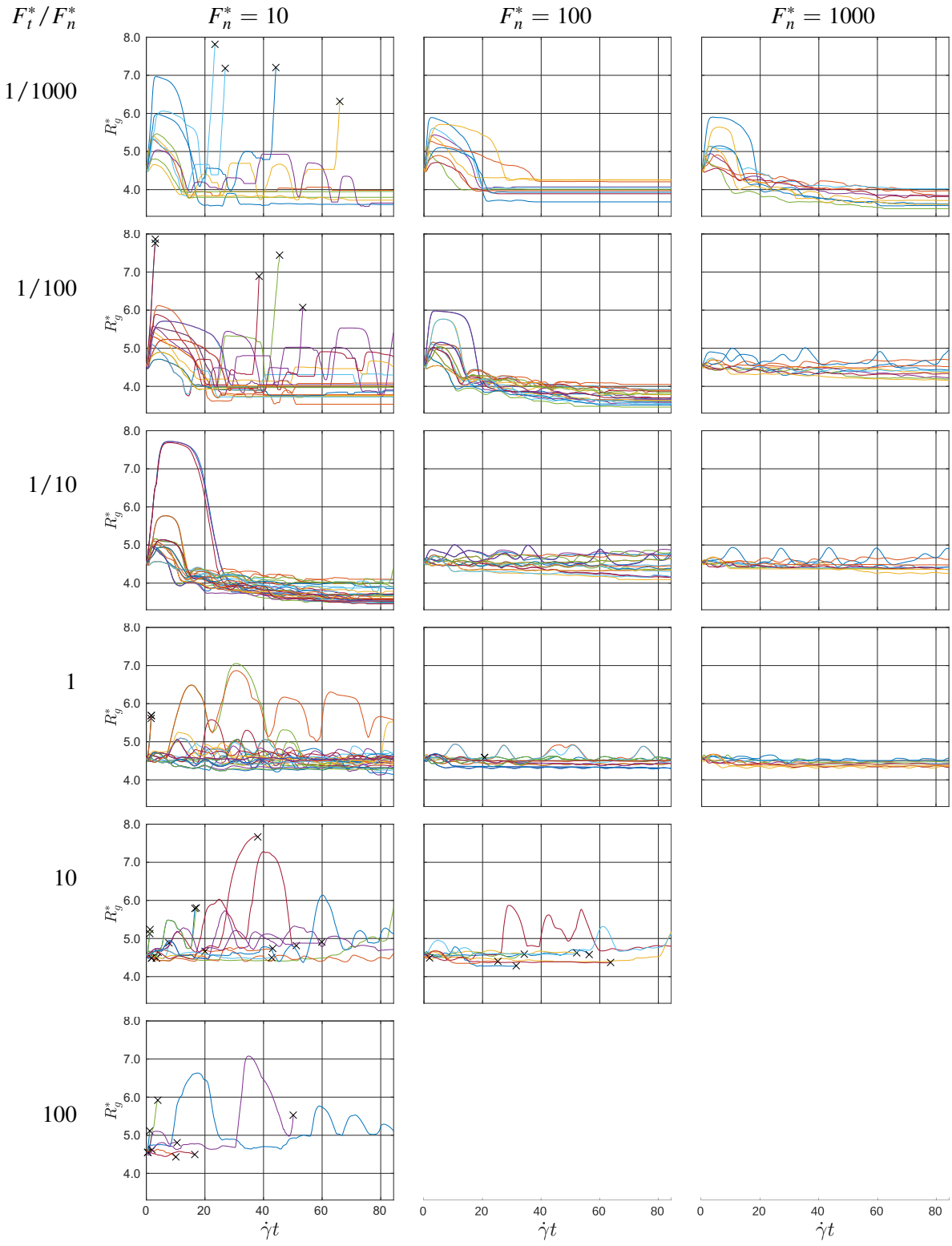

Figure 4.4: Evolution of aggregate size (R_g^*) for the force ratios considered in the present study. All breakage events are marked by '×'.

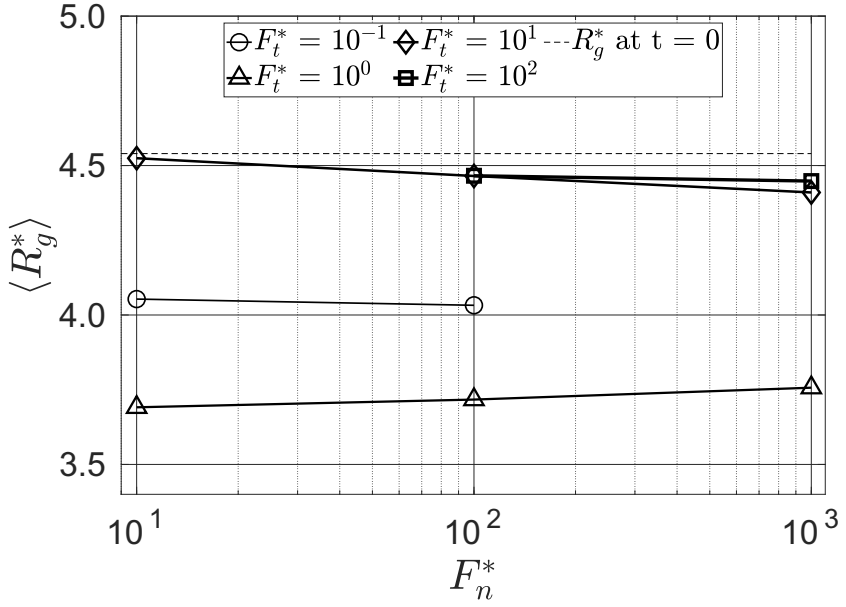

(a) Impact of normal cohesive force on radius of gyration

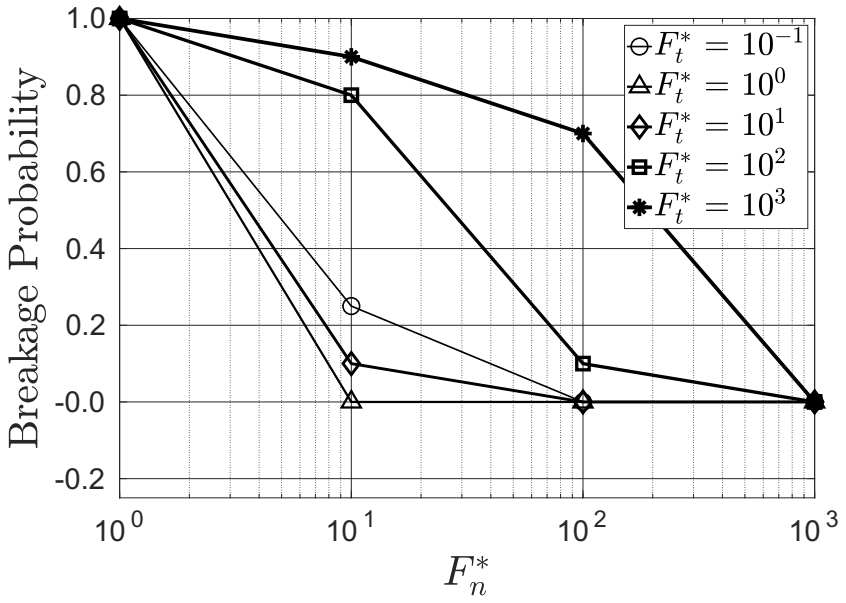

(b) Impact of normal cohesive force on breakage probability

Figure 4.5: Effect of normal cohesive force to drag force ratio F_n^* on (a) restructuring, (b) breakage rate.

indicating no impact of the normal forces on restructuring, which confirms the findings of Becker et al. [18].

Fig. 4.5b shows the impact of F_n^* on breakage probability: as the normal force increases, the probability that the aggregate will break decreases. As expected, when the normal cohesive force is too low, all aggregates break.

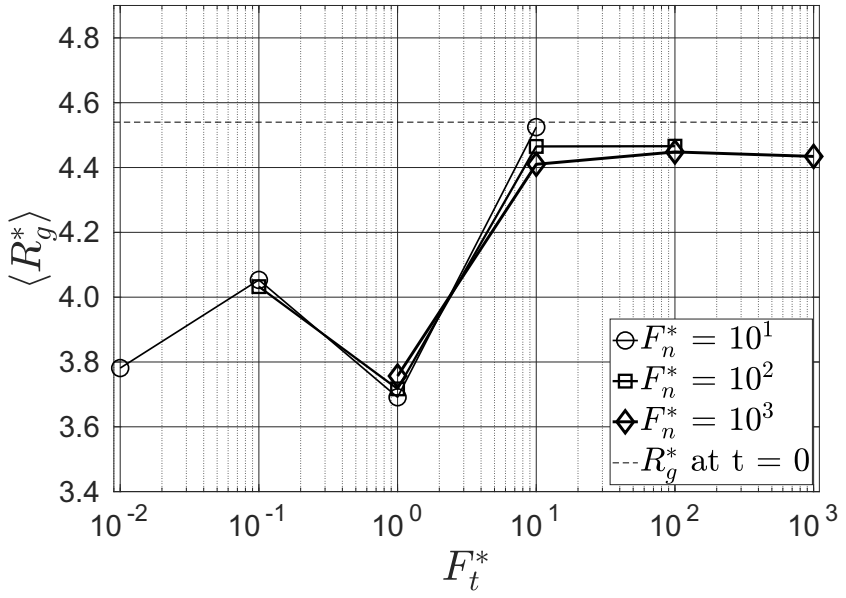

(a) Impact of tangential cohesive force on radius of gyration

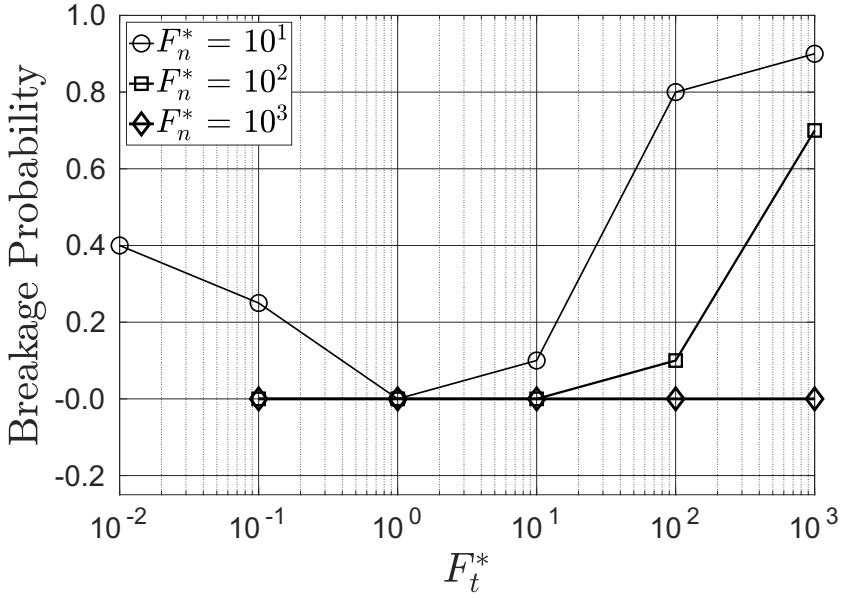

(b) Impact of tangential cohesive force on breakage probability

Figure 4.6: Effect of tangential cohesive force to drag force ratio F_t^* on (a) restructuring, (b) breakage rate.

In conclusion, although the normal forces do not affect the restructuring of aggregates, they govern breakage: as long as the normal forces are strong enough to overcome the drag, they hold particles together within an aggregate; beyond that, their magnitude has no effect on the final structure of aggregates. This is consistent with the suggestion by Eggersdorfer et al. [12] that restructuring mostly occurs due to sliding of particles over each other.

4.4.2 Effect of tangential force

Tangential motion of particles relative to one another (sliding) depends on tangential cohesive forces. To study the effect of tangential forces, the same comparison between simulation outcomes is made for normalized tangential forces F_t^* in Fig. 4.6, as was done for normal forces in Fig. 4.5.

Fig. 4.6a shows the effect of tangential forces on the final structure of the aggregates. Although there is no monotonic trend, it is clear that this force plays a significant role in restructuring since $\langle R_g^* \rangle$ varies significantly when other parameters are kept constant (along the lines in Fig. 4.6a). Several observations can be made from inspection of Fig. 4.6a. First, at very high values of F_t^* (>10), aggregates do not restructure much; hence any F_t^* >10 yields values of $\langle R_g^* \rangle$ that are similar to those of the initial aggregates, that is around 4.5. On the other hand, when F_t^* <10, aggregates evolve to become denser, and their radius of gyration decreases.

Breakage probability also varies non-monotonically with tangential force as can be seen in Fig. 4.6b. Breakage probability reaches high values for both high and low values of F_t^*, and goes through a minimum for moderate tangential forces of $F_t^* \approx 1$. Together, Figures 4.6a and 4.6b suggest that tangential forces play a dual role in aggregate evolution. Since tangential forces induce a bending moment, high tangential forces relative to hydrodynamic actions make aggregates brittle, as they are not flexible and do not restructure to redistribute hydrodynamic stresses among bonds between constituent particles. On the other hand, tangential forces also contribute to the overall bond strength. As long as they do not prevent aggregate restructuring, increasing tangential forces makes aggregate less likely to break, which is the trend that can be seen for relatively low tangential forces. This is reflected by the non-monotonic trend seen in Fig. 4.6a and 4.6b. As the tangential forces increase beyond $F_t^* = 1$, less restructuring and more breakage are observed, showing that the aggregates become brittle with increasing tangential forces. At $F_t^* = 10^{-2}$, more restructuring and higher breakage probability are seen, indicating that there was some contribution of tangential forces to the overall bond strength.

4.4.3 Impact of hydrodynamics on aggregate restructuring

Since shear forces calculated through FDA are modelled though analytical drag laws, FDA can overestimate the magnitude of hydrodynamic forces. To quantify the impact of hydrodynamics

on aggregate restructuring, the flow must be resolved. Therefore, LBM and IBM were used to accurately account for the hydrodynamics. Flow is induced by imposing a shear stress at the top and bottom planes, as shown in Fig. 4.1. As tangential force has been shown to play a prevalent role in restructuring, simulations cover the following conditions

$$F_{f/p} = 10^{-10}\mathrm{N}$$
$$F_n^* = 10$$
$$F_t^* \in \{10^{-2}, 10^{-1}, 10^0, 10^1\}$$

Time evolution of R_g^* for 4 different values of F_t^* are presented in Fig. 4.7. It can be seen that these results differ quite significantly from FDA results for similar conditions presented in the first column of Fig. 4.4. Aggregates do restructure, and show the same general trends as with FDA; that is, evolving towards denser structures over the duration of a simulation while going through significant elongations while rotating, particularly during their first cycles. However, their radii of gyration remain in a narrower range for all aggregates. This is especially noteworthy during the first rotation when the algorithmically created aggregates first adjust to the flow. In contrast, FDA shows much stronger restructuring for the first rotation. When the hydrodynamics are accurately resolved, less aggregate restructuring is observed, and the aggregates also break much less frequently. While small tangential forces lead to frequent breakage with FDA, such breakage does not occur with resolved hydrodynamics. These observations result from the combination of two phenomena induced by hydrodynamic interactions between particles in the aggregate: lubrication and decrease in strain rate.

Impact of lubrication on breakage

When particles move towards one another they displace the liquid between them. This displacement of liquid exerts a reaction force on the particles moving towards each other. This is known as a lubrication force. This short-range hydrodynamic force always acts against the relative motion of the particles. Due to its “stopping" nature, it acts as a repulsive force for any two approaching particles. Therefore, it effectively reduces the bond strength of the approaching particles. On the contrary, when particles close to one another tend to separate, or slide, the same motion retarding lubrication force contributes to the bond strength in both tangential and normal directions. Such

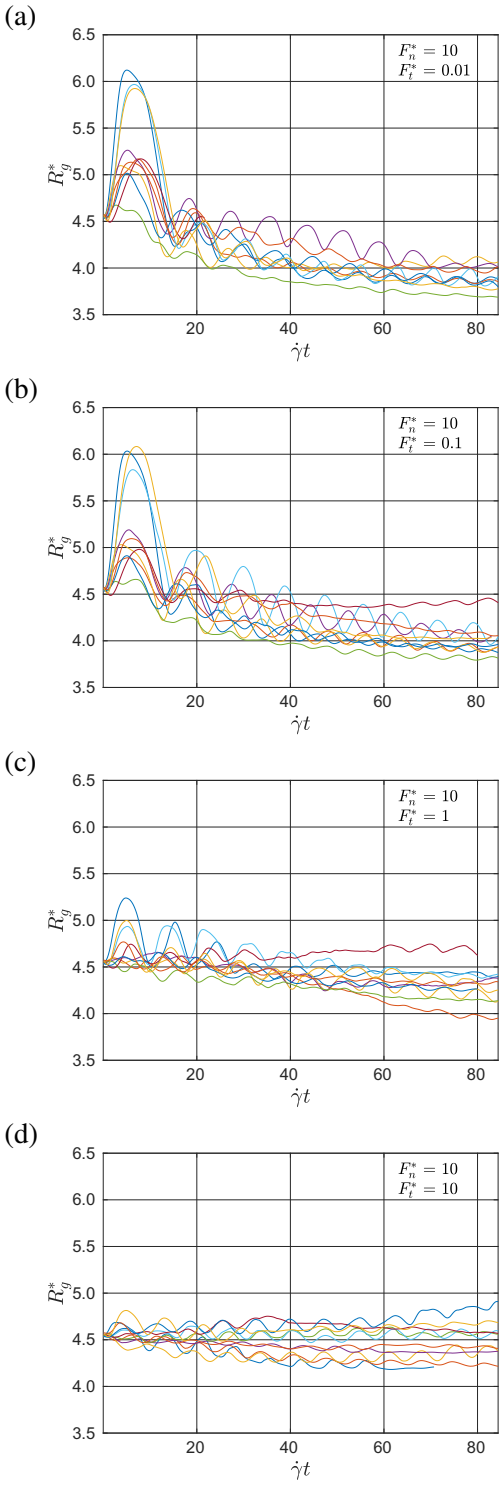

Figure 4.7: Size evolution of the 10 aggregates over a duration of 84.8 γi with resolved hydrodynamics for force ratios $F_n^* = 10$ and (a) $F_t^* = 0.01$, (b) $F_t^* = 0.1$, (c) $F_t^* = 1$, and (d) $F_t^* = 10$.

short-range hydrodynamic interactions increase the required force to be overcome for particles in close proximity to be separated. Therefore, these lubrication effects can explain why aggregates do not break when hydrodynamics are resolved while they would break when simulated using FDA.

The role of bond strength on breakage and restructuring was discussed earlier: bond strength has a clear impact on breakage, but its impact on restructuring is not as straightforward since tangential cohesive forces may either favor or hinder restructuring. When considering the aggregate evolution with resolved hydrodynamics (as in Fig. 4.7), the cyclic amplitude of the variations of the radius of gyration R_g^* is of the same order of magnitude in all cases. However, aggregate evolution over a few rotations shows different trends: the lower the tangential force ratio, the denser the aggregates. Since short-range hydrodynamic interactions are practically the same for each case of the tangential force ratio in Fig. 4.7, the explanation for difference in aggregate evolution flow must come from hydrodynamic interactions at aggregate scale.

Disturbance of the strain rate field

It is clear that when hydrodynamics are taken into account, the whole flow is affected by the presence of the particles. Disturbances in the flow induced by the aggregate are visualized in Fig. 4.8. These disturbances are estimated by calculating the difference between the actual flow velocity and the analytical solution of the shear flow without solids: $\|\boldsymbol{v} - \dot{\gamma} z \boldsymbol{e}_x\|$. Fig. 4.8a shows in red the iso-surface where this difference is $2\dot{\gamma}R_p$ around an aggregate at different times while several iso-contour lines are plotted around a solid sphere for comparison in Fig. 4.8b. They show the same zones of maximum disturbance along the principal axes of strain, which are at a 45° angle. The similar features between the simulated results and the analytical solution around a solid sphere are evidence that the prevailing effect of the aggregate on the flow is to oppose the strain rate because of its own resistance to deformation. Even though colloidal aggregates do restructure, the non-deformation of the primary particles they are made of and the cohesive forces between them makes their impact on the flow close to the one of an equivalent rigid sphere, which rotates at about the same rotation rate as the rotational component of the velocity gradient, but opposes its strain component. The figures also show that maximum disturbance occurs at the periphery of the aggregate and outside of the aggregate. In its core, the flow is much less disturbed, indicating that the velocity field there is close to that of a plane shear flow. In other words, the particles in the center experience hydrodynamic forces closer to

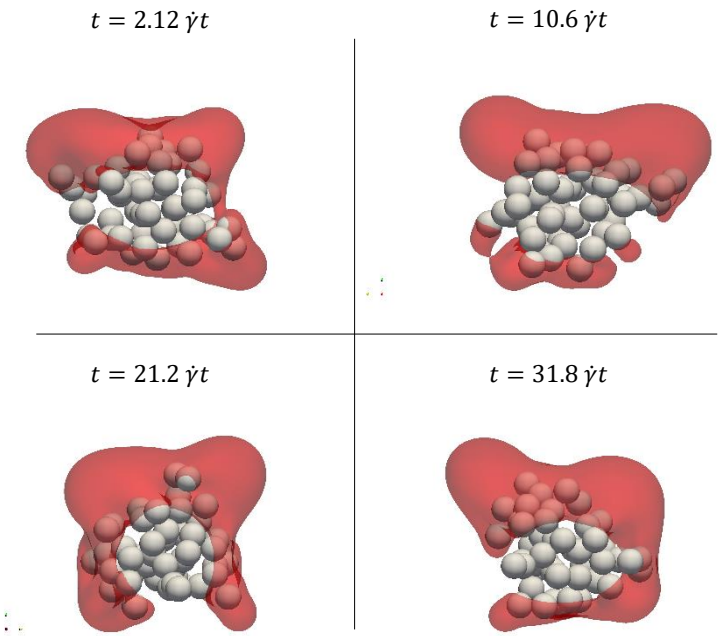

(a) Region of significant disturbance in the shear flow due to the presence of the aggregate: surface where $\|\boldsymbol{v} - \dot{\gamma}z\boldsymbol{e}_x\| = 2\,\dot{\gamma}\,R_p$

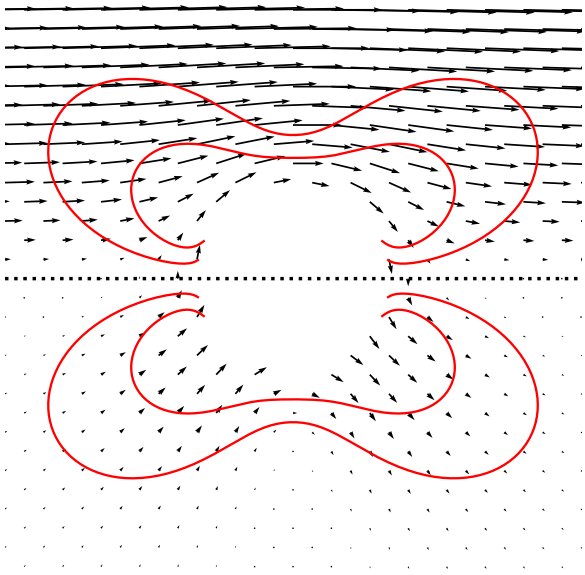

(b) Analytical solutions for the flow (top) and disturbance (bottom) velocity fields around a solid sphere in a shear flow with iso-contours of the disturbance magnitude (in red).

Figure 4.8: (a) Region of the shear flow that sees a significant disturbance due to the presence of the aggregate and (b) comparison with a free-to-rotate solid sphere.

the values estimated using the Stokesian drag expression than particles at a greater distance from the center, which is in accordance with the findings of Vanni [48]. Since the Reynolds number is low, primary particles are small compared to the region of the flow governed by the viscous diffusion of

momentum at the aggregate scale, which suggests that aggregate scale dynamics prevail compared to hydrodynamic interactions between pairs of primary particles.

Now, when comparing simulation results, it should be expected that differences in aggregate evolution between FDA and LBM+IBM arise in the zones of maximum disturbance. Hence, this is the modification of the flow at aggregate scale that governs restructuring rather than lubrication interactions between primary particles. Consequently, this establishes that inaccuracy of FDA does not arise due to the absence of a "shielding effect" of particles from their surrounding neighbors. Instead, the hydrodynamics are overestimated as FDA does not take into account the damping of the strain rate in the flow in the region near the periphery of aggregates. During aggregate rotation, as particles in the periphery cross the eigendirections of strain rate, they are torn apart or pushed towards the aggregate core. However, due to the resistance to deformation of the whole aggregate, including the core particles, the strain rate outside the aggregate is dampened. This disturbance is the most significant in the aggregate periphery. This results in the aggregate going through much lower strain rate variations during a rotation. The driving forces to restructuring and breakage are thus considerably decreased so aggregates restructure more slowly, and break less. However, when looking at the final structure of aggregates after $80\,\dot{\gamma}t$ (6–7 rotations) in the flow, they tend to be denser in the same way as aggregates simulated without hydrodynamic interactions do, as highlighted in Fig. 4.9. In other words, long range hydrodynamic interactions between particles have a strong impact on breakage rate and restructuring kinetics but have much less impact on final aggregate structure.

The comparison between modelled and resolved hydrodynamics presented in Fig. 4.9 sheds light on the overall impacts of hydrodynamic interactions on restructuring. By damping the strain rate field around the aggregate, hydrodynamics allow aggregates to restructure more progressively, making their evolution less dependent on how much they need to adjust to the shear flow, which is particularly significant for algorithmically created aggregates that undergo substantial restructuring. As a consequence, the relation between final aggregate structure and tangential force is smoother, and even becomes monotonic. That is also partially due to the hydrodynamic interactions contributing to apparent cohesive forces between particles as already discussed when the effects of lubrication were considered, so that actual cohesive forces have a lower relative weight in the overall dynamics. In the end, resolved hydrodynamics make aggregates less sensitive to tangential force variations. The

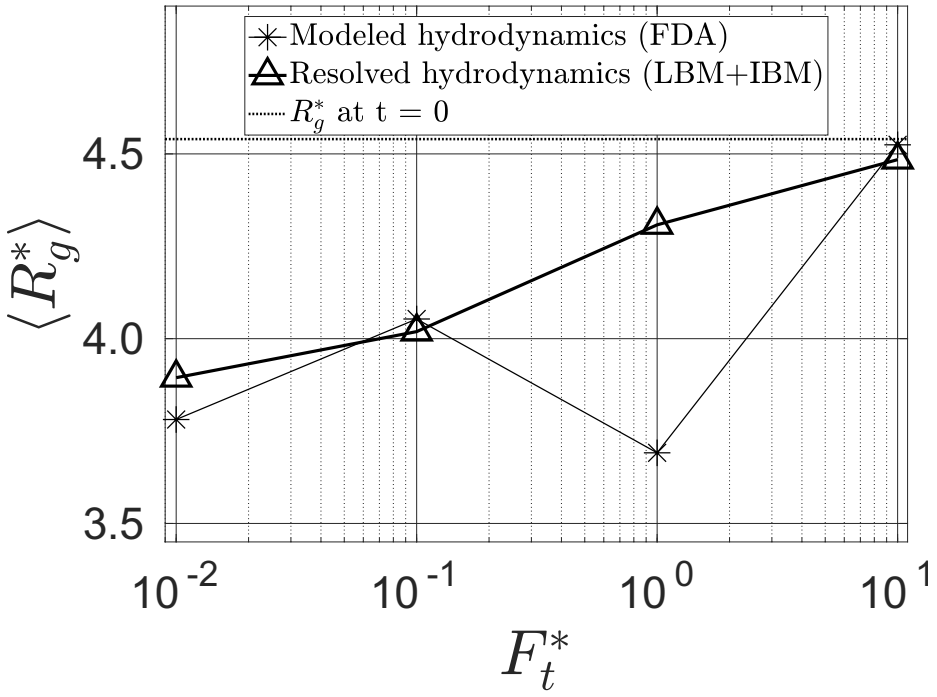

Figure 4.9: Impact of hydrodynamic interaction on evolution of radius of gyration with tangential cohesive force.

impact of tangential cohesive forces quantitatively changes but, qualitatively it remains the governing parameter on aggregate restructuring. As shown in Fig. 4.9, there is a strong correlation between these two quantities, which is even more clear with resolved hydrodynamics.

Aggregate restructuring during the first rotation is less pronounced and overall aggregates are much less prone to breakage with hydrodynamic interactions. Restructuring, being more progressive, also makes aggregate fates less dependent on their initial state and as a result, all 10 aggregates show a more consistent behaviour than they did when FDA was used to approximate the hydrodynamics.

4.5 Conclusion

Numerical investigations of aggregate restructuring and breakage were conducted for a set of artificially created aggregates sharing the same morphological signature, in terms of radius of gyration or fractal dimension. The relative impact of the normal and tangential components of cohesive forces between aggregates on final aggregate structure and breakage probability was initially quantified using simulations that ignored hydrodynamic interactions between particles. These simulations also provided the base cases against which the role played by resolved flow hydrodynamics could be

compared.

These investigations show that normal cohesive forces have no impact on restructuring, but contribute to the strength of the aggregate. On the other hand, the impact of tangential forces is more complex. Large tangential forces make aggregates brittle, making them less prone to restructuring, but more susceptible to breakage. Small tangential forces make flexible bonds in the aggregate and decrease the bending moment of particle rods which provides greater ability to respond to the applied shear by restructuring; however, they can also make aggregates more likely to break due to weakened tangential bond strength.

The hydrodynamics at play at low aggregate Reynolds numbers include lubrication between particles, and more importantly resistance to deformation that decreases the strain rate in the flow in the periphery of an aggregate. This disturbance of the flow is thus the reason for reduced hydrodynamic driving forces on restructuring and breakage. This means that improved FDA models to account for "shielding effect" must primarily focus on the impact of the aggregate's presence on the overall shear flow [33, 49, 50] rather than of hydrodynamic models to correct interactions between primary particles [9, 51].

Complex dynamics arise in particle interactions at finite Reynolds number, even at values down to Re $\sim 10^{-2}$ [52, 53], that may have a significant impact on aggregate behaviour. The LBM as used in this research is well suited for finite Reynolds simulations, unlike SD. Work is in progress to investigate the impact of non-linear flow dynamics on aggregate behaviour, even at low Reynolds numbers.

Acknowledgements

High Performance Computing resources were provided by Westgrid (www.westgrid.ca), Compute Canada (www.computecanada.ca), as well as by the EXPLOR centre hosted by the Université de Lorraine. The authors would like to acknowledge the financial support of the NSERC Industrial Research Chair in Pipeline Transport Processes.

References

[1] J. Masliyah, Z. J. Zhou, Z. Xu, J. Czarnecki, and H. Hamza. Understanding water-based bitumen extraction from Athabasca oil sands. *The Canadian Journal of Chemical Engineering*, 82(4):628–654, 2004. doi:10.1002/cjce.5450820403.

[2] I. L. A. Daoud, N. Rimbert, A. Jardy, B. Oesterlé, S. Hans, and J.-P. Bellot. 3D modeling of the aggregation of oxide inclusions in a liquid steel ladle: Two numerical approaches. *Advanced Engineering Materials*, 13(7):543–549, 2011. ISSN 1527-2648. doi:10.1002/adem.201000355.

[3] K. Rastegari, W. Y. Svrcek, and H. W. Yarranton. Kinetics of asphaltene flocculation. *Industrial & Engineering Chemistry Research*, 43(21):6861–6870, 2004. doi:10.1021/IE049594V.

[4] C. Coufort, D. Bouyer, and A. Liné. Flocculation related to local hydrodynamics in a Taylor-Couette reactor and in a jar. *Chemical Engineering Science*, 60(8):2179–2192, 2005. ISSN 00092509. doi:10.1016/j.ces.2004.10.038.

[5] Y. M. Harshe and M. Lattuada. Breakage rate of colloidal aggregates in shear flow through Stokesian dynamics. *Langmuir*, 28(1):283–292, January 2012. ISSN 0743-7463. doi:10.1021/la2038476.

[6] F. Vaezi, R. S. Sanders, and J. H. Masliyah. Flocculation kinetics and aggregate structure of kaolinite mixtures in laminar tube flow. *Journal of Colloid and Interface Science*, 355(1): 96–105, 2011.

[7] Y. M. Harshe, M. Lattuada, and M. Soos. Experimental and modeling study of breakage and restructuring of open and dense colloidal aggregates. *Langmuir*, 27(10):5739–5752, May 2011. doi:10.1021/la1046589.

[8] S. Blaser. Flocs in shear and strain flows. *Journal of Colloid and Interface Science*, 225(2): 273–284, 2000.

[9] K. Higashitani, K. Iimura, and H. Sanda. Simulation of deformation and breakup of large aggregates in flows of viscous fluids. *Chemical Engineering Science*, 56(9):2927–2938, 2001.

[10] K. Horii, R. Yamada, and S. Harada. Strength deterioration of nonfractal particle aggregates in simple shear flow. *Langmuir*, 31(29):7909–7918, 2015.

[11] G. Frungieri and M. Vanni. Dynamics of a shear-induced aggregation process by a combined Monte Carlo-Stokesian Dynamics approach. In *Proceedings of the 9th International Conference on Multiphase Flow*, 2016.

[12] M. L. Eggersdorfer, D. Kadau, H. J. Herrmann, and S. E. Pratsinis. Fragmentation and restructuring of soft-agglomerates under shear. *Journal of Colloid and Interface Science*, 342 (2):261–268, 2010. ISSN 00219797. doi:10.1016/j.jcis.2009.10.062.

[13] X. D. Niu, C. Shu, Y. T. Chew, and Y. Peng. A momentum exchange-based immersed boundary-lattice Boltzmann method for simulating incompressible viscous flows. *Physics Letters A*, 354 (3):173–182, 2006. doi:10.1016/j.physleta.2006.01.060.

[14] J. P. Pantina and E. M. Furst. Elasticity and critical bending moment of model colloidal aggregates. *Physical Review Letters*, 94(13):138301, April 2005. doi:10.1103/PhysRevLett.94.138301.

[15] U. T. Lieu and S. Harada. Stability of restructured non-fractal aggregates in simple shear flow. *Advanced Powder Technology*, 26(3):705–710, 2015.

[16] M. Zeidan, B. H. Xu, X. Jia, and R. A. Williams. Simulation of Aggregate Deformation and Breakup in Simple Shear Flows Using a Combined Continuum and Discrete Model. *Chemical Engineering Research and Design*, 85(12):1645–1654, January 2007. ISSN 0263-8762. doi:10.1016/S0263-8762(07)73208-2.

[17] M. Kroupa, M. Vonka, M. Soos, and J. Kosek. Size and Structure of Clusters Formed by Shear Induced Coagulation: Modeling by Discrete Element Method. *Langmuir*, 31(28):7727–7737, July 2015. ISSN 0743-7463. doi:10.1021/acs.langmuir.5b01046.

[18] V. Becker, E. Schlauch, M. Behr, and H. Briesen. Restructuring of colloidal aggregates in shear flows and limitations of the free-draining approximation. *Journal of Colloid and Interface Science*, 339(2):362–372, 2009. doi:10.1016/j.jcis.2009.07.022.

[19] V. Becker and H. Briesen. A master curve for the onset of shear induced restructuring of fractal colloidal aggregates. *Journal of Colloid and Interface Science*, 346(1):32–36, June 2010. ISSN 0021-9797. doi:10.1016/j.jcis.2010.02.015.

[20] M. Vanni and A. Gastaldi. Hydrodynamic forces and critical stresses in low-density aggregates under shear flow. *Langmuir*, 27(21):12822–12833, November 2011. ISSN 0743-7463. doi:10.1021/la2024549.

[21] R. Seto, R. Botet, and H. Briesen. Hydrodynamic stress on small colloidal aggregates in shear flow using Stokesian dynamics. *Physical Review E*, 84(4):041405, October 2011. doi:10.1103/PhysRevE.84.041405.

[22] R. Seto, R. Botet, and H. Briesen. Viscosity of rigid and breakable aggregate suspensions Stokesian Dynamics for rigid aggregates. In *Progress in Colloidal and Polymer Science*, volume 139, pages 85–90, 2012. doi:10.1007/978-3-642-28974-3_15.

[23] S. Harada, R. Tanaka, H. Nogami, and M. Sawada. Dependence of fragmentation behavior of colloidal aggregates on their fractal structure. *Journal of Colloid and Interface Science*, 301(1):123–129, 2006.

[24] A. Zaccone, M. Soos, M. Lattuada, H. Wu, M. U. Bäbler, and M. Morbidelli. Breakup of dense colloidal aggregates under hydrodynamic stresses. *Physical Review E*, 79(6):061401, June 2009. doi:10.1103/PhysRevE.79.061401.

[25] G. Frungieri and M. Vanni. Shear-induced aggregation of colloidal particles: A comparison between two different approaches to the modelling of colloidal interactions. *The Canadian Journal of Chemical Engineering*, 95(9):1768–1780, September 2017. ISSN 1939-019X. doi:10.1002/cjce.22843.

[26] S. Harada, R. Tanaka, H. Nogami, M. Sawada, and K. Asakura. Structural change in non-fractal particle clusters under fluid stress. *Colloids and Surfaces A: Physicochemical and Engineering Aspects*, 302(1):396–402, 2007.

[27] R. Seto, R. Botet, G. K. Auernhammer, and H. Briesen. Restructuring of colloidal aggregates in

shear flow. *The European Physical Journal E*, 35(12):128, December 2012. ISSN 1292-8941. doi:10.1140/epje/i2012-12128-4.

[28] D. Chen and M. Doi. Simulation of aggregating colloids in shear flow. II. *The Journal of Chemical Physics*, 91(4):2656–2663, August 1989. doi:10.1063/1.456975.

[29] V. Becker and H. Briesen. Tangential-force model for interactions between bonded colloidal particles. *Physical Review E*, 78(6):061404, December 2008. doi:10.1103/PhysRevE.78.061404.

[30] D. Liu, Z. Wang, X. Chen, and M. Liu. Simulation of agglomerate breakage and restructuring in shear flows: Coupled effects of shear gradient, surface energy and initial structure. *Powder Technology*, 336:102–111, 2018. doi:10.1016/j.powtec.2018.05.051.

[31] R. C. Sonntag and W. B. Russel. Structure and breakup of flocs subjected to fluid stresses: I. Shear experiments. *Journal of Colloid and Interface Science*, 113(2):399–413, 1986.

[32] R. C. Sonntag and W. B. Russel. Structure and breakup of flocs subjected to fluid stresses. *Journal of Colloid and Interface Science*, 115(2):390–395, February 1987. ISSN 00219797. doi:10.1016/0021-9797(87)90054-3.

[33] M. Vanni. Creeping flow over spherical permeable aggregates. *Chemical Engineering Science*, 55(3):685–698, February 2000. ISSN 0009-2509. doi:10.1016/S0009-2509(99)00316-4.

[34] B. O. Conchuir, Y. M. Harshe, M. Lattuada, and A. Zaccone. Analytical model of fractal aggregate stability and restructuring in shear flows. *Industrial & Engineering Chemistry Research*, 53(22):9109–9119, June 2014. ISSN 0888-5885. doi:10.1021/ie4032605.

[35] J. G. M. Eggels and J. A. Somers. Numerical simulation of free convective flow using the lattice-Boltzmann scheme. *International Journal of Heat and Fluid Flow*, 16(5):357–364, 1995. ISSN 0142-727X. doi:10.1016/0142-727X(95)00052-R.

[36] R. Sungkorn and J. J. Derksen. Simulations of dilute sedimenting suspensions at finite-particle reynolds numbers. *Physics of Fluids*, 24(12):123303, 2012.

[37] J. Gregory. The density of particle aggregates. *Water Science and Technology*, 36(4):1–13, 1997. ISSN 02731223. doi:10.1016/S0273-1223(97)00452-6.

[38] L. Gmachowski. Calculation of the fractal dimension of aggregates. *Colloids and Surfaces A: Physicochemical and Engineering Aspects*, 211(2):197–203, 2002. ISSN 09277757. doi:10.1016/S0927-7757(02)00278-9.

[39] Y. M. Harshe, L. Ehrl, and M. Lattuada. Hydrodynamic properties of rigid fractal aggregates of arbitrary morphology. *Journal of Colloid and Interface Science*, 352(1):87–98, 2010. ISSN 0021-9797. doi:10.1016/j.jcis.2010.08.040.

[40] T. Serra and X. Casamitjana. Structure of the aggregates during the process of aggregation and breakup under a shear flow. *Journal of Colloid and Interface Science*, 206(2):505–511, 1998. doi:10.1006/jcis.1998.5714.

[41] P. Jarvis, B. Jefferson, and S. A. Parsons. Breakage, regrowth, and fractal nature of natural organic matter flocs. *Environmental science & technology*, 39(7):2307–2314, 2005. doi:10.1021/es048854x.

[42] A. S. Moussa, M. Soos, J. Sefcik, and M. Morbidelli. Effect of solid volume fraction on aggregation and breakage in colloidal suspensions in batch and continuous stirred tanks. *Langmuir*, 23(4):1664–1673, 2007. doi:10.1021/la062138m.

[43] L. Guerin, C. Frances, A. Liné, and C. Coufort-Saudejaud. Fractal dimensions and morphological characteristics of aggregates formed in different physico-chemical and mechanical flocculation environments. *Colloids and Surfaces A: Physicochemical and Engineering Aspects*, 560:213–222, 2019. doi:10.1016/j.colsurfa.2018.10.017.

[44] J. N. Israelachvili. *Intermolecular and Surface Forces*. Academic press, 2015.

[45] H. C. Hamaker. The London-van der Waals attraction between spherical particles. *Physica*, 4 (10):1058–1072, 1937. ISSN 00318914. doi:10.1016/S0031-8914(37)80203-7.

[46] D. L. Feke, N. D. Prabhu, J. A. J. Mann, and J. A. L. Mann. A formulation of the short-range repulsion between spherical colloidal particles. *The Journal of Physical Chemistry*, 88(23): 5735–5739, November 1984. ISSN 0022-3654. doi:10.1021/j150667a055.

[47] Y. M. Harshe and M. Lattuada. Universal breakup of colloidal clusters in simple shear flow. *The Journal of Physical Chemistry B*, 120(29):7244–7252, 2016. doi:10.1021/acs.jpcb.6b03220.

[48] M. Vanni. Accurate modelling of flow induced stresses in rigid colloidal aggregates. *Computer Physics Communications*, 192:70–90, July 2015. ISSN 0010-4655. doi:10.1016/j.cpc.2015.02.022.

[49] P. Adler. Streamlines in and around porous particles. *Journal of Colloid and Interface Science*, 81(2):531–535, 1981. doi:10.1016/0021-9797(81)90434-3.

[50] B. O. Conchúir and A. Zaccone. Mechanism of flow-induced biomolecular and colloidal aggregate breakup. *Physical Review E*, 87(3):032310, March 2013. doi:10.1103/PhysRevE.87.032310.

[51] R. Di Felice. The voidage function for fluid-particle interaction systems. *International Journal of Multiphase Flow*, 20(1):153–159, 1994. doi:10.1016/0301-9322(94)90011-6.

[52] H. Haddadi and J. F. Morris. Topology of pair-sphere trajectories in finite inertia suspension shear flow and its effects on microstructure and rheology. *Physics of Fluids*, 27(4):043302, 2015. doi:10.1063/1.4917030.

[53] J.-S. Kroll-Rabotin, M. Gisselbrecht, B. Ott, R. May, J. Fröhlich, and J.-P. Bellot. Multiscale simulation of non-metallic inclusion aggregation in a fully resolved bubble swarm in liquid steel. *Metals*, 10(4):517, 2019. doi:10.3390/met10040517.

Chapter 5

Numerical study of aggregate restructuring and breakage at finite Reynolds number

Abstract

Breakage rate, stable size and structure of fractal aggregates in multiphase flows are strongly related to the hydrodynamic forces. While these forces are prevalently viscous for finite Reynolds number conditions, flow inertia cannot be ignored, thereby requiring one to fully resolve the Navier-Stokes equations for the flow. To highlight the effect of flow inertia on aggregate evolution, numerical investigation of aggregate evolution in simple shear flow at finite Reynolds number is conducted. Particle coupling with the flow is resolved with an Immersed Boundary Method, and flow dynamics are solved using a Lattice Boltzmann Method. Particle dynamics are tracked by a Discrete Element Method, accounting for interactions between primary particles composing the aggregates. Aggregates are submitted to the flow, and their evolution is tracked over time. It is observed that, over the range of tested aggregate-scale Reynolds numbers, breakage rate is governed by the combined effect of momentum diffusion and the ratio of particle-particle interaction forces to the drag force resulting from the shear stress. For the higher shear stresses, even when no stable size exists, breakage is not instantaneous because of momentum diffusion kinetics. Later, to isolate the effect of finite-Reynolds

hydrodynamics on aggregate evolution, particle-particle forces are scaled with the viscous drag. It is observed that flow inertia at such moderate aggregate Reynolds numbers has no impact on the aggregate morphology, but it significantly favors breakage; a power-law relationship is found between breakage time and aggregate-scale Reynolds number. This is a first-of-its-kind study which establishes the role of flow inertia in aggregate evolution, and the findings present a novel perspective into breakage kinetics even for systems in low but finite Reynolds number conditions.

5.1 Introduction

The physics of solid-liquid suspensions are often governed by the aggregating behavior of the solid particles transported by the liquid. Consequently, aggregate properties, such as size and structure, govern the efficiency of many industrial processes, including polymer manufacturing [1], waste water treatment [2], mineral processing [3] and liquid metal treatments [4]. In these processes, aggregates are exposed to shear which directly affects their size and structure [5, 6], thus affecting the overall suspension properties such as its rheology. When an aggregate is introduced in a shear flow, it restructures so that particle contacts within the aggregate balance the external action of the flow. The aggregate breaks when force equilibrium cannot be achieved.

Many experimental studies attempted to capture these dynamics by determining the stable size and structure of aggregates in various flow conditions (such as shear, elongational or turbulent flow), or their breakage rate [7–13]. Due to the difficulty in controlling properties of every single aggregate in experiments, and the impossibility to experimentally measure contact forces between particles when exposing (or subjecting) aggregates to shear [12], most investigations of aggregate dynamics have been done using numerical simulations. One of the most commonly used methods has been Stokesian Dynamics (SD) [14], which solves the Stokes equation for the flow, assuming that viscous forces largely prevail. Studies with SD have provided valuable understanding of aggregate behaviour. For example, SD has shown that the stable size of fragments from an aggregate scale exponentially with the hydrodynamic stresses present in the flow [12], with the exponent depending on the structure of the parent aggregate. Consistent observations were obtained with other approaches, like the even simpler Free-Draining Approximation [15] or finite volume resolution of the flow [16] for low Reynolds number conditions.

Due to the intrinsic limits of SD, these results are only applicable to extremely low Reynolds numbers. In aggregation processes, finite Reynolds effects were found to have a significant impact even for Reynolds values as low as 0.03 [17]. Therefore, flow inertia may play a significant role in aggregate breakage and restructuring, and investigations with SD cannot capture such effects. Other authors [18, 19] have studied aggregates in flows using Lattice Boltzmann Method (LBM), demonstrating the viability of the method in studying aggregate evolution for finite Reynolds number conditions. Therefore, LBM is an excellent tool to investigate the effect of inertia on aggregate evolution. In this study, we have reproduced the aggregate physics that have previously been studied using SD, and additionally obtained results under finite Reynolds number conditions, where the inertial effects in the flow at aggregate scale are not negligible. This is a pioneering study in establishing the role of flow inertia at finite Reynolds number conditions on aggregate breakage and restructuring through numerical simulations. The novel findings include the effect of flow inertia and finite Reynolds number dynamics on breakage rate.

5.2 Methodology

5.2.1 Aggregate creation

To have a statistically significant representation of aggregate behaviour, the evolution of ten aggregates investigated. An aggregate generation algorithm described in Chapter 4 is used. The aggregates share similar morphological characteristics and are shown in Figure 5.1. While aggregate size is typically quantified with the radius of gyration R_g [12], density is often characterized using fractal dimension D_f [5]. The fractal dimension D_f is defined such that

$$N = S\frac{R_g}{R_p}^{D_f} = SR_g^{*D_f} \tag{5.1}$$

where N is the number of particles in an aggregate, R_p is the radius of the primary particles and S is the structure factor. It is worth noting that R_g, in the context of aggregates, is the ratio of the second moment of mass around the center of the aggregate to the total mass. Therefore, when N is constant among two aggregates, a comparison of their dimensionless radius of gyration R_g^* also compares their densities. Therefore, R_g^* can be used to quantify both size and density (as in Chapter 4) of

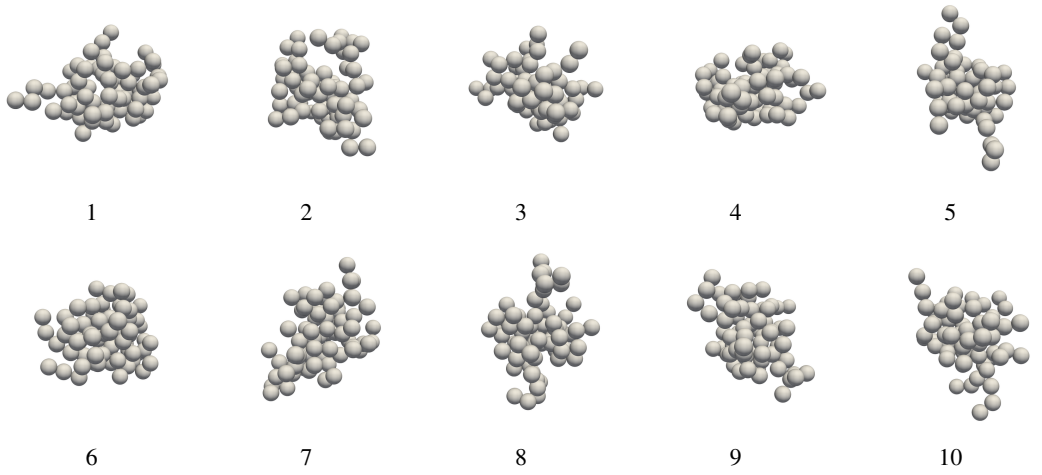

Figure 5.1: The 10 artificially created initial aggregates used in the simulations ($N = 70$, $D_f = 2.30 \pm 0.01$, $R_g^* \approx 5.27$).

aggregates. In this study, each aggregate has a fractal dimension $D_f = 2.3$ and consists of 70 rigid primary spherical particles. Consequently, all aggregates share the same dimensionless radius of gyration $R_g^* = 5.27 \pm 0.04$. The values of these parameters were chosen as a balance to reduce the computational cost of simulations while still being representative of physics involved in larger aggregates. Aggregates consisting of particles as low as 32 have been found to retain their fractal nature [20, 21], that is, results obtained with 32 particle aggregates were physically representative of larger aggregates. Therefore, results obtained with aggregates consisting of 70 particles can be confidently applied to larger aggregates.

While morphological properties characterize the shape and size of the aggregates, the particle-particle interactions characterize the physics of the aggregate. The interaction forces have normal and tangential components. The normal component combines a cohesive (attractive) force and a non-overlapping (repulsive) force. Together, they give a maximum attractive force between two particles in close contact. Therefore, this maximum attractive force must be overcome to break the "bond" between any two adjacent particles within the aggregate. The cohesive forces are modeled as the van der Waals forces [22], while the repulsive forces are modeled using Born repulsion [23]. The tangential forces [24] impart a bending moment to the aggregates. The distance over which these forces are non-negligible is very small compared to particle size. Specifically, the normal forces reach the maximum value at separation distance of about $0.001 \times R_p$ and steeply reduce to about $1/1000^{\text{th}}$ of their maximum value by $\approx 0.01 \times R_p$. The tangential forces, on the other hand,

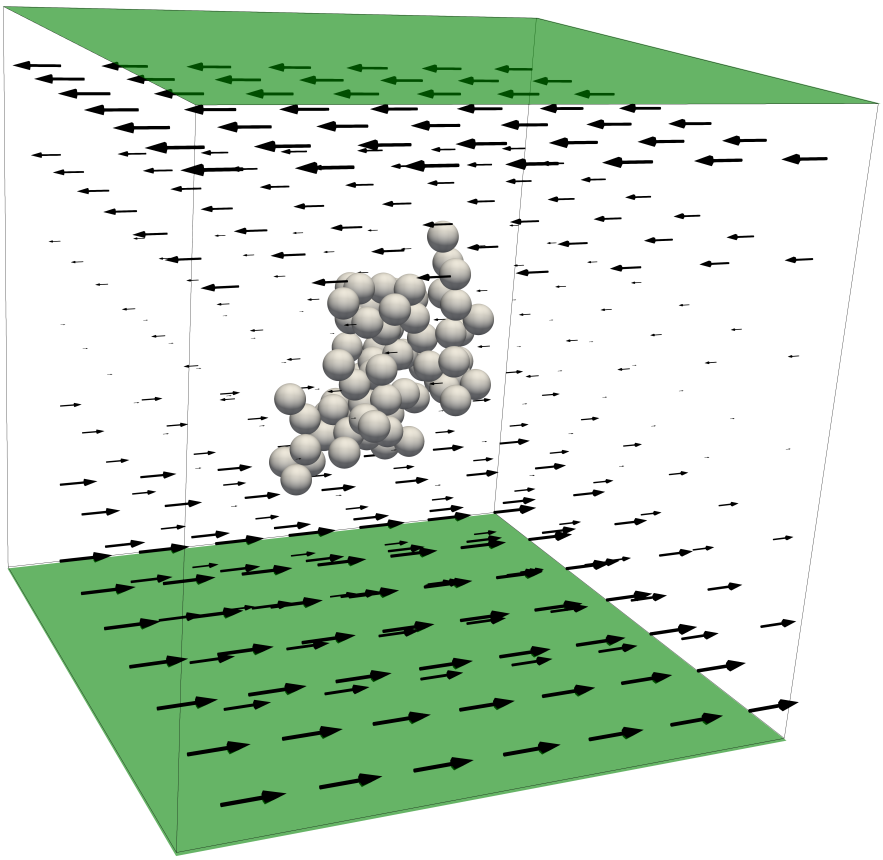

Figure 5.2: Illustration of domain setup, with Aggregate 7 placed at its center. The green planes show the surfaces where shear stress is applied, and the arrows show the expected flow direction.

reach their maximum value at angular displacement of ≈ 0.04 rad. Therefore, the distance at which these forces are non-negligible is not a parameter of interest. Consequently, it is only the maximum values of these forces that influence aggregate evolution, and the origin of these forces is of little consequence. The inconsequence of the exact models used to represent particle-particle interactions makes the results applicable to aggregates with any type of short-ranged interaction forces. Hence, only the maximum tangential and normal forces are considered in the characterization of internal interactions. More details on the modeling and implementation of these forces are given in Chapters 3 and 4.

5.2.2 Numerical schemes

The evolution of an aggregate in shear flow is driven by the hydrodynamics around it. To compute the hydrodynamics correctly, the flow must be resolved. Essentially, the flow around the aggregate transfers momentum to each primary particle; thus, each particle experiences inter-particle forces, and hydrodynamic forces. To allow for dynamic evolution of aggregate in shear flow, the motion of each particle of the aggregate is tracked and updated over time. The dynamics of each particle is determined by solving Newton's laws of motion while accounting for all forces acting on every particle, and trajectory integration, performed through a second order Adams-Bashforth scheme, updates the particle position. In this work, we have used a Lattice Boltzmann Method to solve the flow dynamics, Immersed Boundary Method for two way coupling between the fluid and the particles, and Discrete Element Method for particle tracking. Details of these schemes can be found in Chapter 3.

5.2.3 Simulation setup

A free-to-move aggregate is placed at the center of a cubic domain, as shown in Figure 5.2. The domain size is $198 \times 198 \times 198$ lattice units, and the radius of primary particles, R_p, is 5 lattice units. Flow is induced by applying a constant shear stress τ at the top and bottom walls of the domain (represented by the green planes in Figure 5.2). The other boundaries are assigned periodic conditions.

Since the fluid and aggregate are initially at rest, the time taken for the flow to develop must be considered. The shear stresses τ applied on the top and bottom walls of the domain generate momentum, which diffuses from the shear planes towards the domain center resulting in flow development. Therefore, the flow development time is essentially the time needed for momentum to diffuse through the domain. This can be estimated by the momentum diffusion equation in one dimension:

$$\frac{\partial u}{\partial t} = \nu \frac{\partial^2 u}{\partial y^2} \tag{5.2}$$

where ν is the kinematic viscosity, y is the direction normal to the shear-imposed planes and u is the local velocity in the flow. An order-of-magnitude analysis of Equation (5.2) allows us to quantify the

diffusion time t_d as

$$t_d \equiv \frac{(h/2)^2}{\nu} \tag{5.3}$$

where h is the size of the domain. A non-dimensional diffusion time can be defined as

$$t_d^* = \dot{\gamma} t_d \tag{5.4}$$

where $\dot{\gamma}$ is the shear rate in the flow resulting from the imposed shear stresses at domain boundaries, defined as

$$\dot{\gamma} \equiv \frac{\tau}{\rho \nu} \tag{5.5}$$

where τ is the imposed shear stress, ρ is the fluid density and ν its kinematic viscosity.

Numerical solution of Equation (5.2) shows that at $t_d^* = 1$, the shear rate at the center of the domain reaches 90% of the value imposed at the boundaries.

5.2.4 Quantification of flow conditions and aggregate properties

The shear rate, $\dot{\gamma}$, as defined in Equation (5.5) is the target shear rate, which corresponds to the shear stresses applied at the top and bottom boundaries. Using this definition, the resulting flow conditions at the aggregate scale can then be characterized as

$$\mathrm{Re}_{\mathrm{agg}} = \frac{\dot{\gamma}\,(2R_g)^2}{\nu} = \frac{4\tau R_g^2}{\rho \nu^2}. \tag{5.6}$$

As an aggregate evolves and restructures, its radius of gyration R_g changes, leading to a change in its $\mathrm{Re}_{\mathrm{agg}}$ as well. To reduce the complication of a dynamically varying aggregate Reynolds number, analyses were performed with the initial aggregate Reynolds number, based on the initial radius of gyration for the aggregate R_{ig}:

$$\mathrm{Re}_{\mathrm{agg}}^{\mathrm{init}} = \frac{4\tau R_{ig}^2}{\rho \nu^2}. \tag{5.7}$$

While $\mathrm{Re}_{\mathrm{agg}}$ captures the flow physics at aggregate scale, the dynamics at the scale of primary particles can be quantified with a particle Reynolds number:

$$\mathrm{Re}_{\mathrm{p}} = \frac{4\tau R_p^2}{\rho \nu^2} \tag{5.8}$$

where R_p is the radius of the primary particles. Note that $\mathrm{Re_p}$ is independent of aggregate properties.

While each Reynolds number corresponds to a constant hydrodynamic stress τ, the response of an aggregate to hydrodynamic forces also depends on the inter-particle cohesive and tangential forces. Such forces are thus considered to be characteristic properties of aggregates. More precisely, the maximum values of these forces determine the evolution of the aggregates [16]. In this study, the inter-particle forces are modeled with a normal cohesive component and a tangential component. Since inter-particle forces and hydrodynamic forces compete with each other, ratio of these two competing forces forms a dimensionless parameter which characterizes the strength of the inter-particle bonds against the hydrodynamic forces. Therefore, the two components of the inter-particle forces, F_n^* and F_t^*, are normalized by the hydrodynamic forces F_{drag} estimated through Stokesian drag. This can be represented as

$$F_n^* = \frac{F_n}{F_{drag}} = \frac{F_n}{12\,\pi\,\rho\nu\,R_p^2\,\dot{\gamma}} \tag{5.9}$$

$$F_t^* = \frac{F_t}{F_{drag}} = \frac{F_t}{12\,\pi\,\rho\nu\,R_p^2\,\dot{\gamma}} \tag{5.10}$$

where F_n and F_t are the maximum normal and tangential forces attainable between any two particles in close contact, while the drag force F_{drag} is estimated using the maximum difference of Stokesian drag between two bonded primary particles. Calculation of maximum values of force components has been discussed in Chapter 4.

5.2.5 Breakage detection

The bond between two adjacent particles in an aggregate can be considered to be broken when the distance between them is such that cohesive forces are small compared to the maximum cohesive forces. Since van der Waals forces are inversely proportional to the square of the surface to surface distance, the cohesive forces are negligible at $0.1R_p$. Although this criterion is quite large compared to that of Harshe and Lattuada [20] ($\approx 0.001\ R_p$), it allows for the possibility that particles may reattach, which is realistic in shear flow. Therefore, a breakage event is said to have occurred when two or more groups of particles (fragments) are separated by at least $0.1\ R_p$.

5.3 Results and discussion

An isolated aggregate in shear flow is likely to either restructure or break. Although both outcomes are driven by the hydrodynamic forces, the responsible physical mechanisms are different. The breakage is mostly associated with the strength of the cohesive bonds and the rigidity of the aggregate, whereas Chapter 4 showed that restructuring is known to be mainly dependent on the bending moment in the aggregate. When the flow has non-negligible inertia, the Reynolds number adds a new degree of freedom to the physical problem of aggregate restructuring and breakage.

5.3.1 Evolution of size and breakage rate with shear rate at finite Reynolds number

To highlight the role of flow inertia on aggregate evolution, simulations are performed for aggregate Reynolds numbers $\mathrm{Re}_{\mathrm{agg}}^{\mathrm{init}}$ ranging from 0.4 to 10. In such conditions, inertial flow patterns appear at aggregate scale. In contrast, the corresponding particulate Reynolds numbers, Re_{p}, vary from 0.0143 to 0.3587, implying that the inertial effects at primary particle scale remain comparatively low. The two Reynolds numbers are related by the dimensionless initial radius of gyration of aggregates: $\mathrm{Re}_{\mathrm{p}} = \mathrm{Re}_{\mathrm{agg}}^{\mathrm{init}} / R_g^{*2}$. Since both of the Reynolds numbers depend on the shear rate, they are controlled by imposing shear stresses at boundaries. Physically, this simulation plan is equivalent to exposing each aggregate to different Reynolds number conditions in the same fluid, by varying the shear.

Aggregate fragmentation

Each simulation begins with the aggregate at rest, while flow is induced through shear stresses at the top and bottom boundaries (Figure 5.2). As the flow diffuses towards the center of the domain, the aggregate starts to evolve. The morphological properties of the aggregate (R_g or D_f) are recorded over a period of $80\,\dot{\gamma}t$ or until it breaks, whichever comes first. The stable radius of gyration for the simulated conditions has been defined as the radius of gyration reached by the aggregates that do not break at the end of the $80\,\dot{\gamma}t$. If aggregates break into fragments before the end of the simulation, their breakage time t_{break} as well as the sizes R_g of each broken fragment are recorded.

Under the conditions of this study, 2 out of the 10 aggregates broke at $\mathrm{Re}_{\mathrm{agg}}^{\mathrm{init}} = 0.4$, 9 aggregates broke at $\mathrm{Re}_{\mathrm{agg}}^{\mathrm{init}} = 0.4$, while all 10 aggregates broke for all other $\mathrm{Re}_{\mathrm{agg}}^{\mathrm{init}}$. It can therefore be concluded

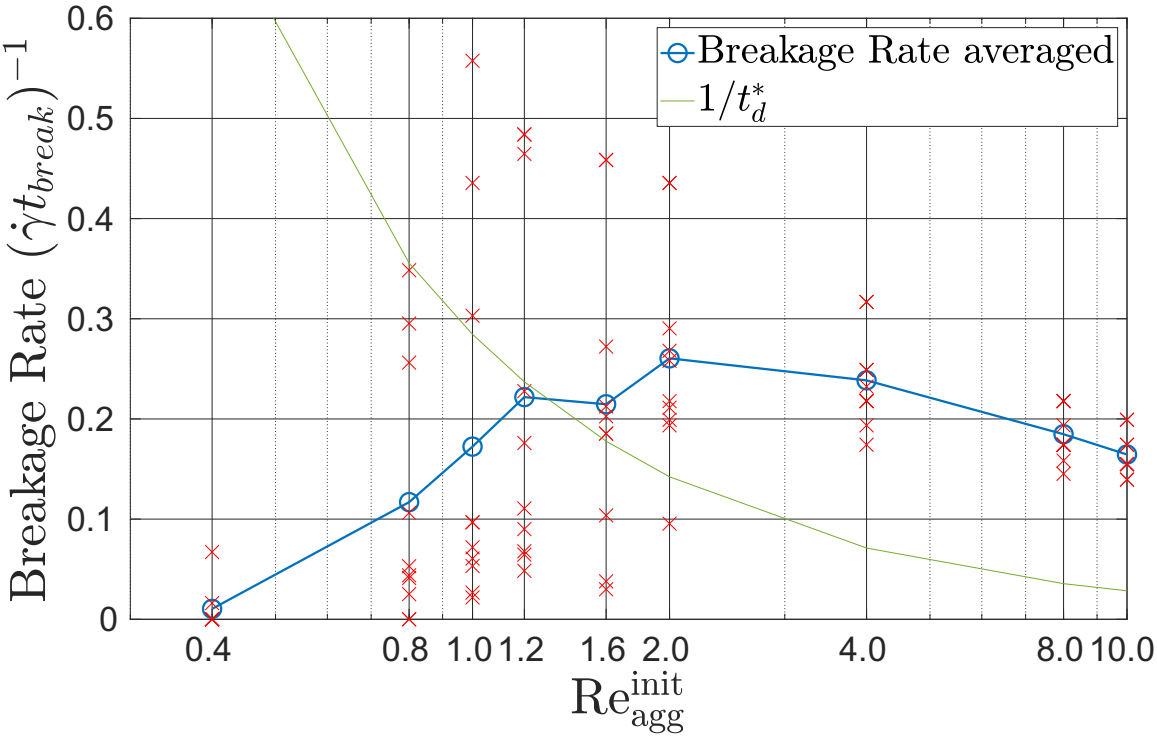

Figure 5.3: Breakage rate of the 10 initial aggregates at Reynolds numbers considered. Crosses (×) mark individual aggregates while the average rate for all the broken aggregates is plotted as circles joined by a continuous line (–).

that aggregates are mostly stable at the low Reynolds number condition. As shown in Chapter 4, aggregate survival depends on whether the cohesive forces between particles can resist the drag force acting on a series of particles rather than on isolated particle pairs. Considering that the aggregates were stable at $\mathrm{Re}_{\mathrm{agg}}^{\mathrm{init}} = 0.4$, the force ratios F_n^* and F_t^* were determined from Equations (5.9) and (5.10) as

$$F_n^* = F_t^* = \frac{F_n}{12\pi\rho\nu R_p^2 \dot{\gamma}} \tag{5.11}$$

$$= \frac{F_n}{3\pi\rho\nu^2 \frac{0.4}{R_g^*}} = \frac{F_n}{3\pi\rho\nu^2\ 0.0143} \tag{5.12}$$

$$\Rightarrow F_n^* = F_t^* = 7.395 \tag{5.13}$$

These force ratios at $\mathrm{Re}_{\mathrm{agg}}^{\mathrm{init}} = 0.4$ are henceforth referred to as $(F_n^*)_{\mathrm{stable}}$.

The Figure 5.3 shows the breakage rate, calculated as the inverse of the dimensionless breakage time $\dot{\gamma} t_{\mathrm{break}}$, of the 10 initial aggregates as a function of their initial aggregate Reynolds number

$\mathrm{Re}_{\mathrm{agg}}^{\mathrm{init}}$. The breakage rate is found to increase in low Reynolds number conditions ($\mathrm{Re}_{\mathrm{agg}}^{\mathrm{init}} < 1.6$). At low Reynolds number, hydrodynamic forces are predominantly viscous. Therefore, when Reynolds number is increased by increasing the shear rate, the hydrodynamic forces increase proportionally. With increasing hydrodynamic forces, the force ratios become smaller than $(F_n^*)_{\mathrm{stable}}$, and aggregates are expected to break faster. This trend of increase in breakage rate for $\mathrm{Re}_{\mathrm{agg}}^{\mathrm{init}} < 1.6$ is consistent with the findings of Harshe and Lattuada [20], where breakage rate was observed to increase with shear rate. However, for values of $\mathrm{Re}_{\mathrm{agg}}^{\mathrm{init}}$ above 1.6 ($\mathrm{Re}_{\mathrm{p}} > 0.0574$), the dimensionless breakage rate stops increasing, and even tends to gradually decrease.

To explain this observed change in behavior at $\mathrm{Re}_{\mathrm{agg}}^{\mathrm{init}} = 1.6$, the cohesive to drag force ratios must again be considered. When the cohesive to drag force ratios are small enough for the aggregates to break instantaneously, the breakage rate is governed only by the time taken for the hydrodynamic forces to develop around the aggregate. At $\mathrm{Re}_{\mathrm{agg}}^{\mathrm{init}} = 1.6$, the cohesive forces are too weak to balance the hydrodynamic forces. The ratio at this critical Reynolds number of 1.6 can be calculated from Equations (5.9) and (5.10). It can be seen that the forces ratios reduce to 0.25 $(F_n^*)_{\mathrm{stable}}$. In other words, an increase in Reynolds number $\mathrm{Re}_{\mathrm{agg}}^{\mathrm{init}}$ by a factor of 4 from 0.4 to 1.6 ($\mathrm{Re}_{\mathrm{p}} > 0.0574$) results in the hydrodynamic forces to be effectively four times stronger than the inter-particle bonds. Under such conditions, the hydrodynamic stresses are too strong for the aggregate's cohesive forces to counter-balance. This results in definite breakage as soon as the aggregates experience the hydrodynamic stresses of the flow. Although aggregates break right away without any restructuring, breakage is not instantaneous (that is, breakage rate is not infinite) since it takes some time for the flow to develop from the boundaries and reach the aggregate. This momentum diffusion in the flow scales with the diffusion time t_d^* defined in Equation (5.4). As a result, when hydrodynamic driving forces are too strong relative to cohesive forces within aggregates, the breakage rate becomes a function of the diffusion time instead of the shear rate. This becomes evident when the dimensionless breakage rate is compared to the similarly constructed diffusion rate defined as the inverse of the dimensionless diffusion time ($1/t_d^*$). It is plotted along with the breakage rate for corresponding Reynolds numbers in Figure 5.3, which shows that once the critical force ratio is reached at $\mathrm{Re}_{\mathrm{agg}}^{\mathrm{init}} = 1.6$ ($\mathrm{Re}_{\mathrm{p}} = 0.0574$), breakage rate is governed by the diffusion time instead of the shear rate.

To conclude, instead of the shear rate, diffusion time is found to govern the breakage rate of aggregates that are too weak for the flow conditions to have broken instantaneously, that is, when the

breakage time of aggregates is shorter than the momentum diffusion time in the flow. In contrast, the breakage rate scales with shear rate when the breakage is governed by the force ratios instead of diffusion time, resulting in aggregates restructuring, breaking or reaching stable configuration.

Breakage mechanism

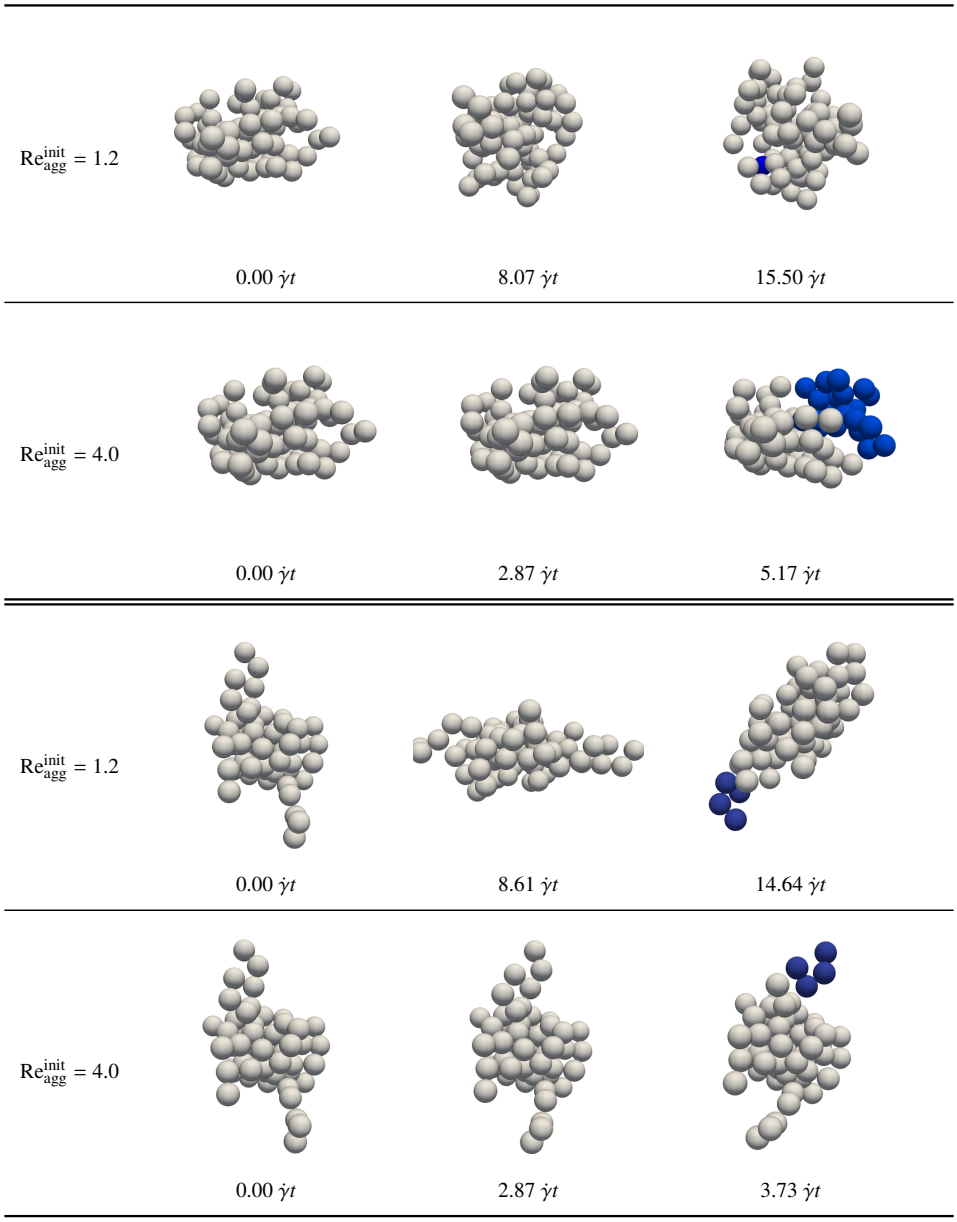

Figure 5.4: Example of evolution over time of two aggregates at different Reynolds numbers. Broken fragment is highlighted in blue.

A statistical analysis of fragment size distributions is attempted to highlight any difference in the

underlying breakage mechanisms. Specifically, fragment sizes were compared between breakage with and without restructuring, such as erosion versus fragmentation. Erosion can be defined as detachment of a few particles from the aggregate, whereas breakage through fragmentation results in formation of smaller aggregates of comparable sizes. The analysis showed no difference in breakage behaviour, implying that the fragmentation dynamics at play were similar for all flow conditions considered. This is due to the fact that although the Reynolds numbers of interest in this study are finite, they are still low. Therefore, the whole aggregate experiences shear forces that remain of similar magnitude between their core and their shell. In the end, there is no significant difference with breakage in a fully developed shear flow. Figure 5.4 presents examples of fragments from two aggregates (Aggregate 4 and 5 from Figure 5.1) and shows that large or small fragments can form at any Reynolds number, with or without significant restructuring before breakage.

Breakage cascade and stable size

To determine the largest stable size for the flow conditions considered, the largest fragment of the broken aggregate is selected and reintroduced into a new domain, that is, with shear stresses at top and bottom boundaries and zero initial velocity in the domain. The shear stresses are kept the constant between the domain where the fragment was formed and in the new domain. Since the new aggregate is smaller, the new simulation has a lower aggregate Reynolds number. Nonetheless, $\mathrm{Re_p}$ remains constant. This process of selecting the largest broken fragment is repeated up to seven times, or until a stable configuration is reached. Figure 5.5 graphically illustrates this breakage cascade. Since fragments have varying sizes, their aggregate Reynolds numbers cannot be used to represent the action of shear. Instead, force ratio as defined in Equation (5.9) is used.

Figure 5.7 shows the breakage rate of initial aggregates and all subsequent fragments at different shear rates. When all points are to be plotted on the same graph, their distribution looks random (See Figure 5.6). To extract a trend, datasets are presented separately according to the two groups of breakage kinetics discussed from Figure 5.3, that is $\mathrm{Re}_{\mathrm{agg}}^{\mathrm{init}} > 1.6$ (Figure 5.7a) and $\mathrm{Re}_{\mathrm{agg}}^{\mathrm{init}} \leq 1.6$ (Figure 5.7b). Since force ratios play a role in determining the effect of diffusion time on breakage kinetics, Figure 5.7 presents aggregates with their force ratios for their corresponding $\mathrm{Re}_{\mathrm{agg}}^{\mathrm{init}}$ conditions.

In Figure 5.7a, the breakage rate is quasi-exclusively non-zero. Therefore, no stable size is

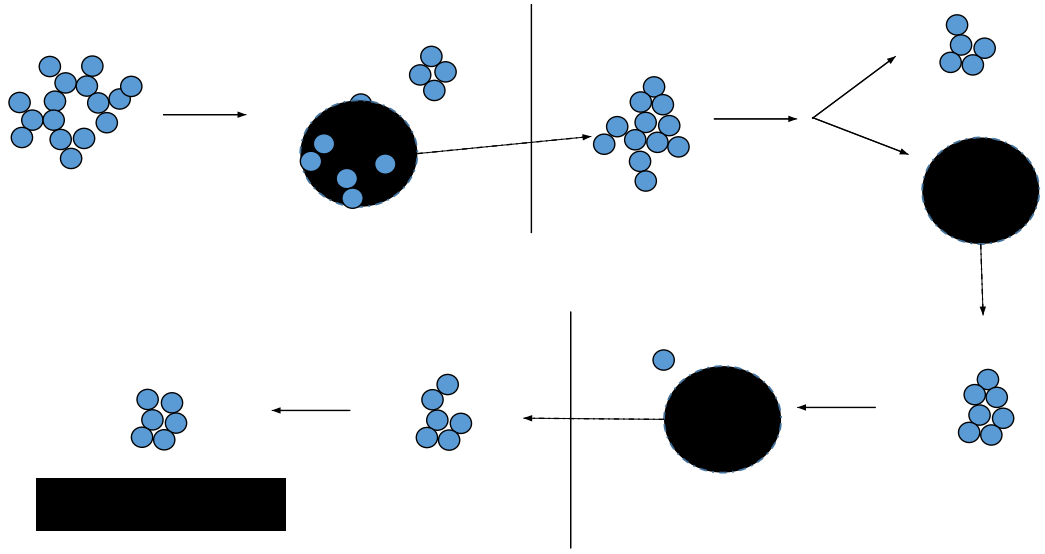

Figure 5.5: Tracking of aggregate evolution through restructuring and breaking: the largest fragment is selected and studied separately under similar flow conditions.

observed in such conditions: only small fragments hold together, and these fragments contain too few primary particles (less than 32 primary particles) to be treated as fractal objects. The breakage rate shows little correlation with aggregate size, and no dependence on force ratio. It must be mentioned that although larger aggregates do break slightly faster, their breakage rates are widely scattered and since hydrodynamic forces prevail for all aggregates in this figure (that is, $F_n^* < (F_n^*)_{\text{stable}}$), they can break regardless of the strength of the cohesive forces.

Figure 5.7b, where $\text{Re}_{\text{agg}}^{\text{init}} \leq 1.6$, shows that when the breakage rates are lower than the rate of flow diffusion $1/t_d^*$, breakage dynamics are governed by the force ratios. Therefore, the breakage rate correlates quite well with the size of the fragment. All the force ratios presented in Figure 5.7b yield a breakage rate of zero after the breakage cascade. The size corresponding to breakage rate of zero is the stable R_g^* for the respective force ratio (or, for the respective shear stresses). This confirms that most aggregate fragments reach a stable size, and that this stable size depends on the hydrodynamic shear stress. To reach this stable size, some aggregates undergo multiple fragmentation stages, while others are stable at much larger sizes. For example, at $F_n^* = 0.5\ (F_n^*)_{\text{stable}}$, Aggregate 8 from Figure 5.1 underwent 5 fragmentations to reach a stable size of $R_g^* = 3.65$, whereas Aggregate 5 underwent breakage only once and the fragment with a size of $R_g^* = 5.23$ was found to be stable. For high enough force ratios, some of the initial 10 aggregates appear to be stable; that is, they restructure

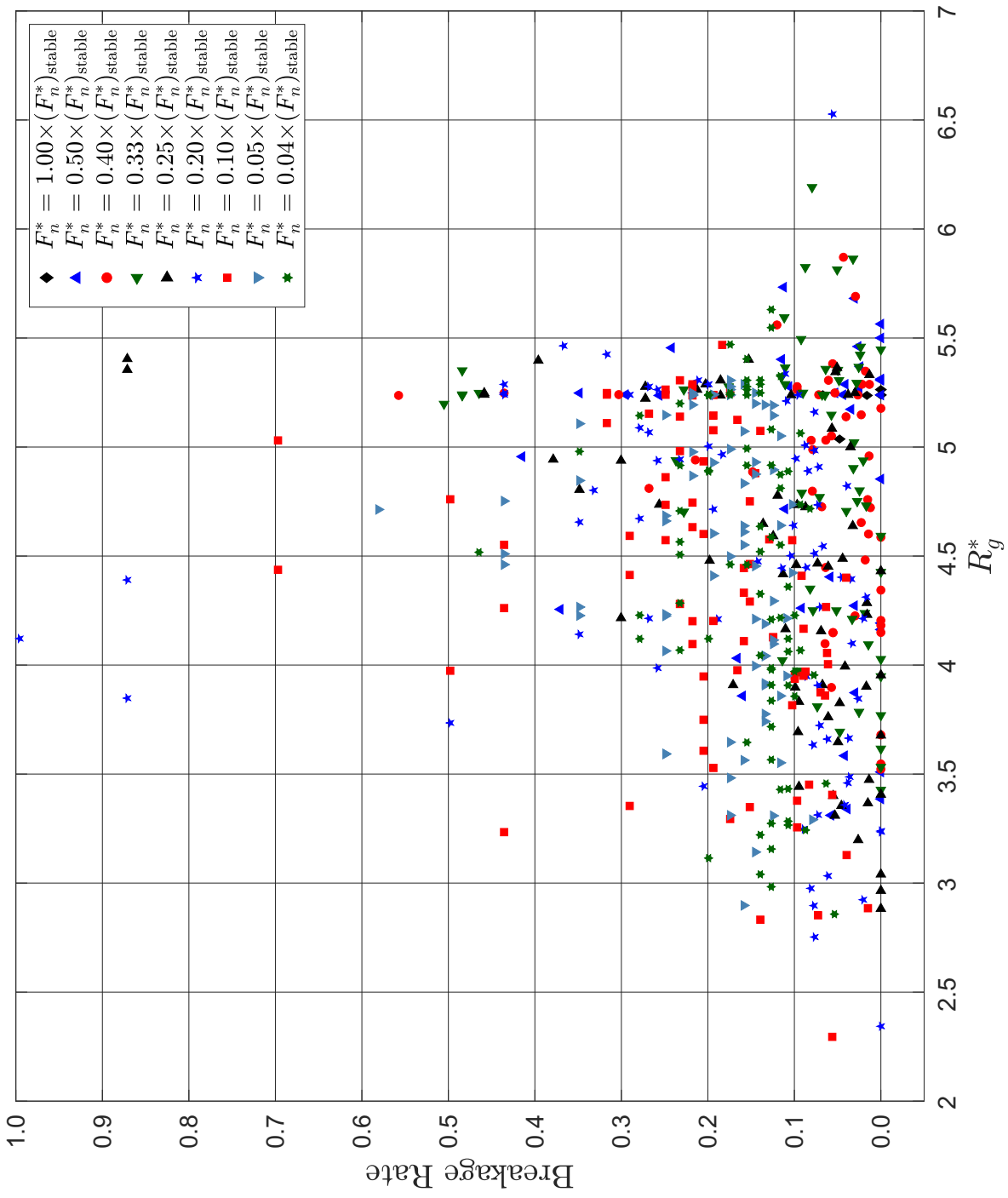

Figure 5.6: Breakage rate at various Reynolds numbers.

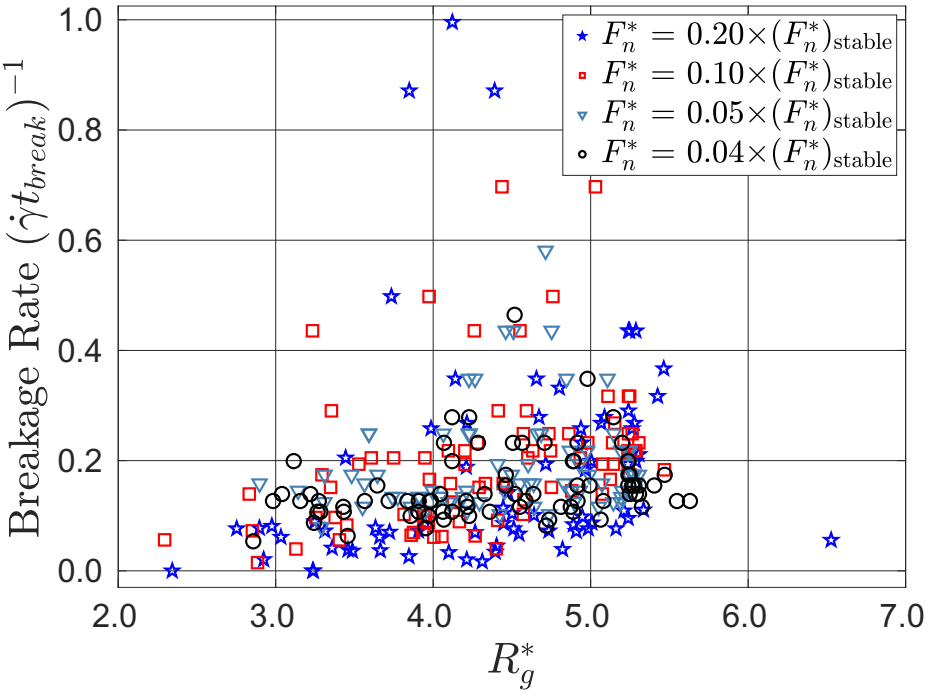

(a) Breakage rate for $\text{Re}_{\text{agg}}^{\text{init}} > 1.6$

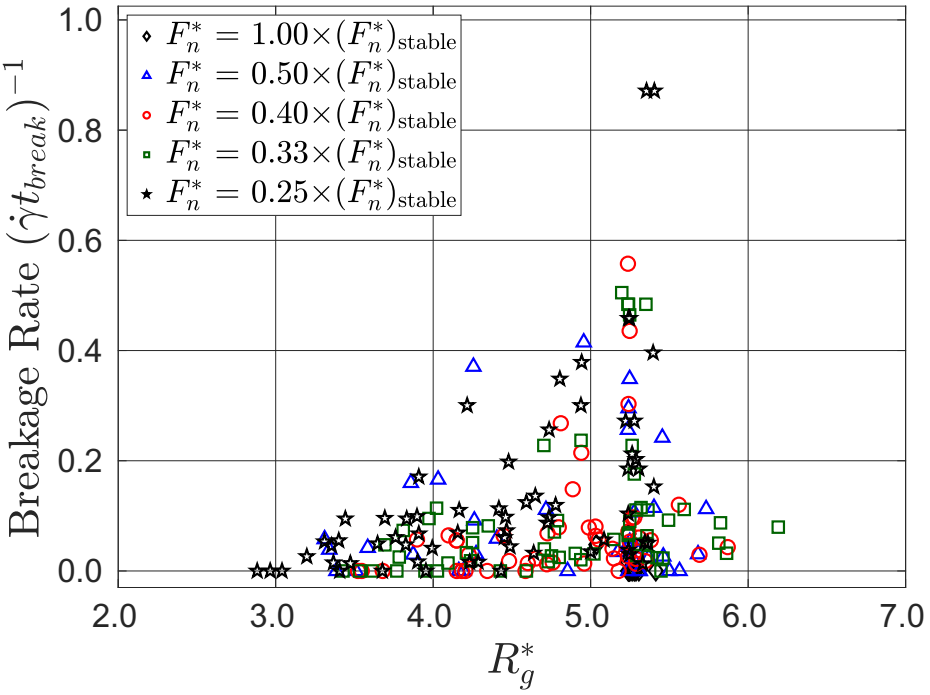

(b) Breakage rate for $\text{Re}_{\text{agg}}^{\text{init}} \leq 1.6$

Figure 5.7: Breakage rate of aggregates and subsequent largest fragments from the breakage cascade, (a) all aggregates and fragments with $\text{Re}_{\text{agg}}^{\text{init}} > 1.6$, that is, with $F_n^* < 0.25\ (F_n^*)_{\text{stable}}$, (b) aggregates and fragments with $\text{Re}_{\text{agg}}^{\text{init}} \leq 1.6$, that is, with $F_n^* \geq 0.25\ (F_n^*)_{\text{stable}}$.

but do not break at all. Hence some points with breakage rate equal to zero correspond to radii of gyration very close to the initial aggregates (some even a little larger). By the end of the breakage cascade, a stable size was found for most aggregates at $\mathrm{Re}_{\mathrm{agg}}^{\mathrm{init}} \leq 1.6$. Overall, smaller aggregates are observed to have a lower breakage rate due to lower hydrodynamic forces at aggregate scale.

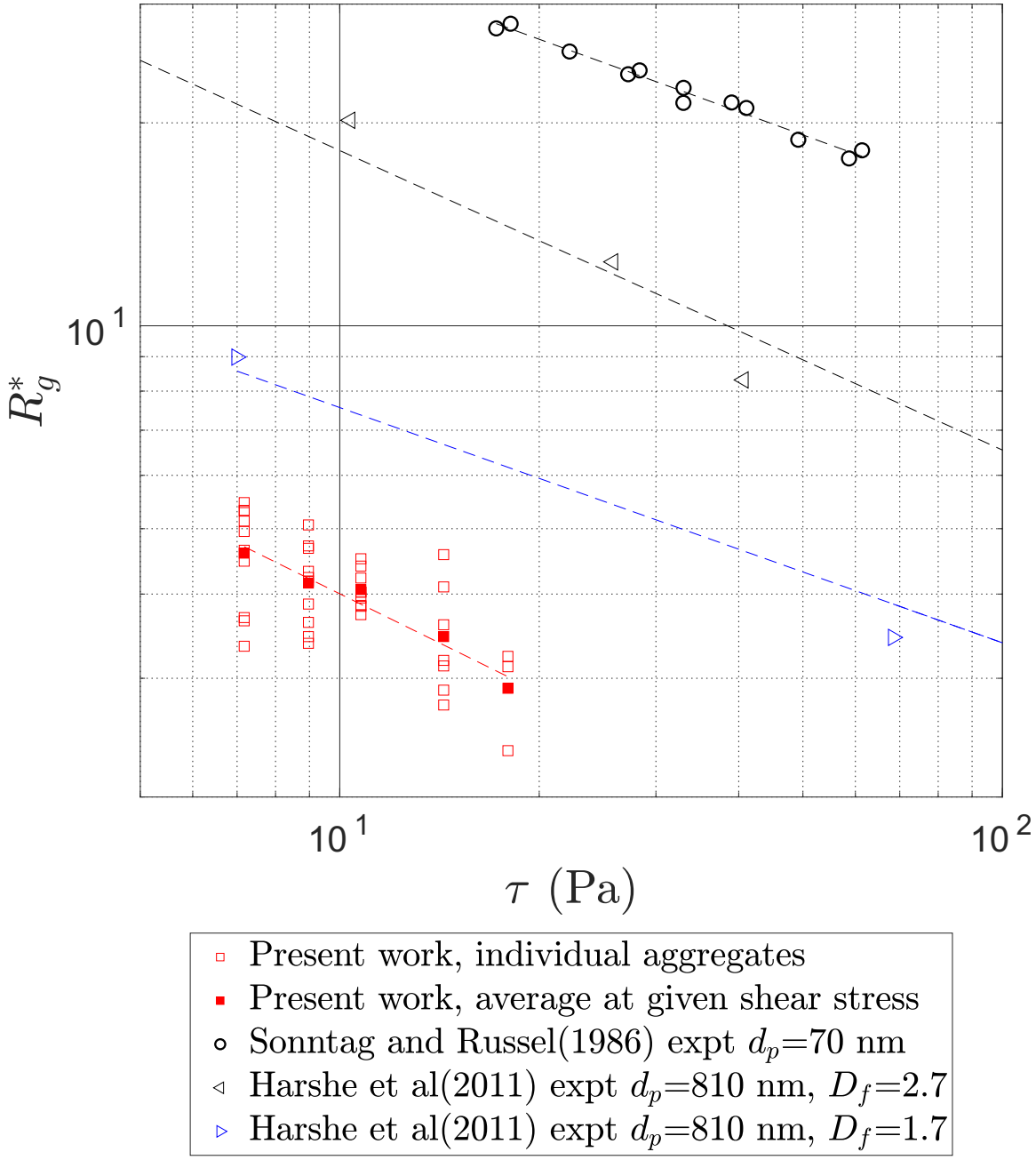

Figure 5.8: Stable size of fragments under different shear conditions compared to other studies.

As previously discussed and as illustrated in Figure 5.4, the nature (mechanism) of the fragmentation does not seem to be impacted by the Reynolds number considered in this study. Therefore,

the correlation of the stable size with shear rate remains consistent with the observations from the literature that studies fragmentation at low Reynolds number. Figure 5.8 shows the scaling of stable size with the shear stress τ collected from several studies, where the largest stable size R_g^* has been reported to scale as $R_g^* \propto \tau^{-p}$. To compare with the literature, the stable size determined through the breakage cascade for the investigated flow conditions is also presented in Figure 5.8. For this comparison, the simulation data had to be converted to physical values by assuming fluid properties, cohesive forces and particle size. Considering water properties for the fluid, the data in Figure 5.8 uses the following conditions for particles:

$$F_n = 1 \times 10^{-9}\ \text{N} \qquad\qquad R_p = 1 \times 10^{-6}\ \text{m}$$

The shear stresses in the flow are estimated from Equation (5.7) as:

$$\tau = \frac{\text{Re}_{\text{agg}}^{\text{init}}\, F_n}{4\,(R_p R_{ig}^*)^2}$$

Most aggregates did not break at $\text{Re}_{\text{agg}}^{\text{init}} = 0.4$, which reflects that the largest stable size is likely to be larger than the aggregates investigated in the study. Therefore, points at $\text{Re}_{\text{agg}}^{\text{init}} = 0.4$ are not represented in Figure 5.8.

The value of the exponent p fitting the data presented in this current work is 0.48, which compares well to literature reported values ranging from 0.35 to 0.55 [7, 10, 12, 15, 16, 26]. Saha et al. [13] reported a value $p = 0.6$ at turbulent conditions with aggregate size larger than the Kolmogorov length scales. Table 5.1 reports the values from these studies. It must be pointed out that the final fractal dimension D_f of the stable fragments from this work ranges between 2.1 and 2.4, while Harshe and Lattuada [21] predicts 2.4. The difference could be due to the geometrical limitation in achieving a high fractal dimension for smaller fragments: when an aggregate consists of too few particles, the scaling exponent of mass with size (that is, the fractal dimension) cannot reach high values even with closely packed aggregates.

To summarize the findings presented so far, when an aggregate is exposed to a Reynolds number condition which scale with the system's shear rate, the breakage rate stops being a function of aggregate size and shear stresses beyond some critical shear. This happens once the hydrodynamic

Table 5.1: Scaling exponents reported in literature for stable size dependence on hydrodynamic shear stress.

Exponent, p $R_g^* \propto \tau^{-p}$	**Literature**	**Conditions**	Simu.	Exp.
0.35	Eggersdorfer et al. [15]	Low Reynolds	FDA	
0.35	Sonntag and Russel [7]	Low Reynolds		✓
0.35 to 0.55	Harshe et al. [12]	Low particulate Reynolds, experiments up to turbulence	SD	✓
0.48	Kroupa et al. [16]	Low Reynolds	FV	
0.48	*Present work*	Laminar, Finite Reynolds	LBM	
0.5	Ehrl et al. [10]	Turbulent, low particulate Reynolds		✓
0.5	Bouyer et al. [25]	Turbulent, low particulate Reynolds		✓
0.52	Zaccone et al. [26]	Laminar and turbulent, low particulate Reynolds		✓
0.6	Saha et al. [13]	Turbulent, low particulate Reynolds		✓

forces are too large compared to cohesive forces. Under such conditions, the breakage rate instead is scaled by the momentum diffusion in the flow. Therefore, the restructuring and breakage of aggregates under shear in finite Reynolds conditions depend on two parameters, the diffusion time and the force ratios F_n^* and F_t^*.

In the data presented so far, the Reynolds number is varied through the shear rate in the flow. Therefore, both the force ratios and diffusion time vary when different Reynolds numbers are investigated. This makes it impossible to distinguish their relative impact on aggregate behaviour independently from each other. The approach described in the next section overcomes this limitation.

5.3.2 Distinguishing the effect of flow inertia from cohesive to drag force ratios

The previous section shows that both the force ratios and finite Reynolds number flow dynamics play a role in morphological evolution and breakage of aggregates. However, the two phenomenon were coupled in the previous section: increase in Reynolds numbers also lead to a change in force ratios, resulting in aggregate evolution under the combined effect of force ratio and finite Reynolds dynamics. While one of the effects of flow inertia was observed as delayed breakage due to diffusion

time, its effect on hydrodynamic forces was not identified. One way to distinguish this is by keeping the force ratios constant over a range of Reynolds number conditions. Thus, in this analysis, the cohesive and tangential forces are scaled with Reynolds number such that their dimensionless forces ratios remain constant within a given dataset. Furthermore, the scaled values of the the forces can be chosen to favor restructuring or breakage. Aggregate evolution studies performed at very low Reynolds number have shown that high tangential forces induce less restructuring (as shown by Becker et al. [27] and in Chapter 4) but more breakage (as in Chapter 4). This information is leveraged to investigate the effect of flow inertia on aggregate evolution. Particularly, evolution of aggregates with high tangential forces is investigated at finite Reynolds number conditions to highlight the role of flow inertia on breakage. Conversely, the effect of flow inertia on restructuring is studied by exposing aggregates with low tangential forces (aggregates more likely to restructure) to different Reynolds number conditions. The following conditions are considered:

$$\begin{aligned} F_n^* &= (F_n^*)_{\text{stable}} = 7.395, \\ F_t^* &\in \{0.01, 0.10, 1.00\} \times F_n^*. \end{aligned} \tag{5.14}$$

While the effect of force ratios under very low Reynolds number conditions has been widely reported in the literature [27–32], it has not been extensively investigated in finite Reynolds number conditions. Among the few studies at finite Reynolds numbers, Saha et al. [13] considered the impact of different constituents of hydrodynamic stresses such as turbulent shear, normal and drag forces on aggregate breakage in turbulent conditions. Despite their attempt to account for hydrodynamic stresses, relative contribution of inter-particle interactions has still not been well examined at finite Reynolds numbers.

The same ten aggregates presented in Figure 5.1 are considered and the maximum cohesive force F_n is set to 7.395 times the Stokesian drag at each Reynolds number tested. Since the probability of breakage and the extent of restructuring are controlled by the tangential force ratio F_t^*, values of F_t^* from 0.01 F_n^* to 1.00 F_n^* are considered, as stated in Equation (5.14). The aggregate Reynolds number ($\text{Re}_{\text{agg}}^{\text{init}}$), on the other hand, varies from 0.4 to 40. To ensure that the aggregates undergo the imposed flow conditions, the time taken for the flow to develop (that is, the diffusion time) must be kept much smaller compared to the overall duration of the simulation. However, this is not always practical

Table 5.2: Dimensionless flow diffusion times t_d^* and simulation duration (expressed as total strain $\dot{\gamma}t$) for the tested Reynolds numbers.

Reynolds number $\mathrm{Re}_{\mathrm{agg}}^{\mathrm{init}}$	diffusion time t_d^*	total duration $\dot{\gamma}t$
0.4	1.4062	80
1.0	3.5156	120
4.0	14.0625	200
10	35.1562	500
40	140.6250	700

as a high t_d^* may require long simulations which can be computationally expensive. Therefore, for each $\mathrm{Re}_{\mathrm{agg}}^{\mathrm{init}}$ considered, the simulation duration has been kept as large as practical compared to the corresponding diffusion time t_d^*. The duration of the simulated period (expressed as dimensionless strain) along with other simulation parameters are listed in Table 5.2.

The graphs in Figure 5.9 show the evolution of aggregate R_g^* over time as a function of Reynolds number for the considered F_n^* and F_t^* from Equation 5.14. As expected, some aggregates break while some attain a stable configuration. The aggregates that do not break by the end of the simulated period are assumed unlikely to break even if the simulations were run for longer durations (more justification for this assumption is discussed towards the end of Section 5.3.2). In the figure, continuous lines show the evolution of the averaged R_g^* of non-breaking aggregates. The corresponding confidence interval (calculated as the standard error) around that average) is represented as a colored area of the same hue. For example, in Figure 5.9b, solid blue line corresponds to the averaged R_g^*, while the shaded area in lighter blue represents the standard error around the averaged R_g^*. Aggregates that break by the end of the simulated period are neither accounted for in the average behaviour, nor in its confidence interval. Instead, they are individually represented as dotted lines and their breakage events are represented as crosses terminating their evolution curve. Moreover, the time needed by the flow to develop is indicated as a vertical line at $\dot{\gamma}t = t_d^*$ for each Reynolds number.

Impact of aggregate Reynolds number on breakage

To find a relation between breakage rate and flow dynamics, aggregates that are likely to break are considered. Since greater inter-particle tangential forces produce more frangible aggregates (as

reported in Chapter 4), the inter-particle forces $F_t^* = 1.0 \times F_n^*$ lead to aggregate breakage. The results of these simulations are presented in Figure 5.9a.

Figure 5.9a shows that aggregates restructure and break for all Reynolds numbers except for $\mathrm{Re}_{\mathrm{agg}}^{\mathrm{init}} = 0.4$. When comparing the breakage events for all $\mathrm{Re}_{\mathrm{agg}}^{\mathrm{init}}$ relative to the diffusion time (t_d^*), it also appears that breakage events occur sooner as the Reynolds number increases. At higher Reynolds numbers, breakage times are less than the diffusion time, indicating that breakage events occur while the flow is still developing and has not reached the target shear rate throughout the domain. To highlight this, the average breakage time over all breaking aggregates, noted $\langle t_{\mathrm{break}} \rangle$, is plotted against Reynolds number in Figure 5.10. The first point (at $\mathrm{Re}_{\mathrm{agg}}^{\mathrm{init}} = 0.4$) is averaged over only two aggregates (since only 2 aggregates broke) and its precision may thus be quite low, however all ten aggregates break at higher Reynolds number. The average data points are aligned along a straight line on a log-log plot. With the standard error indicated for each point, a power law relationship fits well between dimensionless breakage time $\langle t_{\mathrm{break}} \rangle / t_d$ and Reynolds number. The following correlation fits the set of average dimensionless breakage times:

$$\frac{t_{break}}{t_d} \approx 11.46 \left(\mathrm{Re}_{\mathrm{agg}}^{\mathrm{init}}\right)^{-0.9} \tag{5.15}$$

with a correlation coefficient $R^2 = 0.99$.

Since in each sub-figure of Figure 5.9 all aggregates are characterized by the same force ratios, the dependence of breakage on Reynolds number as shown through Figure 5.10 can solely be attributed to the flow inertia. The Reynolds number of primary particles $\mathrm{Re_p}$ ranges from 0.0143 to 1.4350, and thus remains too low to explain the increased breakage rate as an effect of increased drag acting on individual particles. However, aggregate scale Reynolds number is about $R_g^{*2} \sim 25$ times larger than the $\mathrm{Re_p}$, and flow dynamics at aggregate scale start to show some non-linearities associated with finite Reynolds number effects [33]. Specifically, aggregates rotate slightly slower than the surrounding liquid, which is similar to the retarded rotation of a sphere at finite Reynolds numbers [34], leading to higher shear rates around the aggregates. Additionally, the resistance to deformation of the aggregate core, which causes flow disturbance, has previously been identified as an important mechanism that shields the particles in the aggregate shell from the shear stresses (see Chapter 4). This flow disturbance dampens the strain part of the shear. A decrease in the relative effect of viscous

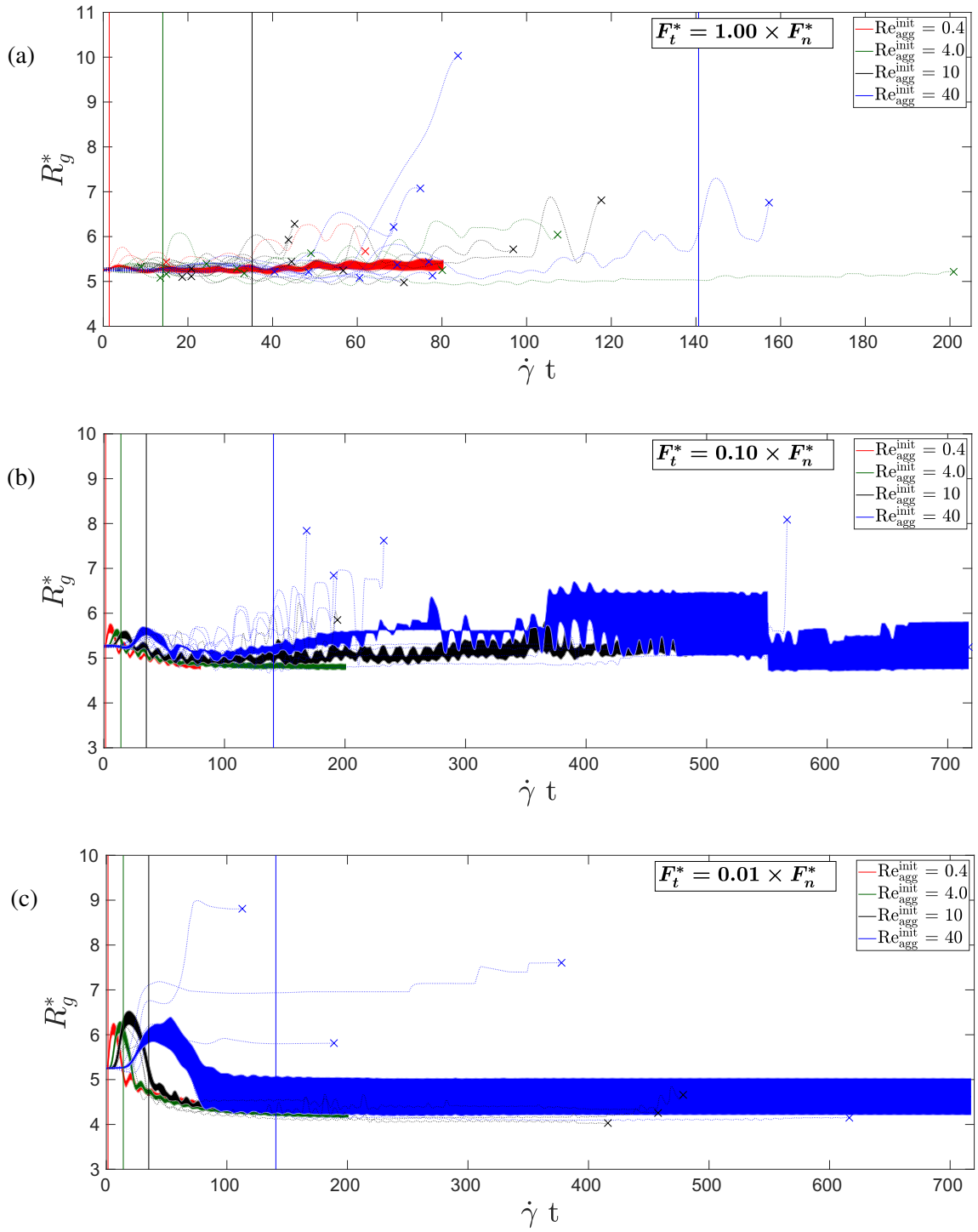

Figure 5.9: Evolution of aggregates over time for three different tangential force ratios (a) $F_t^* = 1.00 \times F_n^*$, (b) $F_t^* = 0.10 \times F_n^*$ and (c) $F_t^* = 0.01 \times F_n^*$. Average R_g^* of non-breaking aggregates for a given shear rate and its standard error are plotted as continuous lines and shaded areas of the same color. Evolution of breaking aggregates is plotted as dashed lines (- -) and breakage events are marked with crosses (×).

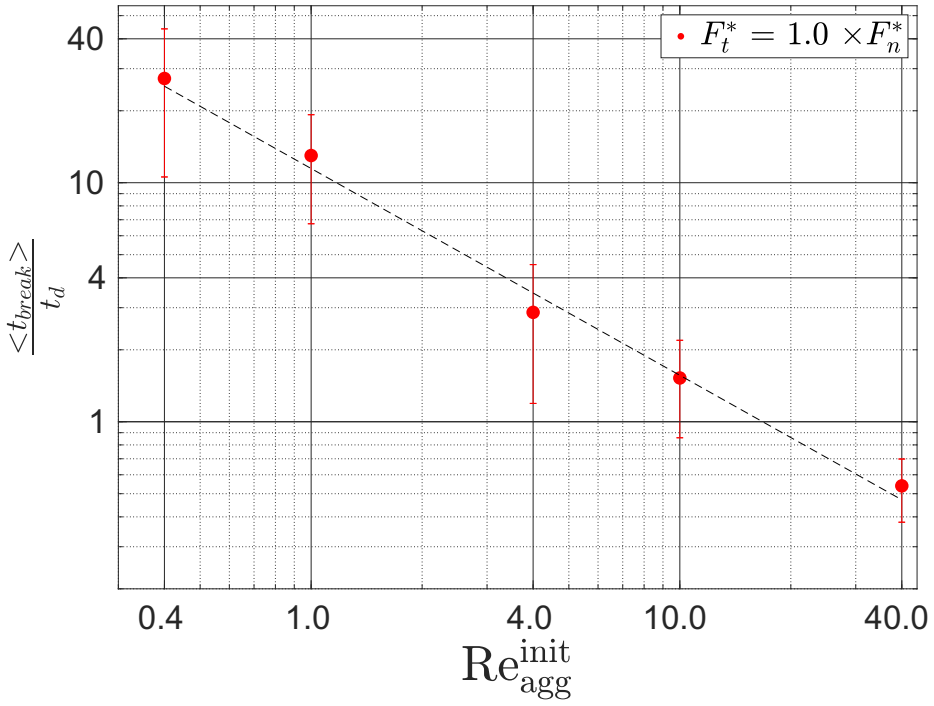

Figure 5.10: Average breakage time $\langle t_{\text{break}} \rangle$ normalized by diffusion time t_d as a function of the Reynolds number.

contributions (due to increasing Reynolds number) tends to shrink the flow disturbances caused by the aggregate, resulting in a decreased shielding effect, and can explain the increase in breakage rate with the Reynolds number.

Lastly, aggregates do not just break more rapidly; they are also more likely to break as the Reynolds number increases. Figure 5.11 shows this as breakage probability against Reynolds number where breakage probability is defined as the ratio of the number of aggregates that broke to the total number of aggregates (10). In Figures 5.9b and 5.9c, most breakage events appear much before the end of the simulation for each Reynolds number, and the radius of gyration of non-broken aggregates remains stable for a significant period of time. This justifies the assumption that the non-broken aggregates found at the end of each simulation are very unlikely to break even if much longer simulations were conducted, and so have reached a stable configuration. Figure 5.11 confirms that for a given Reynolds number, tangential forces tend to favor breakage (as in Chapter 4) and the established effect of inertia on breakage augments this information by showing that increasing Reynolds number also favors breakage.

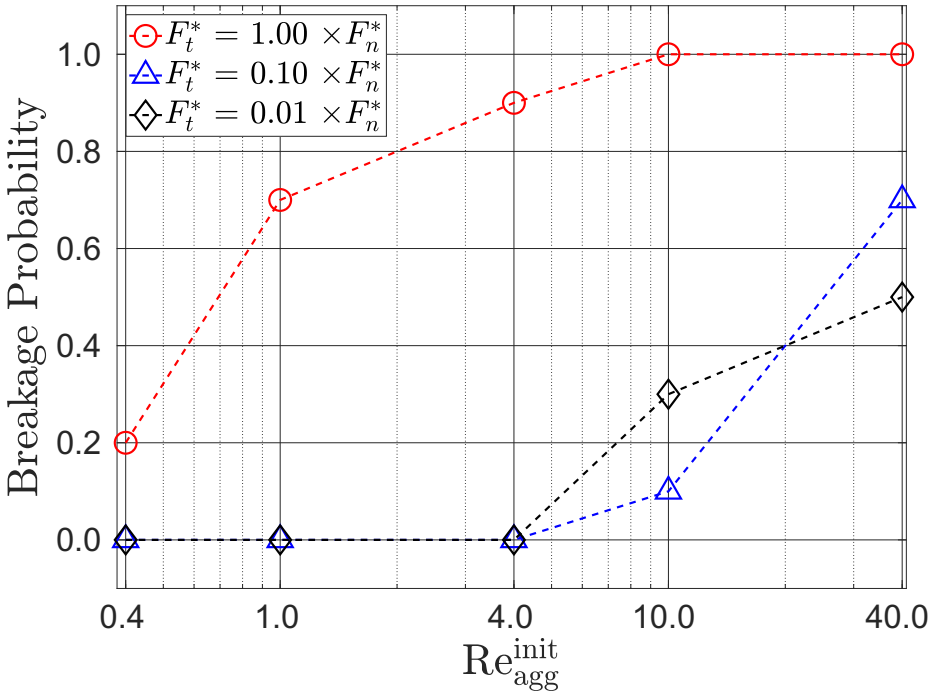

Figure 5.11: Aggregate breakage probability at different Reynolds numbers.

Impact of aggregate Reynolds number on restructuring

With respect to restructuring, there does not seem to be any relation with Reynolds number. In Figure 5.9, the initial differences in restructuring at different Reynolds numbers are related to the fact that the momentum is still diffusing into the domain. Beyond the diffusion time, aggregates restructure significantly during their first rotation to balance hydrodynamic forces with internal cohesive forces, then they quickly break (if no balance is achieved) or reach a stable configuration, as shown by the relatively constant values over time of the average radius of gyration and of its standard error.

Although aggregates with lower tangential inter-particle forces reach denser stable configurations (smaller values of R_g^*) as expected from former observations (Chapter 4), their size seems independent of the Reynolds number. In Figures 5.9b and 5.9c, all continuous lines reach very similar R_g^* values at the end of each simulation. This shows that non-linearities in the flow, such as slower rate of rotation and higher shear rates around the aggregates, have little impact on determining the structure of the aggregate, at least at these moderate Reynolds numbers. This contrasts sharply with the sensitivity of the breakage rate on the Reynolds number, which was discussed in the previous section. Although aggregate stability, in terms of breakage probability and breakage rate, depends on the Reynolds

number, their stable size does not.

Examining the effect of flow inertia in terms of aggregate breakage and restructuring may also indicate how the hydrodynamic forces are balanced through the inter-particle forces within the aggregate. Since breakage is mostly dependent on normal forces and restructuring on the bending moment (Chapter 4), it is possible that the flow inertia is competing against the normal forces to a greater extent, while having little impact on the tangential forces.

5.4 Conclusions

While aggregate evolution at viscosity dominated flows has been extensively investigated, the effect of finite Reynolds number were relatively unknown. The dependence of aggregate evolution on Reynolds number was investigated from simulations. Aggregates were characterized by their radius of gyration and the maxima of the forces responsible for the bonds between their primary particles. Such aggregates were exposed to a shear flow where shear was imposed through stresses acting of opposite faces of the simulation domain. As the aggregates evolved, their sizes and breakage rates were recorded. An analysis of aggregate stable size was conducted by tracking aggregate properties through multiple stages of their breakage cascade. Results were compared and validated against data from other studies and showed that stable size in finite Reynolds conditions is similar to negligible flow inertia conditions.

On the other hand, breakage kinetics are found to be significantly impacted by the Reynolds numbers. It is found that the breakage time is not only a function of the inter-particle and hydrodynamic forces, but also of the time taken for the shear to diffuse into aggregates that is governed by momentum diffusion. This understanding of breakage kinetics is novel, and can be taken into account in breakage kernels used in the population balance equations. Specifically, when the hydrodynamic forces are high compared to the cohesive forces, breakage rate should not be considered infinitely high [20, 35], but should instead be increased progressively to capture the delayed breakage.

At lower shear rates, momentum diffusion is fast compared to aggregate evolution and consequently does not rule aggregate breakage. However, finite Reynolds effects still play a role. An attempt was made to distinguish the effect of flow inertia on aggregate evolution from the combined effect of momentum diffusion and particle-particle interactions by scaling particle-particle interaction

forces with the drag. Flow inertia was found to have no impact on the final structure of aggregates. However, it increases both breakage probability and breakage rate of the aggregates. Based on simulation results, a direct relation between flow inertia at aggregate scale and aggregate evolution was established.

The findings of this first-of-its-kind study expand the fundamental understanding of aggregate evolution to finite Reynolds number conditions. This will improve the accuracy of models describing aggregate morphological evolution in processes by substantially contributing to improvements of fragmentation and restructuring kernels in population balance methods. The implications of these results are important in process modelling since significant finite-Reynolds effects were observed in conditions where they were completely neglected in other studies [21, 36] from which commonly used aggregate evolution kernels are extracted.

Acknowledgements

Most High Performance Computing resources were provided by Westgrid (www.westgrid.ca) and Compute Canada (www.computecanada.ca). Complementary computing resources were provided by the EXPLOR centre hosted by the Université de Lorraine. The authors would like to acknowledge the financial support of the NSERC Industrial Research Chair in Pipeline Transport Processes.

References

[1] B. Pukánszky and J. Móczó. Morphology and properties of particulate filled polymers. In *Macromolecular Symposia*, volume 214, pages 115–134. Wiley Online Library, 2004. doi: 10.1002/masy.200451009.

[2] B. Bolto and J. Gregory. Organic polyelectrolytes in water treatment. *Water Research*, 41(11): 2301–2324, 2007.

[3] J. Laskowski and J. Ralston. *Colloid Chemistry in Mineral Processing*. Elsevier, 2015. ISBN 1-4832-9091-3.

[4] J.-P. Bellot, J.-S. Kroll-Rabotin, M. Gisselbrecht, M. Joishi, A. Saxena, S. Sanders, and A. Jardy.

Toward better control of inclusion cleanliness in a gas stirred ladle using multiscale numerical modeling. *Materials*, 11:1179, July 2018. doi:10.3390/ma11071179.

[5] F. Vaezi, R. S. Sanders, and J. H. Masliyah. Flocculation kinetics and aggregate structure of kaolinite mixtures in laminar tube flow. *Journal of Colloid and Interface Science*, 355(1): 96–105, 2011.

[6] R. Neelakantan, F. Vaezi G., and R. S. Sanders. Effect of shear on the yield stress and aggregate structure of flocculant-dosed, concentrated kaolinite suspensions. *Minerals Engineering*, 123: 95–103, 2018. ISSN 0892-6875. doi:10.1016/j.mineng.2018.03.016.

[7] R. C. Sonntag and W. B. Russel. Structure and breakup of flocs subjected to fluid stresses: I. Shear experiments. *Journal of Colloid and Interface Science*, 113(2):399–413, 1986.

[8] R. C. Sonntag and W. B. Russel. Structure and breakup of flocs subjected to fluid stresses. *Journal of Colloid and Interface Science*, 115(2):390–395, February 1987. ISSN 00219797. doi:10.1016/0021-9797(87)90054-3.

[9] R. Wengeler and H. Nirschl. Turbulent hydrodynamic stress induced dispersion and fragmentation of nanoscale agglomerates. *Journal of Colloid and Interface Science*, 306(2):262–273, 2007. doi:10.1016/j.jcis.2006.10.065.

[10] L. Ehrl, M. Soos, and M. Morbidelli. Dependence of aggregate strength, structure, and light scattering properties on primary particle size under turbulent conditions in stirred tank. *Langmuir*, 24(7):3070–3081, April 2008. ISSN 0743-7463. doi:10.1021/la7032302.

[11] M. Soos, L. Ehrl, M. U. Bäbler, and M. Morbidelli. Aggregate breakup in a contracting nozzle. *Langmuir*, 26(1):10–18, 2010. doi:10.1021/la903982n.

[12] Y. M. Harshe, M. Lattuada, and M. Soos. Experimental and modeling study of breakage and restructuring of open and dense colloidal aggregates. *Langmuir*, 27(10):5739–5752, May 2011. doi:10.1021/la1046589.

[13] D. Saha, M. U. Bäbler, M. Holzner, M. Soos, B. Lüthi, A. Liberzon, and W. Kinzelbach. Breakup of finite-size colloidal aggregates in turbulent flow investigated by three-dimensional

(3d) particle tracking velocimetry. *Langmuir*, 32(1):55–65, 2016. doi:10.1021/acs.langmuir.5b03804.

[14] J. F. Brady and G. Bossis. Stokesian dynamics. *Annual Review of Fluid Mechanics*, 20(1): 111–157, 1988. doi:10.1146/annurev.fluid.20.1.111.

[15] M. L. Eggersdorfer, D. Kadau, H. J. Herrmann, and S. E. Pratsinis. Fragmentation and restructuring of soft-agglomerates under shear. *Journal of Colloid and Interface Science*, 342 (2):261–268, 2010. ISSN 00219797. doi:10.1016/j.jcis.2009.10.062.

[16] M. Kroupa, M. Vonka, M. Soos, and J. Kosek. Size and structure of clusters formed by shear induced coagulation: Modeling by discrete element method. *Langmuir*, 31(28):7727–7737, July 2015. ISSN 0743-7463. doi:10.1021/acs.langmuir.5b01046.

[17] J.-S. Kroll-Rabotin, M. Gisselbrecht, B. Ott, R. May, J. Fröhlich, and J.-P. Bellot. Multiscale simulation of non-metallic inclusion aggregation in a fully resolved bubble swarm in liquid steel. *Metals*, 10(4):517, 2020. doi:10.3390/met10040517.

[18] T. Inamuro and T. Ii. Lattice Boltzmann simulation of the dispersion of aggregated particles under shear flows. *Mathematics and Computers in Simulation*, 72(2):141–146, September 2006. ISSN 0378-4754. doi:10.1016/j.matcom.2006.05.022.

[19] M. Ernst, M. Dietzel, and M. Sommerfeld. A lattice boltzmann method for simulating transport and agglomeration of resolved particles. *Acta Mechanica*, 224(10):2425–2449, 2013.

[20] Y. M. Harshe and M. Lattuada. Breakage rate of colloidal aggregates in shear flow through Stokesian dynamics. *Langmuir*, 28(1):283–292, January 2012. ISSN 0743-7463. doi:10.1021/la2038476.

[21] Y. M. Harshe and M. Lattuada. Universal breakup of colloidal clusters in simple shear flow. *The Journal of Physical Chemistry B*, 120(29):7244–7252, 2016.

[22] H. C. Hamaker. The London-van der Waals attraction between spherical particles. *Physica*, 4 (10):1058–1072, 1937. ISSN 00318914. doi:10.1016/S0031-8914(37)80203-7.

[23] D. L. Feke, N. D. Prabhu, J. A. J. Mann, and J. A. L. Mann. A formulation of the short-range repulsion between spherical colloidal particles. *The Journal of Physical Chemistry*, 88(23): 5735–5739, November 1984. ISSN 0022-3654. doi:10.1021/j150667a055.

[24] V. Becker and H. Briesen. Tangential-force model for interactions between bonded colloidal particles. *Physical Review E*, 78(6):061404, December 2008. doi:10.1103/PhysRevE.78.061404.

[25] D. Bouyer, A. Liné, and Z. Do-Quang. Experimental analysis of floc size distribution under different hydrodynamics in a mixing tank. *AIChE Journal*, 50(9):2064–2081, 2004. doi:10.1002/aic.10242.

[26] A. Zaccone, M. Soos, M. Lattuada, H. Wu, M. U. Bäbler, and M. Morbidelli. Breakup of dense colloidal aggregates under hydrodynamic stresses. *Physical Review E*, 79:061401, Jun 2009. doi:10.1103/PhysRevE.79.061401.

[27] V. Becker, E. Schlauch, M. Behr, and H. Briesen. Restructuring of colloidal aggregates in shear flows and limitations of the free-draining approximation. *Journal of Colloid and Interface Science*, 339(2):362–372, 2009. doi:10.1016/j.jcis.2009.07.022.

[28] M. Zeidan, B. H. Xu, X. Jia, and R. A. Williams. Simulation of aggregate deformation and breakup in simple shear flows using a combined continuum and discrete model. *Chemical Engineering Research and Design*, 85(12):1645–1654, January 2007. ISSN 0263-8762. doi:10.1016/S0263-8762(07)73208-2.

[29] V. Becker and H. Briesen. A master curve for the onset of shear induced restructuring of fractal colloidal aggregates. *Journal of Colloid and Interface Science*, 346(1):32–36, June 2010. ISSN 0021-9797. doi:10.1016/j.jcis.2010.02.015.

[30] M. Vanni and A. Gastaldi. Hydrodynamic forces and critical stresses in low-density aggregates under shear flow. *Langmuir*, 27(21):12822–12833, November 2011. ISSN 0743-7463. doi:10.1021/la2024549.

[31] K. Horii, R. Yamada, and S. Harada. Strength deterioration of nonfractal particle aggregates in simple shear flow. *Langmuir*, 31(29):7909–7918, 2015.

[32] M. Vanni. Accurate modelling of flow induced stresses in rigid colloidal aggregates. *Computer Physics Communications*, 192:70–90, July 2015. ISSN 0010-4655. doi:10.1016/j.cpc.2015.02.022.

[33] H. Haddadi and J. F. Morris. Topology of pair-sphere trajectories in finite inertia suspension shear flow and its effects on microstructure and rheology. *Physics of Fluids*, 27(4):043302, 2015. doi:10.1063/1.4917030.

[34] D. R. Mikulencak and J. F. Morris. Stationary shear flow around fixed and free bodies at finite reynolds number. *Journal of Fluid Mechanics*, 520:215, 2004. doi:10.1017/S0022112004001648.

[35] B. O. Conchúir and A. Zaccone. Mechanism of flow-induced biomolecular and colloidal aggregate breakup. *Physical Review E*, 87(3):032310, March 2013. doi:10.1103/PhysRevE.87.032310.

[36] M. U. Bäbler, L. Biferale, L. Brandt, U. Feudel, K. Guseva, A. S. Lanotte, C. Marchioli, F. Picano, G. Sardina, A. Soldati, and F. Toschi. Numerical simulations of aggregate breakup in bounded and unbounded turbulent flows. *Journal of Fluid Mechanics*, 766:104–128, 2015. doi:10.1017/jfm.2015.13.

Chapter 6

Exposure of fractal aggregates to accelerating flows at finite Reynolds numbers

Abstract

The breakup of small aggregates is governed by the imbalance of imposed hydrodynamic forces and inter-particle cohesive forces between the constituent particles. Aggregate restructuring in ramped shear flows at infinitely low Reynolds number conditions are known to reinforce the aggregates, increasing the effective cohesive strength. However, non-negligible flow inertia is known to increase breakage rates, and is expected to affect breakage kinetics under finite Reynolds number conditions in accelerated flows.

A numerical investigation was conducted to establish the effect of flow acceleration on aggregate evolution. The aggregates were characterized by their size, structure and inter-particle forces. For each simulation, individual aggregates were subjected to accelerating flow conditions imposed through shear stresses at the boundaries, and their structural evolution along with breakage events were recorded. The particles were tracked with Discrete Element Method. The flow was solved using a Lattice Boltzmann method, and two-way coupling between the solid and liquid phase was achieved through an Immersed Boundary Method.

The findings show that although aggregates restructure due to the shear flow, their structure at breakage does not depend on the shear stress in the flow. Increasing flow acceleration, is found to slow down aggregate breakage and its rotation, despite higher imposed shear stresses at the boundaries of the domain. Since higher flow acceleration values result in an increased Reynolds number, the observed delays are found to be a transient effect of flow inertia around the aggregates. The reported findings establish a novel addition to the criteria for aggregate breakage, where along with shear strength of the aggregates, flow accelerations and Reynolds number at the scale of the aggregates must also be considered.

6.1 Introduction

Many industrial processes involve dispersed solids in fluids in the form of aggregates. The properties of these aggregates, for instance their size and structure, are known to greatly influence the efficiency of the processes [1–3]. Thus, control of the aggregate properties is crucial to industrial processes. Hydrodynamic stresses alter the size and structure of the aggregates [4–7]. Therefore, evolution of aggregates under hydrodynamic stresses has been a topic of great interest in colloidal and interface science, multiphase flow research and industrial process development and optimization.

In order to expand the understanding of aggregate behavior when hydrodynamic stresses are imposed, several experimental studies have examined aggregate size and structure under different flow conditions. For example, among the earlier studies, Sonntag and Russel [8] established a power-law relation between the largest stable aggregate size and shear rate in laminar conditions. The power-law relationship was later found to be also valid in turbulent conditions [5, 7]. Ehrl et al. [4] also reported a power-law relationship under turbulent conditions, and established the independence of stable size from the size of the primary particles composing the aggregates. Since the largest stable size of aggregates can be used as a proxy for its strength [9], these studies established the parameters that determine the aggregate strength by measuring the largest stable aggregate size. Through numerical simulations, several numerical studies [10–12] have also reported the power-law relationship between largest stable size and shear stresses, proving the viability of present numerical models to represent aggregate evolution.

While the stable size is important as an indicator of the aggregate strength, breakage dynamics

are required to understand the evolution over time of a population of aggregates. Through numerical simulations, Harshe and Lattuada [13] studied the breakage dynamics of aggregates and established the breakage rate as a functions of shear stress, aggregate size and fractal dimension. The study was performed using Stokesian Dynamics (SD), which is limited to very low Reynolds numbers. Furthermore, the hydrodynamic stresses were applied and given a constant value right from the start of the simulation, resulting in no (or infinite) flow acceleration. Although flow acceleration is not a relevant parameter for creeping flows, it may contribute significantly to aggregate conditioning; that is, their restructuring under shear, and may lead to aggregate reinforcement [14]. Reinforcement allows aggregates to resist stronger shear stresses [13]. Consequently, the approach to estimate breakage rate through SD with initialized flow field may be over simplified in representing conditions where an aggregate experiences a change in flow conditions (for example, in a mixing tank, through pumps or sudden changes in pipe diameter). In similar conditions but at finite Reynolds number, Chapter 5 showed that the flow inertia plays a role in aggregate breakage even for relatively low values of the aggregate scale Reynolds number ($Re_{agg} \geq 0.4$), suggesting that aggregates' dynamic response to transient shear stresses can play a significant role in their breakage.

In a turbulent flow, as per Kolmogorov's theory, the shear rate induced by eddies is inversely proportional to their size. The size of the smallest eddies in a turbulent flow, at which the highest shear rates are reached, is the so-called Kolmogorov length scale. However, since such eddies also last for the smallest duration (Kolmogorov's time scale), aggregates carried in a turbulent flow experience the highest shear stresses only for the smallest duration. In contrast, aggregates are exposed to lower shear stresses for longer durations through interactions with larger eddies. Such a shear history can potentially have an impact on aggregate breakage rates: periods of low shear rates can restructure the aggregates into denser, and thus stronger aggregates.

Only a few studies have investigated the aggregate evolution at sub Kolmogorov length scales. Kusters [15] estimated the aggregate breakup frequency in agitated vessels through the assumption that aggregates break instantaneously when a critical shear stress, corresponding to the aggregate strength, is reached in the fluid surrounding an aggregate. This assumption was used to estimate breakage kinetics under different simulated flow conditions [16–18] assuming the aggregates are transported in the flow as tracer particles. Since breakage depends on the relative strength of cohesive bonds against the competing internal stresses due to hydrodynamic forces, De Bona et al. [19]

estimated breakage kinetics under turbulent fluctuations by determining the growth of stresses between interparticle bonds. However, the aggregates used were isostatic, and no conditioning of aggregates was considered. Furthermore, the flow around the aggregates was simulated using SD, which ignores flow inertia. Therefore, the study could not account for the effect of flow inertia as diffusion time that was observed to play significant role in Chapter 5.

To investigate the phenomenon of aggregate conditioning due to varying shear forces, a simplified case of varying flow is considered where the flow is accelerating at a constant rate. A physical example of accelerating flow could be seen in mixing tanks, when an aggregate moves with the flow from the top of an impeller where energy dissipation is low, to the tip of the impeller where the energy dissipation is the highest [20]. In one study of accelerated flow, Seto et al. [14] showed that with step-wise increasing shear forces, the aggregates' radius of gyration reduces, that is, it restructures to become more dense. This leads to more stable aggregates compared to aggregates undergoing more abrupt flows, as denser aggregates are also more stronger [13]. However, Seto et al. [14] allowed aggregates to restructure for long shear strains (equivalent of approximately 1.6 rotations in the flow), between each shear rate steps. This constant time of shearing at each step of shear rate may not be a realistic model for turbulent flows where high shear rates exist for a shorter time.

In this study, aggregates are subjected to a continuously accelerating flow. Three rates of acceleration are investigated and the acceleration values are high enough so that aggregates reach finite Reynolds number conditions before breakage. Aggregates are allowed to restructure and break. The results show the impact of flow acceleration, and hence flow inertia, on aggregate breakage kinetics. This is a novel study that investigates aggregate conditioning and breakage in accelerating flows at finite Reynolds number. Furthermore, flow acceleration is reasoned to represent shear rate fluctuations around smallest length scales in turbulent flows, and findings are discussed in context of aggregate breakage at sub-Kolmogorov length scales.

6.2 Methodology

6.2.1 Aggregate creation

Size and density are the two primary morphological parameters for aggregates [21]. They are commonly quantified by the radius of gyration (R_g) and the fractal dimension (D_f) respectively. The

aggregates considered in this study were algorithmically created as described in Chapter 4. Each aggregate consists of 70 rigid spherical primary particles, and have a fractal dimension D_f of 2.3. The fractal dimension of 2.3 is chosen as it has been reported widely for colloidal aggregates in shear flows [8, 22–25]. To extract a statistical behaviour from the evolutions of individual aggregates, simulations were performed on a set of twenty different aggregates for each of the flow condition considered. Ten of the aggregates are the same as those used in Chapter 5, whereas all 20 aggregates have the same morphological parameters (number of particles, R_g, D_f). This allows for comparison of results presented for accelerating flows with formerly published results where shear stress changes abruptly.

Aggregate evolution strongly depends on the interactions between primary particles (as shown by Becker et al. [26], and in Chapter 4). Here, inter-particle forces are represented as a combination of normal and tangential components. The normal component, or cohesive force, is described as a summation of an attractive force modeled as van der Waals forces [27] and a short range repulsive force modeled with Born repulsion [28] to prevent particle overlapping. The maximum attractive force derived from the sum of these attractive and repulsive contributions defines the bond strength; that is, the force required to break the bond between any two adjacent particles. The tangential forces are modeled as described by Becker and Briesen [29], which imparts a bending moment to the aggregate. The implementation of these forces are detailed in Chapters 3 and 4. In this investigation, the maximum normal and tangential forces were set to $F_n = F_t = 4\,\rho\nu^2$ respectively, where ρ and ν are the fluid's density and viscosity. Corresponding physical values are presented in Table 6.1, and illustrates that the conditions chosen are applicable generally to colloidal systems. For comparison, Soos et al. [30] estimated the cohesive forces to be 6.2 ± 1 nN, and they also reported the range of 0.01 nN to 10 nN in various other papers [8, 9, 31–34].

To detect aggregate breakage in the simulations, a criterion similar to Chapter 5 is chosen: the breakage distance is set to $0.1R_p$, where R_p is the radius of each of the 70 primary particles comprising each aggregate.

6.2.2 Numerical method

Since hydrodynamics drive aggregate restructuring and breakage, forces of hydrodynamic origin acting on aggregates must be computed accurately. Such forces depend on many parameters,

Table 6.1: Problem variables in physical units assuming reasonable physical values based on literature, which form the basis for dimenionless parameters.

Particle radius	R_p	=	1×10^{-6} m
Fluid density	ρ_f	=	$1\,000$ kg $\cdot$ m^{-3}
Particle density	ρ_p	=	$2\,600$ kg $\cdot$ m^{-3}
Lattice spacing	Δx	=	2×10^{-7} m
Time step	Δt	=	4×10^{-9} s
Interparticle forces:			
• cohesive strength	F_n	=	4×10^{-9} N
• shear strength	F_t	=	4×10^{-9} N
Flow acceleration:	$\ddot{\gamma}_1$	=	$2.78 \cdot 10^6$ s^{-2}
	$\ddot{\gamma}_2$	=	$5.56 \cdot 10^6$ s^{-2}
	$\ddot{\gamma}_3$	=	$8.34 \cdot 10^6$ s^{-2}

including flow conditions, boundary conditions and the aggregate's position, size and structure. Therefore, to calculate the hydrodynamic forces, a full resolution of the flow is necessary, which is achieved here with a Lattice-Boltzmann method (LBM) [35] coupled with the solids through an Immersed Boundary Method (IBM) [36]. Newton's equations of motion are solved for each particle, accounting for particle interactions using the Discrete Element Method [37]. The numerical schemes are detailed in Chapter 3.

When the distance between particles is smaller than the lattice spacing, the flow between the two surfaces cannot be resolved. Its action on the particles is thus modelled through a lubrication force $\boldsymbol{F}_{\text{lub}}$ [38]:

$$\boldsymbol{F}_{\text{lub}} = 3\pi\mu R_p \Big((\boldsymbol{v}_i - \boldsymbol{v}_j) \cdot \boldsymbol{e}_{ij} \Big) \Big(\frac{1}{s} - \frac{1}{s_c} \Big) \boldsymbol{e}_{ij} \qquad (6.1)$$

$$\text{with } \boldsymbol{e}_{ij} = \frac{\boldsymbol{x}_i - \boldsymbol{x}_j}{\|\boldsymbol{x}_i - \boldsymbol{x}_j\|}$$

where R_p is the particle radius, μ is the dynamic viscosity of the fluid, $\boldsymbol{x}_i$ and $\boldsymbol{x}_j$ are the positions of the two particles, and $\boldsymbol{v}_i$ and $\boldsymbol{v}_j$ are their respective velocities. The force comes into play when the surface-to-surface distance s is less than a cutoff distance, s_c. The cutoff distance was determined by reproducing results from Haddadi and Morris [39] for a particle Reynolds number of 2.4, and was found to be $0.05R_p$. It must be pointed out that although lubrication force corrections are included here, the short range interactions in aggregates are dominated by the colloidal forces and lubrication

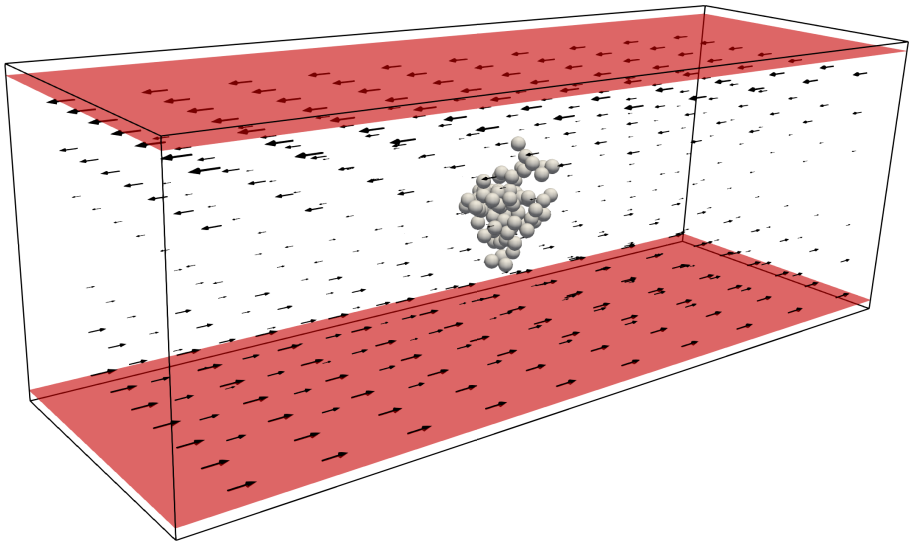

Figure 6.1: Domain setup. The dimensions of the domain are $211 \times 598 \times 198$. The shear planes are highlighted with red color, and are at a distance of 6 lattice units from the domain boundaries.

does not play a significant role in these simulations.

6.2.3 Simulation setup

The objective of the numerical investigations is to capture the dynamic response of aggregates in transient flow conditions representative of various industrial processes. In such processes, flow variation is often caused due to energy dissipation through eddies. Here, we consider aggregates that are smaller than the Kolmogorov length scale of the carrier turbulent flows. To capture the phenomenon, the flow is approximated as a simple shear flow induced by a local accelerating hydrodynamic stress, which combines a strain [11, 40, 41] with a rotation. As per the Kolmogorov theory, eddies are characterized by velocity and time scales, making it straightforward to derive a strain rate. In this problem, this strain rate is imposed as a boundary condition by imposing a shear stress τ, which results in a controlled shear rate $\dot{\gamma}$. When applied to the Newtonian fluid carrying the aggregate, $\dot{\gamma} = \tau/\mu$, where μ is the dynamic viscosity of the carrier fluid.

The free-to-move aggregate is positioned at the center of a domain of size 598 lattice units in the streamwise direction, 211 lattice units in the spanwise direction and 200 lattice units in the cross-flow

cross-shear direction. The shear stresses are imposed at a distance of 6 nodes from boundaries of the domain, so that the domain size in which shear is controlled is effectively 198 lattice units in the cross-shear direction. The diameter of a primary particle is discretized over ten lattice units.

Pressure boundary condition

The stress imposed boundary conditions at the top and bottom planes (highlighted in Figure 6.1) are obtained by applying shear stress and a pressure. While shear stress can be imposed using a source term, pressure is a flow property that is ruled by an equation of state depending on the local Boltzmann distributions.

The most common way to impose pressure boundary conditions in LBM is to follow the approach described by Zou and He [42]. However, their original implementation of pressure boundary condition requires that the tangential velocity is zero, which makes it impractical to control the shear stress imposed at the boundary. In the simulations presented here, a new pressure boundary conditions is used: specifically, it is derived from that described by Zou and He [42] and is combined with a free-slip boundary condition instead of a bounce-back, so that the flow in the tangential direction is not constrained.

Since Zou and He [42] use BGK collision operator (named after Bhatnagar, Gross and Krook [43]), the equation of state for calculating pressure is simple and described as:

$$p_{\mathrm{BGK}} = c_s^2 \rho. \tag{6.2}$$

However, the simulations presented here use the collision operator described by Eggels and Somers [35] (E&S) and presented in greater detail in Sungkorn and Derksen [44]. In this method, the equation of state for pressure is

$$p_{\mathrm{E\&S}} = c_s^2 \rho \left(1 - \frac{1}{2}\boldsymbol{u}\cdot\boldsymbol{u}\right). \tag{6.3}$$

Note that, in the two equations of state, the speed of sound c_s has different values: it is $3^{-1/2}$ in BGK against $2^{-1/2}$ in E&S. The density to be imposed at the boundary nodes in order to obtain the targeted pressure is calculated using the equation of state. Then, instead of using "the bounce-back rule for the non-equilibrium part of the particle distribution, normal to the inlet", the particle distribution normal to the inlet is streamed as a regular free-slip boundary condition. In the end, Equation (25) of

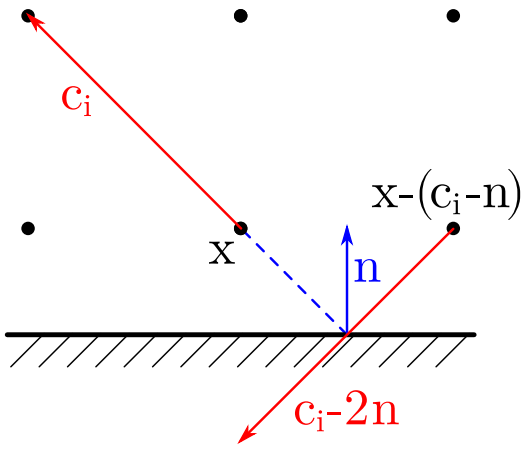

Figure 6.2: Illustration of the calculation of distribution components normal to the inlet in the pressure boundary condition, as defined in Equation (6.4).

Zou and He [42] is replaced by:

$$\forall \boldsymbol{c}_i \cdot \boldsymbol{n} > 0, \quad f(\boldsymbol{c}_i, \boldsymbol{x}) = f(\boldsymbol{c}_i - 2\boldsymbol{n}, \boldsymbol{x} - (\boldsymbol{c}_i - \boldsymbol{n})) \tag{6.4}$$

where $\boldsymbol{n}$ is the normal vector to the boundary condition (pointing inwards), and $f(\boldsymbol{c}_i)$ is the distribution component corresponding to the base velocity vector $\boldsymbol{c}_i$ associated to the direction i of the lattice. Figure 6.2 illustrates this geometrical relation.

Shear driven flow

A shear stress is applied as a source term on LBM nodes at a distance of 6 lattice units from the pressure imposed boundary nodes. The shear stress values are given as

$$\tau = \mu\dot{\gamma} \tag{6.5}$$

where $\dot{\gamma}$ is the target shear rate and μ is the dynamic viscosity of the fluid. To study the dynamic response of aggregates to a variation in their surrounding shear rate, the shear stress imposed at the boundaries is increased linearly with time such that

$$\tau = \mu\ddot{\gamma}t \tag{6.6}$$

where three different values for the flow acceleration $\ddot{\gamma}$, that is the rate of increase of the shear rate with time, are investigated. Consequently, at any instant t the shear rate $\dot{\gamma}(t)$ in the boundary planes is

$$\dot{\gamma} = \ddot{\gamma}\, t \tag{6.7}$$

Since particle size is the smallest governing scale in the system, a characteristic time scale t_c is identified and defined as the time taken for flow to diffuse across a particle, given as

$$t_c = \frac{4R_p^2}{\nu} \tag{6.8}$$

Using this definition, the dimensionless shear rate $\dot{\gamma}^*$, flow acceleration $\ddot{\gamma}^*$ and time t^* can be defined as

$$\dot{\gamma}^* = \dot{\gamma}\, t_c \tag{6.9}$$

$$\ddot{\gamma}^* = \ddot{\gamma}\, t_c^2 \tag{6.10}$$

$$t^* = \frac{t}{t_c} \tag{6.11}$$

The three values of $\ddot{\gamma}^*$, reported in Table 6.2, are chosen to achieve finite Reynolds number conditions and produce significant rotation (or strain) while keeping the computation cost relatively low. The physical values which form the basis for the dimensionless conversion are presented in Table 6.1

Since the flow develops due to momentum diffusion, the characteristic diffusion time t_d can be estimated from a dimensional analysis of the one-dimensional diffusion equation as

$$\frac{\partial u}{\partial t} = \nu \frac{\partial^2 u}{\partial y^2} \tag{6.12}$$

$$t_d \equiv \frac{(h/2)^2}{\nu} \tag{6.13}$$

Table 6.2: Flow accelerations in dimensionless form.

$\ddot{\gamma}_1^*$	$=$	4.45×10^{-6}
$\ddot{\gamma}_2^*$	$= 2 \times \ddot{\gamma}_1^* =$	8.90×10^{-6}
$\ddot{\gamma}_3^*$	$= 3 \times \ddot{\gamma}_1^* =$	13.35×10^{-6}

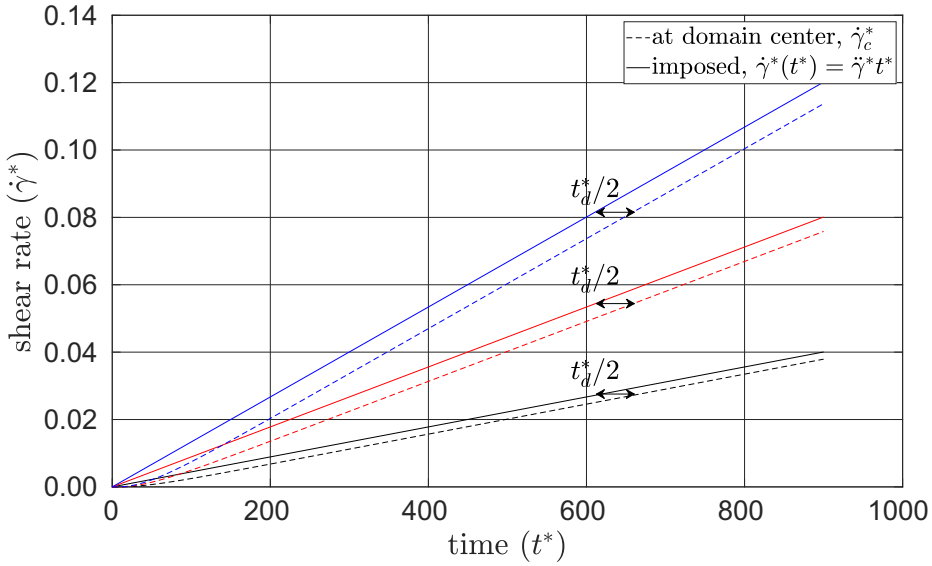

(a) Evolution of shear rate over time expressed through shear stress imposed at the boundaries and computed at the center of the domain through numerical solution of a 1-D diffusion equation.

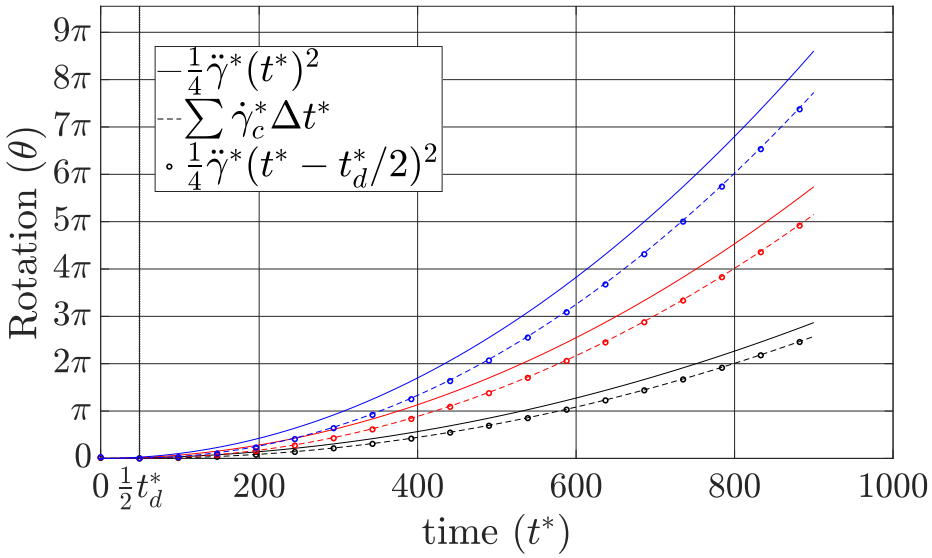

(b) Evolution of rotation over time estimated through imposed shear (—). For comparison, rotation at the center of the domain estimated through numerical solution (- -), and by accounting for diffusion time (∘) is also presented.

Figure 6.3: Variation of shear rate and rotation with time, and with each other. The considered $\ddot{\gamma}$ values of 4.45×10^{-6}, 8.90×10^{-6} and 13.35×10^{-6} are colored black, red and blue respectively.

where u is velocity, ν is the kinematic viscosity and $h/2$ is the distance from the location where the boundary condition is imposed. In this problem, at the center of the domain, this distance is $h/2$, with h the domain height.

Due to this diffusion time, the shear rate at the center of the domain ($\dot{\gamma}_c$) lags behind the shear rate

imposed at boundaries. The numerical solution of the 1-D diffusion, Equation (5.2), with constantly increasing shear stresses at the boundaries is presented in Figure 6.3a. The figure shows the evolution of the shear rate in the domain over time. The shear stresses are imposed in two boundary planes and the momentum diffuses from both sides towards the center of the domain. The momentum diffusion towards the center of the domains is thus twice as fast in this problem than in the derivation of t_d by dimensional analysis. Hence, the delay between the shear rate at the boundaries and at the center is $t_d/2$. Figure 6.3a illustrates this delay; it shows as well, the non-linear progression in the beginning of the simulations lasts only for the duration of t_d, and the shear rate at the center of the domain $\dot{\gamma}_c$ increases linearly afterwards.

Previous studies [41, 45] have shown that aggregate evolution depends on the rotation of the aggregate as its branches enter and leave the zones of traction and compression along the principal axes of the stress tensor, which itself is related to the rotation in the flow through the shear rate $\dot{\gamma}$. The rotation angle θ of the flow imposed at the boundaries can be expressed as

$$\theta \equiv \int \omega(t)\mathrm{d}t = \frac{1}{2}\int_0^t \dot{\gamma}(t)\mathrm{d}t = \frac{1}{4}\ddot{\gamma}t^2 \tag{6.14}$$

The rotation at the center of the domain θ_c is delayed in the same way as the shear rate, that is

$$\begin{aligned}\theta_c(t) &= \frac{1}{2}\int_0^t \dot{\gamma}_c(t)\mathrm{d}t \\ &= \frac{1}{2}\int_0^t \dot{\gamma}(t - t_d/2)\mathrm{d}t \\ &= \frac{1}{4}\ddot{\gamma}(t - t_d/2)^2 \\ &= \theta(t - t_d/2)\end{aligned} \tag{6.15}$$

Accounting for diffusion time t_d, the rotation θ_c at the center of the domain can thus be estimated as

$$\theta_c = \frac{1}{4}\ddot{\gamma}\left(t - \frac{t_d}{2}\right)^2 = \frac{1}{4}\ddot{\gamma}^*\left(t^* - \frac{t_d^*}{2}\right)^2 \tag{6.16}$$

Figure 6.3b compares the numerical solution and the delayed analytical solution for rotation over time. It confirms that a delay in strain by half of the dimensionless diffusion time t_d^*, scaled according to Equation (6.11), closely matches the numerical solution.

As the imposed shear stresses increase, the flow accelerates, leading to constantly increasing

inertia in the flow. It is quantified at the scale of primary particles by

$$\mathrm{Re_p} = \frac{4\tau R_p^2}{\rho\nu^2} \tag{6.17}$$

In this particle Reynolds number, the shear stress τ is the only parameter which varies over time in the problem considered in this study. Since τ also determines the shear rate in the system, $\mathrm{Re_p}$ can also be expressed as

$$\mathrm{Re_p} \equiv \dot{\gamma}^* \tag{6.18}$$

Inertial effects in the flow at aggregate scale are characterized by a different Reynolds number, $\mathrm{Re_{agg}}$, defined as

$$\mathrm{Re_{agg}} = \frac{4\dot{\tau}R_g^2}{\rho\nu^2} \tag{6.19}$$

Since aggregates restructure over time when exposed to shear, their radius of gyration R_g evolves over time. Therefore, $\mathrm{Re_{agg}}$ is not constant throughout a simulation run. Nonetheless, it can be obtained from other reported quantities as

$$\mathrm{Re_{agg}} = \mathrm{Re_p}\frac{R_g^2}{R_p^2} \equiv \dot{\gamma}^* R_g^{*2} \tag{6.20}$$

6.3 Results and discussion

Each simulation begins with both the aggregate and the fluid at rest. With time steps of the simulation, the shear stresses increase as per the applied flow acceleration $\ddot{\gamma}$ at the planes of imposed stresses. As momentum diffuses from the boundary planes and reaches the aggregate, hydrodynamic forces begin to act on the primary particles. As a consequence, the aggregate starts to rotate and restructure. Since the imposed shear stresses linearly increase with time, the hydrodynamic stresses around the aggregate also become stronger over time. Eventually, the hydrodynamic forces acting on the aggregate overcome the cohesive forces between its primary particles, resulting in its breakage.

6.3.1 Aggregate size at breakage

As the aggregates break, their size at breakage are analyzed for the effect of flow acceleration. In general, it is observed that flow acceleration does not seem to affect aggregate size at breakage.

This can be seen in Figure 6.5, where the size of aggregates at breakage $R_g^*(t_b^*)$ is plotted for the three considered flow accelerations $\ddot{\gamma}^*$. This is consistent with former observations in Chapter 5 that aggregate structure (either stable or at breakage) does not depend on Reynolds number, and hence neither on flow acceleration nor on flow inertia. It also suggests that although aggregates do restructure over rotation cycles in the flow, as illustrated by evolution of individual aggregates presented in the Supporting Material as Figure 6.4, it does not affect their size at breakage $R_g^*(t_b^*)$. Furthermore, the average size at breakage $\langle R_g^*(t_b^*)\rangle$ is close to their initial radius of gyration $R_g^*(t=0)$, implying that the aggregates did not densify. Therefore, conditioning seems of little importance in determining the aggregate size at breakage. The lack of effect of conditioning on aggregate breakage may be a consequence of the fact that the initial radius of gyration of the investigated aggregates is already close to their breakage size. In contrast, Seto et al. [14] started with much less dense aggregates exposed to a very low effective flow acceleration, and observed significant aggregate reinforcement at low shear rates. The reported reinforcement by Seto et al. [14], along with lack of it in this study suggest that although aggregate restructuring under shear produces reinforced and denser aggregates (increase D_f), this mechanism stops once the aggregates reach a fractal dimension D_f of around 2.3. This is consistent with the analysis of Conchuir et al. [46], which indicated that a critical value of $D_f = 2.4$ exists for shear flow. Similarly, Harshe and Lattuada [47] also reported final $D_f = 2.4$ for aggregates with initial $D_f < 2.1$ through numerical simulations. Lastly, it is worth pointing out that the aggregates in this study are algorithmically created and may not mimic exactly the aggregates produced by the physical process that drive aggregation in shear flows.

Figure 6.4 shows the size evolution of each of the 20 aggregates under the considered flow accelerations with rotation in the flow while accounting for diffusion time. The trends terminate at their respective breakage events. It is evident from the figure that initial restructuring for all flow accelerations is quite similar, and diverges later.

Chapter 5 highlighted a strong correlation between breakage probability and Reynolds number, even for relatively low Reynolds numbers. Therefore, even though aggregate conditioning seems negligible here, breakage is still likely to depend on the flow acceleration. Therefore, the evolution of aggregate structure over time should reveal such effects.

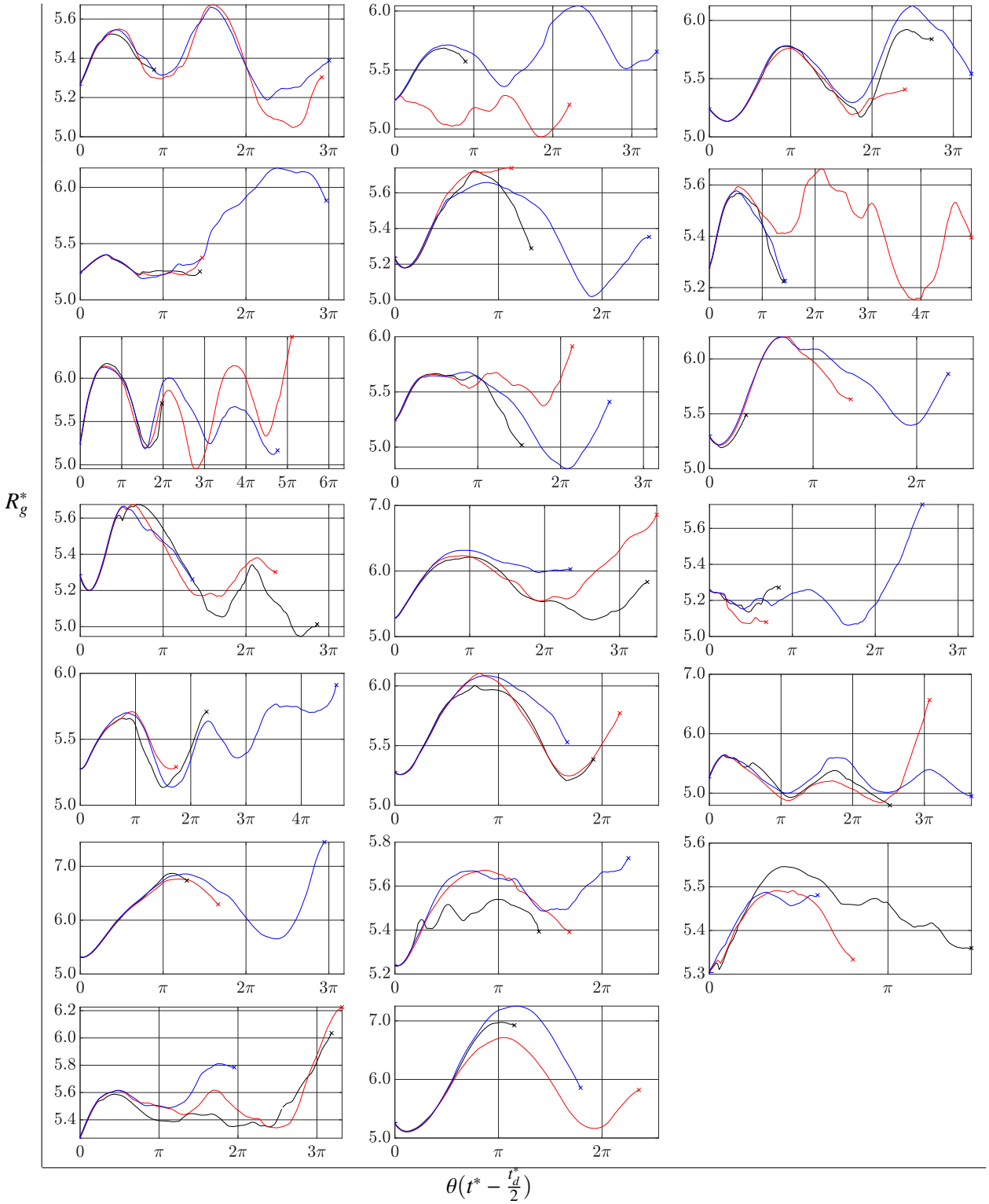

Figure 6.4: Evolution of each aggregate under different flow accelerations: (—) = 4.45×10^{-6}, (—) = 8.90×10^{-6}, (—) = 13.35×10^{-6}.

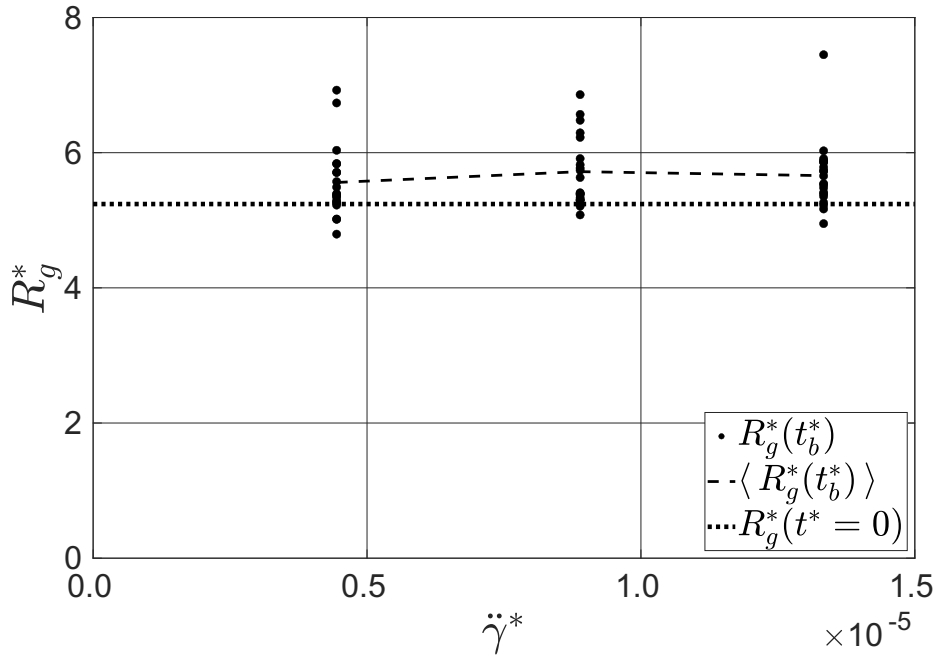

Figure 6.5: Normalized radius of gyration R_g^* at breakage for different flow accelerations $\ddot{\gamma}^*$. Average for each flow acceleration $\ddot{\gamma}^*$ are represented by $\langle R_g^*(t_b^*) \rangle$, and $R_g^*(t = 0)$ shows the initial aggregate size.

6.3.2 Effect of flow acceleration on aggregate evolution over time

Since hydrodynamic stresses drive aggregate evolution, higher flow acceleration consequently leads to more rapid aggregate evolution. This can be seen in Figure 6.6, where evolution of all aggregates for different flow acceleration values with respect to time is presented. The time at which breakage occurs for each aggregate is noted, and is scaled according to Equation (6.11) to give breakage time t_b^*.

Figure 6.6a shows that aggregates under higher flow acceleration start to show structural changes sooner and they occur more quickly. Rapid evolution of aggregates also leads to earlier breakage. This can be seen in Figure 6.6b, where the breakage time t_b^* decreases with increasing values of flow acceleration. This is a direct consequence of flow acceleration: the hydrodynamic stresses on the aggregate required to break the aggregate are attained faster due to higher flow acceleration.

In Figure 6.6b, breakage times from Figure 6.6a are presented against the flow acceleration values. The figure also includes the corrected breakage time which accounts for momentum diffusion. It clearly shows that the problem is not ruled by momentum diffusion as the two curves are quite close to each other, implying that diffusion time is short compared to aggregate breakage time. In

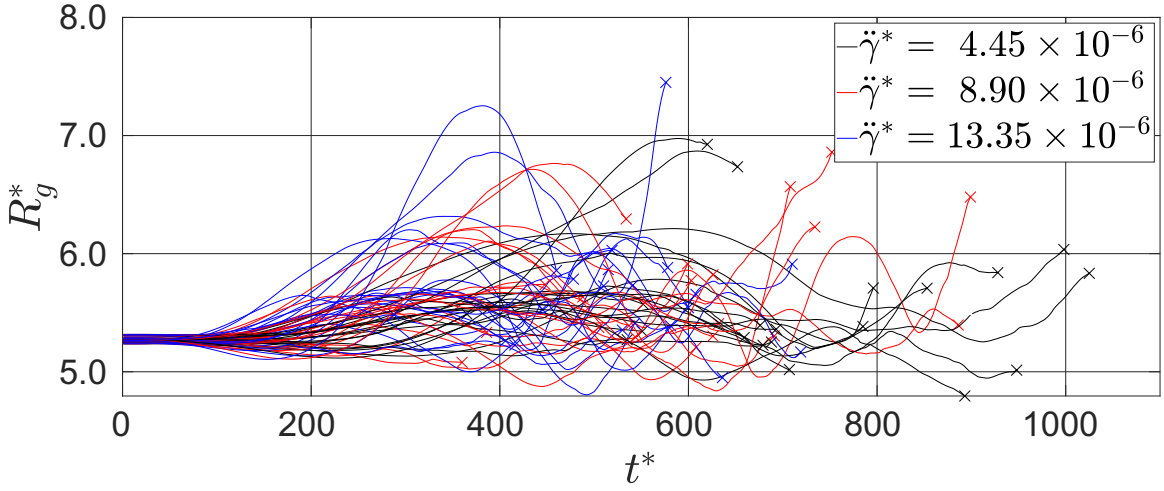

(a)

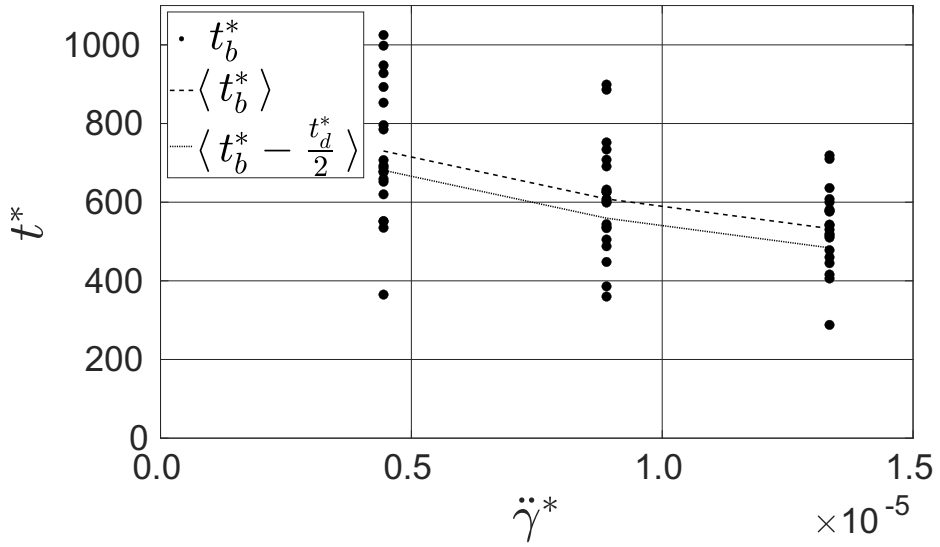

(b)

Figure 6.6: Evolution of all 20 aggregates with time. (a) Aggregate size R_g^* for each value of $\ddot{\gamma}$ considered here. Breakage events are marked by '×'. (b) Breakage time t_b^* with respect to flow acceleration $\ddot{\gamma}^*$. The average breakage time $\langle t_b^* \rangle$, and average breakage time considering diffusion time $\langle (t_b^* - \frac{t_d}{2}) \rangle$ are also shown.

other words, at a given time the shear rate at the boundaries is not significantly different from the shear rate perceived by an aggregate since its diffusion is fast compared to characteristic times scales of aggregate evolution. Consequently, the structural evolution and breakage of aggregates under shear stress cannot depend on diffusion time and thus originate from phenomena other than momentum diffusion.

While it is clear that breakage is not dependent on diffusion time, it is difficult to deconvolute the effects of Reynolds number and flow acceleration on aggregate structure from analyzing aggregate evolution over time. As illustrated in Figure 6.6a, since aggregates rotate at different speeds under different shear conditions, their structures at a given time are not comparable from one flow acceleration to another. Therefore, structural evolution in Figure 6.6a for each flow acceleration value are, in fact, scaling differently with time. To overcome this limitation and to observe the effect of the Reynolds number, aggregate evolution is studied as a function of aggregate orientation in the flow, which can be derived from flow rotation.

6.3.3 Aggregate evolution with rotation angle

Aggregates restructure during rotation, as they undergo cycles of compression and traction along the principal axes of the strain rate tensor [41, 45]. Several studies normalize the time with the inverse of shear rate to obtain non-dimensional time as $\dot{\gamma}t$ [10, 41, 48–53]. Physically, $\dot{\gamma}t$ is equivalent to the strain of the flow and consequently relates to the its rotation. Since aggregates rotate, the strain does not accumulate. Therefore, the angle of rotation of the flow, evaluated from the rotation part of shear flow, has instead been used as an indicator of aggregate's orientation in the flow. It is worth noting that rotation and strain are equivalent since there is only a factor $1/2$ between the two quantities, as expressed in Equation (6.14).

Restructuring during rotation

To track aggregate evolution as a function of rotation angle, the abscissa of Figure 6.7a is scaled with the rotation θ_c estimated by Equation (6.16), which accounts for the delay in rotation at the domain center due to diffusion time. Figure 6.7a shows groups (bands of red, black and blue) of very similar evolution in size R_g^* in the initial phase of restructuring (up to $\theta(t^* - t_d^*/2) = 5$), irrespective of the imposed flow acceleration. Each group of these trends belongs to the same

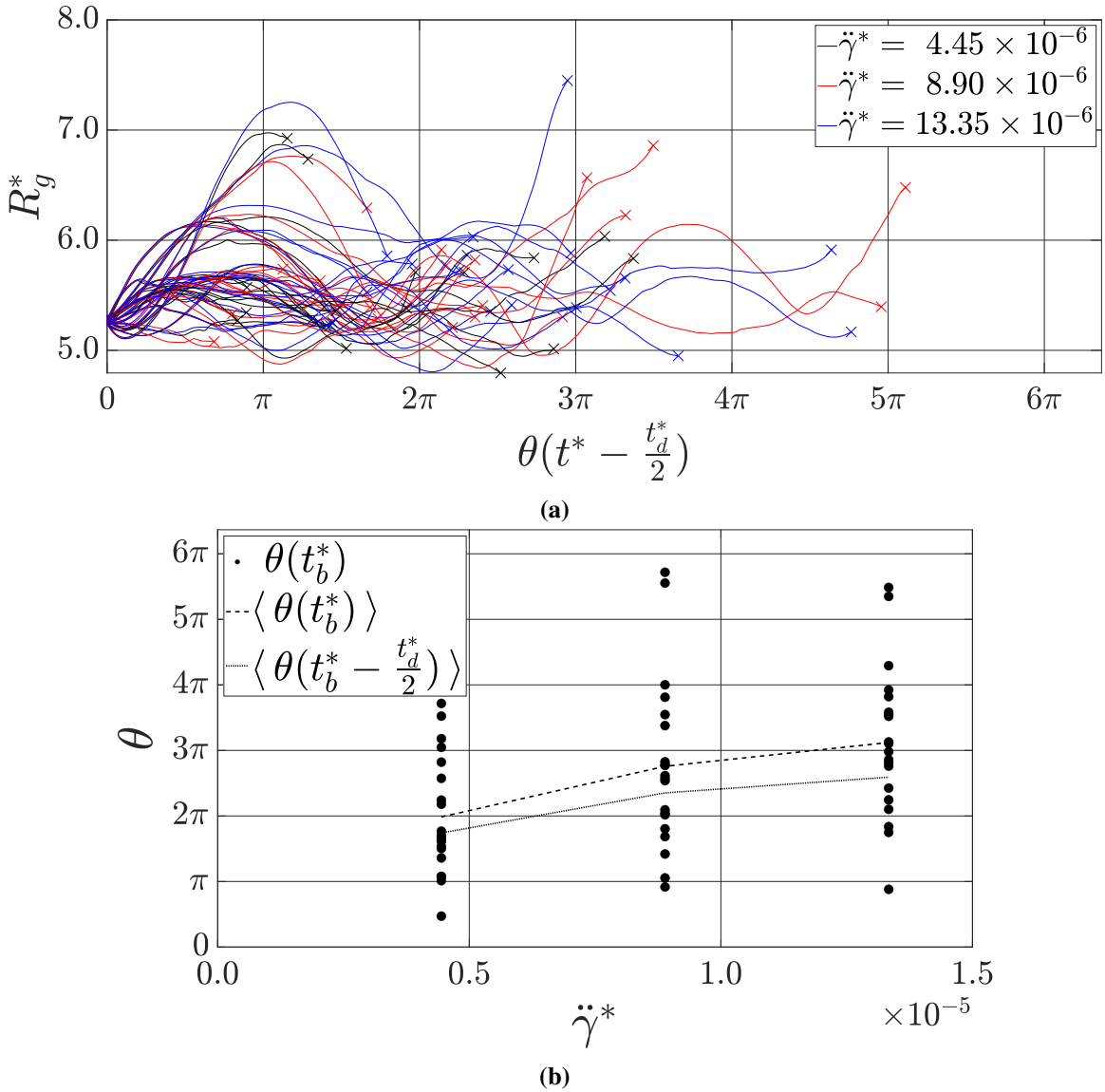

Figure 6.7: Evolution of all 20 aggregates tracked with flow rotation θ for each value of flow acceleration $\ddot{\gamma}^*$ considered here. (a) Aggregate size R_g^* evolution over flow rotation θ estimated at the center of the domain for each aggregate. Breakage events are marked by '×'. (b) Rotation θ at breakage with respect to flow acceleration $\ddot{\gamma}^*$ for each aggregate. The average rotation $\langle\theta(t_b^*)\rangle$ and rotation estimated at center $\langle\theta(t_b^* - \frac{t_d}{2})\rangle$ are also shown.

aggregate. Figure 6.4 in the Supporting Material shows this more clearly with the evolution of individual aggregates shown. From the Figures 6.7a and 6.4, it can be inferred that as the aggregate orientation changes, the restructuring of any individual aggregate is very similar irrespective of the flow acceleration. This can be explained as an effect of an aggregate's branches, which are prone to change their alignment as the aggregate starts to rotate. At any instance of rotation under flow accelerations $\ddot{\gamma}_a$ and $\ddot{\gamma}_b$, respective shear rates $\dot{\gamma}_a$ and $\dot{\gamma}_b$ can be related as

$$\frac{1}{4}\ddot{\gamma}_a t_a^2 = \frac{1}{4}\ddot{\gamma}_b t_b^2 \tag{6.21}$$

$$\Rightarrow \frac{\ddot{\gamma}_a}{\ddot{\gamma}_b} = \left(\frac{t_b}{t_a}\right)^2 \tag{6.22}$$

Therefore, for the three flow accelerations considered in this study, a relation between the corresponding shear rates at any particular rotation angle θ can be written as

$$\dot{\gamma}_1 = \frac{\dot{\gamma}_2}{\sqrt{2}} = \frac{\dot{\gamma}_3}{\sqrt{3}} \tag{6.23}$$

Therefore, at the beginning of its restructuring, the response of any given aggregate is identical while shear rates vary by a factor $\sqrt{3}$ and despite significant restructuring happening, as illustrated by the variations of the radius of gyration from 5 to 7.5., implying that the response of aggregate branches is not very sensitive to the magnitude of the hydrodynamic forces under accelerated flow conditions. One possible explanation for this lack of sensitivity could be due to restructuring in torsional direction (around the axis joining centers of two particles) as the bonds between primary particles in the aggregates do not transmit torques, only normal and tangential forces. Therefore, the early restructuring is dominated by bond resistance to tearing, sliding and bending but free torsional motion between primary particles, which makes it independent on the hydrodynamic forces acting on particles. To verify this, simulations with resistance to torsion between primary particles would be required [26]. However, there is no commonly admitted value for such a resistant torque, and it is expected that most colloidal particles will oppose much less resistance to deformation in torsion than for tangential and normal forces. Consequently, assuming no torsion resistance is a sound first assumption to model generic colloidal aggregates, and the observations about aggregate restructuring discussed here probably apply to many real-world colloidal aggregates. After some

time, the increasing hydrodynamic forces start to compete with the bond strength and the aggregate starts restructuring differently as per their respective flow conditions. However, when this happens, the Reynolds number can be finite, and some inertial effects in the flow can play a role.

Breakage with aggregate rotation

When inertia in the system is low, that is, under low Reynolds and Stokes number conditions, the response of particles to applied forces is instantaneous. In case of accelerated flows, higher flow acceleration yields higher shear stresses for the same rotation angle θ. Therefore, in the absence of inertial effects, aggregates are expected to break after fewer rotations when flow acceleration is increased. Breakage events are reported as rotation angles at breakage $\theta(t_b^*)$ in Figure 6.7b. This figure contradicts the expected behaviour in the absence of inertial effects as it shows increasing flow acceleration increases the rotation angle at breakage. That is to say, a higher flow acceleration leads to 'longer' aggregate survival times in terms of rotation. This also implies that higher flow acceleration results in an aggregate that is more resistant to traction and compression cycles and to stronger hydrodynamic shear stresses, as expressed in Equation (6.23). This clearly shows a strong effect of finite Reynolds hydrodynamics that make aggregates less likely to break for a given shear stress as flow acceleration increases. This can be observed in Figure 6.8, where shear rate at breakage increases with flow acceleration.

The lack of impact of flow acceleration on aggregate size at breakage, along with the fact that initial aggregate evolution trends tend to be very similar, show that the aggregates did not reinforce. This also confirms that this behaviour cannot be explained by aggregates getting stronger. Therefore, it can be inferred that for a given rotation angle, aggregates undergo lower hydrodynamic forces for higher flow acceleration despite higher imposed shear stresses on domain boundaries. Additionally, the close resemblance of the plots with and without correction accounting for diffusion time confirms that this behaviour cannot be explained by limited diffusion of momentum towards the aggregate either. In the end, the only remaining explanation must be finite Reynolds effects in the flow patterns at the aggregate scale.

Since $\dot{\gamma}^*$ is equivalent to $\mathrm{Re_p}$ as shown through Equation (6.17), Figure 6.8 also represents the particle Reynolds number at breakage. Although $\mathrm{Re_p} \ll 1$ for any $\ddot{\gamma}^*$, Reynolds number at the aggregate scale converted through Equation (6.20) is finite and ranges from 0.5 to 4.2 (refer to

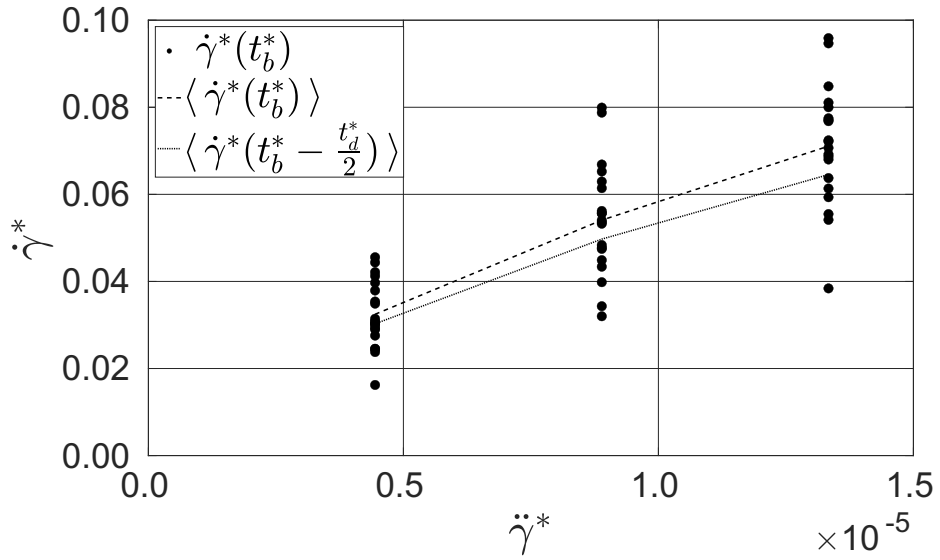

Figure 6.8: Shear rate $\dot{\gamma}^*$ at breakage time t_b^* for each aggregate for different flow accelerations $\ddot{\gamma}^*$, along with average shear rate at breakage $\langle \dot{\gamma}^*(t_b^*) \rangle$ and its estimation at aggregate center $\langle \dot{\gamma}^*(t_b^* - \frac{t_d^*}{2}) \rangle$.

Figure 6.9 of the Supporting Material). As the flow accelerates around the aggregates, the inertia of the fluid around the aggregates also increases. As flow inertia increases, flow recirculations around the aggregate develop as demonstrated by Haddadi and Morris [39]. Under accelerated flows, these recirculations will take some time to respond to the imposed stresses when the Reynolds number is increased. The higher the inertia, the slower they develop, which effectively delays the perceived flow patterns to which the aggregates are exposed and damps the traction and compression stresses acting on them. To summarize, under the conditions investigated here, it is not the shear history of the aggregates, but the history of the flow that determines the evolution of aggregates.

6.3.4 Discussion

The shear rate experienced by aggregates in turbulent flows fluctuates over time. This fluctuation can be spatial due to aggregates travelling through zones of varying energy dissipation (for example, in turbulent boundary layer flows), or temporal with sudden bursts of energy dissipation due to short-lived vortex structures [54, 55]. In either case, there is a general understanding that aggregates break instantaneously when the critical shear rate $\dot{\gamma}_{\text{crit}}$ (or, critical energy dissipation) is reached around them [15–18]. Consequently, the breakage time can be deduced as the time taken for an aggregate to undergo a shear rate of $\dot{\gamma}_{\text{crit}}$. However, in the frame of reference of an aggregate at sub-Kolmogorov length scales, the turbulent fluctuations considered in the aforementioned studies

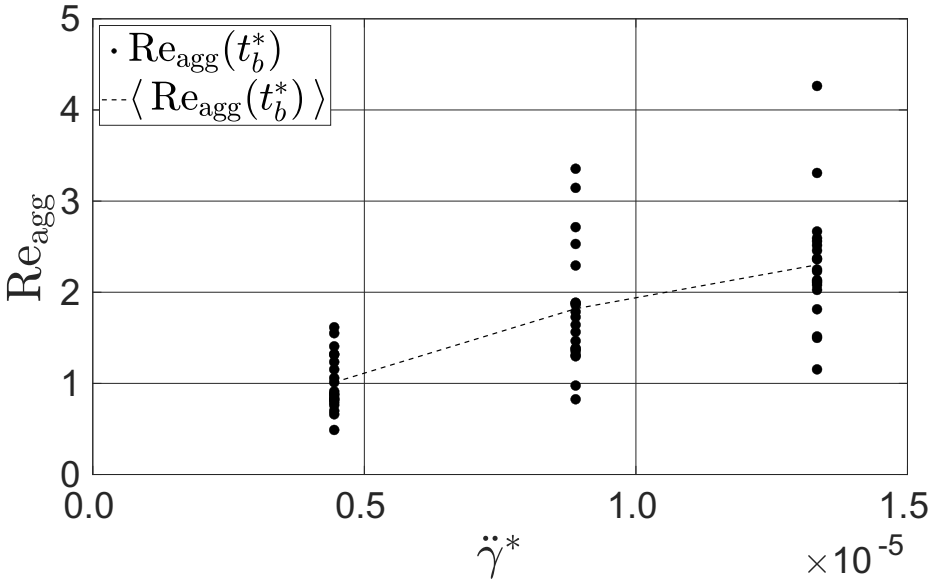

Figure 6.9: Reynolds number at aggregate scale $\mathrm{Re}_{\mathrm{agg}}(t_b^*)$ calculated from shear rate at breakage $\dot{\gamma}^*(t_b^*)$ and as $\mathrm{Re}_{\mathrm{agg}}(t_b^*) = \dot{\gamma}^*(t_b^*)R_g(t_b^*)$.

are effectively equivalent to accelerated flows. In turbulent flows, the shear rate at the smallest scale $\dot{\gamma}_K$ can be estimated from Kolmogorov's theory. The corresponding time scale τ_K for which the shear rates at smallest scales last is thus

$$\tau_K = \frac{1}{\dot{\gamma}_K} \tag{6.24}$$

We can thus estimate the flow acceleration at sub-Kolmogorov length scale $\ddot{\gamma}_K$ from the shear rate and time scales as

$$\ddot{\gamma}_K = \frac{\dot{\gamma}_K}{\tau_K} = \dot{\gamma}_K^2 \tag{6.25}$$

For comparison with values presented in Table 6.1, estimates of $\ddot{\gamma}_K$ from De Bona et al. [19] and Soos et al. [30] as $\ddot{\gamma} = \langle\epsilon\rangle/\nu$ respectively give 1.14×10^5 s^{-2} and 2.2×10^6 s^{-2}. In Baldi et al. [20], the maximum reaches 313×10^6 s^{-2} and the average, although not reported in the paper, seems to be of the order of 50×10^6 s^{-2}.

Following the same scaling parameters as defined in Equation (6.10), the dimensionless form of the flow acceleration reads

$$\ddot{\gamma}^* = \dot{\gamma}_K^2 t_c^2 = \mathrm{Re_p}^2 \tag{6.26}$$

from which aggregate Reynolds number follows as

$$\mathrm{Re}_{\mathrm{agg}} = \mathrm{Re}_{\mathrm{p}}\, {R_g^*}^2 = {\ddot{\gamma}^*}^{1/2}\, {R_g^*}^2 \tag{6.27}$$

The equivalent aggregate Reynolds number presented in this research would thus be of the order of magnitude of $\mathrm{Re}_{\mathrm{agg}} \sim \left(10^{-5}\right)^{1/2} 5.5^2 \approx 0.1$ which could be seen as low enough to neglect flow inertia at their scale. However, as shown in Figure 6.8, inertial effects, which slow down the development of the flow around the aggregates may play a very significant role, even for such low Reynolds numbers, effectively increasing the ability of such aggregates to resist turbulence induced stresses. Indeed, Figure 6.8 shows that in the specified range for aggregate Reynolds number, the critical shear required to break aggregates increases with the flow acceleration and thus depends strongly on the Reynolds number.

Consequently, the breakage rates predicted with the assumption of instantaneous breakage when reaching critical shear rates in turbulent flows [15, 17, 18, 56] may miss a significant effect even for $\mathrm{Re}_{\mathrm{agg}} < 0.1$. Additionally, determination of the exact time of breakage must take into account not only the complex structure of the aggregates [19], but also the flow history. Now the exact impact of such effects can unfortunately not be inferred from Figure 6.8 since the aggregates represented in that figure would not break in turbulent flows as described through Equation (6.24). Indeed, to limit the dependence on initial aggregate properties, the aggregates presented here break after a few rotations in the shear flow, while the scaling presented in Equation (6.24) assumes that eddies do not last longer than a full revolution. Effectively, the breakage Reynolds number corresponding to the critical shear rate, that is the vertical axis of Figure 6.8, is closer to 1 and above, which could only be reached by aggregates of the same size or larger than the Kolmogorov length scale. To reproduce the breakage conditions modeled by [19], one would need to study weaker aggregates that break faster. This is not an easy study to conduct as the results would depend more strongly on initial conditions and diffusion time would play a more significant role.

Overall, although the aggregates studied were too strong to break during the peaks of turbulent fluctuations, the analysis presented above shows the importance of flow inertia in delaying aggregate breakage at the smallest scales in turbulent flows.

6.4 Conclusions

A numerical investigation of aggregate restructuring and breakage under accelerating flow conditions was conducted. As the aggregates evolved with the flow, their size and breakage events were recorded. No conditioning of aggregates was observed despite significant restructuring for the accelerated flow conditions studied here; that is, all three shear ramps lead to the same aggregate size (and thus same fractal dimension) at breakage. The fact that the aggregate structure at breakage is found to be independent of the flow conditions (for those conditions tested here) can be explained by their initial fractal dimension of 2.3 which is the value towards which aggregates evolve during conditioning in shear flow.

Although aggregate response to the applied shear stresses is slightly delayed due to momentum diffusion, aggregate breakage kinetics are not at all ruled by momentum diffusion. At higher flow accelerations, which result in finite aggregate scale Reynolds number, the aggregates rotate more before breaking, undergoing more cycles of compression and traction. Additionally, the shear rate at breakage is found to increase with increasing flow acceleration. This is attributed to the flow inertia: as shear rate increases, so does the flow inertia around an aggregate, resulting in a transient development of the flow around the aggregate that induces a delay in the stresses perceived by the aggregate. In other words, the history of the flow at aggregate scale is found to play a significant role in aggregate kinetics even for $\mathrm{Re}_{\mathrm{agg}} < 0.1$.

The demonstrated dependence of breakage on the flow inertia in accelerated flows also suggests that the criteria of critical shear rates for aggregate breakage at sub-Kolmogorov in turbulent flows might be insufficient. The delay in flow development due to flow inertia may prevent aggregates from undergoing peak fluctuations in shear stresses. In other words, the assumption of instantaneous breakage when a critical shear rate is reached probably leads to overestimated breakage rates. As a consequence, breakage kernels in population balance equations should also consider the local flow acceleration, even for relatively low aggregate Reynolds numbers.

References

[1] B. Pukánszky and J. Móczó. Morphology and properties of particulate filled polymers. In *Macromolecular Symposia*, volume 214, pages 115–134. Wiley Online Library, 2004. doi:

10.1002/masy.200451009.

[2] B. Bolto and J. Gregory. Organic polyelectrolytes in water treatment. *Water Research*, 41(11): 2301–2324, 2007.

[3] J.-P. Bellot, J.-S. Kroll-Rabotin, M. Gisselbrecht, M. Joishi, A. Saxena, S. Sanders, and A. Jardy. Toward better control of inclusion cleanliness in a gas stirred ladle using multiscale numerical modeling. *Materials*, 11:1179, July 2018. doi:10.3390/ma11071179.

[4] L. Ehrl, M. Soos, and M. Morbidelli. Dependence of aggregate strength, structure, and light scattering properties on primary particle size under turbulent conditions in stirred tank. *Langmuir*, 24(7):3070–3081, April 2008. ISSN 0743-7463. doi:10.1021/la7032302.

[5] A. Zaccone, M. Soos, M. Lattuada, H. Wu, M. U. Bäbler, and M. Morbidelli. Breakup of dense colloidal aggregates under hydrodynamic stresses. *Phys. Rev. E*, 79:061401, Jun 2009. doi:10.1103/PhysRevE.79.061401.

[6] F. Vaezi, R. S. Sanders, and J. H. Masliyah. Flocculation kinetics and aggregate structure of kaolinite mixtures in laminar tube flow. *Journal of Colloid and Interface Science*, 355(1): 96–105, 2011.

[7] D. Saha, M. U. Bäbler, M. Holzner, M. Soos, B. Lüthi, A. Liberzon, and W. Kinzelbach. Breakup of finite-size colloidal aggregates in turbulent flow investigated by three-dimensional (3d) particle tracking velocimetry. *Langmuir*, 32(1):55–65, 2016. doi:10.1021/acs.langmuir.5b03804.

[8] R. C. Sonntag and W. B. Russel. Structure and breakup of flocs subjected to fluid stresses: I. Shear experiments. *Journal of Colloid and Interface Science*, 113(2):399–413, 1986.

[9] M. Kobayashi, Y. Adachi, and S. Ooi. Breakup of fractal flocs in a turbulent flow. *Langmuir*, 15(13):4351–4356, 1999. doi:10.1021/la980763o.

[10] M. L. Eggersdorfer, D. Kadau, H. J. Herrmann, and S. E. Pratsinis. Fragmentation and restructuring of soft-agglomerates under shear. *Journal of Colloid and Interface Science*, 342 (2):261–268, 2010. ISSN 00219797. doi:10.1016/j.jcis.2009.10.062.

[11] Y. M. Harshe, M. Lattuada, and M. Soos. Experimental and modeling study of breakage and restructuring of open and dense colloidal aggregates. *Langmuir*, 27(10):5739–5752, May 2011. doi:10.1021/la1046589.

[12] M. Kroupa, M. Vonka, M. Soos, and J. Kosek. Size and structure of clusters formed by shear induced coagulation: Modeling by discrete element method. *Langmuir*, 31(28):7727–7737, July 2015. ISSN 0743-7463. doi:10.1021/acs.langmuir.5b01046.

[13] Y. M. Harshe and M. Lattuada. Breakage rate of colloidal aggregates in shear flow through Stokesian dynamics. *Langmuir*, 28(1):283–292, January 2012. ISSN 0743-7463. doi:10.1021/la2038476.

[14] R. Seto, R. Botet, G. K. Auernhammer, and H. Briesen. Restructuring of colloidal aggregates in shear flow. *The European Physical Journal E*, 35(12):128, December 2012. ISSN 1292-8941. doi:10.1140/epje/i2012-12128-4.

[15] K. A. Kusters. *The influence of turbulence on aggregation of small particles in agitated vessels*. PhD Thesis, Technische Universiteit Eindhoven, 1991.

[16] M. U. Bäbler, M. Morbidelli, and J. Baldyga. Modelling the breakup of solid aggregates in turbulent flows. *Journal of Fluid Mechanics*, 612:261–289, 2008. doi:10.1017/S002211200800298X.

[17] M. U. Bäbler, L. Biferale, and A. S. Lanotte. Breakup of small aggregates driven by turbulent hydrodynamical stress. *Phys. Rev. E*, 85:025301, Feb 2012. doi:10.1103/PhysRevE.85.025301.

[18] M. U. Bäbler, L. Biferale, L. Brandt, U. Feudel, K. Guseva, A. S. Lanotte, C. Marchioli, F. Picano, G. Sardina, A. Soldati, and F. Toschi. Numerical simulations of aggregate breakup in bounded and unbounded turbulent flows. *Journal of Fluid Mechanics*, 766:104–128, 2015. doi:10.1017/jfm.2015.13.

[19] J. De Bona, A. S. Lanotte, and M. Vanni. Internal stresses and breakup of rigid isostatic aggregates in homogeneous and isotropic turbulence. *Journal of Fluid Mechanics*, 775:365–396, 2014. doi:10.1017/jfm.2014.421.

[20] S. Baldi, A. Ducci, and M. Yianneskis. Determination of dissipation rate in stirred vessels

through direct measurement of fluctuating velocity gradients. *Chemical Engineering & Technology*, 27(3):275–281, 2004. doi:10.1002/ceat.200401979.

[21] J. Gregory. The density of particle aggregates. *Water Science and Technology*, 36(4):1–13, 1997. ISSN 02731223. doi:10.1016/S0273-1223(97)00452-6.

[22] T. Serra and X. Casamitjana. Structure of the aggregates during the process of aggregation and breakup under a shear flow. *Journal of Colloid and Interface Science*, 206(2):505–511, 1998. doi:10.1006/jcis.1998.5714.

[23] P. Jarvis, B. Jefferson, and S. A. Parsons. Breakage, regrowth, and fractal nature of natural organic matter flocs. *Environmental science & technology*, 39(7):2307–2314, 2005. doi:10.1021/es048854x.

[24] A. S. Moussa, M. Soos, J. Sefcik, and M. Morbidelli. Effect of solid volume fraction on aggregation and breakage in colloidal suspensions in batch and continuous stirred tanks. *Langmuir*, 23(4):1664–1673, 2007. doi:10.1021/la062138m.

[25] L. Guerin, C. Frances, A. Liné, and C. Coufort-Saudejaud. Fractal dimensions and morphological characteristics of aggregates formed in different physico-chemical and mechanical flocculation environments. *Colloids and Surfaces A: Physicochemical and Engineering Aspects*, 560:213–222, 2019. doi:10.1016/j.colsurfa.2018.10.017.

[26] V. Becker, E. Schlauch, M. Behr, and H. Briesen. Restructuring of colloidal aggregates in shear flows and limitations of the free-draining approximation. *Journal of Colloid and Interface Science*, 339(2):362–372, 2009. doi:10.1016/j.jcis.2009.07.022.

[27] H. C. Hamaker. The London-van der Waals attraction between spherical particles. *Physica*, 4 (10):1058–1072, 1937. ISSN 00318914. doi:10.1016/S0031-8914(37)80203-7.

[28] D. L. Feke, N. D. Prabhu, J. A. J. Mann, and J. A. L. Mann. A formulation of the short-range repulsion between spherical colloidal particles. *The Journal of Physical Chemistry*, 88(23): 5735–5739, November 1984. ISSN 0022-3654. doi:10.1021/j150667a055.

[29] V. Becker and H. Briesen. Tangential-force model for interactions between bonded colloidal

particles. *Physical Review E*, 78(6):061404, December 2008. doi:10.1103/PhysRevE.78.061404.

[30] M. Soos, A. S. Moussa, L. Ehrl, J. Sefcik, H. Wu, and M. Morbidelli. Effect of shear rate on aggregate size and morphology investigated under turbulent conditions in stirred tank. *Journal of Colloid and Interface Science*, 319(2):577–589, 2008. doi:10.1016/j.jcis.2007.12.005.

[31] C. S. Hodges, J. A. S. Cleaver, M. Ghadiri, R. Jones, and H. M. Pollock. Forces between polystyrene particles in water using the AFM: Pull-off force vs particle size. *Langmuir*, 18(15):5741–5748, 2002. doi:10.1021/la025604q.

[32] M. Kobayashi. Breakup and strength of polystyrene latex flocs subjected to a converging flow. *Colloids and Surfaces A: Physicochemical and Engineering Aspects*, 235(1):73–78, 2004. ISSN 0927-7757. doi:10.1016/j.colsurfa.2004.01.008.

[33] M. Kobayashi. Strength of natural soil flocs. *Water Research*, 39(14):3273–3278, 2005. ISSN 0043-1354. doi:10.1016/j.watres.2005.05.037.

[34] C. S. Hodges, L. Looi, J. A. S. Cleaver, and M. Ghadiri. Use of the JKR model for calculating adhesion between rough surfaces. *Langmuir*, 20(22):9571–9576, 2004. doi:10.1021/la035790f.

[35] J. G. M. Eggels and J. A. Somers. Numerical simulation of free convective flow using the lattice-Boltzmann scheme. *International Journal of Heat and Fluid Flow*, 16(5):357–364, 1995. ISSN 0142-727X. doi:10.1016/0142-727X(95)00052-R.

[36] X. D. Niu, C. Shu, Y. T. Chew, and Y. Peng. A momentum exchange-based immersed boundary-lattice Boltzmann method for simulating incompressible viscous flows. *Physics Letters A*, 354(3):173–182, 2006. doi:10.1016/j.physleta.2006.01.060.

[37] P. A. Cundall and O. D. Strack. A discrete numerical model for granular assemblies. *Geotechnique*, 29(1):47–65, 1979.

[38] N.-Q. Nguyen and A. Ladd. Lubrication corrections for lattice-Boltzmann simulations of particle suspensions. *Physical Review E*, 66(4):046708, 2002. doi:10.1103/PhysRevE.66.046708.

[39] H. Haddadi and J. F. Morris. Topology of pair-sphere trajectories in finite inertia suspension shear flow and its effects on microstructure and rheology. *Physics of Fluids*, 27(4):043302, 2015. doi:10.1063/1.4917030.

[40] S. Blaser. Flocs in shear and strain flows. *Journal of Colloid and Interface Science*, 225(2): 273–284, 2000.

[41] K. Horii, R. Yamada, and S. Harada. Strength deterioration of nonfractal particle aggregates in simple shear flow. *Langmuir*, 31(29):7909–7918, 2015.

[42] Q. Zou and X. He. On pressure and velocity boundary conditions for the lattice Boltzmann BGK model. *Physics of Fluids*, 9:1591, 1997. doi:10.1063/1.869307.

[43] P. L. Bhatnagar, E. P. Gross, and M. Krook. A model for collision processes in gases. I. Small amplitude processes in charged and neutral one-component systems. *Physical Review*, 94(3): 511–525, 1954. doi:10.1103/PhysRev.94.511.

[44] R. Sungkorn and J. J. Derksen. Simulations of dilute sedimenting suspensions at finite-particle reynolds numbers. *Physics of Fluids*, 24(12):123303, 2012.

[45] M. Vanni. Accurate modelling of flow induced stresses in rigid colloidal aggregates. *Computer Physics Communications*, 192:70–90, July 2015. ISSN 0010-4655. doi:10.1016/j.cpc.2015.02.022.

[46] B. O. Conchuir, Y. M. Harshe, M. Lattuada, and A. Zaccone. Analytical model of fractal aggregate stability and restructuring in shear flows. *Industrial & Engineering Chemistry Research*, 53(22):9109–9119, June 2014. ISSN 0888-5885. doi:10.1021/ie4032605.

[47] Y. M. Harshe and M. Lattuada. Universal breakup of colloidal clusters in simple shear flow. *The Journal of Physical Chemistry B*, 120(29):7244–7252, 2016.

[48] S. Harada, R. Tanaka, H. Nogami, and M. Sawada. Dependence of fragmentation behavior of colloidal aggregates on their fractal structure. *Journal of Colloid and Interface Science*, 301(1): 123–129, 2006.

[49] S. Harada, R. Tanaka, H. Nogami, M. Sawada, and K. Asakura. Structural change in non-fractal particle clusters under fluid stress. *Colloids and Surfaces A: Physicochemical and Engineering Aspects*, 302(1):396–402, 2007.

[50] M. Vanni and A. Gastaldi. Hydrodynamic forces and critical stresses in low-density aggregates under shear flow. *Langmuir*, 27(21):12822–12833, November 2011. ISSN 0743-7463. doi: 10.1021/la2024549.

[51] U. T. Lieu and S. Harada. Stability of restructured non-fractal aggregates in simple shear flow. *Advanced Powder Technology*, 26(3):705–710, 2015.

[52] U. T. Lieu and S. Harada. Restructuring capability of non-fractal aggregate in simple shear flow. *Advanced Powder Technology*, 27(4):1037–1046, July 2016. ISSN 0921-8831. doi: 10.1016/j.apt.2016.03.009.

[53] G. Frungieri and M. Vanni. Shear-induced aggregation of colloidal particles: A comparison between two different approaches to the modelling of colloidal interactions. *The Canadian Journal of Chemical Engineering*, 95(9):1768–1780, September 2017. ISSN 1939-019X. doi:10.1002/cjce.22843.

[54] P. K. Yeung. Lagrangian characteristics of turbulence and scalar transport in direct numerical simulations. *Journal of Fluid Mechanics*, 427:241–274, 2001. doi:10.1017/S0022112000002391.

[55] L. Biferale, G. Boffetta, A. Celani, A. Lanotte, and F. Toschi. Particle trapping in three-dimensional fully developed turbulence. *Physics of Fluids*, 17(2):021701, 2005. doi:10.1063/1.1846771.

[56] C. Marchioli and A. Soldati. Turbulent breakage of ductile aggregates. *Phys. Rev. E*, 91:053003, May 2015. doi:10.1103/PhysRevE.91.053003.

Chapter 7

Conclusion and recommendations

7.1 General summary of findings and conclusions

Aggregate evolution in shear flows has been an area of active research for the last 50 years [1–4]. The research began with simplified description of the systems involved (for example, representation of an aggregate as a porous sphere [5, 6]). Gradually, investigations focused more on the fundamentals of aggregate evolution, such as those involving particle-particle interactions [3, 7–10]. Despite recent advances, certain knowledge gaps regarding particle-particle and hydrodynamic forces were identified in this project. While particle-particle interactions result in formation of “bonds" between particles, the impact of tangential and normal components of these forces on aggregate restructuring and breakage were not understood. Furthermore, the presence of aggregates in the flow affect hydrodynamic forces on each of the constituent particles, and are known to reduce the hydrodynamic forces acting on the particles [9]. However, the mechanics of these hydrodynamic interactions between particles were not well investigated. While recent studies [11–15] have greatly expanded our understanding of aggregate evolution in viscosity dominated flows, the impact of flow inertia on aggregate evolution was largely unknown.

The objective of this thesis is to address these knowledge gaps. Numerical methods (Discrete Element Method, Lattice-Boltzmann method and Immersed Boundary Method) were used to investigate the role of interactions between primary particles on aggregate restructuring and breakage. Three contributions of the particle interactions were considered: the normal and tangential force components of the particle-particle forces that vary with the nature of the bond (colloidal, flocculant,

etc), and the hydrodynamic interactions induced by the disturbance of the flow from each primary particle being perceived by other surrounding particles. Assuming very short-range interactions, only the maximum forces transmissible through particle bonds govern non-hydrodynamic interactions between particles. For a generalized description of short-range particle-particle interactions, inter-particle forces were modeled as a combination of a normal cohesive force and a tangential force. The results show that while the normal forces contribute to breakage strength, they do not have any significant impact on aggregate restructuring. On the other hand, although tangential forces contribute to bond strength to some extent, they also make aggregates more brittle. To quantify the hydrodynamic interactions, the investigation was conducted in two steps. First, the hydrodynamic action on particles was modelled through Stokesian drag and torque that apply to individual particles in a dilute medium and hence do not account for hydrodynamic interactions between particles. A second set of simulations reproduced the same flow conditions, but this time resolving the fully coupled hydrodynamics and particle motion. By comparing the two sets of simulation results, the role of hydrodynamic interactions could be distinguished from other parameters and this comparison showed that long range hydrodynamic interactions were crucial in determining aggregate evolution. The details of this investigation are reported in Chapter 4.

The long range shielding of particles from the shear flow is caused due to the aggregate core's resistance to deformation. This shielding effect plays a significant role in aggregate evolution in viscosity dominated flow. When increasing the Reynolds number, as flow inertia increases, the range of such hydrodynamic interactions tends to shorten. This raised questions regarding aggregate evolution when the flow inertia is not completely negligible. Therefore, an investigation into the effect of finite Reynolds number conditions on aggregate evolution was conducted, in which aggregates were allowed to restructure and break. Flow inertia was found to have two possibly significant effects depending on the cohesive force to drag force ratio. When aggregates are too weak or too brittle, they break right away when the shear stress in the flow reaches them, and consequently their breakage kinetics are governed by viscous momentum diffusion in the flow (which is not instantaneous at finite Reynolds number). To observe the effect of flow inertia alone, simulations were run where cohesive forces were scaled with viscous forces, so that their force ratio was kept constant and only the Reynolds number was varied. These simulations revealed that flow inertia impacts the breakage rate of aggregates, but does not play a significant role in aggregate restructuring. These results are

reported in Chapter 5.

The established effect of flow inertia in finite Reynolds number conditions raised the question of an aggregate's dynamic response in shear flow where inertial effects are non-negligible. In a previous study, Seto et al. [16] had reported that reinforcement (increased density due to restructuring) of a given aggregate occurred under accelerating flows. However, that study was limited to conditions with negligible flow inertia. Since inertial effects were found to greatly impact breakage in Chapter 5, aggregate evolution under different flow accelerations with non-negligible flow inertia was studied. The findings showed that the aggregates did not reinforce into stronger aggregates and the structure at breakage was found to be independent of the flow conditions. Furthermore, aggregate breakage was found to be delayed on increasing the flow acceleration. This delay is caused by the inertia of recirculations at the scale of the aggregates, which require time to grow. This has important consequences on the evolution of aggregates in turbulent flows, even for aggregates smaller than the Kolmogorov length scale. Their breakage rate may be significantly overestimated when the delay induced by flow inertia is not taken into account. More details on this can be found in Chapter 6.

7.2 Applicability of results to general short-range particle-particle interactions

While the results were obtained by using commonly available colloidal force models (i.e., van der Waals forces, Born repulsion and tangential forces imparting a bending moment), it is worth mentioning the general applicability of the results to any short-range particle-particle interactions. Since it is only the maximum values of the normal and tangential forces that determine the "bond" strength between particles, the exact model used to represent these short-range interactions is of little consequence. For example, in the classical DLVO theory, forces are caused by electric double layers and van der Waals interactions. This study will apply to such interactions. Furthermore, the investigation covers several orders of magnitude of the normal and tangential contributions, making the study comprehensive by covering particle-particle interactions where one contribution is more significant compared to the other. Therefore, the results obtained here are applicable to most short-ranged particle-particle interactions, such as those caused by gas bridges between inclusions in molten metal refining, or by polymer bridges in flocculated aggregates in oil sands tailings treatment.

Consequently, while the findings reported here have implications in developing breakage kernels for non-DLVO interactions, there are more direct applications for findings such as the established role of tangential forces in aggregate breakage. For example, the contribution of tangential forces in making aggregates brittle provides fresh perspectives into aggregate breakage observed in experimental studies, regardless of the exact mechanism of the short-range particle-particle interactions. It is possible that the observed breakage is due to aggregates becoming too brittle due to high tangential contributions, and not just because of weak cohesive forces between particles. This finding also has applications in designing polymers for flocculation; polymers that induce high normal forces but do not make the aggregate too brittle will result in aggregates that are more resilient to hydrodynamic forces.

7.3 Impact, novel contributions and key findings

Overall, this is a pioneering study in its ability to capture the fundamental physics at play in aggregate restructuring and breakage. It is among the first to quantify the relative effects of the involved forces (particle-particle and hydrodynamic interactions) on aggregate evolution, especially when flow inertia is negligible. While such conditions are met in many industrial processes, they cannot be fully accounted for using common simulation approaches such as Stokesian Dynamics. Some key findings and their potential impacts are:

- Modeling of inter-particle forces as normal and tangential force maxima allows one to model short-range interactions of any nature, even those for which no widely accepted mathematical expression exists, e.g. polymer bridging forces. The relative contributions of normal and tangential forces show how they individually affect breakage and restructuring. Before this study, it was believed that aggregate strength is directly related to the cohesive forces of the aggregates: the stronger the particle-particle interactions, the stronger the aggregates [17, 18]. The new information provided here, regarding the effects of tangential forces, provides a different perspective of the relationship between aggregate strength and particle-particle interactions. In particular, strong particle-particle interactions may not always result in stronger aggregates.

- Long-range hydrodynamic interactions were identified as the root cause for a reduced breakage

probability when the Reynolds number was low. This was achieved by comparing aggregate evolution with fully resolved hydrodynamics (LBM+DEM+IBM) with simplified hydrodynamics (Stokesian drag). While the fully coupled approach (LBM+DEM+IBM) is significantly more accurate, such fully resolved simulations for viscosity dominated flow regimes are computationally expensive. This limits the investigations to small aggregates, and the Free Draining Approximation (FDA) is still widely used to investigate large aggregates. Stokesian Dynamics (SD) is an intermediate solution that accounts for hydrodynamic interactions at infinitely low Reynolds numbers, which has been extensively used for aggregate simulations, but by definition it cannot capture the impact of the Reynolds number on aggregate behavior. In this study, such effects have been shown to play a non-negligible role, even in conditions where the Reynolds number is low (i.e. $Re_{agg} \sim 0.1$).

- For the range of Reynolds numbers investigated here, the fact that the largest stable aggregate size is insensitive to flow inertia suggests that flow dynamics have little impact on the nature of the breakage; in other words, the breakage mechanism is unchanged (i.e. it does not change from fragmentation to erosion). Therefore, the largest aggregate size at finite Reynolds numbers follows the same power-law relationship with shear stresses as derived under viscosity dominated flows. Consequently, comparing the largest stable size from simulations with breakage kinetics against experimental to validate numerical studies is not suitable as the effect of hydrodynamics is not captured by the largest stable size.

- Presently, most commonly used breakage kernels in Population Balance Models (PBMs) use the instantaneous breakage criterion, such as that obtained by Harshe and Lattuada [13] where flow is already developed around the aggregates, or as defined by Bäbler et al. [19] where breakage occurs as soon as a critical shear stress is observed around the aggregate. In this research, the importance of flow inertia in delaying aggregate breakage, through diffusion time (Chapter 5) and by introducing a lag in development of flow circulations around the aggregate (Chapter 6), was demonstrated. This effect is expected to lead to significant changes to breakage kernels used while solving PBM equations for aggregates. Furthermore, based on the investigations performed at finite Reynolds number from this work, breakage kernels could be expanded to include the effect of increased breakage probabilities due to flow inertia.

- The methodology developed and implemented in this project could potentially be extended to investigate aggregate evolution in more complex systems. For example, in higher Reynolds number conditions, the Stokes number becomes non-negligible, making particle inertia another parameter of interest. Among the degrees of freedom that were not explored here is the effect of a torsional component acting through particle bonds. Although such a study becomes costly since it increases the parametric space to cover, torsional motion between particles has been identified as the main source of deformation of aggregates undergoing low shear stress (see Chapter 6), so adding a resistance to torsion may induce significantly different behaviour from what was observed. While most colloidal particles are not able to transmit large torsional efforts, it remains a parameter of interest in an attempt to describe short-range interactions of any nature, such as solid bridges between agglomerates [20].

7.4 Uncertainties, limitations and challenges

Although aggregate evolution was investigated with particular focus on particle-particle interactions and hydrodynamics, some aspects of the study had to be simplified to focus on the stated objectives. Consequentially, specific decisions were made to focus on certain aspects at the expense of others. Some examples include the following:

1. Since the objectives of this study were to evaluate aggregate evolution in shear, aggregates with well characterized size and density were required. While there are many methods to generate aggregates [21], they mostly require separate studies as aggregation is severely affected by the hydrodynamics in the system [22, 23]. On the other hand, other studies [15] have also used artificial aggregates as generated by Ehrl et al. [24]. Therefore, to save time and to keep the focus on the objectives, aggregates used in this study were generated artificially using an algorithm. Due to their artificial nature, these aggregates may not be quite representative of actual aggregates seen in fluid-particle systems. Nonetheless, the results were extracted after the aggregates had undergone significant restructuring in the flow, suggesting that the aggregates were conditioned by the flow, and the results are relatively insensitive to the method of aggregate generation. The agreement of some of the results with already available literature, such as the effect of normal and tangential forces on restructuring (discussed in Chapter 4) and

scaling of size with hydrodynamic stresses (Figure 5.8), further emboldens this claim.

2. Aggregate density, characterized through its fractal dimension, is one of the most important parameters that determines the aggregate behavior. While aggregates with fractal dimensions ranging from 1.8 to 2.7 may exist in various systems, the study had to be limited to a certain aggregate density to reduce the parametric space, and thus the number of simulations. Therefore, a fractal dimensions of 2.3 was chosen as it is commonly observed in sheared colloidal systems. Due to this limitation, the results may not necessarily apply to other fractal dimensions.

3. Other than size and density, aggregate morphology can be characterized by many other parameters such as coordination number and higher order moments of the distribution of mass. These parameters may shed more light on morphological changes within the aggregate. For example, a radial distribution function might show the regions within an aggregate where changes in structure were high. It must be pointed out that an analysis for such relations was attempted. However, no meaningful conclusions were found, perhaps because the aggregates were not large enough. The aggregates sizes were chosen such that they were large enough to be fractal, and small enough to be studied through simulations. This lead to the compromise of not capturing morphological changes through coordination numbers or radial distribution functions.

4. To extract general trends from the aggregate evolution studies conducted here, a statistically significant number of aggregates needed to be considered. In order to keep the total number of simulations practical, the number of aggregates studied had to be kept reasonably low. The investigations of Chapter 4 showed that 10 aggregates were sufficient to extract general trends from their average behavior, despite the dispersion in their evolution. Furthermore, the investigation in Chapter 6 was initially conducted with 10 aggregates, and when 10 additional aggregates were added, no difference in the original trends emerged. Therefore, the general trends obtained from evolution of 10 aggregates are statistically significant. However, due to the limited number of aggregates studied, reported quantities such as breakage probabilities remain of low precision. Nonetheless, the values reported here fulfill their purpose in establishing the effect of the governing physical phenomenon (for example effect of flow inertia) on aggregate breakage.

7.5 Recommendations for future work

With the accomplishments of this study, i.e. improved understanding of aggregate evolution at finite Reynolds number conditions and establishing the roles of particle-particle interactions, a number of immediate next steps and longer-term activities can be suggested.

7.5.1 Immediate next steps

1. While the flow at sub-Kolmogorov length scale was modeled as an accelerating shear flow in this project, the very next step is to better approximate flow at such length scales. Since there is no ideal way to model flow at sub-Kolmogorov scale, various flow types may be considered. Therefore, aggregate evolution could be studied in accelerating shear flows in multiple directions. Pure straining and torsional shear flows may also be considered.

2. An experimental study to compare the findings such as the effect of diffusion time and flow inertia on breakage rates is necessary. Furthermore, very few experimental studies exist where breakage rates are captured [25, 26]. More studies of this type conducted under various flow conditions will be of great value.

3. One of the findings of this project is the lack of effect of flow inertia on aggregate restructuring, while strongly affecting aggregate breakage. This raises the question of how inertial effects impact the inter-particle stresses of the aggregates. Therefore, a study where evolution of inter-particle stresses are captured, similar to Vanni [14], but at finite Reynolds number conditions, may improve the understanding of why inertial forces do not affect restructuring. Also, such a study will investigate the validity of the statement by Saha et al. [26] that the hydrodynamic stresses do not transfer to an aggregate's core quickly enough.

4. Since aggregate scale Reynolds numbers were found to have an impact on aggregate breakage, aggregation at finite Reynolds number conditions may be of great interest as well. Therefore a study similar to that of Frungieri [22], but at finite Reynolds number conditions, may highlight the role of flow inertia in cluster-cluster aggregation.

5. There is still a knowledge gap in developing a generalized relation between cohesive strength of the aggregate and the inter-particle forces. Therefore, more studies, such as those done in

Chapter 4, but with different aggregate size and densities, must be conducted.

7.5.2 Longer-term activities

1. There is still no good way to quantify the apparent inter-particle forces for particles in the presence of hydrodynamics. This gap can be addressed by a combined experimental and simulation study. Aggregate evolution in shear flow through experiments can be compared to simulation data for various combinations of normal and tangential forces, giving possible values of inter-particle forces. Further, the obtained force values can then be compared to values obtained through Atomic Force Microscopy or with optical tweezers as done by Pantina and Furst [27]. This may also help further refine the aggregate modeling techniques, for example, by including a torsional constraint between particles.

2. With the established importance of flow inertia in breakage kinetics, breakage kernels must be redeveloped to account for the added delay at finite Reynolds numbers. Correlations among breakage rate, aggregate size and hydrodynamic stresses, as given by Harshe and Lattuada [13], could be expanded to include the effect of flow inertia. As shown in this thesis, the breakage rates depend on the cohesive forces of the aggregates, hydrodynamic stresses and diffusion time. In order to be comprehensive, such a study should also include a wider range of fractal dimensions as well as aggregate sizes. A correlation between fractal dimension, breakage rate, aggregate size, Reynolds number and diffusion time may also be established. This information will be useful when estimating breakage kinetics in turbulent flow conditions [19, 28, 29].

3. Models describing an aggregate's strength as a function of cohesive forces between particles [30] do not account for the contribution of tangential forces towards making aggregates brittle. Therefore, better models to describe the aggregate strength as a function of inter-particle forces must be developed using numerical as well as experimental data.

4. Since strong tangential forces have been found to contribute to aggregate breakage, systems can be designed to have low tangential forces in order to make stronger aggregates. Therefore, research could be conducted to develop particle-particle interactions (such as, through polymers) where the tangential component is weak. For example, polymers attach to the surfaces

of the particles through loops, trains and tails (see Figure 1.1a). Longer tails may allow two attached particles a greater degree of freedom to slide tangentially with little resistance.

5. The data reported in this investigation can also be utilized to generate breakage kernels for the range of conditions studied here. These breakage kernels can be used to design a population balance model (PBM) for the conditions studied in this project. Finally, a statistical comparison between experimental data for similar flow conditions (that is, Reynolds number) and populations obtained through PBM can be made, and performance of breakage kernels can be evaluated.

6. Attempts could be made to improve computation time of the simulations in order to run more simulations more rapidly. Each simulation in this study was performed on a single CPU (node) with up to 32 cores. For more rapid simulations, Machine Passing Interface (MPI) could be used to distribute workload of a single simulation among multiple nodes. Also, due to the highly parellelizable nature of LBM, the code “Flua" used for this thesis could potentially be adapted for graphical processing units (GPUs), which are known to be suitable for LBM.

References

[1] S. Hannah, J. Cohen, and G. Robeck. Measurement of floc strength by particle counting. *American Water Works Association*, 59(7):843–858, 1967.

[2] R. C. Sonntag and W. B. Russel. Structure and breakup of flocs subjected to fluid stresses: I. Shear experiments. *Journal of Colloid and Interface Science*, 113(2):399–413, 1986.

[3] D. Chen and M. Doi. Simulation of aggregating colloids in shear flow. II. *The Journal of Chemical Physics*, 91(4):2656–2663, August 1989. doi:10.1063/1.456975.

[4] S. Blaser. Flocs in shear and strain flows. *Journal of Colloid and Interface Science*, 225(2): 273–284, 2000.

[5] P. M. Adler and P. M. Mills. Motion and rupture of a porous sphere in a linear flow field. *Journal of Rheology*, 23(1):25–37, February 1979. doi:10.1122/1.549514.

[6] P. Adler. Streamlines in and around porous particles. *Journal of Colloid and Interface Science*, 81(2):531–535, 1981. doi:10.1016/0021-9797(81)90434-3.

[7] M. Zeidan, B. H. Xu, X. Jia, and R. A. Williams. Simulation of Aggregate Deformation and Breakup in Simple Shear Flows Using a Combined Continuum and Discrete Model. *Chemical Engineering Research and Design*, 85(12):1645–1654, January 2007. ISSN 0263-8762. doi:10.1016/S0263-8762(07)73208-2.

[8] V. Becker and H. Briesen. Tangential-force model for interactions between bonded colloidal particles. *Physical Review E*, 78(6):061404, December 2008. doi:10.1103/PhysRevE.78.061404.

[9] V. Becker, E. Schlauch, M. Behr, and H. Briesen. Restructuring of colloidal aggregates in shear flows and limitations of the free-draining approximation. *Journal of Colloid and Interface Science*, 339(2):362–372, 2009. doi:10.1016/j.jcis.2009.07.022.

[10] M. L. Eggersdorfer, D. Kadau, H. J. Herrmann, and S. E. Pratsinis. Fragmentation and restructuring of soft-agglomerates under shear. *Journal of Colloid and Interface Science*, 342 (2):261–268, 2010. ISSN 00219797. doi:10.1016/j.jcis.2009.10.062.

[11] Y. M. Harshe, M. Lattuada, and M. Soos. Experimental and modeling study of breakage and restructuring of open and dense colloidal aggregates. *Langmuir*, 27(10):5739–5752, May 2011. doi:10.1021/la1046589.

[12] M. Vanni and A. Gastaldi. Hydrodynamic forces and critical stresses in low-density aggregates under shear flow. *Langmuir*, 27(21):12822–12833, November 2011. ISSN 0743-7463. doi:10.1021/la2024549.

[13] Y. M. Harshe and M. Lattuada. Breakage rate of colloidal aggregates in shear flow through Stokesian dynamics. *Langmuir*, 28(1):283–292, January 2012. ISSN 0743-7463. doi:10.1021/la2038476.

[14] M. Vanni. Accurate modelling of flow induced stresses in rigid colloidal aggregates. *Computer Physics Communications*, 192:70–90, July 2015. ISSN 0010-4655. doi:10.1016/j.cpc.2015.02.022.

[15] Y. M. Harshe and M. Lattuada. Universal breakup of colloidal clusters in simple shear flow. *The Journal of Physical Chemistry B*, 120(29):7244–7252, 2016. doi:10.1021/acs.jpcb.6b03220.

[16] R. Seto, R. Botet, G. K. Auernhammer, and H. Briesen. Restructuring of colloidal aggregates in shear flow. *The European Physical Journal E*, 35(12):128, December 2012. ISSN 1292-8941. doi:10.1140/epje/i2012-12128-4.

[17] M. Kobayashi. Breakup and strength of polystyrene latex flocs subjected to a converging flow. *Colloids and Surfaces A: Physicochemical and Engineering Aspects*, 235(1):73–78, 2004. ISSN 0927-7757. doi:10.1016/j.colsurfa.2004.01.008.

[18] M. Soos, A. S. Moussa, L. Ehrl, J. Sefcik, H. Wu, and M. Morbidelli. Effect of shear rate on aggregate size and morphology investigated under turbulent conditions in stirred tank. *Journal of Colloid and Interface Science*, 319(2):577–589, 2008. doi:10.1016/j.jcis.2007.12.005.

[19] M. U. Bäbler, L. Biferale, L. Brandt, U. Feudel, K. Guseva, A. S. Lanotte, C. Marchioli, F. Picano, G. Sardina, A. Soldati, and F. Toschi. Numerical simulations of aggregate breakup in bounded and unbounded turbulent flows. *Journal of Fluid Mechanics*, 766:104–128, 2015. doi:10.1017/jfm.2015.13.

[20] H. Lee and C. Kim. Experimental study on reversible formation of 2d flocs from plate-like particles dispersed in newtonian fluid under torsional flow. *Colloids and Surfaces A: Physicochemical and Engineering Aspects*, 548:70–84, 2018. ISSN 0927-7757. doi:10.1016/j.colsurfa.2018.03.043.

[21] P. Meakin. A historical introduction to computer models for fractal aggregates. *Journal of Sol-Gel Science and Technology*, 15(2):97–117, 1999.

[22] G. Frungieri. *A novel Monte Carlo - Discrete Element Method approach for the micro-mechanics of colloidal suspensions*. PhD thesis, Politecnico di Torino, 2018.

[23] J.-S. Kroll-Rabotin, M. Gisselbrecht, B. Ott, R. May, J. Fröhlich, and J.-P. Bellot. Multiscale simulation of non-metallic inclusion aggregation in a fully resolved bubble swarm in liquid steel. *Metals*, 10(4):517, 2019. doi:10.3390/met10040517.

[24] L. Ehrl, M. Soos, and M. Lattuada. Generation and geometrical analysis of dense clusters with variable fractal dimension. *The Journal of Physical Chemistry B*, 113(31):10587–10599, 2009. doi:10.1021/jp903557m.

[25] D. Saha, M. Soos, B. Lüthi, M. Holzner, A. Liberzon, M. U. Babler, and W. Kinzelbach. Experimental characterization of breakage rate of colloidal aggregates in axisymmetric extensional flow. *Langmuir*, 30(48):14385–14395, 2014.

[26] D. Saha, M. U. Bäbler, M. Holzner, M. Soos, B. Lüthi, A. Liberzon, and W. Kinzelbach. Breakup of finite-size colloidal aggregates in turbulent flow investigated by three-dimensional (3d) particle tracking velocimetry. *Langmuir*, 32(1):55–65, 2016. doi:10.1021/acs.langmuir.5b03804.

[27] J. P. Pantina and E. M. Furst. Colloidal aggregate micromechanics in the presence of divalent ions. *Langmuir*, 22(12):5282–5288, 2006. doi:10.1021/LA0534120.

[28] K. A. Kusters. *The influence of turbulence on aggregation of small particles in agitated vessels*. Phd thesis, Technische Universiteit Eindhoven, 1991.

[29] C. Marchioli and A. Soldati. Turbulent breakage of ductile aggregates. *Phys. Rev. E*, 91:053003, May 2015. doi:10.1103/PhysRevE.91.053003.

[30] M. Kobayashi, Y. Adachi, and S. Ooi. Breakup of fractal flocs in a turbulent flow. *Langmuir*, 15(13):4351–4356, 1999. doi:10.1021/la980763o.

Global references

Abdel-Khalik, S. and Bird, R. B. Estimation of the zero shear rate viscosity for dilute solutions of rigid macromolecules with complex configurations. *Biopolymers: Original Research on Biomolecules*, 14(9):1915–1932, 1975.

Adler, P. M. and Mills, P. M. Motion and rupture of a porous sphere in a linear flow field. *Journal of Rheology*, 23(1):25–37, Feb. 1979. doi:10.1122/1.549514.

Adler, P. Streamlines in and around porous particles. *Journal of Colloid and Interface Science*, 81 (2):531–535, 1981. doi:10.1016/0021-9797(81)90434-3.

Ancheyta, J., Trejo, F., and Rana, M. S. *Asphaltenes: Chemical Transformation during Hydroprocessing of Heavy Oils*. CRC Press, 2009.

Bäbler, M. U., Sefcik, J., Morbidelli, M., and Bałdyga, J. Hydrodynamic interactions and orthokinetic collisions of porous aggregates in the stokes regime. *Physics of fluids*, 18(1):013302, 2006.

Bäbler, M. U., Morbidelli, M., and Baldyga, J. Modelling the breakup of solid aggregates in turbulent flows. *Journal of Fluid Mechanics*, 612:261–289, 2008. doi:10.1017/S002211200800298X.

Babler, M. U., Biferale, L., and Lanotte, A. S. Breakup of small aggregates driven by turbulent hydrodynamical stress. *Physical Review E*, 85(2):025301, 2012.

Bäbler, M. U., Biferale, L., Brandt, L., Feudel, U., Guseva, K., Lanotte, A. S., Marchioli, C., Picano, F., Sardina, G., Soldati, A., and Toschi, F. Numerical simulations of aggregate breakup

in bounded and unbounded turbulent flows. *Journal of Fluid Mechanics*, 766:104–128, 2015. doi:10.1017/jfm.2015.13.

Bagster, D. F. and Tomi, D. The stresses within a sphere in simple flow fields. *Chemical Engineering Science*, 29(8):1773–1783, Aug. 1974. doi:10.1016/0009-2509(74)87036-3.

Baldi, S., Ducci, A., and Yianneskis, M. Determination of dissipation rate in stirred vessels through direct measurement of fluctuating velocity gradients. *Chemical Engineering & Technology*, 27(3): 275–281, 2004. doi:10.1002/ceat.200401979.

Becker, V. and Briesen, H. Tangential-force model for interactions between bonded colloidal particles. *Physical Review E*, 78(6):061404, Dec. 2008. doi:10.1103/PhysRevE.78.061404.

Becker, V., Schlauch, E., Behr, M., and Briesen, H. Restructuring of colloidal aggregates in shear flows and limitations of the free-draining approximation. *Journal of Colloid and Interface Science*, 339(2):362–372, 2009. doi:10.1016/j.jcis.2009.07.022.

Becker, V. and Briesen, H. A master curve for the onset of shear induced restructuring of fractal colloidal aggregates. *Journal of Colloid and Interface Science*, 346(1):32–36, June 2010. ISSN 0021-9797. doi:10.1016/j.jcis.2010.02.015.

Bellot, J.-P., Kroll-Rabotin, J.-S., Gisselbrecht, M., Joishi, M., Saxena, A., Sanders, S., and Jardy, A. Toward better control of inclusion cleanliness in a gas stirred ladle using multiscale numerical modeling. *Materials*, 11:1179, July 2018. doi:10.3390/ma11071179.

Bhatnagar, P. L., Gross, E. P., and Krook, M. A model for collision processes in gases. i. small amplitude processes in charged and neutral one-component systems. *Phys. Rev.*, 94:511–525, May 1954. doi:10.1103/PhysRev.94.511.

Biferale, L., Boffetta, G., Celani, A., Lanotte, A., and Toschi, F. Particle trapping in three-dimensional fully developed turbulence. *Physics of Fluids*, 17(2):021701, 2005. doi:10.1063/1.1846771.

Bird, R. B., Curtiss, C. F., Armstrong, R. C., and Hassager, O. *Dynamics of Polymeric Liquids, Volume 2: Kinetic Theory*. Wiley, 1987.

Blaser, S. Flocs in shear and strain flows. *Journal of Colloid and Interface Science*, 225(2):273–284, 2000a.

Blaser, S. Break-up of flocs in contraction and swirling flows. *Colloids and Surfaces A: Physicochemical and Engineering Aspects*, 166(1):215–223, 2000b. ISSN 0927-7757. doi: 10.1016/S0927-7757(99)00450-1.

Bolto, B. and Gregory, J. Organic polyelectrolytes in water treatment. *Water Research*, 41(11): 2301–2324, 2007.

Bouyer, D., Liné, A., and Do-Quang, Z. Experimental analysis of floc size distribution under different hydrodynamics in a mixing tank. *AIChE Journal*, 50(9):2064–2081, 2004. doi:10.1002/aic.10242.

Brady, J. F. and Bossis, G. Stokesian dynamics. *Annual Review of Fluid Mechanics*, 20(1):111–157, 1988. doi:10.1146/annurev.fluid.20.1.111.

Chapman, S. Vi. on the law of distribution of molecular velocities, and on the theory of viscosity and thermal conduction, in a non-uniform simple monatomic gas. *Philosophical Transactions of the Royal Society of London. Series A, Containing Papers of a Mathematical or Physical Character*, 216(538-548):279–348, 1916.

Chen, D. and Doi, M. Simulation of aggregating colloids in shear flow. II. *The Journal of Chemical Physics*, 91(4):2656–2663, Aug. 1989. doi:10.1063/1.456975.

Chen, W., Feng, Q., Zhang, G., Li, L., and Jin, S. Effect of energy input on flocculation process and flotation performance of fine scheelite using sodium oleate. *Minerals Engineering*, 112:27–35, 2017. ISSN 0892-6875. doi:10.1016/j.mineng.2017.07.002.

Conchúir, B. O. and Zaccone, A. Mechanism of flow-induced biomolecular and colloidal aggregate breakup. *Physical Review E*, 87(3):032310, Mar. 2013. doi:10.1103/PhysRevE.87.032310.

Conchuir, B. O., Harshe, Y. M., Lattuada, M., and Zaccone, A. Analytical model of fractal aggregate stability and restructuring in shear flows. *Industrial & Engineering Chemistry Research*, 53(22): 9109–9119, June 2014. ISSN 0888-5885. doi:10.1021/ie4032605.

Coufort, C., Bouyer, D., and Liné, A. Flocculation related to local hydrodynamics in a Taylor-Couette reactor and in a jar. *Chemical Engineering Science*, 60(8):2179–2192, 2005. ISSN 00092509. doi:10.1016/j.ces.2004.10.038.

Crowley, R. P. Solvent deasphalting, 1978. US Patent No. 4,101,415.

Cundall, P. A. and Strack, O. D. A discrete numerical model for granular assemblies. *Geotechnique*, 29(1):47–65, 1979.

Daoud, I. L. A., Rimbert, N., Jardy, A., Oesterlé, B., Hans, S., and Bellot, J.-P. 3D modeling of the aggregation of oxide inclusions in a liquid steel ladle: Two numerical approaches. *Advanced Engineering Materials*, 13(7):543–549, 2011. ISSN 1527-2648. doi:10.1002/adem.201000355.

De Felice, V., Daoud, I. L. A., Dussoubs, B., Jardy, A., and Bellot, J.-P. Numerical modelling of inclusion behaviour in a gas-stirred ladle. *ISIJ International*, 52(7):1273–1280, 2012.

De Bona, J., Lanotte, A. S., and Vanni, M. Internal stresses and breakup of rigid isostatic aggregates in homogeneous and isotropic turbulence. *Journal of Fluid Mechanics*, 775:365–396, 2014. doi:10.1017/jfm.2014.421.

Demoz, A., Munoz, V., and Mikula, R. Optimizing mft dewatering by controlling polymer mixing. In *Second International Oil Sands Tailings Conference*, pages 107–121, 2010.

Derjaguin, B. V., Churaev, N. V., and Muller, V. M. The Derjaguin-Landau-Verwey-Overbeek (DLVO) theory of stability of lyophobic colloids. In *Surface Forces*, pages 293–310. Springer US, Boston, MA, 1987. ISBN 978-1-4757-6639-4.

d'Humieres, D. Multiple–relaxation–time lattice boltzmann models in three dimensions. *Philosophical Transactions of the Royal Society of London. Series A: Mathematical, Physical and Engineering Sciences*, 360(1792):437–451, 2002.

Dominik, C. and Nübold, H. Magnetic aggregation: dynamics and numerical modeling. *Icarus*, 157 (1):173–186, may 2002. doi:10.1006/icar.2002.6813.

Eggels, J. G. M. and Somers, J. A. Numerical simulation of free convective flow using the lattice-Boltzmann scheme. *International Journal of Heat and Fluid Flow*, 16(5):357–364, 1995. ISSN 0142-727X. doi:10.1016/0142-727X(95)00052-R.

Eggersdorfer, M. L., Kadau, D., Herrmann, H. J., and Pratsinis, S. E. Fragmentation and restructuring of soft-agglomerates under shear. *Journal of Colloid and Interface Science*, 342(2):261–268, 2010. ISSN 00219797. doi:10.1016/j.jcis.2009.10.062.

Ehrl, L., Soos, M., and Morbidelli, M. Dependence of aggregate strength, structure, and light scattering properties on primary particle size under turbulent conditions in stirred tank. *Langmuir*, 24(7):3070–3081, Apr. 2008. ISSN 0743-7463. doi:10.1021/la7032302.

Ehrl, L., Soos, M., and Lattuada, M. Generation and geometrical analysis of dense clusters with variable fractal dimension. *The Journal of Physical Chemistry B*, 113(31):10587–10599, 2009. doi:10.1021/jp903557m.

Enskog, D. *Kinetische theorie der vorgänge in mässig verdünnten gasen: I. Allgemeiner teil*, volume 1. Almqvist & Wiksells boktryckeri-a.-b., 1917.

Office of Water (4606), . 25 years of the safe drinking water act: History and trends, 1999.

Ernst, M., Dietzel, M., and Sommerfeld, M. A lattice boltzmann method for simulating transport and agglomeration of resolved particles. *Acta Mechanica*, 224(10):2425–2449, 2013.

Ernst, M. and Sommerfeld, M. Resolved numerical simulation of particle agglomeration. In *Colloid Process Engineering*, pages 45–71. Springer, 2015.

Feke, D. L., Prabhu, N. D., Mann, J. A. J., and Mann, J. A. L. A formulation of the short-range repulsion between spherical colloidal particles. *The Journal of Physical Chemistry*, 88(23): 5735–5739, Nov. 1984. ISSN 0022-3654. doi:10.1021/j150667a055.

Di Felice, R. The voidage function for fluid-particle interaction systems. *International Journal of Multiphase Flow*, 20(1):153–159, 1994. doi:10.1016/0301-9322(94)90011-6.

Frappier, G., Lartiges, B. S., and Skali-Lami, S. Floc cohesive force in reversible aggregation: A couette laminar flow investigation. *Langmuir*, 26(13):10475–10488, 2010. doi:10.1021/la9046947.

Frisch, U., d'Humieres, D., Hasslacher, B., Lallemand, P., Pomeau, Y., Rivet, J.-P., and others, . Lattice gas hydrodynamics in two and three dimensions. *Complex Systems*, 1:649–707, 1987.

Frungieri, G. and Vanni, M. Dynamics of a shear-induced aggregation process by a combined Monte Carlo-Stokesian Dynamics approach. In *Proceedings of the 9th International Conference on Multiphase Flow*, 2016.

Frungieri, G. and Vanni, M. Shear-induced aggregation of colloidal particles: A comparison between two different approaches to the modelling of colloidal interactions. *The Canadian Journal of Chemical Engineering*, 95(9):1768–1780, 2017.

Frungieri, G. *A novel Monte Carlo - Discrete Element Method approach for the micro-mechanics of colloidal suspensions*. PhD thesis, Politecnico di Torino, Turin, Italy, 2018.

Gastaldi, A. and Vanni, M. The distribution of stresses in rigid fractal-like aggregates in a uniform flow field. *Journal of Colloid and Interface Science*, 357(1):18–30, 2011.

Ghosh, M. M., Cox, C. D., and Prakash, T. M. Polyelectrolyte selection for water treatment. *Journal AWWA*, 77(3):67–73, 1985. doi:10.1002/j.1551-8833.1985.tb05510.x.

Glasgow, L. A. and Hsu, J. P. An experimental study of floc strength. *AIChE Journal*, 28(5):779–785, 1982. doi:10.1002/aic.690280512.

Glasgow, L. A. and Liu, X. Response of aggregate structures to hydrodynamic stress. *AIChE journal*, 37(9):1411–1414, 1991.

Gmachowski, L. Calculation of the fractal dimension of aggregates. *Colloids and Surfaces A: Physicochemical and Engineering Aspects*, 211(2):197–203, 2002. ISSN 09277757. doi:10.1016/S0927-7757(02)00278-9.

Gosselin, P., Hrudey, S. E., Naeth, M. A., Plourde, A., Therrien, R., Van Der Kraak, G., and Xu, Z. Environmental and health impacts of canada's oil sands industry, 2010.

Gregory, J. and Guibai, L. Effects of dosing and mixing conditions on polymer flocculation of concentrated suspensions. *Chemical Engineering Communications*, 108(1):3–21, 1991. doi:10.1080/00986449108910948.

Gregory, J. The density of particle aggregates. *Water Science and Technology*, 36(4):1–13, 1997. ISSN 0273-1223. doi:10.1016/S0273-1223(97)00452-6. The Role of Particle Characteristics in Separation Processes.

Griborio, A. G. *Secondary Clarifier Modeling: A multi-process approach*. PhD thesis, University of New Orleans, 2004.

Guerin, L., Frances, C., Liné, A., and Coufort-Saudejaud, C. Fractal dimensions and morphological characteristics of aggregates formed in different physico-chemical and mechanical flocculation environments. *Colloids and Surfaces A: Physicochemical and Engineering Aspects*, 560:213–222, 2019. doi:10.1016/j.colsurfa.2018.10.017.

Guo, Z., Zheng, C., and Shi, B. Discrete lattice effects on the forcing term in the lattice boltzmann method. *Physical Review E*, 65:046308, 2002. doi:10.1103/PhysRevE.65.046308.

Haddadi, H. and Morris, J. F. Topology of pair-sphere trajectories in finite inertia suspension shear flow and its effects on microstructure and rheology. *Physics of Fluids*, 27(4):043302, 2015. doi:10.1063/1.4917030.

Hallberg, M., Jönsson, P. G., Jonsson, T. L. I., and Eriksson, R. Process model of inclusion separation in a stirred steel ladle. *Scandinavian Journal of Metallurgy*, 34(1):41–56, 2005. doi:10.1111/j.1600-0692.2005.00716.x.

Hamaker, H. C. The London-van der Waals attraction between spherical particles. *Physica*, 4(10):1058–1072, 1937. ISSN 00318914. doi:10.1016/S0031-8914(37)80203-7.

Hannah, S., Cohen, J., and Robeck, G. Measurement of floc strength by particle counting. *American Water Works Association*, 59(7):843–858, 1967.

Harada, S., Tanaka, R., Nogami, H., and Sawada, M. Dependence of fragmentation behavior of colloidal aggregates on their fractal structure. *Journal of Colloid and Interface Science*, 301(1):123–129, 2006.

Harada, S., Tanaka, R., Nogami, H., Sawada, M., and Asakura, K. Structural change in non-fractal particle clusters under fluid stress. *Colloids and Surfaces A: Physicochemical and Engineering Aspects*, 302(1):396–402, 2007.

Hardy, W. B. A preliminary investigation of the conditions which determine the stability of irreversible hydrosols. *The Journal of Physical Chemistry*, 4(4):235–253, 1900. doi:10.1021/j150022a001.

Harshe, Y. M., Ehrl, L., and Lattuada, M. Hydrodynamic properties of rigid fractal aggregates

of arbitrary morphology. *Journal of Colloid and Interface Science*, 352(1):87–98, 2010. ISSN 0021-9797. doi:10.1016/j.jcis.2010.08.040.

Harshe, Y. M., Lattuada, M., and Soos, M. Experimental and modeling study of breakage and restructuring of open and dense colloidal aggregates. *Langmuir*, 27(10):5739–5752, May 2011. doi:10.1021/la1046589.

Harshe, Y. M. and Lattuada, M. Breakage rate of colloidal aggregates in shear flow through Stokesian dynamics. *Langmuir*, 28(1):283–292, Jan. 2012. ISSN 0743-7463. doi:10.1021/la2038476.

Harshe, Y. M. and Lattuada, M. Universal breakup of colloidal clusters in simple shear flow. *The Journal of Physical Chemistry B*, 120(29):7244–7252, 2016. doi:10.1021/acs.jpcb.6b03220.

Higashitani, K., Iimura, K., and Sanda, H. Simulation of deformation and breakup of large aggregates in flows of viscous fluids. *Chemical Engineering Science*, 56(9):2927–2938, 2001.

Higuera, F. J., Succi, S., and Benzi, R. Lattice gas dynamics with enhanced collisions. *Europhysics Letters (EPL)*, 9(4):345–349, jun 1989. doi:10.1209/0295-5075/9/4/008.

Higuera, F. J. and Jiménez, J. Boltzmann approach to lattice gas simulations. *Europhysics Letters (EPL)*, 9(7):663–668, aug 1989. doi:10.1209/0295-5075/9/7/009.

Hodges, C. S., Cleaver, J. A. S., Ghadiri, M., Jones, R., and Pollock, H. M. Forces between polystyrene particles in water using the AFM: Pull-off force vs particle size. *Langmuir*, 18(15): 5741–5748, 2002. doi:10.1021/la025604q.

Hodges, C. S., Looi, L., Cleaver, J. A. S., and Ghadiri, M. Use of the JKR model for calculating adhesion between rough surfaces. *Langmuir*, 20(22):9571–9576, 2004. doi:10.1021/la035790f.

Horii, K., Yamada, R., and Harada, S. Strength deterioration of nonfractal particle aggregates in simple shear flow. *Langmuir*, 31(29):7909–7918, 2015.

Inamuro, T. and Ii, T. Lattice Boltzmann simulation of the dispersion of aggregated particles under shear flows. *Mathematics and Computers in Simulation*, 72(2):141–146, Sept. 2006. ISSN 0378-4754. doi:10.1016/j.matcom.2006.05.022.

Israelachvili, J. N. *Intermolecular and Surface Forces*. Academic press, 2015.

International Union of Pure and Applied Chemistry. *Compendium of Polymer Terminology and Nomenclature, IUPAC Recommendations 2008*. Cambridge - Royal Society of Chemistry, 2008.

Iwashita, K. and Oda, M. Rolling resistance at contacts in simulation of shear band development by DEM. *Journal of Engineering Mechanics*, 124(3):285–292, mar 1998. doi:10.1061/(ASCE)0733-9399(1998)124:3(285).

Jarvis, P., Jefferson, B., and Parsons, S. A. Breakage, regrowth, and fractal nature of natural organic matter flocs. *Environmental Science & Technology*, 39(7):2307–2314, 2005. doi:10.1021/es048854x.

Kadau, D., Bartels, G., Brendel, L., and Wolf, D. E. Contact dynamics simulations of compacting cohesive granular systems. *Computer Physics Communications*, 147(1-2):190–193, aug 2002. doi:10.1016/S0010-4655(02)00242-4.

Rastegari, K., Svrcek, W. Y., and Yarranton, H. W. Kinetics of asphaltene flocculation. *Industrial & Engineering Chemistry Research*, 43(21):6861–6870, 2004. doi:10.1021/IE049594V.

Kinoshi, M. and Koyanagi, A. Effect of nonmetallic inclusions on rolling-contact fatigue life in bearing steels. *Bearing Steels: The Rating Nonmetallic Inclusion*, 575:138, 1975.

Kobayashi, M., Adachi, Y., and Ooi, S. Breakup of fractal flocs in a turbulent flow. *Langmuir*, 15 (13):4351–4356, 1999.

Kobayashi, M. Breakup and strength of polystyrene latex flocs subjected to a converging flow. *Colloids and Surfaces A: Physicochemical and Engineering Aspects*, 235(1):73–78, 2004. ISSN 0927-7757. doi:10.1016/j.colsurfa.2004.01.008.

Kobayashi, M. Strength of natural soil flocs. *Water Research*, 39(14):3273–3278, 2005. ISSN 0043-1354. doi:10.1016/j.watres.2005.05.037.

Kroll-Rabotin, J.-S., Gisselbrecht, M., Ott, B., May, R., Fröhlich, J., and Bellot, J.-P. Multiscale simulation of non-metallic inclusion aggregation in a fully resolved bubble swarm in liquid steel. *Metals*, 10:517, 2020. doi:10.3390/met10040517.

Kroupa, M., Vonka, M., Soos, M., and Kosek, J. Size and structure of clusters formed by shear induced coagulation: Modeling by discrete element method. *Langmuir*, 31(28):7727–7737, July 2015. ISSN 0743-7463. doi:10.1021/acs.langmuir.5b01046.

Kusters, K. A. *The influence of turbulence on aggregation of small particles in agitated vessels*. PhD thesis, Technische Univ., Eindhoven (Netherlands), 1991.

Laskowski, J. and Ralston, J. *Colloid Chemistry in Mineral Processing*. Elsevier, 2015. ISBN 1-4832-9091-3.

Lazzari, S., Nicoud, L., Jaquet, B., Lattuada, M., and Morbidelli, M. Fractal-like structures in colloid science. *Advances in Colloid and Interface Science*, 235:1–13, 2016.

Krüger, T., Kusumaatmaja, H., Kuzmin, A., Shardt, O., Silva, G., and Viggen, E. M. *The Lattice Boltzmann Method: Principles and Practice*. Springer, 2016.

Lee, H. and Kim, C. Experimental study on reversible formation of 2d flocs from plate-like particles dispersed in newtonian fluid under torsional flow. *Colloids and Surfaces A: Physicochemical and Engineering Aspects*, 548:70–84, 2018. ISSN 0927-7757. doi:10.1016/j.colsurfa.2018.03.043.

Lian, G., Thornton, C., and Adams, M. J. Discrete particle simulation of agglomerate impact coalescence. *Chemical Engineering Science*, 53(19):3381–3391, 1998.

Lichti, G., Gilbert, R. G., and Napper, D. H. The mechanisms of latex particle formation and growth in the emulsion polymerization of styrene using the surfactant sodium dodecyl sulfate. *Journal of Polymer Science Part A: Polymer Chemistry*, 21(1):269–291, 1983.

Lieu, U. T. and Harada, S. Stability of restructured non-fractal aggregates in simple shear flow. *Advanced Powder Technology*, 26(3):705–710, 2015.

Lieu, U. T. and Harada, S. Restructuring capability of non-fractal aggregate in simple shear flow. *Advanced Powder Technology*, 27(4):1037–1046, July 2016. ISSN 0921-8831. doi:10.1016/j.apt.2016.03.009.

Liu, S. X. and Glasgow, L. A. Aggregate disintegration in turbulent jets. *Water, Air, and Soil Pollution*, 95(1-4):257–275, 1997.

Liu, H., Qi, Z., and Xu, M. Numerical simulation of fluid flow and interfacial behavior in three-phase argon-stirred ladles with one plug and dual plugs. *Steel Research International*, 82(4):440–458, 2011.

Liu, D., Wang, Z., Chen, X., and Liu, M. Simulation of agglomerate breakage and restructuring in shear flows: Coupled effects of shear gradient, surface energy and initial structure. *Powder Technology*, 336:102–111, 2018. doi:10.1016/j.powtec.2018.05.051.

Long, Y., Dabros, T., and Hamza, H. Structure of water/solids/asphaltenes aggregates and effect of mixing temperature on settling rate in solvent-diluted bitumen. *Fuel*, 83(7-8):823–832, 2004.

Lurie, M. and Rebhun, M. Effect of properties of polyelectrolytes on their interaction with particulates and soluble organics. *Water Science and Technology*, 36(4):93–101, 1997. ISSN 0273-1223. doi:10.1016/S0273-1223(97)00425-3. The Role of Particle Characteristics in Separation Processes.

Madan, M., Satish, D., and Mazumdar, D. Modeling of mixing in ladles fitted with dual plugs. *ISIJ International*, 45(5):677–685, 2005.

Marchioli, C. and Soldati, A. Turbulent breakage of ductile aggregates. *Phys. Rev. E*, 91:053003, May 2015. doi:10.1103/PhysRevE.91.053003.

Masliyah, J. H., Czarnecki, J., and Xu, Z. *Handbook on theory and practice of bitumen recovery from Athabasca oil sands*. Kingsley, 2011.

Masliyah, J., Zhou, Z. J., Xu, Z., Czarnecki, J., and Hamza, H. Understanding water-based bitumen extraction from Athabasca oil sands. *The Canadian Journal of Chemical Engineering*, 82(4): 628–654, 2004.

Matijević, E. and Babu, S. Colloid aspects of chemical–mechanical planarization. *Journal of Colloid and Interface Science*, 320(1):219–237, 2008.

Gisselbrecht, M. *Simulation des interactions hydrodynamiques entre inclusions dans un métal liquide : établissement de noyaux d'agrégation dans les conditions représentatives du procédé de flottation*. PhD thesis, Université de Lorraine, 2019.

McFarlane, A. J., Addai-Mensah, J., Bremmell, K., and others, . Rheology of flocculated kaolinite dispersions. *Korea-Australia Rheology Journal*, 17(4):181–190, 2005.

McNamara, G. R. and Zanetti, G. Use of the boltzmann equation to simulate lattice-gas automata. *Phys. Rev. Lett.*, 61:2332–2335, Nov 1988. doi:10.1103/PhysRevLett.61.2332.

Meakin, P. A historical introduction to computer models for fractal aggregates. *Journal of Sol-Gel Science and Technology*, 15(2):97–117, 1999.

Méndez, C. G., Nigro, N., and Cardona, A. Drag and non-drag force influences in numerical simulations of metallurgical ladles. *Journal of Materials Processing Technology*, 160(3):296–305, 2005.

Mezzenga, R., Schurtenberger, P., Burbidge, A., and Michel, M. Understanding foods as soft materials. *Nature Materials*, 4(10):729–740, 2005.

Miao, Q., Huang, L., and Chen, L. Advances in the control of dissolved and colloidal substances present in papermaking processes: A brief review. *BioResources*, 8(1):1431–1455, 2013.

Mikulencak, D. R. and Morris, J. F. Stationary shear flow around fixed and free bodies at finite reynolds number. *Journal of Fluid Mechanics*, 520:215, 2004. doi:10.1017/S0022112004001648.

Moussa, A. S., Soos, M., Sefcik, J., and Morbidelli, M. Effect of solid volume fraction on aggregation and breakage in colloidal suspensions in batch and continuous stirred tanks. *Langmuir*, 23(4): 1664–1673, 2007. doi:10.1021/la062138m.

Murray R., G. *Upgrading Oilsands Bitumen and Heavy Oil*. Pica Pica Press, 2015.

Neelakantan, R., Vaezi G., F., and Sanders, R. S. Effect of shear on the yield stress and aggregate structure of flocculant-dosed, concentrated kaolinite suspensions. *Minerals Engineering*, 123: 95–103, 2018. ISSN 0892-6875. doi:10.1016/j.mineng.2018.03.016.

Nguyen, N.-Q. and Ladd, A. Lubrication corrections for lattice-Boltzmann simulations of particle suspensions. *Physical Review E*, 66(4):046708, 2002. doi:10.1103/PhysRevE.66.046708.

Nicoud, L., Owczarz, M., Arosio, P., and Morbidelli, M. A multiscale view of therapeutic protein aggregation: a colloid science perspective. *Biotechnology Journal*, 10(3):367–378, 2015.

Nir, A. and Acrivos, A. On the creeping motion of two arbitrary-sized touching spheres in a linear shear field. *Journal of Fluid Mechanics*, 59(2):209–223, 1973.

Niu, X. D., Shu, C., Chew, Y. T., and Peng, Y. A momentum exchange-based immersed boundary-lattice Boltzmann method for simulating incompressible viscous flows. *Physics Letters A*, 354(3): 173–182, 2006. doi:10.1016/j.physleta.2006.01.060.

O'Neill, M. On asymmetrical slow viscous flows caused by the motion of two equal spheres almost in contact. In *Mathematical Proceedings of the Cambridge Philosophical Society*, volume 65, pages 543–556. Cambridge University Press, 1969.

Pantina, J. P. and Furst, E. M. Elasticity and critical bending moment of model colloidal aggregates. *Physical Review Letters*, 94(13):138301, Apr. 2005. doi:10.1103/PhysRevLett.94.138301.

Pantina, J. P. and Furst, E. M. Colloidal aggregate micromechanics in the presence of divalent ions. *Langmuir*, 22(12):5282–5288, 2006. doi:10.1021/LA0534120.

Peskin, C. S. Flow patterns around heart valves: A numerical method. *Journal of Computational Physics*, 10(2):252–271, Oct. 1972. ISSN 00219991. doi:10.1016/0021-9991(72)90065-4.

Phung, T. N., Brady, J. F., and Bossis, G. Stokesian Dynamics simulation of brownian suspensions. *Journal of Fluid Mechanics*, 313:181–207, 1996. doi:10.1017/S0022112096002170.

Pukánszky, B. and Móczó, J. Morphology and properties of particulate filled polymers. In *Macromolecular Symposia*, volume 214, pages 115–134. Wiley Online Library, 2004. doi:10.1002/masy.200451009.

Frank, R. A., Roy, J. W., Bickerton, G., Rowland, S. J., Headley, J. V., Scarlett, A. G., West, C. E., Peru, K. M., Parrott, J. L., Conly, F. M., and Hewitt, L. M. Profiling oil sands mixtures from industrial developments and natural groundwaters for source identification. *Environmental Science & Technology*, 48(5):2660–2670, 2014. doi:10.1021/es500131k.

Roma, A. M., Peskin, C. S., and Berger, M. J. An adaptive version of the immersed boundary method. *Journal of Computational Physics*, 153:509–534, 1999.

Rundlöf, M. *Interaction of dissolved and colloidal substances with fines of mechanical pulp-Influence on sheet properties and basic aspects of adhesion*. PhD thesis, Institutionen för pappers-och massateknologi, 2002.

Rwei, S.-P., Manas-Zloczower, I., and Feke, D. Observation of carbon black agglomerate dispersion in simple shear flows. *Polymer Engineering & Science*, 30(12):701–706, 1990.

Saha, D., Soos, M., Lüthi, B., Holzner, M., Liberzon, A., Babler, M. U., and Kinzelbach, W. Experimental characterization of breakage rate of colloidal aggregates in axisymmetric extensional flow. *Langmuir*, 30(48):14385–14395, 2014.

Saha, D., Bäbler, M. U., Holzner, M., Soos, M., Lüthi, B., Liberzon, A., and Kinzelbach, W. Breakup of finite-size colloidal aggregates in turbulent flow investigated by three-dimensional (3d) particle tracking velocimetry. *Langmuir*, 32(1):55–65, 2016. doi:10.1021/acs.langmuir.5b03804.

Schlauch, E., Ernst, M., Seto, R., Briesen, H., Sommerfeld, M., and Behr, M. Comparison of three simulation methods for colloidal aggregates in Stokes flow: Finite elements, lattice Boltzmann and Stokesian dynamics. *Computers & Fluids*, 86:199–209, 2013. doi:10.1016/j.compfluid.2013.07.005.

Schroeder, C. M., Teixeira, R. E., Shaqfeh, E. S., and Chu, S. Characteristic periodic motion of polymers in shear flow. *Physical Review Letters*, 95(1):018301, 2005.

Selomulya, C., Bushell, G., Amal, R., and Waite, T. Aggregation mechanisms of latex of different particle sizes in a controlled shear environment. *Langmuir*, 18(6):1974–1984, 2002.

Serra, T. and Casamitjana, X. Structure of the aggregates during the process of aggregation and breakup under a shear flow. *Journal of Colloid and Interface Science*, 206(2):505–511, 1998.

Seto, R., Botet, R., and Briesen, H. Hydrodynamic stress on small colloidal aggregates in shear flow using Stokesian dynamics. *Physical Review E*, 84(4):041405, Oct. 2011. doi:10.1103/PhysRevE.84.041405.

Seto, R., Botet, R., Auernhammer, G. K., and Briesen, H. Restructuring of colloidal aggregates in shear flow. *The European Physical Journal E*, 35(12):128, Dec. 2012a. ISSN 1292-8941. doi:10.1140/epje/i2012-12128-4.

Seto, R., Botet, R., and Briesen, H. Viscosity of rigid and breakable aggregate suspensions Stokesian Dynamics for rigid aggregates. In *Progress in Colloid and Polymer Science*, volume 139, pages 85–90, 2012b. doi:10.1007/978-3-642-28974-3_15.

Sivamohan, R. The problem of recovering very fine particles in mineral processing—a review. *International Journal of Mineral Processing*, 28(3-4):247–288, 1990.

Smith, P. and Van De Ven, T. Shear-induced deformation and rupture of suspended solid/liquid clusters. *Colloids and Surfaces*, 15:191–210, 1985.

v. Smoluchowski, M. Grundriß der Koagulationskinetik kolloider Lösungen. *Kolloid-Zeitschrift*, 21 (3):98–104, Sept. 1917. ISSN 0303-402X. doi:10.1007/BF01427232.

Sonntag, R. C. and Russel, W. B. Structure and breakup of flocs subjected to fluid stresses: I. Shear experiments. *Journal of Colloid and Interface Science*, 113(2):399–413, 1986.

Sonntag, R. C. and Russel, W. B. Structure and breakup of flocs subjected to fluid stresses: Ii. theory. *Journal of Colloid and Interface Science*, 115(2):378–389, 1987.

Soos, M., Moussa, A. S., Ehrl, L., Sefcik, J., Wu, H., and Morbidelli, M. Effect of shear rate on aggregate size and morphology investigated under turbulent conditions in stirred tank. *Journal of Colloid and Interface Science*, 319(2):577–589, 2008. doi:10.1016/j.jcis.2007.12.005.

Soos, M., Ehrl, L., Bäbler, M. U., and Morbidelli, M. Aggregate breakup in a contracting nozzle. *Langmuir*, 26(1):10–18, 2010. doi:10.1021/la903982n.

Spicer, P. T. and Pratsinis, S. E. Shear-induced flocculation: the evolution of floc structure and the shape of the size distribution at steady state. *Water Research*, 30(5):1049–1056, 1996.

Strausz, O. P. and Lown, E. M. *The chemistry of Alberta oil sands, bitumens and heavy oils*. Alberta Energy Research Institute Calgary, AB, 2003.

Sungkorn, R. and Derksen, J. J. Simulations of dilute sedimenting suspensions at finite-particle reynolds numbers. *Physics of Fluids*, 24(12):123303, 2012.

Vaezi, F., Sanders, R. S., and Masliyah, J. H. Flocculation kinetics and aggregate structure of kaolinite mixtures in laminar tube flow. *Journal of Colloid and Interface Science*, 355(1):96–105, 2011.

Vajihinejad, V. and Soares, J. B. Monitoring polymer flocculation in oil sands tailings: A population balance model approach. *Chemical Engineering Journal*, 346:447–457, 2018.

Van Ende, M.-A. *Formation and morphology of non-metallic inclusions in aluminium killed steels*. PhD thesis, Université Catholique de Louvain, Leuven, Belgium, 2010.

Vanni, M. Creeping flow over spherical permeable aggregates. *Chemical Engineering Science*, 55 (3):685–698, Feb. 2000. ISSN 0009-2509. doi:10.1016/S0009-2509(99)00316-4.

Vanni, M. and Gastaldi, A. Hydrodynamic forces and critical stresses in low-density aggregates under shear flow. *Langmuir*, 27(21):12822–12833, Nov. 2011. ISSN 0743-7463. doi:10.1021/la2024549.

Vanni, M. Accurate modelling of flow induced stresses in rigid colloidal aggregates. *Computer Physics Communications*, 192:70–90, July 2015. ISSN 0010-4655. doi:10.1016/j.cpc.2015.02.022.

Vernerey, F., Benet, E., Blue, L., Fajrial, A., Sridhar, S. L., Lum, J., Shakya, G., Song, K., Thomas, A., and Borden, M. Biological active matter aggregates: Inspiration for smart colloidal materials. *Advances in Colloid and Interface Science*, 263:38–51, 2019. ISSN 0001-8686. doi:10.1016/j.cis.2018.11.006.

Vlieghe, M., Coufort-Saudejaud, C., Frances, C., and Liné, A. In situ characterization of floc morphology by image analysis in a turbulent taylor–couette reactor. *AIChE Journal*, 60(7): 2389–2403, 2014.

Mewis, J. and Wagner, N. J. *Colloidal Suspension Rheology*. Cambridge Series in Chemical Engineering. Cambridge University Press, 2011. doi:10.1017/CBO9780511977978.

Wallwork, V., Xu, Z., and Masliyah, J. Processibility of athabasca oil sand using a laboratory hyd ro t ransport extraction system (lhes). *The Canadian Journal of Chemical Engineering*, 82(4): 687–695, 2004.

Walther, J. H. and Sbalzarini, I. F. Large-scale parallel discrete element simulations of granular flow. *Engineering Computations*, 26(6), 2009. doi:10.1108/02644400910975478.

Wang, B. and Peng, Y. The effect of saline water on mineral flotation – a critical review. *Minerals Engineering*, 66-68:13–24, 2014. ISSN 0892-6875. doi:10.1016/j.mineng.2014.04.017. Froth Flotation.

Watson, P., Fenderson, T., Mahmoudkhani, A., Nair, M., Patel, A., and Roberts, G. Breakage and reformation of flocs in oil sands tailings slurries. In *Tailings and Mine Waste*, pages 293–302, 2011.

Wengeler, R. and Nirschl, H. Turbulent hydrodynamic stress induced dispersion and fragmentation of nanoscale agglomerates. *Journal of Colloid and Interface Science*, 306(2):262–273, 2007. doi:10.1016/j.jcis.2006.10.065.

Wiehe, I. A. *Process Chemistry of Petroleum Macromolecules*. CRC Press, 2008.

Wiese, G. and Healy, T. W. Effect of particle size on colloid stability. *Transactions of the Faraday Society*, 66:490–499, 1970.

Yeung, P. K. Lagrangian characteristics of turbulence and scalar transport in direct numerical simulations. *Journal of Fluid Mechanics*, 427:241–274, 2001. doi:10.1017/S0022112000002391.

Zaccone, A., Soos, M., Lattuada, M., Wu, H., Bäbler, M. U., and Morbidelli, M. Breakup of dense colloidal aggregates under hydrodynamic stresses. *Phys. Rev. E*, 79:061401, Jun 2009. doi:10.1103/PhysRevE.79.061401.

Zeidan, M., Xu, B. H., Jia, X., and Williams, R. A. Simulation of aggregate deformation and breakup in simple shear flows using a combined continuum and discrete model. *Chemical Engineering Research and Design*, 85(12):1645–1654, Jan. 2007. ISSN 0263-8762. doi:10.1016/S0263-8762(07)73208-2.

Zhang, L. and Thomas, B. G. State of the art in evaluation and control of steel cleanliness. *ISIJ International*, 43(3):271–291, 2003. doi:10.2355/isijinternational.43.271.

Zhou, S., McCorquodale, J., Richardson, J., and Wilson, T. State of the art clarifier modeling technology-part ii. In *Proceedings of the WEFTEC 78th Annual Technical Exhibition and Conference*, 2005.

Zia, I., Cox, R., and Mason, S. Ordered aggregates of particles in shear flow. *Proceedings of the Royal Society of London. Series A. Mathematical and Physical Sciences*, 300(1463):421–441, 1967.

Zou, Q. and He, X. On pressure and velocity boundary conditions for the lattice Boltzmann BGK model. *Physics of Fluids*, 9:1591, 1997. doi:10.1063/1.869307.